An Observational Study of the Structure and Evolution of Protostar Envelopes

Munetake MOMOSE

Doctor of Science

Department of Astronomical Science
School of Mathematical and Physical Science
The Graduate University for Advanced Studies

1997

Contents

ACKNOWLEDGEMENTS

First of all, I would like to express my hearty thanks to Prof. Takenori Nakano, my supervisor, for his advice and encouragement. I have benefited so much from his insight into astrophysics. I also thank Drs. Nagayoshi Ohashi, Ryohei Kawabe, Masahiko Hayashi and Masao Saito for their invaluable suggestions and comments on this work.

I thank Prof. Masato Ishiguro, Drs. Koh-Ichiro Morita, Sachiko K. Okumura, Seiichi Sakamoto, and Takahiro Tsutsumi for their effort to improve the Nobeyama Millimeter Array. I am greatful to Kiyoshi Nakajima, Hiroyuki Iwashita, Kazuyuki Handa, Toshikazu Takahashi, Naohisa Sato, and Tomio Kanzawa for their excellent technical work for the Nobeyama Millimeter Array. I also thank Drs. Nobuharu Ukita and Kazuyoshi Sunada for their help during the observations with the Nobeyama 45 m telescope. I have learned so much from discussion with Drs. Motohide Tamura, Naomi Hirano, Saeko S. Hayashi, Yoshimi Kitamura, and Ken'ichi Tatematsu. I thank Kazushi Sakamoto, Duk-Gyoo Roh, Kotaro Kohno, Yoshiaki Hagiwara, Takeshi Kamazaki, Satoki Matsushita, and Ray Furuya for their friendly help and encouragement.

Finally, I would like to thank my family, especially my mother who passed away in August 1996. I could never complete this dissertation without their continuous support and encouragement.

ABSTRACT

This thesis examines the structure and evolution of protostar envelopes through aperture synthesis observations of young stellar objects in the Taurus Molecular Cloud.

First, we made the $C^{18}O$ ($J = 1 - 0$) observations of the two protostar candidates L 1551 IRS 5 and L 1551 NE to investigate the structure of envelopes in the main accretion stage. These observations revealed the existence of centrally condensed, flattened envelopes with sizes greater than 1400 AU around these sources. The internal density structure and velocity field of the infalling envelope around L 1551 IRS 5 are obtained through the analysis of the high-resolution $C^{18}O$ ($J = 1 - 0$) images as follows:
(1) The envelope has either a moderately flattened density distribution or a spherical density distribution with a bipolar cavity whose half opening angle is about 50°.
(2) The velocity field in the envelope is composed of infall and slight rotation. The infall velocity is equal to the free-fall velocity around the central mass of $\sim 0.1 M_{\odot}$, or 0.5km s^{-1} at $r = 700$ AU, while the rotation velocity, 0.24km s^{-1} at the same radius, gets prominent at inner radii with a radial dependence of r^{-1}.
(3) The mass infall rate in the envelope is derived to be $\sim 6 \times 10^{-6} M_{\odot}$ yr^{-1}.

In order to investigate the evolution of protostar envelopes, it is necessary to select the objects that are in "the transitional phase" between the protostar stage and the T Tauri stage. For this purpose, we secondly made aperture synthesis ^{13}CO ($J = 1 - 0$) observations of 4 T Tauri stars with flat infrared spectra (flat-spectrum T Tauri stars), which are the most likely candidates for such objects. These observations revealed that most of the flat-spectrum T Tauri stars are accompanied by spatially extended gaseous structure that can be regarded as the remanant parts of the parent molecular cloud cores. In particular, the spatial distribution and velocity field of the observed gas around T Tauri can be interpreted in terms of the dispersion of the parent cloud core induced by the strong stellar wind. Such circumstellar environments around the flat-spectrum T Tauri stars strongly suggest that these sources are in the transitional phase from the protostars, which are deeply embedded in molecular cloud cores, to the typical T Tauri stars, around which the parent cloud cores have perfectly been dissipated.

Based on these results, we thirdly made the $C^{18}O$ ($J = 1 - 0$) observations of 4 flat-spectrum T Tauri stars that are accompanied by spatially-extended ^{13}CO ($J = 1 - 0$) emissions, and compared the observational results with those for protostar candidates. The $C^{18}O$ ($J = 1 - 0$) emissions around these sources commonly show spatially extended

structure with a size exceeding 10^3 AU, indicating the existence of the remaining parts of the parent cloud cores. However, the distributions of the $C^{18}O$ ($J = 1 - 0$) emissions are quite different from those around protostar candidates; unlike the cases of protostar candidates, the observed $C^{18}O$ ($J = 1 - 0$) emissions show no prominent peak at the stellar positions but have several bright peaks located far from the central stars. Such a difference in the spatial distribution of the $C^{18}O$ ($J = 1 - 0$) emission suggests that the degree of density concentration in the protostellar envelopes becomes weaker in the course of evolution from the protostar stage to the T Tauri stage probably because the matter in the central regions collapses to form protostars.

Chapter I

General Introduction

I.1. A Brief Review of Previous Studies of Star Formation

I.1.1. Before the 1980s

The formation of stars is one of the most important issues in modern astrophysics. Since the 1960s, it has been expected that the formation process of main-sequence stars from the interstellar medium can be divided into the following two stages: one is the stage where an interstellar cloud contracts dynamically due to its self-gravity, and the other is the succeeding stage where a central stellar core contracts quasi-statically (e.g., Hayashi 1966)[1]. The central hydrostatic cores, or young stellar objects, in the first stage are generally called "protostars", whereas those in the second stage are called "T Tauri stars". In this thesis, I also use this terminology.

T Tauri stars can be observed at optical wavelengths, and physical properties of these stars were obtained with the observational studies even before the 1980s (e.g., Cohen & Kuhi 1979). On the other hand, protostars themselves cannot be observed at optical wavelengths, because the interstellar medium surrounding protostars contains dust particles with a size $\sim 0.1\mu$m that absorb and scatter the light from central protostars. For this reason, the observational information on the physical property of protostars was quite limited, though some candidates for protostars were found with near-infrared observations (e.g., Strom, Strom, & Vrba 1976). However, theoretical studies revealed general characteristics of the cloud contraction in the protostar stage (e.g., Narita, Nakano & Hayashi 1970; Shu 1977): first a small hydrostatic core (protostar) forms at the center of a cloud, and next the protostar gradually grows by accretion of matter caused by dynamical collapse of the surrounding cloud. The region in a cloud where dynamical infall is taking place is usually called "a protostar envelope" or "an infalling envelope".

I.1.2. After the 1980s

[1]In this thesis, I concentrate on the formation of low-mass ($\lesssim 3M_\odot$) stars. For stars with higher masses, the timescale for the quasi-static contraction of a stellar core (the Kelvin-Helmholtz timescale) is not so long as the timescale for the dynamical contraction of a cloud (the free-fall timescale), and such classifications are no longer valid (e.g., Palla 1991).

— The Current View on the Formation of Low Mass Stars —

After the 1980s, the situation was dramatically changed by the developement of the observational astronomy at infrared and millimeter wavelengths. These techniques enable us to observe the emissions from cold dust and molecular gas associated with young stellar objects. The current view on the formation of low-mass stars are largely based on studies made after the 1980s. In the following, I briefly review some previous studies and summarize the current view on the formation of low mass stars.

I.1.2.1. Molecular Cloud Cores — Formation Sites of Low Mass Stars —

Dense gas from which stars are formed can be observed with various emission lines of molecules at millimeter and submillimeter wavelengths. Myers and his collaborators made observations of visually opaque regions with various emission lines of molecules such as NH_3, $C^{18}O$, and ^{13}CO, and found many dense regions in dark clouds (Myers, Linke, & Benson 1982; Benson & Myers 1989 and references therein). Such dense regions in molecular clouds are now ususally called "molecular cloud cores". The typical size, kinetic temperature, and density of these molecular cloud cores were estimated to be $\sim$ 0.05 pc or $\sim 10^4$ AU in radius, $\sim$ 10 K, and $\sim 3 \times 10^4$ cm^{-3} in number density of hydrogen molecule (Myers & Benson 1983). In the mid-1980s, the infrared astronomical satellite (IRAS) conducted all sky surveys at far-infrared wavelengths, and found that around half of these molecular cloud cores contain infrared sources without optical counterpart (Beichman et al. 1986; Myers et al. 1987). As described later, these sources can be regarded as candidates for protostars, indicating that the molecular cloud cores are the formation sites of low-mass stars. So far, systematic surveys of molecular cloud cores have been made for dark clouds (e.g., Onishi et al. 1995) and also for giant molecular clouds (e.g., Tatematsu et al. 1993), and their physical properties have extensively been studied.

I.1.2.2. Classification of Young Stellar Objects by their Spectral Energy Distributions (SEDs)

Understanding of the physical properties and evolution of young stellar objects has been improved by the considerations of the emitting mechanisms of their spectral energy distributions (SEDs). Based on the results of the IRAS survey, Lada (1987) proposed that

young stellar objects can be divided into three classes by their spectral indices $\alpha_{\rm IR}$, which is the mean value of $d(\log \lambda F_\lambda)/d(\log \lambda)$ in the wavelength range between $\lambda = 1\mu$m and 10μm: class I with $\alpha_{\rm IR} > 0$, class II with $-2 < \alpha_{\rm IR} \leq 0$, and class III with $-3 < \alpha_{\rm IR} \leq -2$ (see Figure I.1). Class I sources are often found at the centers of molecular cloud cores without optical counterparts, and their SEDs can be reproduced by the emission from mass-accreting protostars (Adams & Shu 1986; Kenyon, Calvet, & Hartmann 1993a): cold dust particles contained in an infalling envelope absorb the emission from a central protostar and re-emit radiation at longer (i.e., mid- to far-infrared) wavelenghts. On the other hand, class II and class III sources correspond to T Tauri stars. The SEDs of class II sources can be well explained with a system composed of a central star and a circumstellar disk (Kenyon & Hartmann 1987; Adams, Lada, & Shu 1987): the emissions in the wavelength region of $\lambda \lesssim 2\mu$m is well fitted by reddened blackbodies originating from central stars, whereas the "excess" emissions in the longer wavelength region can be explained by the thermal emissions of dust paricles contained in circumstellar disks with temperature $10 - 2000$ K. The SEDs of class III sources can easily be explained with only the emission from a central star. On the basis of these considerations, it has been accepted that these SED classes correspond to different evolutionary stages of young stellar objects; class I sources are strong candidates for protostars, class II sources are T Tauri stars with circumstellar disks, and class III sources are T Tauri stars with no siginificant amount of circumstellar material (e.g., Adams et al. 1987).

I.1.2.3. Circumstellar Environment around Young Stellar Objects

The above picture of the evolution of young stars has been confirmed by high-resolution observations at millimeter wavelengths in the 1990s, as described in the following.

(a) Circumstellar Disks around T Tauri Stars

Although the existence of circumstellar disks around T Tauri stars were suggested by infrared observations, the disk mass cannot be obtained solely from these observations because disks are optically thick for the radiation whose wavelength is shorter than $\sim 100\mu$m. Beckwith et al. (1990) observed dust continuum emissions at 1.3 mm toward 86 T Tauri stars in the Taurus Molecular Cloud, and found that these T Tauri stars are commonly accompanied by circumstellar disks with mass $(0.001 - 1.0)\ M_\odot$. Since the global characteristics of these disks are quite similar to those of the "primodial solar nebula"

assumed in some models of the formation of the solar system (e.g., Hayashi, Nakazawa, & Nakagawa 1985), these disks are believed to be the precursors of the planetary systems, and are called "protoplanetary disks".

On the other hand, high-resolution millimeter observations detected the gaseous emissions from circumstellar disks around several T Tauri stars, e.g., GG Tauri (Kawabe et al. 1993; Dutrey, Guilloteau, & Simon 1994), GM Aurigae (Koerner, Sargent, & Beckwith 1993), DM Tauri (Saito et al. 1995), and four other T Tauri stars (Koerner & Sargent 1995). These gaseous components have a radius smaller than 10^3 AU, and most of their velocity fields can be explained in terms of the Keplerian rotation.

(b) Difference in the Circumstellar Environment between the Class I and Class II Sources

Aperture synthesis observations with a millimeter array are effective ways to investigate the circumstellar environment around young stellar objects. This is not only because of their high spatial resolutions but also because they can selectively pick up spatially compact components around young stars. Ohashi et al. (1996b) made aperture synthesis observations of 13 protostar candidates (class I sources) and 6 T Tauri stars (class II sources) in the Taurus Molecular Cloud with the 3 mm continuum and CS($J = 2 - 1$) emissions, and found that the mass distributions of circumstellar material around protostar candidates and those around T Tauri stars are quite different from each other: the amount of circumstellar material within $\sim 10^4$ AU around protostar candidates is much larger than that around T Tauri stars, but the amount of circumstellar material within the central $\sim$ 500 AU regions around protostar candidates tends to be smaller than that around T Tauri stars (see also Beckwith et al. 1990). Such difference in mass distribution can naturally be interpreted as the results of evolution, i.e., the central stars and circumstellar disks grow by mass accretion from the outer regions in the course of evloution from the protostar stage to the T Tauri stage (Figure I.2).

(c) Indication of Infall Motion around Protostar Candidates

Observations of class I sources with molecular lines have revealed that many of them commonly show features which can be regarded as indirect indications that circumstellar material around these sources are now infalling dynamically. For example, (i) these sources are associated with mass outflows, which must be driven by the energy released by mass accretion onto the central stellar objects (e.g., Kőnigl & Ruden 1993); and (ii) asymmetric

profiles of optically thick molecular lines from these sources can be reproduced by the emission from infalling spherical envelopes in which the excitation temperature of the gas is higher at inner radii (Zhou 1992).

More recently, aperture synthesis observations with molecular emission lines directly detected infall motion of circumstellar gas around several young stellar objects, e.g., HL Tauri (Hayashi, Ohashi, & Miyama 1993), L 1551 IRS 5 (Ohashi et al. 1996a; Saito et al. 1996), and L 1527 (Ohashi et al. 1997a). These observations are quite important, because the observational results straightfowardly provide the physical properties of infalling envelopes, namely, the density and kinematical structures of the envelope, and the mass infall rate.

I.2. The Motivation and Contents of the Thesis

Although the picture for the evolutionary process of young stellar objects has greatly been improved over the last decade as described above, there still remain a lot of problems to be solved. In this thesis, I focus on the following two issues.

(i) The detailed structure of infalling envelopes around protostars:

Since star-disk systems grow by mass inflow from protostar envelopes, it is important to investigate the desnity structure and kinematics of infalling envelopes in detail. Although recent interferometric observations have revealed the global physical properties of several infalling envelopes, observations with higher spatial resolutions are required in order to understand the internal structures of infalling envelopes and clarify the formation process of star-disk systems.

(ii) The evolution of envelopes in the course from the protostar stage to the T Tauri stage:

It is desired to reveal the termination mechanism of infall, because it must be deeply related to the mechanism that determines the mass of forming stars (Nakano, Hasegawa, & Norman 1995). However, it is one of the least understood issues in the star formation process. In order to solve this issue, it is important to understand the evolution of circumstellar envelopes in the course from the protostar stage to the T Tauri stage.

For the above purposes, I have made observations of circumstellar gas around young

stellar objects in the Taurus Molecular Cloud, which is one of the nearest ($d = 140$ pc, Elias 1978) formation sites of low-mass stars, by using the Nobeyama Millimeter Array (NMA) and the Nobeyama 45 m telescope. Using these telescopes, I investigate the structure of circumstellar gas within ~ 5000 AU (corresponding to $\sim 36''$) in radius around these young stars with a spatial resolution higher than ~ 1000 AU.

The outline of the thesis is as follows; In Chapters II and III, aperture synthesis $C^{18}O$ ($J = 1 - 0$) observations of the two protostar candidates L 1551 IRS 5 and L 1551 NE are described. These observations have revealed the existence of flattened envelopes with their sizes greater than 1400 AU around these sources. The detailed structure of the envelope around L 1551 IRS 5 is also discussed in Chapter II. In Chapters IV and V, ^{13}CO ($J = 1 - 0$) observations of four T Tauri stars with so-called "flat-spectrum " are reproted. The results strongly suggest that these flat-spectrum T Tauri stars are in the "transitional phase" from the protostar stage to the T Tauri stage. In Chapter VI, aperture synthesis $C^{18}O$ ($J = 1 - 0$) observations of four flat-spectrum T Tauri stars are described. The evolution of circumstellar envelopes from the protostar stage to the T Tauri stage can be discussed through the comparisons of the circumstellar environments between protostar candidates and flat-spectrum T Tauri stars.

— Figure Captions —

Fig. I.1.— Classification of young stellar objects by their spectral energy distributions (from Lada et al. 1993).

Fig. I.2.— A schematic illustration showing the difference in circumstellar mass distribution between protostars and T Tauri stars (from Hayashi 1994).

Fig. I.1

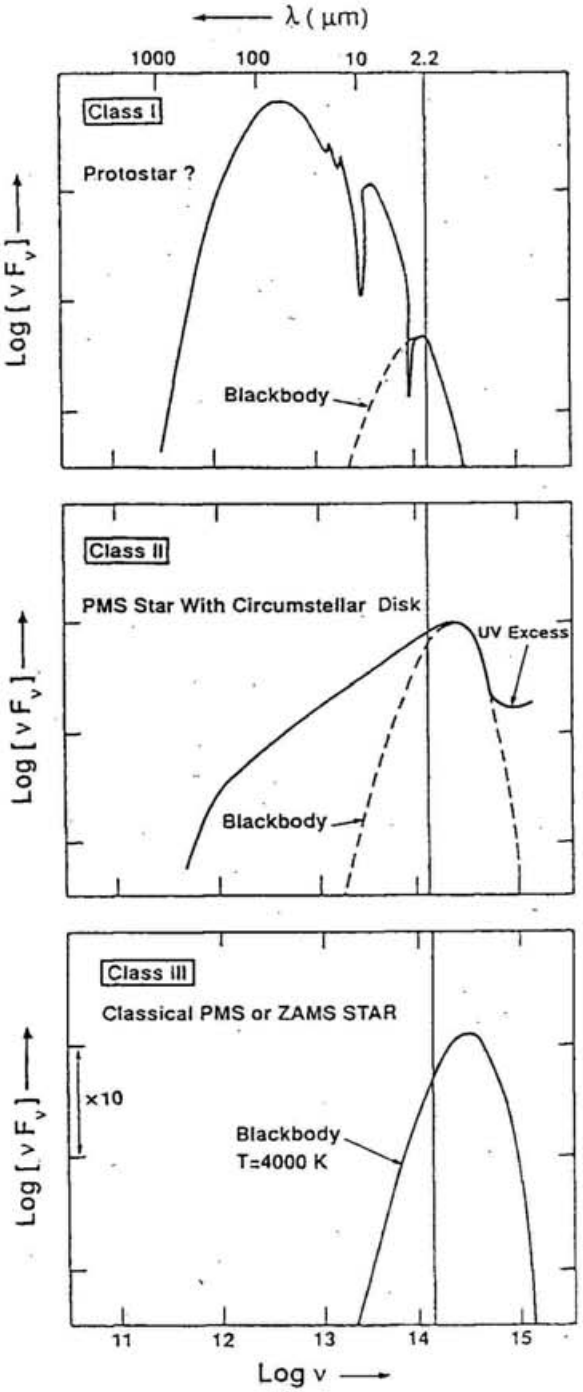
λ (μm)
1000
100
10
2.2
Class I
Protostar ?
Blackbody
Log [ν F_ν]
Class II
PMS Star With Circumstellar Disk
UV Excess
Blackbody
Log [ν F_ν]
Class III
Classical PMS or ZAMS STAR
×10
Blackbody
T=4000 K
Log [ν F_ν]
11
12
13
14
15
Log ν

Fig. I.2

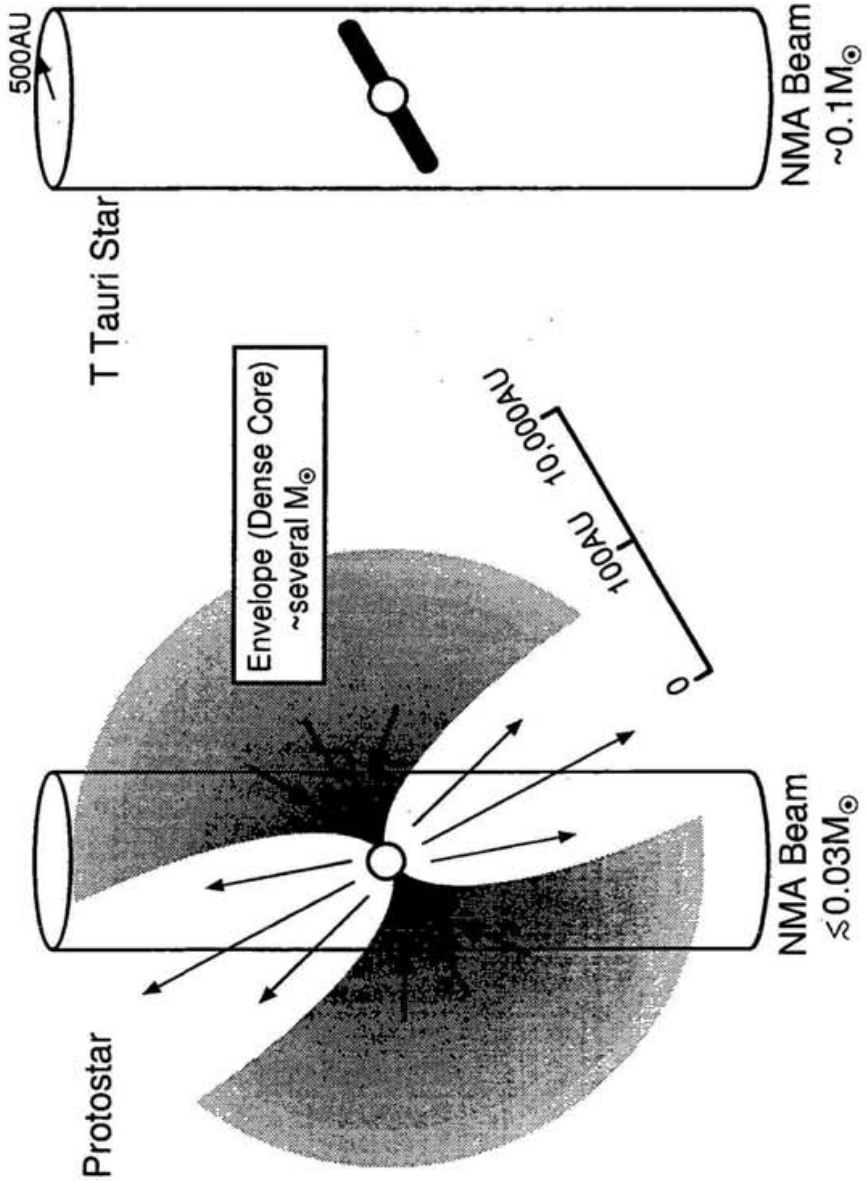
500AU
T Tauri Star
NMA Beam
~0.1M⊙
Envelope (Dense Core)
~several M⊙
100AU
10,000AU
0
NMA Beam
≲0.03M⊙
Protostar

Chapter II

Aperture Synthesis $C^{18}O$ ($J = 1 - 0$) Observations of L 1551 IRS 5: Detailed Structure of the Infalling Envelope

This chapter has been submitted to *The Astrophysical Journal* as

Aperture Synthesis $C^{18}O$ ($J = 1 - 0$) Observations of L 1551 IRS 5: Detailed Structure of the Infalling Envelope

by

Munetake MOMOSE[1], Nagayoshi OHASHI[2,3], Ryohei KAWABE[4], Takenori NAKANO[4], and Masahiko HAYASHI[5]

[1] Department of Astronomical Science, The Graduate University for Advanced Studies, Nobeyama Radio Observatory, Nobeyama, Minamimaki, Minamisaku, Nagano 384-1305, Japan

[2] Harvard-Smithsonian Center for Astrophysics, MS78, 60 Garden Street, Cambridge, MA 02138.

[3] present address: Academia Sinica Institute of Astronomy & Astrophysics, P.O. Box 1-87, Nankang, Taipei, Taiwan 115, R.O.C.

[4] Nobeyama Radio Observatory, Nobeyama, Minamimaki, Minamisaku, Nagano 384-1305, Japan

[5] Subaru Telescope, 650 North Aohoku Place, Hilo, Hawaii 96720.

ABSTRACT

We report aperture synthesis $C^{18}O$ ($J = 1 - 0$) observations of L 1551 IRS 5 with a spatial resolution of $2''.8 \times 2''.5$ using the Nobeyama Millimeter Array. We have detected an emission component centrally condensed around IRS 5, as well as a diffuse component extending in the north-south direction from the centrally condensed component. The centrally condensed component, 2380 AU $\times$ 1050 AU in size, is elongated in the direction perpendicular to the outflow axis, indicating the existence of a flattened circumstellar envelope around L 1551 IRS 5. The mass of the centrally condensed component is estimated to be $0.062 M_\odot$. The position-velocity (P-V) diagrams reveal that the velocity field in the centrally condensed component is composed of infall and slight rotation. The infall velocity in the outer part is equal to the free-fall velocity around a central mass of $\sim 0.1 M_\odot$, e.g., 0.5 km s^{-1} at $r = 700$ AU, while the rotation velocity, 0.24 km s^{-1} at the same radius, gets prominent at inner radii with a radial dependence of r^{-1}.

We make up P-V diagrams for the model envelopes with vertical structure, in which the matter falls under the gravity and eventually settles down in Keplerian rotation inside the centrifugal radius, and compare them with the observed P-V diagrams of the centrally condensed component. The main characteristics of the observed P-V diagrams are reproduced by either (1) an envelope with a moderately flattened density distribution, or (2) a spherical envelope with a bipolar cavity whose half-opening angle is about 50°. Detailed comparison of the observed and model P-V diagrams suggests that the $C^{18}O$ ($J = 1 - 0$) emission from the outer part of the centrally condensed component is well reproduced with the models with the central mass $\sim 0.15 M_\odot$ and the mass infall rate $\sim 6 \times 10^{-6} M_\odot$ yr^{-1}. However, the higher velocity features of the emission near the star cannot be reproduced unless the central mass is taken to be $\sim 0.5 M_\odot$. These facts suggest either that the gas pressure and/or magnetic force dilute the effect of the gravity in the outer part of the envelope, or that the velocity structure inside the centrifugal radius deviates significantly from the Keplerian rotation.

Subject headings: accretion, accretion disks — circumstellar matter — ISM: molecules — ISM: structure — stars: formation — stars: individual (L 1551 IRS

5) — stars: pre-main sequence

II.1. Introduction

It is widely accepted that forming stars grow by accretion of matter caused by dynamical collapse of circumstellar envelopes in the central parts of molecular cloud cores. Young stellar objects surrounded by dynamically infalling envelopes are generally called protostars. Observations conducted by the IRAS revealed the existence of many infrared sources which have no optical counterparts in molecular cloud cores (Beichman et al. 1986; Myers et al. 1987). These infrared sources are regarded as protostar candidates because they show common features which can be indirect evidences for ongoing infall. For example, (i) their spectral energy distributions can be reproduced by the emission from model protostars with mass accretion (e.g., Adams & Shu 1986; Kenyon, Calvet, & Hartmann 1993a); (ii) these sources are associated with mass outflows which are widely considered to be driven by the activities induced by mass accretion onto the central stellar objects (e.g., Kőnigl & Ruden 1993); and (iii) asymmetric profiles of optically thick molecular lines from these sources can be reproduced by the emission from infalling spherical envelopes in which the excitation temperatures of the molecules are higher at inner radii (Zhou 1992; Zhou et al. 1993; Walker, Narayanan, & Boss 1994; Myers et al. 1996). Although the above facts suggest that these IRAS sources are mass-accreting protostars, direct measurements of infall motions are desired since they can provide straightforwardly the information on the physical situations of the infalling envelopes such as their density distribution, kinematics, and mass infall rates.

Recent progress in the technique of aperture synthesis at millimeter wavelengths and developement of low-noise radio receivers have enabled us to make sensitive imaging observations of molecular gas around protostar candidates with high angular and velocity resolutions. Such observations have a potential to directly detect infalling envelopes around protostars. In fact, infalling envelopes around three young stellar objects in the Taurus Molecular Cloud have been imaged with the Nobeyama Millimeter Array (NMA) (Hayashi, Ohashi, & Miyama 1993; Ohashi et al. 1996a; Saito et al. 1996; Ohashi et al. 1997a). Table II.1 shows the physical parameters of the infalling envelopes of these objects obtained by them. These observations revealed that the infalling envelopes have flattened structures with radii greater than 1000 AU.

Although these observations have supplied clear evidences for the infall around young stellar objects and the global physical properties of their infalling envelopes, the density and kinematical structures inside a radius of $\sim$ 500 AU are poorly known because of the insufficient angular resolutions, which are typically $\sim 5''$ (see column 4 of Table II.1) corresponding to $\sim$ 700 AU at a distance of 140 pc to the Taurus Molecular Cloud (Elias 1978). In order to clarify the formation process of the star-disk systems in more detail, it is essential to reveal the inner structures of the infalling envelopes. Kinematics in the innermost parts of the envelopes is particularly important to investigating the formation process of protoplanetary disks, which are commonly found around T Tauri stars (e.g., Beckwith & Sargent 1993) and are believed to form through mass accretion from the envelopes in the protostellar stage (Ohashi et al. 1991; Ohashi et al. 1996b; Lin et al. 1994). Much higher angular resolution is a key to the detailed study of the formation of the star-disk systems.

Since the circumstellar environment has been best studied for L 1551 IRS 5 among the protostars listed in Table II.1, this is one of the best targets for higher resolution observations. Following the pioneering observations by Kaifu et al. (1984) who discovered a dense gaseous disk of radius 0.05 pc around IRS 5, Sargent et al. (1988) imaged the smaller-scale structure of the circumstellar envelope with the $C^{18}O$ ($J = 1 - 0$) line at $\sim 3''.5$ resolution, and found that the gaseous envelope has a disklike structure with a radius of 700 AU elongated in the direction perpendicular to the associated outflows. However, their obsevations did not have high enough sensitivity to study the kinematics of the envelope. Recently, Ohashi et al. (1996a) and Saito et al. (1996) (hereafter referred to as Paper I and Paper II, respectively) made aperture synthesis observations of the gaseous envelope around IRS 5 with the NMA, and revealed a velocity gradient along the minor axis of the disklike component. This velocity gradient suggests that the envelope material is infalling toward the central star-disk system (see Table II.1 for the physical quantities of the infalling envelope obtained by these observations). Observations with a much higher angular resolution have been performed in continuum emissions at millimeter and submillimeter wavelengths, and revealed the existence of an even more compact circumstellar disk with a radius smaller than 100 AU at the center of the infalling envelope (Keene & Masson 1990; Lay et al. 1994; Looney, Mundy, & Welch 1997). These continuum observations, however, cannot provide any kinematical information on the innermost part of the infalling envelope.

In this paper, we report the results of aperture synthesis observations of L 1551 IRS 5 with the 110 GHz continuum and $C^{18}O$ ($J = 1 - 0$) emissions using the NMA. Since

the ambient cloud around IRS 5 is optically thin to the $C^{18}O$ ($J = 1 - 0$) line, this is an appropriate line to reveal the density and kinematical structures of the infalling envelope. Obtained high sensitivity maps of $C^{18}O$ ($J = 1 - 0$) at a $2''.8 \times 2''.5$ resolution have revealed the detailed structure of the infalling envelope. We describe the details of the observations in § II.2, and present observational results in § II.3. We make model calculations and compare the results with the observational results in § II.4, and discuss the density and kinematical structures of the infalling envelope of L 1551 IRS 5 in § II.5.

II.2. Observations

The aperture synthesis $C^{18}O$ ($J = 1 - 0$) observations were carried out during a period from 1995 December to 1996 February with the NMA, which is composed of six 10 m dishes. We used the tunerless SIS receivers (Sunada, Kawabe, & Inatani 1993) whose system noise temperatures were typically 300 K (double sideband [DSB]) at the zenith. We employed the digital FFT spectral correlator FX (Chikada et al. 1987), which gave a frequency resolution of 78 kHz, corresponding to the velocity resolution of 0.215 km s^{-1} at the frequency of the $C^{18}O$ ($J = 1 - 0$) line. The continuum level, which was estimated by averaging line-free channels with an effective bandwidth of 65 MHz, was subtracted from the visibility. Three different array configurations, giving 45 baselines, were used for the observations. Because the minimum projected baseline length was 9 m, our observations were insensitive to structures of size greater than $62''$, corresponding to 8700 AU at the Taurus Molecular Cloud.[1] The phase and gain of the array system were calibrated by observing 0528+134 every 30 minutes. We used the same observations of 0528+134 to obtain the complex pass band of the FX. The flux density of 0528+134 was determined from observations of Uranus. The systematic error in the flux calibration is expected to be less than 10 %. The more details of the observational parameters are shown in Table II.2.

[1]When the projected baseline length is less than 10 m, which is the diameter of the dishes, the surface of one antenna is shaded by the other. However, for the projected baseline of 9 m the shaded area is only 4 % of the full aperture, and the error brought about on the visibility by the "shadowing effect" is small enough.

II.3. Results of the Observations

II.3.1. The 110 GHz Continuum Emission

We have made two maps of the 110 GHz continuum emission with the CLEAN algorithm by using the NRAO AIPS package as shown in Figure II.1. These maps were made from different sets of visivility data, and consequently have different angular resolutions and rms noise level, as listed in Table II.3. Also listed in Table II.3 are the position of the emission peak and the total flux density of the emission for each map. The continuum emission in Fig. II.1*a*, which was made with all the visibility data, is slightly elongated in the north-south direction compared with the synthesized beam, and spreads irregularly at the lowest contour level. Such irregular extensions imply that dust emission from the circumstellar envelope significantly contributes to the image in Fig. II.1*a*. In order to minimize the contribution of the emission from the extended envelope and assess the physical quantities of the circumstellar disk, we made the map in Fig. II.1*b* using only the visibility data taken with the sparsest configuration in our observations, achieving a $1\farcs3 \times 1\farcs2$ resolution. We can notice the north-south elongation in Fig. II.1*b*, which is more conspicuous than in Fig. II.1*a*. The beam deconvolved size (FWHM) of the emission is $(1\farcs55 \pm 0\farcs03) \times (0\farcs54 \pm 0\farcs04)$, corresponding to (220 ± 4) AU $\times$ (76 ± 6) AU, with a position angle (P.A.) of $171\fdg7 \pm 1\fdg4$. This size is consistent with that of Lay et al. (1994) when the difference in the observed frequency is taken into account. A similar north-south elongation of the dust emission from L 1551 IRS 5 has also been detected at $\lambda = 2.7$ mm by Looney et al. (1997). However, the elongation seen in our map is almost symmetric with respect to the peak position, whereas the dust emission resolved by Looney et al. (1997) extends more to the south of the peak than to the north. In this paper, we regard the peak position of the continuum emission in Fig. II.1*b* as the position of IRS 5.

Assuming that the circumstellar disk is optically thin at the 110 GHz continuum and the dust temperature within the disk, $T_{\rm dust}$, is uniform, we can estimate the disk mass by

$$M_{\rm disk} = \frac{F_\lambda d^2}{\kappa_\lambda B_\lambda (T_{\rm dust})}, \qquad \text{(II.1)}$$

where κ_λ is the mass absorption coefficient by dust grains, $B_\lambda(T)$ is the Planck function, F_λ is the total flux density of the continuum emission, and d is the distance to L 1551 IRS 5. With $T_{\rm dust} = 120$ K (Keene & Masson 1990), $\kappa_{2.7{\rm mm}} = 5.5 \times 10^{-3}$ cm^2 g^{-1} (see Ohashi et al. 1996b for details), and $d = 140$ pc, the total flux density of the continuum emission

in Fig. II.1*b*, 149±18 mJy, gives a disk mass of $0.057 \pm 0.007 M_{\odot}$, which is in reasonable agreement with Ohashi et al. (1991).

II.3.2. The $C^{18}O$ ($J = 1 - 0$) Emission

II.3.2.1. The Spatial Distribution of the Emission

We have made the $C^{18}O$ ($J = 1 - 0$) maps by applying natural weighting to the visibility data. The resultant synthesized beam size (HPBW) is $2''.8 \times 2''.5$ (P.A. = $0°.0$), and the rms noise level in the channel maps is 115 mJy beam^{-1} corresponding to 2.0 K. The $C^{18}O$ emissions above the 3σ level are detected within the velocity range of $V_{\rm LSR} = 4.75 - 7.73$ km s^{-1}.

Figure II.2 shows the integrated intensity map of the $C^{18}O$ ($J = 1 - 0$) emission superposed on a K'-band image (Hodapp 1994). As the ^{13}CO ($J = 1 - 0$) integrated intensity map in Paper I, the $C^{18}O$ emission can be decomposed into two components: a centrally condensed component with its peak at the stellar position, and a component extending north and south of the centrally condensed component at lower contour levels. The former component is elongated in the direction perpendicular to the outflow axis, which is defined by the symmetry axis of the fan-shaped reflection nebula in the K'-image, indicating the existence of a dense flattened envelope around the central star. The size of this emission component measured at the 3σ contour level is about $17'' \times 7''.5$, corresponding to 2380 AU × 1050 AU, and the position angle of its major axis is 162°. On the other hand, the component extending in the north-south direction in Fig. II.2 well deliniates the southern edge of the reflection nebula, suggesting that this component traces dense shells swept up by the energetic outflow, as was discussed in Paper I. In the following, we will mainly discuss the centrally condensed component.

Figure II.3 shows the distribution of the intensity-weighted mean velocity in the central region of the $C^{18}O$ ($J = 1 - 0$) emission. For comparison the distribution of the integrated intensity above the 3σ level is also shown by gray countours. The mean velocity contours manifest systematic velocity gradient in the centrally condensed component. The contour for $V_{\rm LSR} = 6.2$ km s^{-1}, which is the systemic velocity of L 1551 IRS 5 determined by the $C^{17}O$ ($J = 2 - 1$) observations (Fuller et al. 1995), passes through the stellar position, and the southwestern part of the centrally condensed component is blueshifted with respect to

the systemic velocity while the northeastern part is redshifted. This velocity gradient along the minor axis of the component (i.e., southwest[blue] - northeast[red]) is basically the same as those revealed in the previous works (Papers I and II), and can be interpreted by the infall motion within the flattened envelope because the southwestern part of the centrally condensed component has been confirmed to be the far side while the northeastern part to be the near side. However, inspecting more carefully the mean velocity distribution, we find that the velocity gradient in the vicinity of the central star is almost in the south(blue) to north(red) direction tilted from the global gradient described above. Such a velocity gradient near the star was not detected in the mean velocity map of the ^{13}CO line in Paper I. As will be described below, the south(blue) to north(red) velocity gradient near the star implies that the rotation velocity increases as the distance from the star decreases.

Figure II.4 shows the channel maps of the $C^{18}O$ ($J = 1 - 0$) emission, which provide detailed information on the velocity field. In the three channel maps near the systemic velocity (Figs. II.4g – 4i), strong emission features are seen along the major axis of the centrally condensed component. In addition to these features, weak and spatially extended features can also be seen: $\sim 10''$ south to the central star in Fig. II.4g, $\sim 15''$ north, $\sim 15''$ east, and $\sim 8''$ south to the star in Fig. II.4h, and $15'' - 20''$ north to the star in Fig. II.4i. These weak features must originate from dense shells swept up by the outflows, as discussed in Paper I. In the channel maps for the velocities blueshifted or redshifted by 0.43 km s^{-1} from the systemic velocity (Figs. II.4f and II.4j), one can find a pair of emission features; in Fig. II.4f a bright emission covers the southwestern part of the centrally condensed component, while in Fig. II.4j an emission above the 3σ level covers the northeastern part of the component. These two features well correspond to the general trend of the velocity shift blue(southwest)-red(northeast) along the minor axis of the component seen in Fig. II.3 that can be attributed to the infall motion in the flattened envelope. In the channel maps for the velocities blueshifted or redshifted by more than 0.86 km s^{-1} (Figs. II.4a – 4d and II.4l – 4o), one can find another pair of emission features. In the channel maps for the blueshifted velocities (Figs. II.4a – 4d), emissions are located at $\lesssim 1''$ south to the star, while in the maps for the redshifted velocities (Figs. II.4l – 4o), emissions are seen at $\lesssim 1''$ north to the star. All these higher velocity emissions are spatially compact and confined to the vicinity of the central star. More importantly, their velocity gradient is almost in the north to south direction, which is different from both the major and minor axes of the centrally condensed component. These features of the higher velocity emissions strongly suggest that the rotation becomes prominent as the gas approaches the central star, and as

a result, the rotation velocity gets comparable to the infall velocity in the innermost region. Otherwise, the velocity gradient would be observed either along the minor axis when the infall motion is dominant or along the major axis when the rotation is dominant.

In the following subsection (§ II.3.2.2), we will examine more quantitatively the velocity field of the centrally condensed component from the viewpoint that this component is a flattened envelope contracting dynamically with rotation. Since L1551 IRS 5 drives an energetic bipolar outflow (Uchida et al. 1987; Moriarty-Schieven & Snell 1988), one may anticipate that the centrally condensed component might be contaminated by the emission from the outflowing gas. However, this is unlikely, as will be shown in § II.3.2.3.

II.3.2.2. A Simple Analysis of the Position-Velocity Diagrams

We can confirm the characteristics of the velocity field described in § II.3.2.1 by inspecting the position-velocity (P-V) diagrams. Figure II.5 shows P-V diagrams along four different cuts; Fig. II.5*a* is along the major axis (P.A. = 162°: the cut A_1-A_2 in Fig. II.5*e*) of the centrally condensed component, Fig. II.5*b* is along the cut B_1-B_2 offset by 1.″65 southwest from the major axis, Fig. II.5*c* is along the cut C_1-C_2 offset by 1.″65 northeast from the major axis, and Fig. II.5*d* is along the minor axis (D_1-D_2). In Fig. II.5*a* one can easily find the following two features; (i) the southeastern part (relative position $\Delta < 0''$) of the centrally condensed component is mostly blueshifted while the northwestern part ($\Delta > 0''$) is redshifted, and (ii) these velocity shifts (blue or red) increase as the position approches the central star. These two features can be explained by rotation whose velocity is higher in the inner regions. In contrast to the P-V diagram along the major axis, the blueshifted emission is dominant in most parts in the diagram along the cut offset to the southwest (Fig. II.5*b*), whereas the redshifted emission is dominant along the cut offset to the northeast (Fig. II.5*c*). The blueshifted emission in Fig. II.5*b* gets bluer and the redshifted one in Fig. II.5*c* gets redder as the position approaches the center. These features can be explained by the infall motion in the flattened envelope. In addition, the most blueshifted emission in Fig. II.5*b* is not located at the center but is slightly shifted to the southeast ($\Delta < 0''$). This deviation can be explained by the rotation of the infalling envelope. The similar effect of the rotation can also be seen in Fig. II.5*c*. In Fig. II.5*d*, on the other hand, the blueshifted emission is dominant in the southwest part ($\Delta < 0''$) while the redshifted one is dominant in the northeast part, indicating the velocity gradient along the minor axis. Figure II.5*d* also shows a trend that higher velocity emissions are located

closer to the central star. These features along the minor axis can be attributed to the infall motion whose velocity is higher at the position closer to the central star.

A simple analysis under the assumption that the infalling envelope is geometrically thin is quite helpful in understanding the velocity structure of the envelope; we will make a detailed analysis in § II.4 with some elaborate model envelopes having vertical structure. In the following of this subsection we assume that the infalling envelope is infinitesimally thin and has an inclination angle equal to $\arccos(7\farcs5/17'') = 64°$ calculated from the shape of the centrally condensed component. Under these assumptions we first estimate the rotation velocity in the envelope from the P-V diagram along the major axis (Fig. II.5*a*), and then estimate the infall velocity from the P-V diagrams along the cuts offset from the major axis (Figs. II.5*b* & II.5*c*). The infall motions estimated from these two diagrams turn out to be consistent with the velocity features in the P-V diagram along the minor axis (Fig. II.5*d*).[2]

The velocity structure in Fig. II.5*a* can be well fitted by the dashed lines representing a rotation law

$$V_{\rm rot} = 0.24 \left(\frac{r}{700 \text{ AU}} \right)^{-1} \text{km s}^{-1}, \qquad \text{(II.2)}$$

at least at radius $r \gtrsim 300$ AU. This rotation law means that the specific angular momentum of the gas is constant at least in this region of the envelope. The Keplerian rotation velocity $\propto r^{-0.5}$ cannot reproduce the entire velocity structure; the observed line-of-sight velocity in the outer part ($|\Delta| \geq 5''$) is significantly smaller than the Keplerian velocity around a central star of mass 0.15 $M_\odot$ (solid lines in Fig. II.5*a*). This suggests that the gas in the centrally condensed component is not centrifugally supported but is infalling dynamically conserving the angular momentum. The innermost part ($|\Delta| \sim 1''$), however, can be fitted by either the r^{-1} or $r^{-0.5}$ law, suggesting that the gas shifts from dynamical infall motion with a constant angular momentum to rotationally supported motion at the innermost part because the centrifugal force increases as the gas contracts.

On the other hand, the observed features in Figures II.5*b* and II.5*c* can be well reproduced by the superposition of the rotaion and infall motions whose velocities are given,

---

[2]In principle, the P-V diagram along the minor axis can be used to investigate the infall motion, as was done in Papers I and II. However, it is rather difficult to estimate the infall velocity using this P-V diagram, because the spatial resolution is worst along the minor axis when the projection effect on the plane of the sky is taken into account. This is why we do not use the P-V diagram along the minor axis.

respectively, by equation (II.2) and by

$$V_{\rm infall} = \left(\frac{2GM}{r}\right)^{1/2} = 1.59 \left(\frac{M}{1\ M_\odot}\right)^{1/2} \left(\frac{r}{700\ {\rm AU}}\right)^{-1/2} {\rm km\ s^{-1}} \qquad \text{(II.3)}$$

The resultant distributions of the line-of-sight velocity are shown by the dashed lines for the cases of $M = 0.1M_\odot$ and $0.5M_\odot$ in Figures II.5*b* and II.5*c*. Most of the emission features in the two diagrams are well reproduced for the case of $M = 0.1M_\odot$, suggesting that the central stellar mass is close to $0.1M_\odot$. Equation (II.3) with $M = 0.1M_\odot$ also explains the main emission features in the P-V diagram along the minor axis, as shown in Fig. II.5*d*. This is consistent with Paper II, which concluded that the radial velocity in the envelope is much smaller than the free-fall velocity around a star of $1M_\odot$. However, in Figures II.5*b* and II.5*c* there also exist weak higher velocity features near the central star, which may be fitted well in the case of $M = 0.5M_\odot$ rather than $M = 0.1M_\odot$. This inconsistency cannot be attributed to the simplifications we have made here; even a more realistic model cannot reproduce all of the major emission features in Figs. II.5*b* and II.5*c* as will be shown in § II.4. We will discuss the physical implication of this in § II.5.1.

There are additional features such as the weak redshifted emission seen at $\Delta \geq 0''$ in Fig. II.5*b* and the weak blueshifted emission at $\Delta \leq 0''$ in Fig. II.5*c*, which cannot be reproduced by the above-mentioned simple model. Such emission features are observed when the infalling envelope with a finite geometrical thickness is seen nearly edge-on; the redshifted and blueshifted components can be attributed to the emissions arising from the near-side and the far-side of the infalling envelope, respectively, as will be shown in § II.4.

Equations (II.2) and (II.3) show that the rotation velocity is much smaller than the infall velocity in the outer regions while both velocities become comparable at the innermost parts of the infalling envelope resolved by our observations. According to equations (II.2) and (II.3), $V_{\rm rot}$ becomes equal to $V_{\rm infall}$ at $r \approx 160$ AU for $M = 0.1M_\odot$, which is comparable to the size of the 110 GHz continuum emission. The infall motion shifts to the centrifugally supported motion around the radius where $V_{\rm rot} \approx V_{\rm infall}$ is attained. Thus, the velocity distribution shown in equations (II.2) and (II.3) gives a natural scenario of the formation of a cenrifugally supported disk in the vicinity of the central star (Hayashi et al. 1993; Lin et al. 1994).

II.3.2.3. Possibility of Contamination of the Outflowing Gas

Although the velocity field in the centrally condensed component can well be explained by the motion composed of infall and rotation, the emissions contained in this component might partly arise from the outflowing gas. Three different kinds of outflows could contaminate the centrally condensed component, but none of them can explain consistently the present observational results as described in the following.

(i) If the $C^{18}O$ ($J = 1 - 0$) emissions in the centrally condensed component arose from outflowing gas with a disklike structure, the northeastern part should be the far-side while the southwestern part should be the near-side. However, this configuration is incompatible with the existence of the reflection nebula seen in the southwest of L 1551 IRS 5 (see Fig. II.2), and is easily ruled out.

(ii) If a considerable fraction of the $C^{18}O$ ($J = 1 - 0$) emissions originated from a well-collimated outflow, there would be emissions elongated in the outflow direction, as is the case of the optical jet ejected from IRS 5 (Mundt & Fried 1983). However, there are no clear tendencies of such emissions in the channel maps of the $C^{18}O$ ($J = 1 - 0$) emissions (Fig. II.4); either emission blueshifted or redshifted by ~ 0.43 km s^{-1} from the systemic velocity (Figs. II.4*f* and II.4*j*) is elongated in the direction perpendicular to the outflows. It is also unlikely that the higher-velocity emissions near the star (north[red]-south[blue], see Figs. II.4*a* – 4*d* and II.4*l* – 4*o*) originate from the outflowing gas because no outflows or jets along the north-south direction have been found around IRS 5.

(iii) If the $C^{18}O$ ($J = 1 - 0$) emissions partly originated from a poorly-collimated outflow such as a disk wind or a spherical wind, the blueshifted emissions would overlap the redshifted emissions near the central star because both velocity components would be observed along the same line-of-sight.[3] However, the channel maps show fairly clear difference in the spatial distribution between the blueshifted and the redshifted emissions, as described in § II.3.2.1. It is therefore quite difficult to explain the velocity field of the centrally condensed component in terms of the poorly-collimated outflow.

In addition to the above three arguments, the velocity structure of the $C^{18}O$ ($J = 1 - 0$) emissions around IRS 5 is qualitatively different from that of outflow emissions obtained

---

[3]This statement is also valid when the emissions originate from infalling envelopes with nearly spherically symmetric density distribution. See § II.4.

with the previous observations; the velocity of an outflow emission increases as the separation from the driving source increases even at a scale as small as $\sim$ 1000 AU (Tamura et al. 1996; Chandler et al. 1996), while the $C^{18}O$ ($J = 1 - 0$) emission around IRS 5 increases its velocity as the position gets closer to the central star. This velocity structure is naturally explained by the motion composed of infall and rotation whose velocities are higher in the inner regions, as shown in Fig. II.5.

In summary, any kinds of outflows cannot consistently explain the spatial distribution and the velocity field of the $C^{18}O$ ($J = 1 - 0$) emissions contained in the centrally condensed component. We therefore conclude that most of these $C^{18}O$ ($J = 1 - 0$) emissions originate from the envelope dynamically contracting with rotation.

II.3.2.4. Gas Mass and Mass Infall Rate in the Envelope

We can estimate the mass of the gas detected with the NMA by the following equation (Scoville et al. 1986):

$$M_{\rm gas} = 5.45 \times 10^{-4} T_{\rm ex} \exp\left(\frac{5.27}{T_{\rm ex}}\right) \frac{\tau_{\rm C^{18}O}}{1 - \exp\left(-\tau_{\rm C^{18}O}\right)} \left(\frac{d}{140\ {\rm pc}}\right)^2 \left[\frac{10^{-7}}{X({\rm C^{18}O})}\right] \int S_\nu dv\ M_\odot, \quad \text{(II.4)}$$

where $T_{\rm ex}$ is the excitation temperature of $C^{18}O$ at the $J = 1$ level, d is the distance to L 1551 IRS 5, $X(C^{18}O)$ is the fractional abundance of $C^{18}O$ relative to H_2, $\tau_{\rm C^{18}O}$ is the mean optical thickness of the gas for the $C^{18}O$ ($J = 1 - 0$) line, and $\int S_\nu dv$ is the integrated flux in units of Jy km s^{-1}. The integrated flux of $C^{18}O$ ($J = 1 - 0$) is 18.6 Jy km s^{-1} for the entire emission region, and is 10.9 Jy km s^{-1} for the centrally condensed component. By assuming $\tau_{\rm C^{18}O} \ll 1$, the total gas mass and the mass contained in the centrally condensed component are derived to be $0.106 M_\odot$ and $0.062 M_\odot$, respectively, with $T_{\rm ex} = 20$ K and $X(C^{18}O) = 2.5 \times 10^{-7}$ (Chernicharo & Guélin 1987). The former value, $0.106 M_\odot$, is half the mass contained within a radius of 2800 AU around L 1551 IRS 5, but is equal to the mass contained in the spatially compact structure with a radius of $\sim$ 1900 AU around the star (Fuller et al. 1995). These comparisons imply that our aperture synthesis observations are sensitive enough to almost completely detect the spatially compact, dense ($n(H_2)$ $\gtrsim 2 \times 10^5$ cm^{-3}, see Fuller et al. 1995) gaseous structure around L 1551 IRS 5, though the emission arising from the extended material seems to have been missed.

If $\tau_{\rm C^{18}O}$ were considerably larger than 1, the gas masses would be much larger than

those obtained above. However, the $C^{18}O$ ($J = 1 - 0$) emission has a brightness fainter than $B_\nu(T$=12 K), and the $C^{18}O$ ($J = 1 - 0$) emission detected by our observations has a symmetric profile with its peak at the systemic velocity (Figure II.6). These facts suggest that the $C^{18}O$ ($J = 1 - 0$) emission coming from the infalling envelope is neither optically saturated nor significantly suffering from the absorption by the foreground gas. Therefore we can conclude that the above estimations of the gas mass with the assumption $\tau_{C^{18}O} \ll 1$ are fairly good.

The mass infall rate in the envelope is estimated from the mass contained in the centrally condensed component and the infall velocity. By assuming that the surface density distribution of the envelope is given by $\Sigma(r) \propto r^{-1/2}$ and the radial velocity in the envelope is given by equation (II.3), the mass infall rate in the envelope is given by

$$M_{\rm infall} = 2\pi r \Sigma(r) V_{\rm infall}(r) = \frac{3}{2}\left(\frac{M_{\rm env}}{R_{\rm env}}\right)\left(\frac{2GM}{R_{\rm env}}\right)^{1/2} \qquad \text{(II.5)}$$

independent of r, where $M_{\rm env}$ and $R_{\rm env}$ is the total mass and the outer radius of the envelope, respectively. For $M_{\rm env} = 0.062 M_\odot$, $R_{\rm env} = 1200$ AU, and $M = 0.1 M_\odot$, we have $\dot{M}_{\rm infall} = 6.4 \times 10^{-6} M_\odot$ yr^{-1}, which is about half the previous estimations (Papers I and II)

II.4. Comparison with Model Calculations

II.4.1. Analytic Models of Infalling Envelopes

We have obtained in § II.3 the detailed structure of the spatially compact and dense gaseous envelope around L 1551 IRS 5. To clarify the physical situation of the envelope we compare the observational results with some envelope models with vertical structure. Although there are many theoretical works which dealt with protostellar collapse and derived the density and kinematical structures of infalling envelopes (e.g., Terebey, Shu, & Cassen 1984; Galli & Shu 1993a; Galli & Shu 1993b; Hartmann et al. 1994; Nakamura, Hanawa, & Nakano 1995; Saigo & Hanawa 1998), it is not easy to calculate the emergent emission with these envelope models. In this paper, we adopt some simple analytic models obtained by modifying the solution of Cassen & Moosman (1981) and Ulrich (1976) (hereafter referred to as the CMU solution).

The CMU solution is obtained under the following three assumptions; (i) the circumstellar material is freely falling with slight rotation, following parabolic trajectories

that terminate at the midplane of the envelope, (ii) the mass accretion rate and the central mass are constants of time, and (iii) the density on the spherical shell of radius r_0 (far from the central star) is constant. Taking into account the conservation of mass along a streamline in addition to the above three assumptions, one can obtain the density distribution for the CMU solution as

$$\rho_{\rm CMU}(r,\mu) = \frac{\dot{M}_{\rm infall}}{4\pi\,(GMr^3)^{1/2}} \left(1+\frac{\mu}{\mu_0}\right)^{-1/2} \left[\frac{\mu}{\mu_0}+\frac{2\mu_0^2}{(r/R_{\rm c})}\right]^{-1}, \tag{II.6}$$

where M is the central mass, $\dot{M}_{\rm infall}$ is the mass infall rate in the envelope, $\mu = \cos\theta$ is the direction cosine of a position angle θ on the streamline measured from the symmetry axis, $\mu_0 = \cos\theta_0$ is the direction cosine on the same streamline at r_0, and $R_{\rm c}$ is the so-called centrifugal radius, which is equivalent to the radius of the circumstellar disk. In the CMU solution, a streamline at $r \ll r_0$ is given by

$$r = R_{\rm c}(1-\mu_0^2)\left(1-\frac{\mu}{\mu_0}\right)^{-1} \tag{II.7}$$

As seen from equation (II.7), the circumstellar material eventually lands on the surface of the circumstellar disk ($\mu = 0$) at a radius $r \leq R_{\rm c}$.

Here we make two kinds of the envelope models by modifying the third assumption. In the first model the density distribution at r_0 is taken to be that of an isothermal gaseous sheet in hydrostatic equilibrium. This model was originally introduced by Hartmann, Calvet, & Boss (1996) to mimic the results of their numerical calculations (Hartmann et al. 1994). The density distribution for this model, $\rho_{\rm sheet}$, is given by

$$\rho_{\rm sheet}(r,\mu) = \rho_{\rm CMU}(r,\mu)\,\mathrm{sech}^2\,(\eta\mu_0)\,[\eta/\tanh\eta]\,, \tag{II.8}$$

where $\eta = r_0/H$ with H the scale height of the sheet. In this model, η characterizes the degree of modulation on the CMU solution; $\eta = 0$ corresponds to a spherically symmetric case, or the CMU solution, and as η increases, $\rho_{\rm sheet}$ approaches the case of an infinitesimally thin disk (see Hartmann et al. 1996 for further details of this model).

We make the second model by removing the circumstellar material at $|\mu| > \mu_{\rm cav} = \cos\theta_{\rm cav}$ from the CMU solution, which was originally introduced by Whitney & Hartmann (1993). The density distribution for this model, $\rho_{\rm cav}$, is expressed by

$$\rho_{\rm cav}(r,\mu) = \begin{cases} {\mu_{\rm cav}}^{-1}\rho_{\rm CMU}(r,\mu) & |\mu| \leq \mu_{\rm cav}, \\ 0 & |\mu| > \mu_{\rm cav}. \end{cases} \tag{II.9}$$

The conical holes around the symmetry axis in this model may be regarded as bipolar cavities evacuated by the energetic outflows, and $2\theta_{\rm cav}$ corresponds to the opening angle of the cavity at the far distance.

The overall structures of $\rho_{\rm sheet}$ and $\rho_{\rm cav}$ are different from each other, though both models have the same kinematical characteristics (the shape of streamlines and velocity field) as the CMU solution. In order to clarify this point, we show some examples of $\rho_{\rm sheet}$ and $\rho_{\rm cav}$ in Figure II.7. As seen from Fig. II.7, there are high density zones near the equatorial plane (abscissa) for $\rho_{\rm sheet}$, while $\rho_{\rm cav}$ is almost spherically symmetric except for the existence of the bipolar cavities. The structure of the envelopes obtained by numerical simulations of cloud collapse can also be classified into two categories; one is a group of envelopes which have strong density enhancement near the equatorial plane as the case of $\rho_{\rm sheet}$ (e.g., Galli & Shu 1993b; Nakamura et al. 1995; Saigo & Hanawa 1998), and the other is characterized by nearly spherical iso-density contours like the case of $\rho_{\rm cav}$ without cavity (e.g., Terebey et al. 1984). Therefore, these two analytic models may be regarded as the representatives of various envelope models.

The envelope models described above do not contain inner circumstellar disks. We add a disk of radius $R_{\rm c}$ at the center of the envelope when we calculate the emergent line emission. In our calculations, the velocity field in the disk is assumed to be Keplerian around the central mass M, and the surface density of the disk is taken to be $M_{\rm disk}/\pi R_{\rm c}^2$, constant throughout the disk.

II.4.2. Outline of Model Calculations

Before making comparison between the observational results and the results of model calculations, we outline the method of model calculations. See Appendix II.A for the details of the calculation procedure.

We calculate the emergent emission by the following steps. First, along each line of sight, we solve the radiative transfer equation by using the local column density of $C^{18}O$ in each bin of line-of-sight velocity, which is calculated from the density and velocity distributions of the model. In this step we obtain the brightness distributions of the emergent emission for all the velocity channels. Secondly, we make the channel maps for the model by convolving the brightness distributions with the synthesized beam of the observations. Finally, from the obtained channel maps we make P-V diagrams along the

major axis and those along the cut offset by 1".65 southwest from the major axis. In the first step, we neglect the contribution of the $C^{18}O$ emission arising from the regions with $n_{H_2} < 10^5$ cm^{-3}, because the emission components from these low-density regions are expected to be spatially too much extended to be detectable in our observations (see § II.3.2.4). The excitation temperature of $C^{18}O$ is taken to be 20 K in the envelope and 120 K in the circumstellar disk.

In this calculation we have to specify the following seven parameters; (1) the central mass, M, (2) the mass accretion rate in the envelope, $\dot{M}_{\rm infall}$, (3) the parameter η for the density distribution of the envelope $\rho_{\rm sheet}$, or $\theta_{\rm cav}$ for the case of $\rho_{\rm cav}$, (4) the centrifugal radius $R_{\rm c}$, (5) the mass of the circumstellar disk, $M_{\rm disk}$, (6) the inclination angle i of the disk around L 1551 IRS 5, and (7) the velocity dispersion (FWHM) ΔV of $C^{18}O$. Among these parameters, $R_{\rm c}$, $M_{\rm disk}$, i, and ΔV are fixed at the constant values shown in Table II.4, which are determined either by our observations or by some physical considerations as described in Appendix II.B. This simplification is reasonable because the resultant P-V diagrams are not very sensitive to these four parameters within their probable ranges (see Appendix II.B). On the other hand, the other three parameters M, $\dot{M}_{\rm infall}$, and η or $\theta_{\rm cav}$ define the density and kinematical structures of the model envelope, and as a result determine the major characteristics of calculated P-V diagrams. We therefore treat M, $\dot{M}_{\rm infall}$, and η or $\theta_{\rm cav}$ as free parameters, and try to reproduce the observed P-V diagrams by adjusting these parameters as shown in § II.4.3 and § II.4.4. Since P-V diagrams along the cut offset from the major axis contain the effect of infall as well as the effect of rotation, they are more convenient than those along the major axis for comparing the observational results with the model calculation. In § II.4.3 and § II.4.4, we use only the P-V diagrams along the southwest cut.[4] The calculated P-V diagrams along the major axis are shown in Appendix II.C.

---

[4]We assume that the model envelopes are isothermal, and that their density distribution and velocity field are axisymmetric. As a result, the calculated P-V diagrams along the southwest cut and those along the northeast cut are symmetric with respect to the point where the relative velocity = 0 km s^{-1} and $\Delta = 0''$. Since the observed P-V diagram along the southwest cut (Fig. II.5*b*) and that along the northeast cut (Fig. II.5*c*) are almost symmetric, we use only the P-V diagrams along the southwest cut when we compare the model calculation with the observations.

II.4.3. Comparison with the Sheet-Like Envelope Models

The left-hand panels in Figure II.8 show P-V diagrams along the cut offset by 1".65 southwest from the major axis for the sheet-like envelopes whose density structures are shown in the corresponding right-hand panels. The main difference among the three cases is in η. For each η, M has been adjusted so that the location of the brightest emission agrees with the observed location, and then $\dot{M}_{\rm infall}$ has been determined so that the calculated peak intensity agrees with the observed one. Since most of the material in the envelope is confined near the equatorial plane in this model, particularly in the cases of $\eta = 2$ and 3, M and $\dot{M}_{\rm infall}$ almost agree with the values for the geometrically thin model presented in § II.3.2, $M \approx 0.15 M_\odot$ and $\dot{M}_{\rm infall} \approx 6 \times 10^{-6} M_\odot$ yr^{-1}.

The calculated P-V diagrams basically have both blueshifted and redshifted emissions, which is one of the basic characteristics of the observed P-V diagram shown in Fig. II.5*b*. This is because in the sheet-like envelope with a finite thickness, both near- and far-sides of the envelope are observed along the same line of sight. The redshifted emission, which arises from the near-side of the envelope, weakens as η increases, or as the envelope becomes geometrically thinner. Among the three cases, the case of $\eta = 2$ (Fig. II.8*c*) gives the best fit to the observations (Fig. II.5*b*); this case reproduces well the observed emission feature at the velocity $\sim +0.3$ km s^{-1} and the relative position $\sim +3''$, while the other two cases cannot reproduce this feature. It should also be noted that the emission feature in Fig. II.8*c* is asymmetric with respect to the axis of the relative position at 0"; the peak in the blueshifted emission is shifted southeastward by $\sim 2''$, while the redshifted emission in the northwestern part ($\Delta > 0''$) is much more prominent than that in the southeastern part ($\Delta < 0''$). These features of the emission pattern is also seen in the observed P-V diagram shown in Fig. II.5*b*. These asymmetric patterns are due to rotation around the symmetry axis of the envelope.

Although the model of $\eta = 2$, $M = 0.15 M_\odot$, and $\dot{M}_{\rm infall} = 6 \times 10^{-6} M_\odot$ yr^{-1} gives the best fit to the observations, it cannot reproduce some of the emission features in the observed P-V diagrams. For example, in the observed P-V diagram (Fig. II.9*a*) there are emission features more than 0.7 km s^{-1} blueshifted or redshifted from the systemic velocity near the star, whereas there are no emissions corresponding to them in the best-fitted model P-V diagram (Fig. II.9*b*). This is because the higher velocity components in the case of $M = 0.15 M_\odot$ are so compact that they are diluted with the synthesized beam. In order to reproduce these higher velocity components with this model, a higher stellar mass is

required. In fact, when we take $M = 0.5 M_{\odot}$, the higher velocity components seem to be reproduced as shown in Fig. II.9*c*. In this case, however, the brightest emission appears at velocities ~ -0.8 km s^{-1} significantly higher than the observed ones ~ -0.3 km s^{-1}. As was described in § II.3.2.2, all of the major features in the observed P-V diargam cannot be reproduced with either a small or large stellar mass. We will discuss possible solutions to this dilemma in § II.5.1.

One might argue that the velocity widths in the calculated P-V diagrams at large distances $\sim 10''$ or ~ 1400 AU from the star are much wider than the observed widths (Fig. II.9). This is mainly due to the assumption that the gas takes such a velocity as is obtained when it started free-fall contraction at an infinite distance. This is a good approximation only at small distances from the central star; at large distances which are not much smaller than the distances where the gas began contraction, the actual contraction velocity is significantly smaller than the assumed one. Thus, under this assumption, the velocity width at large distances must be overestimated.

II.4.4. Comparison with the Envelope Models with Bipolar Cavity

Figure II.10 shows the resultant P-V diagrams for the envelope models with bipolar cavity. As in Fig. II.8 the left-hand panels show the P-V diagrams along the cut offset by $1''.65$ southwest from the major axis for the density structures $\rho_{\rm cav}$ shown in the corresponding right-hand panels. Three cases for $\theta_{\rm cav}$ are shown. For each $\theta_{\rm cav}$, we have determined M and $\dot{M}_{\rm infall}$ in the same way as in the case of the sheet-like envelopes.

The global characteristics of the P-V diagrams for these models are quite similar to those for the sheet-like envelopes; as the density distribution gets more flattened, or $\theta_{\rm cav}$ becomes larger, the redshifted emissions in the P-V diagram become weaker. In particular, there are no redshifted emissions when $\theta_{\rm cav} > i = 65°$ (see Fig. II.10*e*), because only the emissions arising from the far-side of the envelope are observed along this cut. We have found that the P-V diagram for the case of $\theta_{\rm cav} = 50°$ (Fig. II.10*c*) gives the best fit to the observations (Fig. II.5*b*). This value of $\theta_{\rm cav}$ is consistent with the results of Lucus & Roche (1996), who compared their high-resolution image at 2.2 μm with the emergent scattered light obtained for the same models with $\rho_{\rm cav}$. However, the higher-velocity components in the observed P-V diagram cannot be reproduced unless M is taken to be $\sim 0.5 M_{\odot}$, although the brightest emission in the case of a larger M appears at higher velocities than

the observed ones, as in the case of the sheet-like envelopes.

II.5. Discussion

II.5.1. Structure of the Circumstellar Envelope and the Stellar Mass

As shown in § II.4, the main characteristics of the observed P-V diagram along the cut offset by 1".65 southwest from the major axis can be well reproduced by the envelope models with geometrically thick, disklike structure. There are some other observational results which suggest the existence of geometrically thick disklike envelopes around protostars. For example, the polarization maps around protostar candidates at near-infrared wavelengths can be explained as due to the light scattered by dust particles in the geometrically thick envelopes (Whitney & Hartmann 1993; Kenyon et al. 1993b; Hartmann et al. 1996; Lucus & Roche 1996). Geometrically thick, disklike structure of an infalling envelope was also directly imaged around IRAS 04368+2557, which is another protostar candidate in Taurus (Ohashi et al. 1997a).

However, there still remains a problem to be solved in the P-V diagram: the low-velocity components in the infalling envelope can be reproduced with the central mass $M \sim 0.15 M_{\odot}$, while the high-velocity components in the stellar vicinity require $M \sim 0.5 M_{\odot}$. We have made the P-V diagrams under the assumptions that (1) the envelope material falls freely due to the gravity of the central point mass M, and (2) the circumstellar disk of radius R_c rotates with the Keplerian velocity under the gravity of the same point mass. Hence, either of the assumptions must be inappropriate.

One possibility is that the radial velocity in the envelope is significantly smaller than the free-fall velocity. According to Saigo & Hanawa's (1998) similarity solutions for the collapse of rotating protostellar clouds, the gas pressure and the centrifugal force dilute considerably the gravitational force, and as a result the radial velocity is much smaller than $(2GM_*/r)^{1/2}$, even when the magnetic force is neglected, where M_* is the mass of the central star. In our model, we have taken into account the effect of centrifugal force, but have neglected the effect of gas pressure and magnetic force (see Appendix II.A). If the sum of the pressure and magnetic forces in the outer part of the envelope is half the gravitational force, and their effects become negligible compared with the gravitational and centrifugal forces in the innermost part which is smaller than our synthesized beam, or at $r < 200$ AU,

the observed velocity structure around L 1551 IRS 5 can be explained with $M_* \sim 0.5 M_\odot$.

Another possibility is that the gas inside the centrifugal radius R_c is quite different from the Keplerian rotation. If the gas inside R_c has a complex velocity field such as non-circular motion, the emission at higher velocities must come from a large spatial region compared with the case of the Keplerian rotation, and therefore must be observed much more strongly because the dilution with our synthesized beam becomes smaller. Such a situation may arise from perturbations of the circumstellar gas by a protobinary system (Looney et al. 1997). In such circumstances the velocity structure around L 1551 IRS 5 may be realized with $M_* \sim 0.15 M_\odot$.

Because it is difficult to judge which case is more plausible from our observations, we cannot narrow down the possible range of the central stellar mass from $0.15 M_\odot < M_* < 0.5 M_\odot$. It may also be possible to estimate the stellar mass from the infall rate $\dot{M}_{\rm infall}$ and the infall timescale $t_{\rm infall}$ according to $M_* \approx \dot{M}_{\rm infall} \times t_{\rm infall}$. Substituting for $t_{\rm infall}$ the dynamical timescale of the outflow associated with L 1551 IRS 5, which was estimated to be 3×10^4 yr by Moriarty-Schieven & Snell (1988) and $\sim 10^5$ yr for the oldest part of the outflow by Bachiller, Taffala, & Chernicharo (1994), and taking $\dot{M}_{\rm infall} = 6 \times 10^{-6} M_\odot$ yr^{-1}, we obtain $0.18 M_\odot < M_* < 0.6 M_\odot$, which is in good agreement with the above-mentioned mass range.

II.5.2. High Mass Accretion Rate in the Circumstellar Disk

Because most of the luminosity of a low-mass protostar is expected to come from mass accretion, the mass accretion rate $\dot{M}_*$ can be estimated by

$$\dot{M}_* \approx \frac{L_{\rm bol} R_*}{G M_*} = 7.7 \times 10^{-6} \left(\frac{L_{\rm bol}}{30 L_\odot} \right) \left(\frac{R_*}{4 R_\odot} \right) \left(\frac{M_*}{0.5 M_\odot} \right)^{-1} M_\odot \ {\rm yr}^{-1}, \qquad \text{(II.10)}$$

where $L_{\rm bol}$ is the bolometric luminosity of the protostar and R_* is the radius of the central stellar core. With $L_{\rm bol} \sim 30 L_\odot$ for L 1551 IRS 5 (Cohen et al. 1984), the mass range obtained above, $0.15 M_\odot < M_* < 0.5 M_\odot$, and $R_* \sim 4 R_\odot$ (Stahler, Shu & Taam 1980), we obtain a possible range of the accretion rate $7.7 \times 10^{-6} M_\odot$ yr^{-1} $< \dot{M}_* < 2.6 \times 10^{-5} M_\odot$ yr^{-1}, which is comparable to or ~ 4 times higher than the infall rate in the outer envelope ($\dot{M}_{\rm infall}$). Thus, it is possible that the mass accretion rate at the stellar surface is considerably higher than the mass infall rate in the outer envelope.

Since $\dot{M}_{\rm infall}$ does not change much in a timescale significantly shorter than the protostellar stage, a possible situation of $\dot{M}_* > \dot{M}_{\rm infall}$ suggests that L 1551 IRS 5 is in the phase where the mass accretion rate from the inner circumstellar disk to the star is episodically high. Kenyon et al. (1993a) found that $\dot{M}_*$ is smaller than $\dot{M}_{\rm infall}$ by an order of magnitude for the cases of protostar candidates in Taurus except L 1551 IRS 5, and derived a similar conclusion. This interpretation is consistent with the fact that the reflection nebula associated with IRS 5 shows an FU Ori type spectrum (Mundt et al. 1985; Hartmann, Kenyon, & Hartigan 1993) and the outflow lobe shows successive high-velocity features along its axis, suggesting that the mass ejection events occured episodically (Bachiller et al. 1994). The circumstellar disk around L 1551 IRS 5 seems to be relatively massive compared with the central stellar mass ($M_{\rm disk} \gtrsim 0.1 M_*$, see § II.3.1 and § II.5.1). This may be a cause for the high mass accretion rate in the inner disk around L 1551 IRS 5.

II.6. Summary

We have made aperture synthesis observations of L 1551 IRS 5 with the 110 GHz continuum and $C^{18}O$ ($J = 1 - 0$) emissions by using the Nobeyama Millimeter Array (NMA). Our main results are summarized as follows:

1. A spatially compact continuum emission originating from the circumstellar disk has been imaged with a synthesized beam size of $1\farcs3 \times 1\farcs2$ (P.A.= 155°). The beam deconvolved size of the continuum emission is $1\farcs55 \times 0\farcs54$ (P.A.= 171°.7), corresponding to 220 AU × 76 AU at the distance of L 1551 IRS 5. The disk mass is derived to be $0.057 M_\odot$.

2. The $C^{18}O$ ($J = 1 - 0$) map with a spatial resolution of $2\farcs8 \times 2\farcs5$ (P.A.= 0°) shows two emission components: a centrally condensed component with its peak at the stellar position, and a diffuse component extending north and south of the centrally condensed component. The centrally condensed component is elongated in the direction perpendicular to the outflow axis, indicating the existence of a dense circumstellar envelope around IRS 5. The size of this component measured at the 3σ level is $17'' \times 7\farcs5$, corresponding to 2380 AU × 1050 AU. On the other hand, the diffuse component deliniates well the edge of the reflection nebula, suggesting that this emission arises from the shells swept up by the energetic outflows.

3. The total gas mass is derived to be $0.106 M_\odot$ and the gas mass contained in the centrally condensed component to be $0.062 M_\odot$. Comparison with the previous mapping

observations of the L 1551 IRS 5 region suggests that our observations have almost completely detected the emission which originates from the region of $n_{H_2} > 2 \times 10^5$ cm^{-3}.

4. A simple analysis of the observed P-V diagrams has revealed that the velocity field in the centrally condensed component is explained in terms of infall with rotation. In the outer part of the centrally condesed component, the infall velocity has a radial dependence $V_{\rm infall} \propto r^{-1/2}$ with $V_{\rm infall} = 0.5$ km s^{-1} at $r = 700$ AU, which is the free-fall velocity around the central mass of $\sim 0.1 M_\odot$, while the rotation velocity, 0.24 km s^{-1} at $r = 700$ AU, gets prominent at inner radii with a radial dependence of $V_{\rm rot} \propto r^{-1}$.

5. For some analytic models of the infalling envelope we have made up P-V diagrams under the assumptions that the envelope contracts freely under the gravity of the central star and that there is a thin, compact disk in Keplerian rotation. The main characteristics of the observed P-V diagram are reproduced by either (1) an envelope with a moderately flattened density distribution, or (2) a spherical envelope with bipolar cavities whose half-opening angle is about 50°. Detailed comparison of the observed and calculated P-V diagrams suggests that the C^{18}O ($J = 1 - 0$) emission from the outer part of the centrally condensed component is well reproduced for the cases where the central mass is $\sim 0.15 M_\odot$ and the mass infall rate is $\sim 6 \times 10^{-6} M_\odot$ yr^{-1}. However, the higher velocity features of the emission near the star cannot be reproduced with the models unless the central stellar mass is taken to be $\sim 0.5 M_\odot$. These facts suggest either that the gravitational force is significantly opposed by the pressure force and/or magnetic force in the outer part of the envelope, or that the velocity structure inside the centrifugal radius deviates significantly from the Keplerian rotation.

6. Based on the bolometric luminosity $\sim 30 L_\odot$ of L 1551 IRS 5 and the possible range of the stellar mass, (0.15-0.5) $M_\odot$, the mass accretion rate from the inner circumstellar disk to the star is estimated to be $(0.77 - 2.6) \times 10^{-5} M_\odot$ yr^{-1}, which is higher than the infall rate in the envelope. This suggests that L 1551 IRS 5 is in a phase of episodically high mass accretion rate.

APPENDIX

II.A. The Procedure of Model Calculation

We explain the calculation procedure of the P-V diagram for a model cloud that consists of an infalling envelope and an inner circumstellar disk. The kinematical characteristics of the envelopes adopted in this paper with the density distribution $\rho_{\rm sheet}$ and $\rho_{\rm cav}$ are the same as those of the CMU solution (Ulich 1976; Cassen & Moosman 1981).

We define a spherical coordinate system (r, θ, ϕ) where $\theta = 0$ is along the polar axis of the flattened envelope. The streamline of the infalling material at $r \ll r_0$ is then given by

$$r = R_{\rm c}(1 - \mu_0^2)\left(1 - \frac{\mu}{\mu_0}\right)^{-1}, \tag{II.A1}$$

where $R_{\rm c}$ is the centrifugal radius, and $\mu = \cos\theta$ and $\mu_0 = \cos\theta_0$ are the direction cosines at r and at the distant reference radius r_0, respectively. The velocity field can be given by

$$\begin{aligned} v_r &= -\left(\frac{GM}{r}\right)^{1/2}\left(1 + \frac{\cos\theta}{\cos\theta_0}\right)^{1/2}, \\ v_\theta &= \left(\frac{GM}{r}\right)^{1/2}\left(\frac{\cos\theta_0 - \cos\theta}{\sin\theta}\right)\left(1 + \frac{\cos\theta}{\cos\theta_0}\right)^{1/2}, \\ v_\phi &= \left(\frac{GM}{r}\right)^{1/2}\left(\frac{\sin\theta_0}{\sin\theta}\right)\left(1 - \frac{\cos\theta}{\cos\theta_0}\right)^{1/2}. \end{aligned} \tag{II.A2}$$

The above expressions of the streamline and the velocity field can be obtained under the assumptions that gas falls freely under the gravity of the central point mass M from infinity, and that the specific angular momentum of the gas is conserved along the streamline.

Next, we define for convenience the two cartesian coordinate systems (X, Y, Z) and (X', Y', Z') as shown in Figure II.11. We take the X- and Y-axes along the major and minor axes, respectively, of the infalling envelope projected on the plane of the sky, and the Z-axis along the line of sight. The X'-axis is taken along the X-axis and the Z'-axis along the symmetry (polar) axis of the envelope. The Y'-axis is taken perpendicular to both X'- and Z'-axes. The relations between (X, Y, Z) and (X', Y', Z') are given by

$$\begin{aligned} X &= X', \\ Y &= Y'\cos i + Z'\sin i, \\ Z &= -Y'\sin i + Z'\cos i, \end{aligned} \tag{II.A3}$$

where i is the inclination angle of L 1551 IRS 5. By taking the $\phi = 0$ direction along the X'-axis, the relations between (r, θ, ϕ) and (X', Y', Z') are given by

$$\begin{aligned} X' &= r \sin\theta \cos\phi, \\ Y' &= r \sin\theta \sin\phi, \\ Z' &= r \cos\theta. \end{aligned} \tag{II.A4}$$

For numerical calculation of the brightness distribution, we set up a mesh with spacings $\Delta X = \Delta Y = 10$ AU in the plane of the sky and $\Delta Z = 100$ AU along the line of sight. We then calculate the emergent brightness for each line of sight by solving the radiative transfer equation in the following way:

(i) We determine (r, θ, ϕ) for arbitrary values of (X, Y, Z) by solving equations (II.A3) and (II.A4).

(ii) We determine μ_0 for given values of r, θ, and R_c by solving equation (II.A1).

(iii) We calculate the local density $\rho(X, Y, Z)$ according to equation (II.8) or (II.9).

(iv) We calculate the line-of-sight velocity according to

$$v_{\rm los} = v_r\,(-\sin\theta \sin\phi \sin i + \cos\theta \cos i) - v_\theta\,(\cos\theta \sin\phi \sin i + \sin\theta \cos i) - v_\phi \cos\phi \sin i, \tag{II.A5}$$

which is obtained by differentiating equations (II.A3) and (II.A4) with time. The velocities v_r, v_θ, and v_ϕ in this expression are given by equations (II.A2).

(v) We approximate the local column density of $C^{18}O$ between the two positions $(X, Y, Z + \Delta Z/2)$ and $(X, Y, Z - \Delta Z/2)$ in the envelope in the line-of-sight velocity range $[v_1, v_2]$ by

$$\Delta N_{\rm env}(X, Y, Z, v_1, v_2) = \rho(X, Y, Z) \Delta Z \left(\frac{X(\mathrm{C^{18}O})}{m(\mathrm{H_2})} \right) \frac{1}{\sqrt{2\pi}} \int_{v_1}^{v_2} \exp\left(-\frac{4 \ln 2 (v - v_{\rm los})^2}{\Delta V^2} \right) dv, \tag{II.A6}$$

where $m(H_2)$ is the mass of an H_2 molecule.

(vi) We calculate the optical thickness between the two points for the $C^{18}O$ $(J = 1 - 0)$ line in the same line-of-sight velocity range according to

$$\Delta\tau(X, Y, Z, v_1, v_2) = \frac{8\pi^3 B \mu^2_{\mathrm{C^{18}O}}}{3kT_{\rm ex}|v_2 - v_1|} \Delta N_{\rm env}(X, Y, Z, v_1, v_2) \left[1 - \exp\left(-\frac{h\nu}{kT_{\rm ex}} \right) \right], \tag{II.A7}$$

where B and $\mu_{\mathrm{C^{18}O}}$ are the rotational constant and permanent dipole moment of the $C^{18}O$ molecule (see Scoville et al. 1986).

(vii) We determine the intensity I of the $C^{18}O$ ($J = 1 - 0$) line along the line of sight by solving the radiative transfer equation

$$I(X, Y, Z - \Delta Z/2, v_1, v_2) = I(X, Y, Z + \Delta Z/2, v_1, v_2)e^{-\Delta\tau} + B_\nu(T_{\rm ex})(1 - e^{-\Delta\tau}), \quad \text{(II.A8)}$$

where $B_\nu(T_{\rm ex})$ is the Planck function at the temperature $T_{\rm ex}$ and $\Delta\tau$ stands for $\Delta\tau(X, Y, Z, v_1, v_2)$ given by equation (II.A7). We take the boundary value at the far-side, $I(X, Y, +\infty, v_1, v_2) = 0$. In the actual calculation the contribution from the regions of $n_{\rm H_2} < 10^5$ cm^{-3} is neglected.

For the lines of sight crossing the disk, or $X^2 + (Y/\cos i)^2 \leq R_{\rm c}^2$, we take into account the contribution of the disk in step (vii). With the asssumption that the surface density of the disk is uniform and the disk is in Keplerian rotation, the line-of-sight velocity and the column density of $C^{18}O$ in each velocity bin in the disk are given, respectively, by

$$v_{\rm los} = -\left(\frac{GM}{\sqrt{X^2 + (Y/\cos i)^2}}\right)^{1/2} \cos\phi \sin i, \quad \text{(II.A9)}$$

$$N_{\rm disk}(X, Y, v_1, v_2) = \frac{M_{\rm disk}}{\pi R_{\rm c}^2 \cos i}\left(\frac{X(\rm C^{18}O)}{m(\rm H_2)}\right)\frac{1}{\sqrt{2\pi}}\int_{v_1}^{v_2} \exp\left(-\frac{4\ln 2(v - v_{\rm los})^2}{\Delta V^2}\right) dv, \quad \text{(II.A10)}$$

where $\cos\phi = X/\left[X^2 + (Y/\cos i)^2\right]^{1/2}$. The velocity dispersion ΔV in the disk is generally different from that in the envelope; see Table II.4 and Appendix II.B. The optical thickness of the disk is then calculated in a similar way as equation (II.A7) with a different value of $T_{\rm ex}$ from the envelope (see § II.4.2). In solving the radiative transfer equation like (II.A8) the disk is added to as a single zone.

With the above procedure we obtain the brightness distributions on the plane of the sky for all the velocity bins. We convolve them with the gaussian beam whose size is equal to the CLEANed beam in our observations, and make the P-V diagram for the model, which is to be compared with the observed P-V diagram.

II.B. Fixed Values in the Model Calculations

In § II.4.2, we have fixed the four parameters, $R_{\rm c}$, $M_{\rm disk}$, i, and ΔV at the values listed in Table II.4. We describe here how sensitive the results are to these quantities.

(i) The centrifugal radius $R_{\rm c}$ has been taken to be 100 AU, which is nearly equal to the observed size of the continuum emission (see § II.3.1). Although we also made calculations

for the cases of $R_c = 50$ AU and 150 AU, the resultant P-V diagrams showed no significant difference from those for the case of $R_c = 100$ AU. This is because the emission from the inner disk is negligible unless the disk radius is greater than the size of the synthesized beam.

(ii) The disk mass $M_{\rm disk}$ has been taken to be $0.057 M_\odot$, which was obtained from the continuum observations (see § II.3.1). We also made calculations for the case of $M_{\rm disk} = 0.1 M_\odot$, but the resultant P-V diagrams showed little difference from those for the case of $M_{\rm disk} = 0.057 M_\odot$.

(iii) The inclination angle i has been taken to be 65°, which was obtained from the ratio of the major to the minor axis of the centrally condensed component of the $C^{18}O$ ($J = 1 - 0$) emission. We also made calculations for the cases of $i = 55°$ and $i = 75°$, and found that the resultant P-V diagrams have almost the same characteristics as those for the case of $i = 65°$, and that the parameters of the best-fitting model, $M, \dot{M}_{\rm infall}$, and η or $\theta_{\rm cav}$, are hardly affected by i.

(iv) The velocity dispersion (FWHM) ΔV has been estimated in the following way. The effective random speed of $C^{18}O$, $C_{\rm eff}$, can be given by

$$C_{\rm eff} = \left(C^2 + v_{\rm turb}^2\right)^{1/2}, \tag{II.B1}$$

where $C = [kT/m(C^{18}O)]^{1/2}$ is the thermal speed of $C^{18}O$, and $v_{\rm turb}$ is the turbulent velocity in the circumstellar gas. Since recent studies have suggested that the gravitational collapse in a molecular cloud core occurs after the turbulent motions in the core decays substantially (e.g., Mizuno et al. 1994; Zhou et al. 1994; Nakano 1998), we assume that the turbulent motions in the envelope and the disk are subsonic, and take $v_{\rm turb}$ to be half of the thermal speed of molecular hydrogen, $C(H_2)$. In this case we have

$$C_{\rm eff} \approx v_{\rm turb} \approx \frac{1}{2} C(H_2). \tag{II.B2}$$

The velocity dispersion (FWHM) ΔV is then given by

$$\Delta V = (8 \ln 2)^{1/2} C_{\rm eff} \approx (2 \ln 2)^{1/2} C(H_2). \tag{II.B3}$$

By supposing that the kinetic temparature of the gas is equal to the excitaion temparature of $C^{18}O$, ΔV is given by

$$\Delta V = 0.34 \text{ km s}^{-1} \times \left(\frac{T_{\rm ex}}{20\text{K}}\right)^{1/2} \tag{II.B4}$$

Even if the turbulent velocity or ΔV is significantly smaller than our assumed value, the resultant P-V diagrams show little difference from those shown in this paper, because for a rather small velocity dispersion, the shape of the P-V diagram is determined mainly by the velocity resolution (0.215 km s^{-1}) of the observations. When we adopt much larger ΔV than the above, the velocity widths in the P-V diagram become wider than the observed ones.

II.C. P-V Diagrams along the Major Axis: Comparison of Model Calculations with Observations

Figure II.12 shows the resultant P-V diagrams along the major axis of the centrally condensed component for the sheet-like envelope models (Figs. II.12*a* – 12*c*) and for the envelope models with bipolar cavity (Figs. II.12*d* – 12*f*). The model parameters for Figures II.12*a* – 12*c* and for Figures II.12*d* – 12*f* are the same as those for Figures II.8*a*, II.8*c*, and II.8*e* and for Figures II.10*a*, II.10*c*, and II.10*e*, respectively. The calculated P-V diagrams commonly show the following two characteristics, which can also be identified in the observed P-V diagram (Fig. II.12*g*); (i) the distribution of the $C^{18}O$ ($J = 1 - 0$) emission is symmetric with respect to the central star (relative velocity = 0 km s^{-1} and $\Delta = 0''$), and (ii) the relative velocity of the emission increases as its position approaches the central star. The former characteristic is due to the axisymmetry of our envelope models, and the latter is mainly due to the increase of rotational velocity near the central star.

In addition to the above characteristics, additional observed features that the blueshifted emissions in the region $\Delta > 0''$ and the redshifted emissions in the region $\Delta < 0''$ (Fig. II.12*g*, see also § II.3.2.2) can be reproduced in the calculated P-V diagrams although these features cannot be explained by the simple analysis with the geometrically thin envelope (Fig. II.5*a*). As the thickness of the model envelope increases (i.e., η or θ_{cav} decreases), these additional emission features become more prominent. Among the calculated P-V diagrams in Figure II.12, the case of $\eta = 2$ (Fig. II.12*b*) and the case of $\theta_{cav} = 50°$ (Fig. II.12*e*) give the best fit to the observed P-V diagram (Fig. II.12*g*). However, even these best models cannot reproduce the higher velocity features near the star in the observed P-V diagrams. In order to reproduce the higher velocity features without changing the location of the brighter emissions in the outer regions, a higher stellar mass ($\sim 0.5 M_{\odot}$) is required. All these situations described above, including the best model parameters, are the same as in the P-V diagrams along the cut offset by 1.″65 southwest

from the major axis (see § II.4.3 and § II.4.4).

Table II.1. Infalling Gas around Young Stellar Objects in the Taurus Molecular Cloud.

Ref.	Source	Line	Beam Size (HPBW)	Mass ($M_\odot$)	Size[a] (AU)	Infall Rate ($M_\odot$ yr^{-1})
(1)	HL Tau	^{13}CO $(1-0)$	$5''.4 \times 4''.6$	0.03	2800×1100[b]	5×10^{-6}
(2)	L 1551 IRS 5	^{13}CO $(1-0)$	$5''.1 \times 3''.9$	$0.039 - 0.081$	1200×670[b]	$(1.3 - 2.6) \times 10^{-5}$
(3)	L 1551 IRS 5	$H^{13}CO^+$ $(1-0)$	$7''.9 \times 5''.8$	0.27	5600×2800[c]	1.1×10^{-5}
(4)	L 1527	$C^{18}O$ $(1-0)$	$6''.0 \times 4''.9$	0.038	2200×1200[b]	1.1×10^{-6}

References: (1) Hayashi et al. 1993, (2) Ohashi et al. 1996a, (3) Saito et al. 1996, (4) Ohashi et al. 1997a

[a]For the distance of 140 pc to the Taurus molecular cloud (Elias 1978)

[b]Measured by gaussian fitting (FWHM).

[c]Measured at the 3σ contour level.

Table II.2. Observational Parameters.

Array Configuration	D	C	AB
Date	Dec. 22, 1995	Feb. 5, 1996	Jan. 12 & 13, 1996
Min. Baseline Length	3.3 kλ	3.7 kλ	9.8 kλ
Max. Baseline Length	30 kλ	58 kλ	134 kλ
Flux Density of 0528+134	7.2 Jy	6.4 Jy	8.8 Jy

Field Center : $(\alpha_{1950}, \delta_{1950}) = (04^h28^m40\overset{s}{.}240, 18°01'42\overset{''}{.}1)$

Velocity Resolution : 0.215 km s^{-1}

Table II.3. Parameters for the Maps of the Continuum Emission.

	Fig. II.1a	Fig. II.1b
Array Configuration	D, C, and AB	AB
Weighting	Natural	Natural
Beam Size (HPBW)	$2\overset{''}{.}8 \times 2\overset{''}{.}5$	$1\overset{''}{.}3 \times 1\overset{''}{.}2$
P.A. of the Beam	0°	155°
RMS Noise Level	5.5 mJy beam^{-1}	5.8 mJy beam^{-1}
Peak Position		
R.A. (B1950)	$04^h28^m40\overset{s}{.}244$	$04^h28^m40\overset{s}{.}237$
Dec. (B1950)	$18°01'41\overset{''}{.}93$	$18°01'42\overset{''}{.}03$
Total Flux Density[a]	171 ± 19 mJy	149 ± 18 mJy

[a]The uncertainties of the flux densities include both the statistical uncertainty in each map (1σ) and the uncertainty in the flux calibration. The uncertainty in the flux calibration is taken to be 10 % of the total flux density.

Table II.4. The Fixed Parameters for the Models.

R_c (AU)	M_{disk} ($M_\odot$)	i (°)	ΔV(in the Envelope) (km s^{-1})	ΔV(in the Disk) (km s^{-1})
100[a]	0.057[a]	65[b]	0.34[c]	0.83[c]

[a]Estimated from the continuum emission (see § II.3.1).

[b]Estimated from the $C^{18}O$ emission (see § II.3.2).

[c]Based on the assumption that the turbulent velocity is half the isothermal sound speed of molecular hydrogen (see Appendix II.B).

— Figure Captions —

Fig. II.1.— The 110 GHz continuum emission maps of L 1551 IRS 5; (*a*) the map made with data from the three array configurations, and (*b*) the map made with data from the AB configuration. The natural weighting was applied in making both maps. The contour spacing in each panel is 1.5σ, starting at $\pm 1.5\sigma$ with $1\sigma = 5.5$ and 5.8 mJy beam^{-1} for (*a*) and (*b*), respectively. Negative contours are drawn by dashed lines.

Fig. II.2.— The $C^{18}O$ ($J = 1 - 0$) integrated intensity map (contours) of L 1551 IRS 5 superposed on the K'-band image of the reflection nebula obtained by Hodapp (1994). The contour spacing is 1.5σ, starting at $\pm 1.5\sigma$ with $1\sigma = 46.9$ mJy beam^{-1}. The white cross indicates the stellar position.

Fig. II.3.— The intensity-weighted mean velocity map of L 1551 IRS 5 obtained from the $C^{18}O$ ($J = 1 - 0$) emission. The integrated intensity distribution is also shown by gray lines, whose contour spacing is 1.5σ, starting at 3σ.

Fig. II.4.— The velocity channel maps of the $C^{18}O$ ($J = 1 - 0$) line. The corresponding LSR velocity in km s^{-1} is shown at the upper right corner of each panel. The cross indicates the stellar position. The contour spacing is 1.5σ, starting at $\pm 1.5\sigma$ with $1\sigma = 115$ mJy beam^{-1}.

Fig. II.5.— The position-velocity diagrams (a, b, c, d) of the $C^{18}O$ ($J = 1 - 0$) emission along four different cuts shown in the $C^{18}O$ integrated intensity map (*e*). Contours in (a) – (d) are drawn in the same manner as in Fig. II.4, and those in (*e*) are in the same way as in Fig. II.3. (*a*) The P-V diagram along the major axis [A_1A_2 in (*e*)] of the centrally condensed component. The dashed curves indicate the velocity distribution given by equation (II.2), while the thin solid curves show the Keplerian rotation velocity around a central mass of $0.15M_\odot$. (*b*) The P-V diagram along the cut B_1B_2 offset by 1.″65 southwest from the major axis. The dashed curves indicate the velocity distribution given by equations (II.2) and (II.3); the inner curve is for $M = 0.1M_\odot$, and the outer curve for $M = 0.5M_\odot$. (*c*) The P-V diagram along the cut C_1C_2 offset by 1.″65 northeast from the major axis. The dashed curves are the same as in (*b*). (*d*) The P-V diagram along the minor axis [D_1D_2 in (*e*)] of the centrally condensed component. The dashed curves indicate the velocity distribution given by equation (II.3); the inner curves are for $M = 0.1M_\odot$, and the outer curves for $M = 0.5M_\odot$. $\Delta = 0''$ for (*a*) and (*d*) indicates the stellar position, and that for (*b*) and (*c*)

indicates the intersection with the minor axis.

Fig. II.6.— The $C^{18}O$ ($J = 1-0$) line profiles in units of the flux density (Jy). The solid line is for the emission from the entire region, and the dashed line from the centrally condensed component.

Fig. II.7.— The density distributions for the two analytic envelope models; (*a*) $\rho_{\rm sheet}$ with $\eta = 2$ for a sheet-like envelope, (*b*) $\rho_{\rm cav}$ with $\theta_{\rm cav} = 60°$ for an envelope with bipolar cavities; $M = 0.15 M_\odot$ and $\dot{M}_{\rm infall} = 6 \times 10^{-6} M_\odot$ yr^{-1} are adopted for both models. The solid lines show the isodensity contours labelled with the values of $\log n_{\rm H_2}$ in cm^{-3}. The ordinate is along the polar axis, and the abscissa is in the midplane of the envelope.

Fig. II.8.— The P-V diagrams (left-hand panels) made up for the sheet-like envelope models whose density distributions are shown in the corresponding right-hand panels. All the P-V diagrams are along the cut offset by 1.″65 southwest from the major axis of the model envelopes. The contours in the P-V diagrams are drawn in the same way as in Fig. II.4, and those in the density distributions are labelled by the values of $\log n_{\rm H_2}$ in cm^{-3}. The model parameters are $\eta = 1$, $M = 0.2 M_\odot$, and $\dot{M}_{\rm infall} = 8 \times 10^{-6} M_\odot$ yr^{-1} for (*a*) and (*b*); $\eta = 2$, $M = 0.15 M_\odot$, and $\dot{M}_{\rm infall} = 6 \times 10^{-6} M_\odot$ yr^{-1} for (*c*) and (*d*); and $\eta = 3$, $M = 0.15 M_\odot$, and $\dot{M}_{\rm infall} = 6 \times 10^{-6} M_\odot$ yr^{-1} for (*e*) and (*f*).

Fig. II.9.— Comparisons between the P-V diagrams along the cut offset by 1.″65 southwest from the major axis for sheet-like envelope models (b, c) and the observed diagram (*a*). Contours are drawn in the same manner as in Fig. II.4. The parameters are $\eta = 2$, $M = 0.15 M_\odot$, and $\dot{M}_{\rm infall} = 6 \times 10^{-6} M_\odot$ yr^{-1} for (*b*), and $\eta = 2$, $M = 0.5 M_\odot$, and $\dot{M}_{\rm infall} = 6 \times 10^{-6} M_\odot$ yr^{-1} for (*c*).

Fig. II.10.— The P-V diagrams (left-hand panels) made up for the envelope models with bipolar cavity whose density distributions are shown in the corresponding right-hand panels. All the diagrams are along the cut offset by 1.″65 southwest from the major axis of the model envelopes. The contours in the P-V diagrams are drawn in the same manner as in Fig. II.4, and those in the density distributions are labelled by the values of $\log n_{\rm H_2}$ in cm^{-3}. The model parameters are $\theta_{\rm cav} = 30°$, $M = 0.15 M_\odot$, and $\dot{M}_{\rm infall} = 6 \times 10^{-6} M_\odot$ yr^{-1} for (*a*) and (*b*); $\theta_{\rm cav} = 50°$, $M = 0.15 M_\odot$, and $\dot{M}_{\rm infall} = 6 \times 10^{-6} M_\odot$ yr^{-1} for (*c*) and (*d*); and $\theta_{\rm cav} = 70°$, $M = 0.15 M_\odot$, and $\dot{M}_{\rm infall} = 6 \times 10^{-6} M_\odot$ yr^{-1} for (*e*) and (*f*).

Fig. II.11.— The coordinate systems for model calculation. The X- and Y-axes are the

major and minor axes, respectively, of the envelope projected on the plane of the sky, and the Z-axis is along the line of sight. The X'-axis is along the X-axis, and Z'-axis is the symmetry axis of the envelope. The Y'-axis is taken perpendicular to both X'- and Z'-axes.

Fig. II.12.— The P-V diagrams along the major axis; $(a) - (c)$ the diagrams for the sheet-like envelopes, $(d) - (f)$ the diagrams for the envelopes with bipolar cavity, and (g) the observed diagram. The contours in the P-V diagrams are drawn in the same way as in Fig. II.4. The model parameters are (a) $\eta = 1$, $M = 0.2M_\odot$, and $\dot{M}_{\rm infall} = 8 \times 10^{-6} M_\odot$ yr^{-1}: (b) $\eta = 2$, $M = 0.15M_\odot$, and $\dot{M}_{\rm infall} = 6 \times 10^{-6} M_\odot$ yr^{-1}; (c) $\eta = 3$, $M = 0.15M_\odot$, and $\dot{M}_{\rm infall} = 6 \times 10^{-6} M_\odot$ yr^{-1}; (d) $\theta_{\rm cav} = 30°$, $M = 0.15M_\odot$, and $\dot{M}_{\rm infall} = 6 \times 10^{-6} M_\odot$ yr^{-1}; (e) $\theta_{\rm cav} = 50°$, $M = 0.15M_\odot$, and $\dot{M}_{\rm infall} = 6 \times 10^{-6} M_\odot$ yr^{-1}; and (f) $\theta_{\rm cav} = 70°$, $M = 0.15M_\odot$, and $\dot{M}_{\rm infall} = 6 \times 10^{-6} M_\odot$ yr^{-1}.

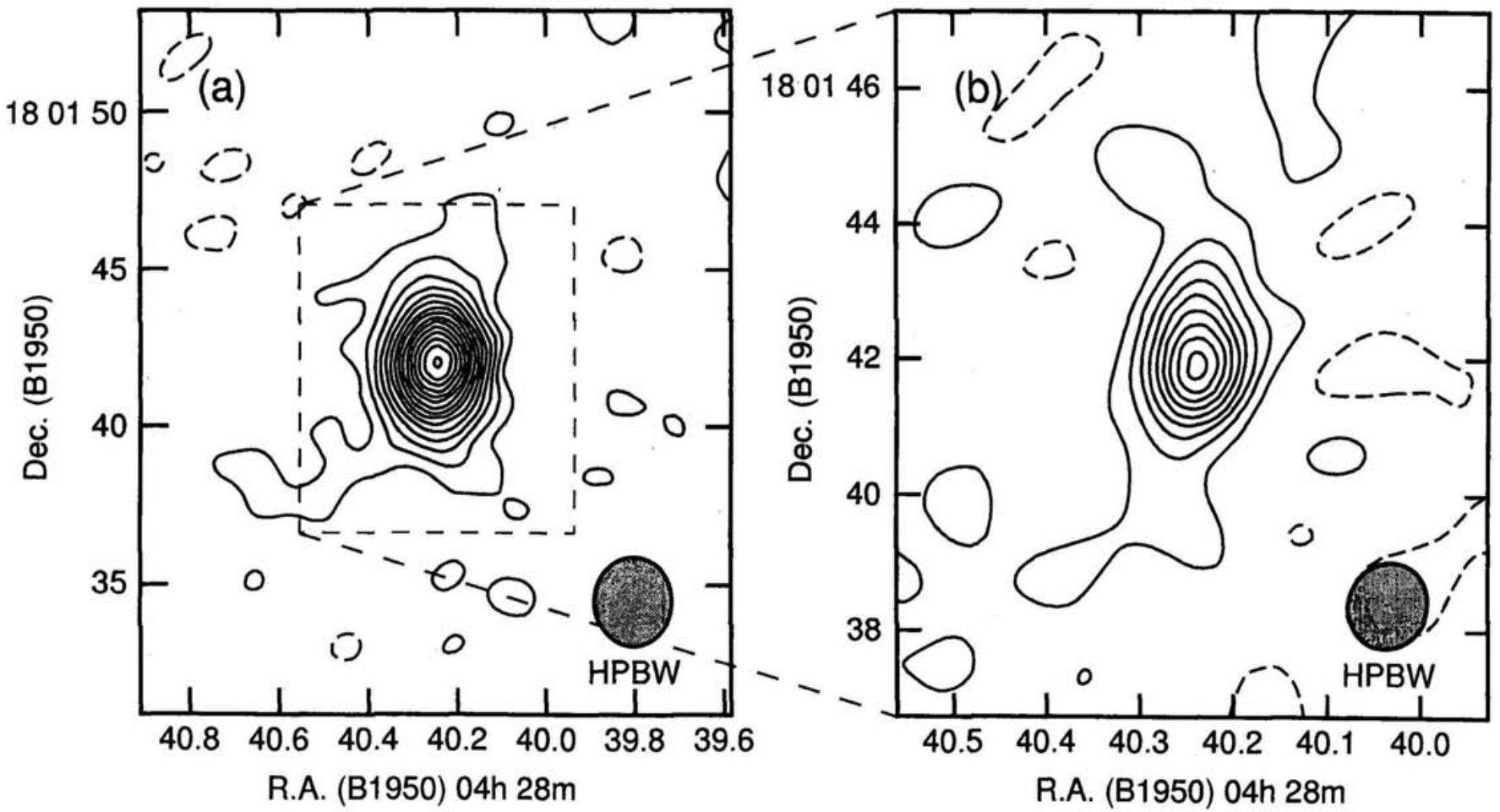
(a)
18 01 50
45
40
35
Dec. (B1950)
HPBW
40.8 40.6 40.4 40.2 40.0 39.8 39.6
R.A. (B1950) 04h 28m
(b)
18 01 46
44
42
40
38
Dec. (B1950)
HPBW
40.5 40.4 40.3 40.2 40.1 40.0
R.A. (B1950) 04h 28m

Figure II.1

Figure II. 2

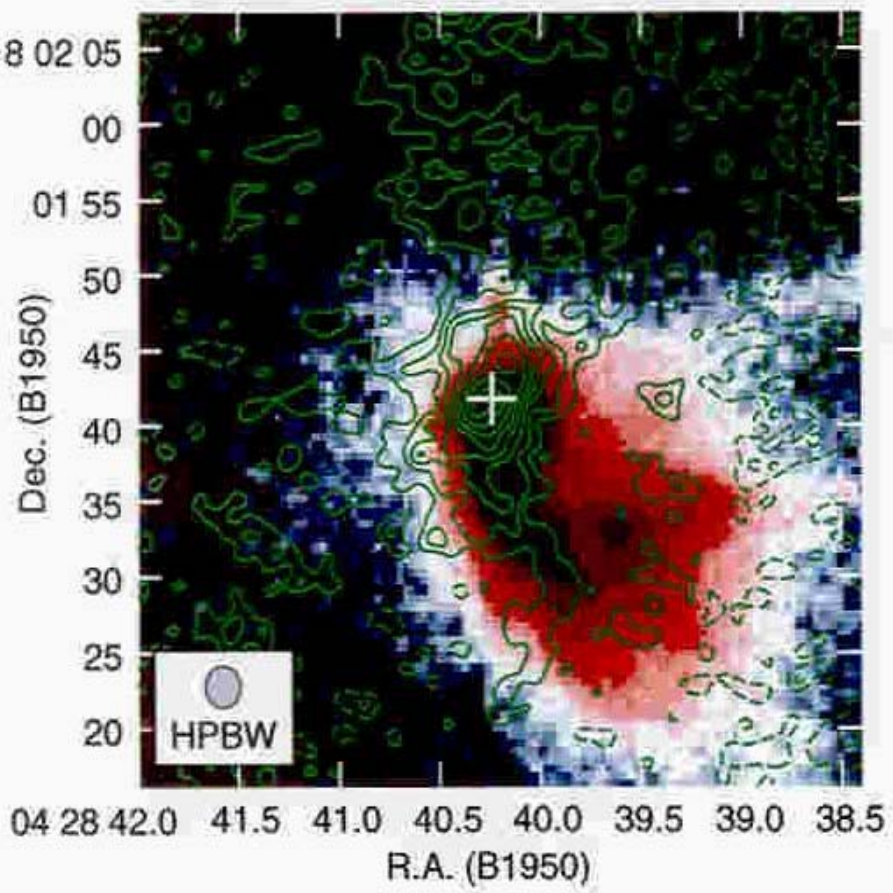

Figure II.3

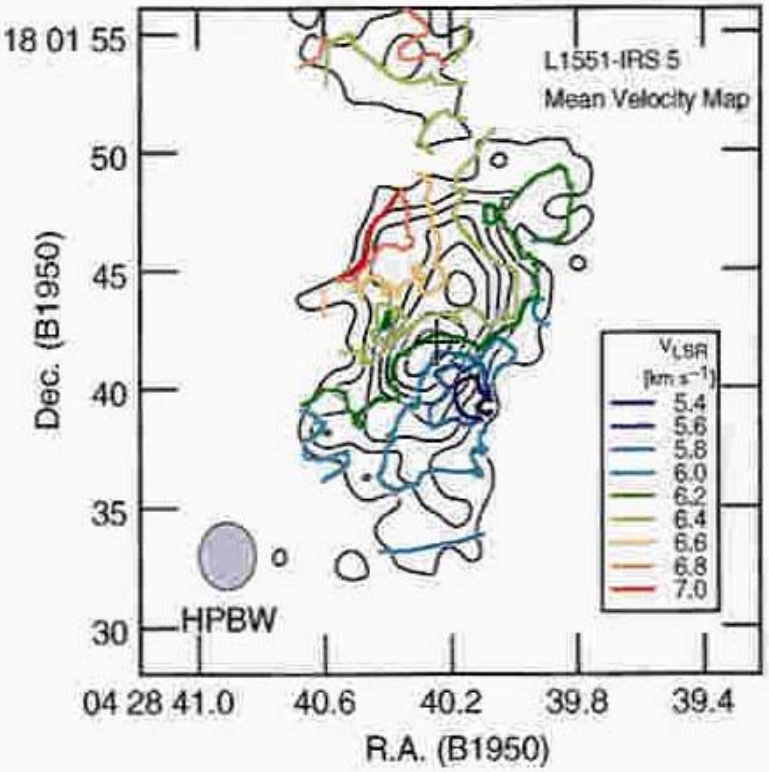

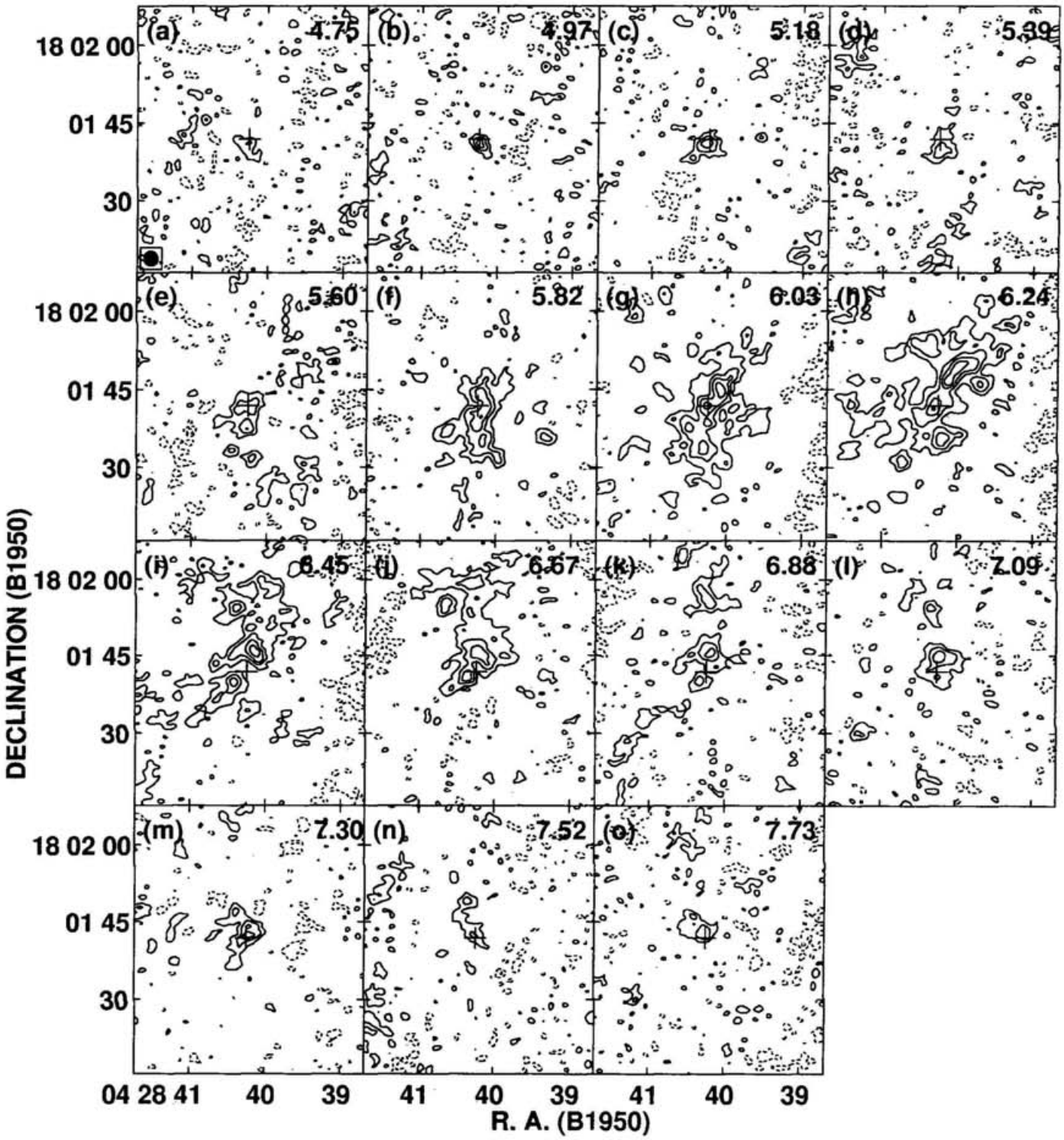
(a) 4.75
(b) 4.97
(c) 5.18
(d) 5.39
(e) 5.60
(f) 5.82
(g) 6.03
(h) 6.24
(i) 6.45
(j) 6.67
(k) 6.88
(l) 7.09
(m) 7.30
(n) 7.52
(o) 7.73
18 02 00
01 45
30
04 28 41
40
39
DECLINATION (B1950)
R. A. (B1950)

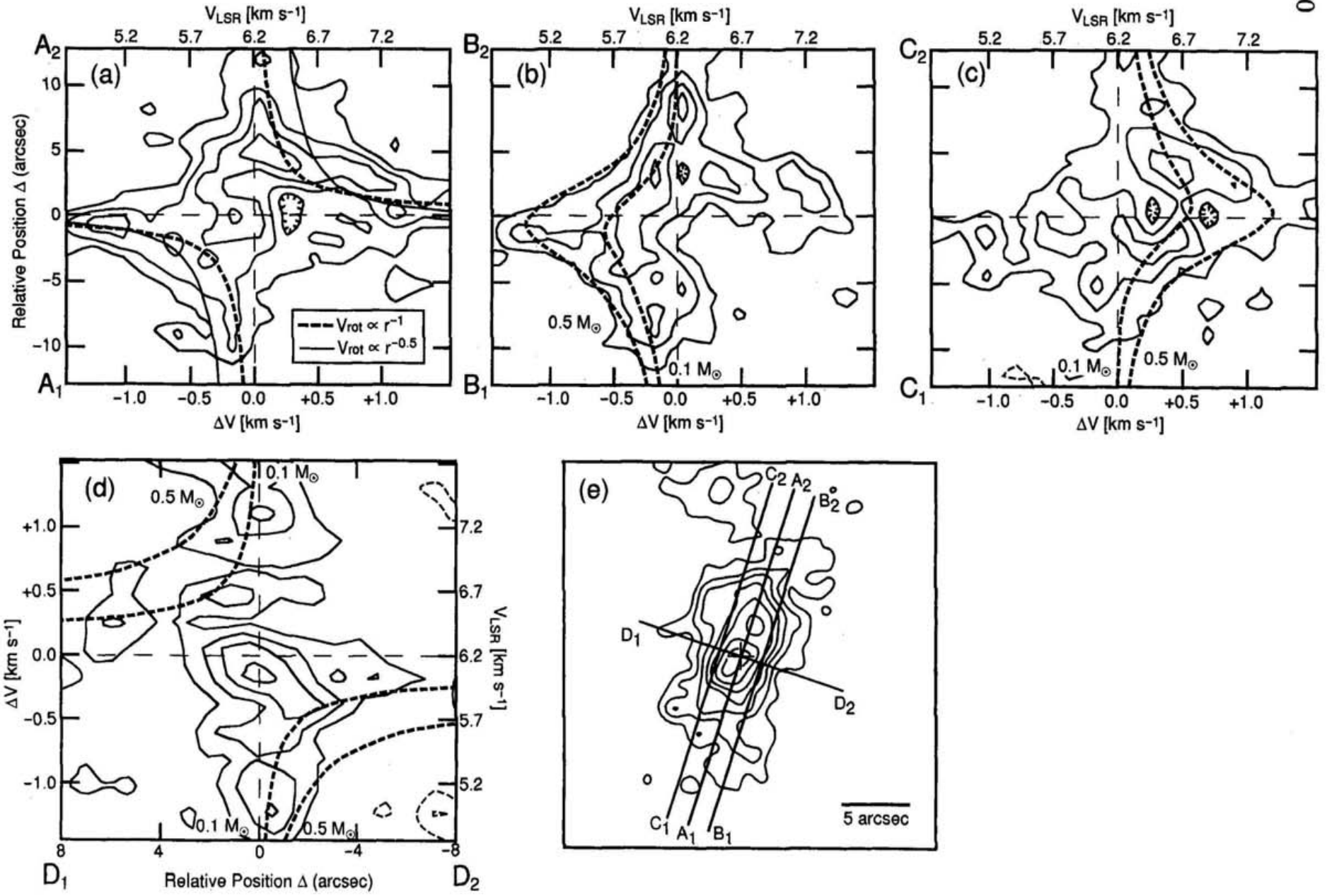
(a)
(b)
(c)
(d)
(e)
V_{LSR} [km s^{-1}]
5.2 5.7 6.2 6.7 7.2
Relative Position Δ (arcsec)
ΔV [km s^{-1}]
A_2
A_1
B_2
B_1
C_2
C_1
D_1
D_2
$V_{rot} \propto r^{-1}$
$V_{rot} \propto r^{-0.5}$
0.5 $M_\odot$
0.1 $M_\odot$
Relative Position Δ (arcsec)
5 arcsec

Fig. II.5

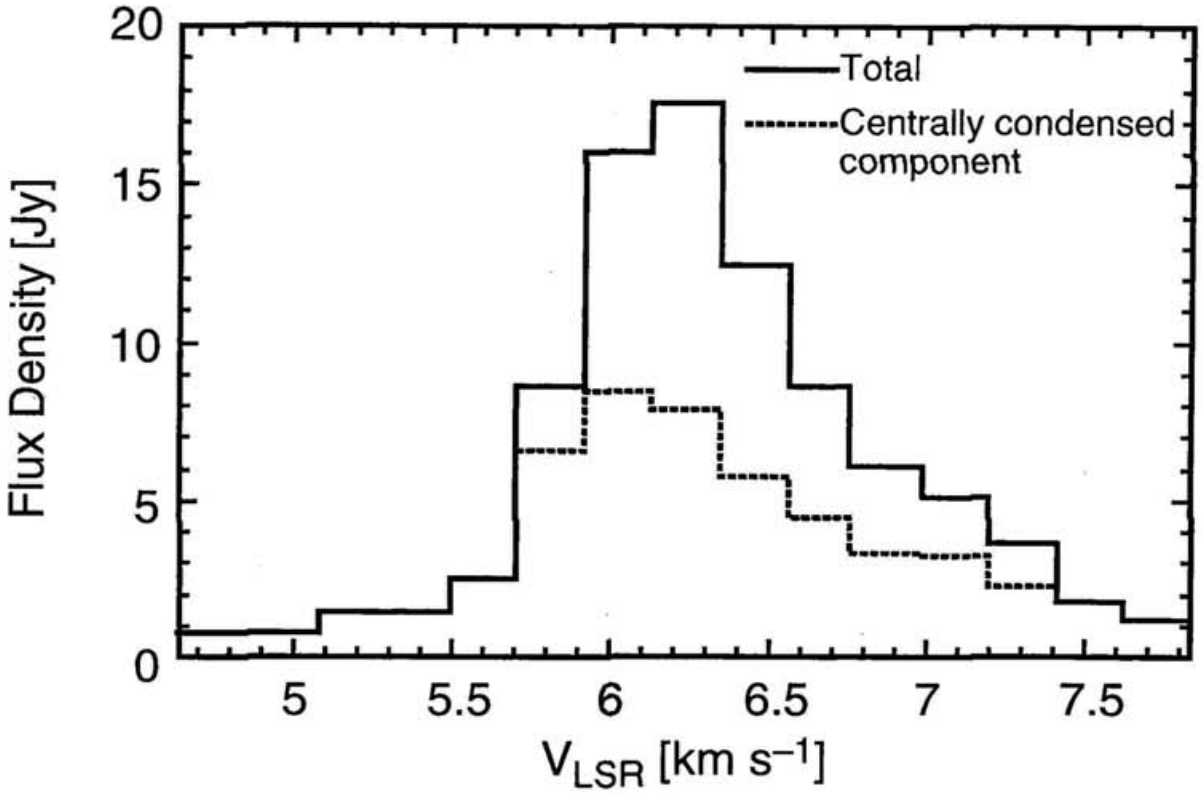
Total
Centrally condensed component
Flux Density [Jy]
0
5
10
15
20
5
5.5
6
6.5
7
7.5
V_{LSR} [km s^{-1}]

Fig. II.6

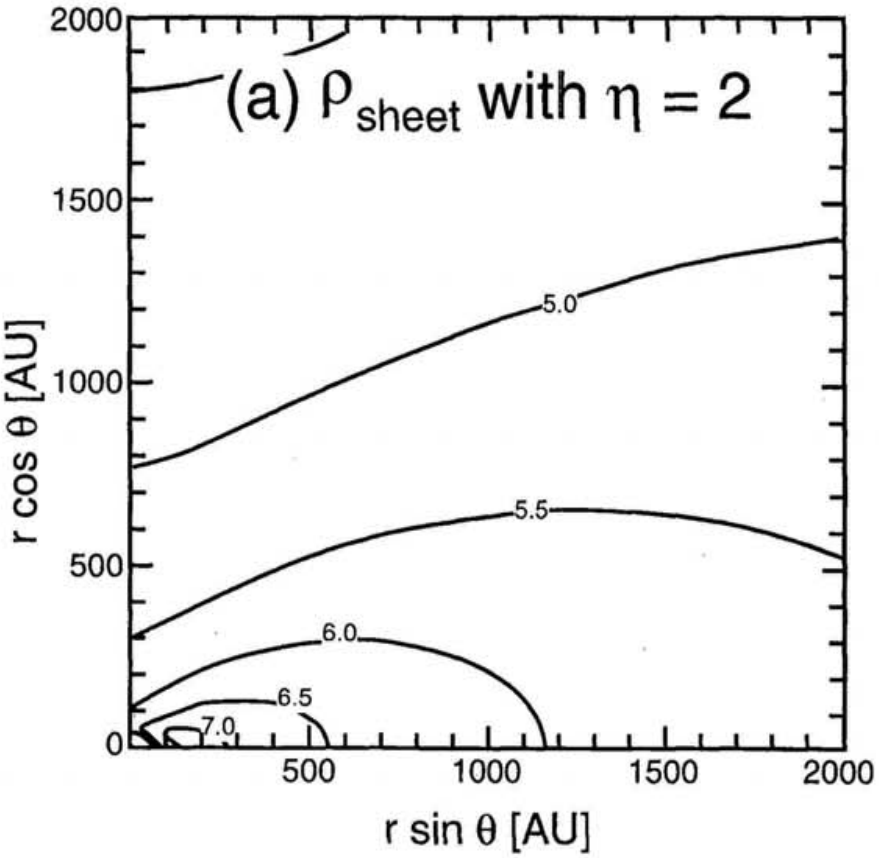
(a) ρ_{sheet} with $\eta = 2$
r cos θ [AU]
r sin θ [AU]
2000
1500
1000
500
0
500
1000
1500
2000
5.0
5.5
6.0
6.5
7.0

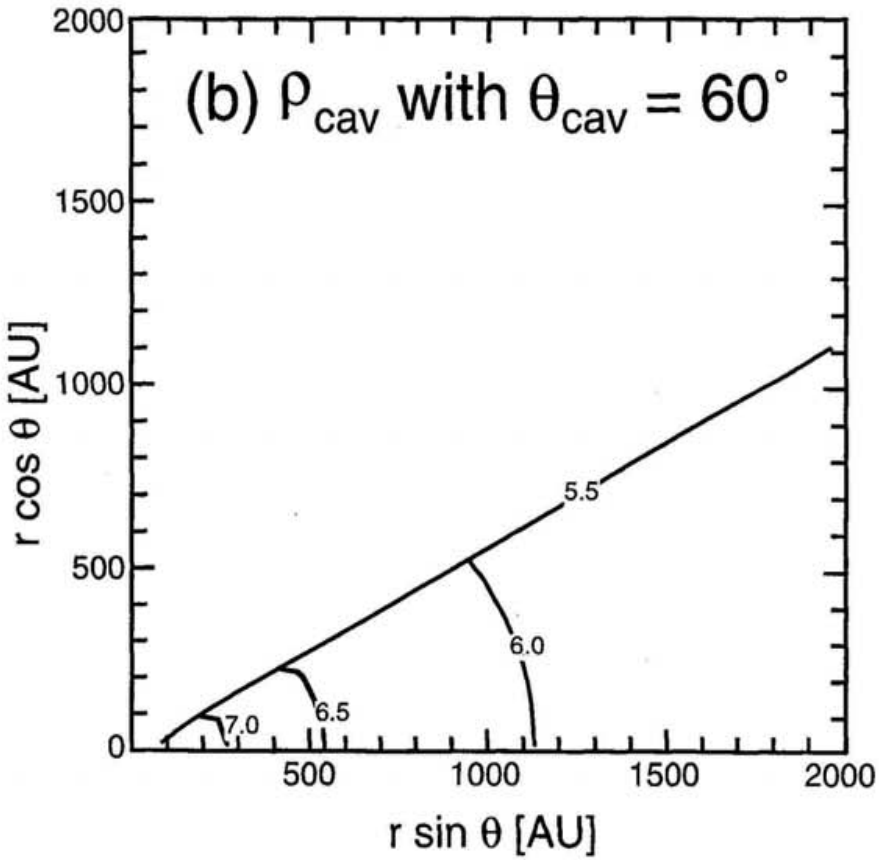
(b) ρ_{cav} with $\theta_{cav} = 60°$
r cos θ [AU]
r sin θ [AU]
2000
1500
1000
500
0
500
1000
1500
2000
5.5
6.0
6.5
7.0

Fig. II.7

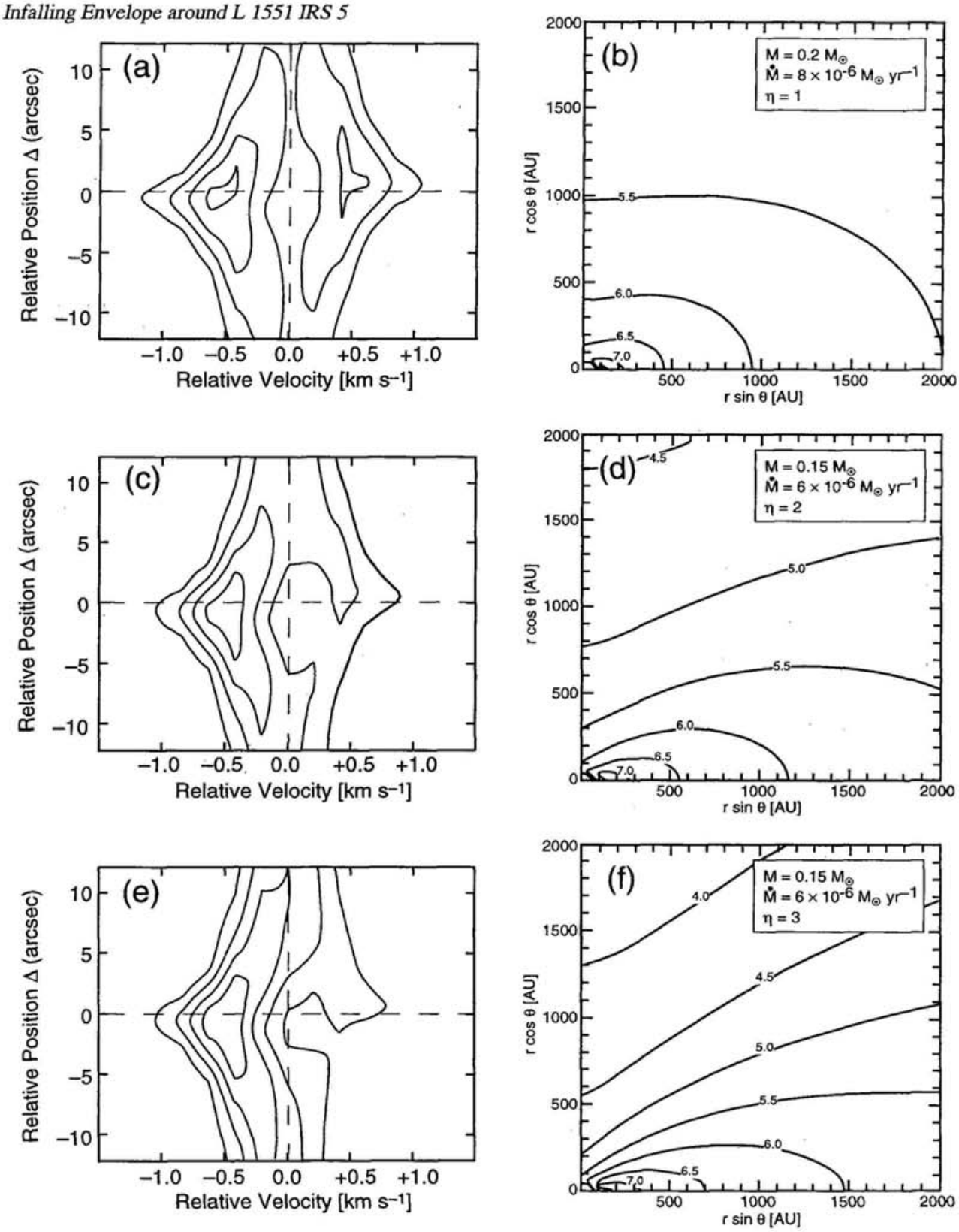
(a)
(b)
(c)
(d)
(e)
(f)
Relative Position Δ (arcsec)
Relative Velocity [km s⁻¹]
r cos θ [AU]
r sin θ [AU]
M = 0.2 M⊙
Ṁ = 8 × 10⁻⁶ M⊙ yr⁻¹
η = 1
M = 0.15 M⊙
Ṁ = 6 × 10⁻⁶ M⊙ yr⁻¹
η = 2
η = 3
4.0
4.5
5.0
5.5
6.0
6.5
7.0

Fig. II.8

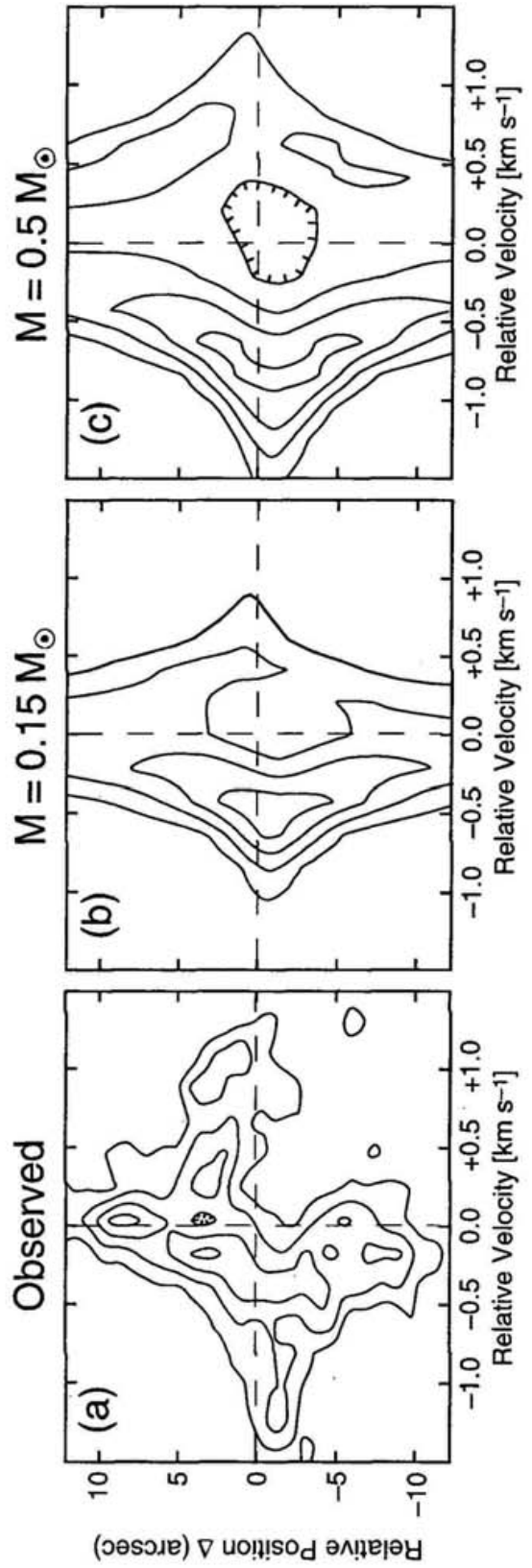
Observed
M = 0.15 M⊙
M = 0.5 M⊙
(a)
(b)
(c)
Relative Position Δ (arcsec)
10
5
0
−5
−10
−1.0 −0.5 0.0 +0.5 +1.0
Relative Velocity [km s−1]

Fig. II.9

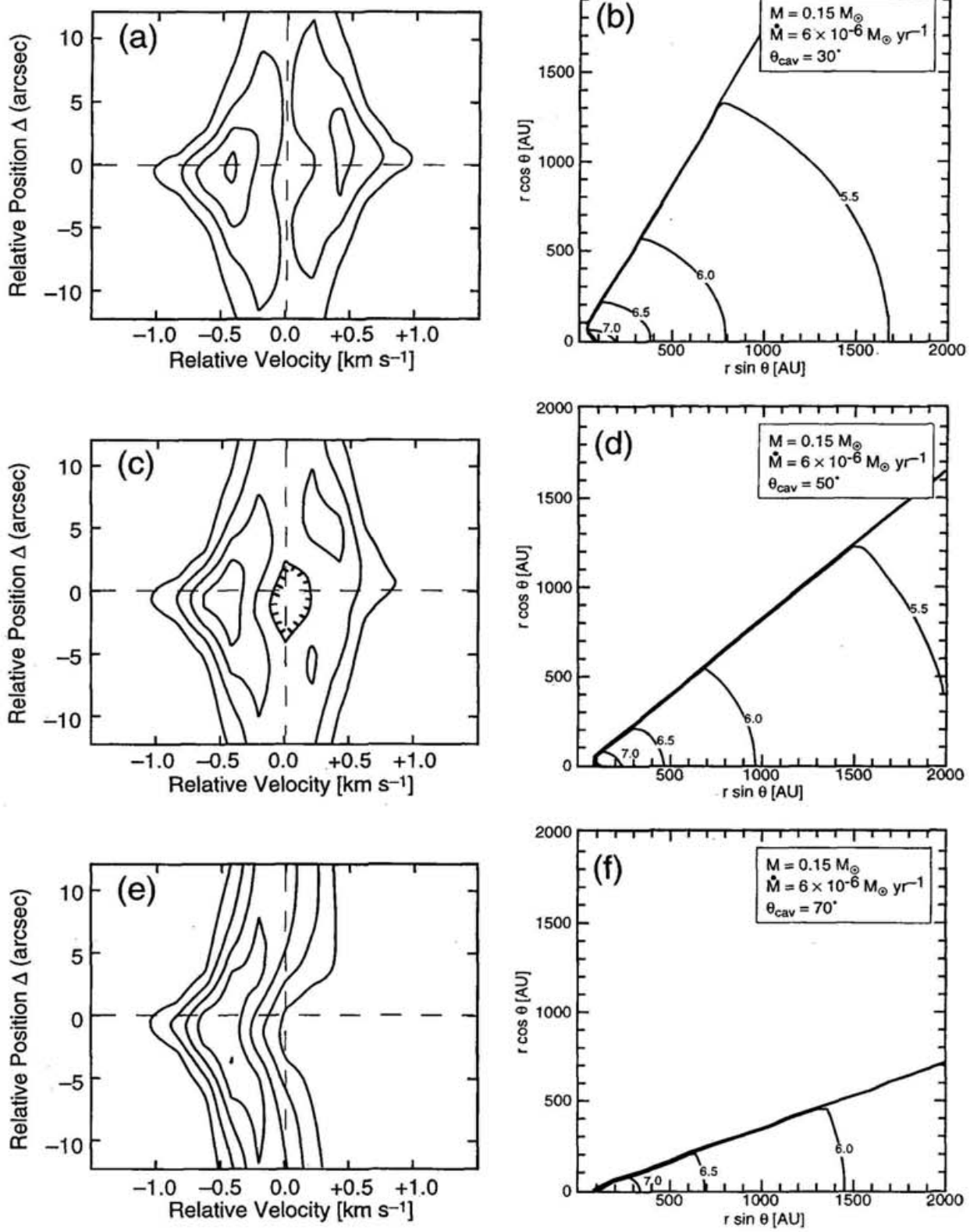
(a)
(b)
(c)
(d)
(e)
(f)
Relative Position Δ (arcsec)
Relative Velocity [km s⁻¹]
r cos θ [AU]
r sin θ [AU]
M = 0.15 M⊙
Ṁ = 6 × 10⁻⁶ M⊙ yr⁻¹
θcav = 30°
θcav = 50°
θcav = 70°
5.5
6.0
6.5
7.0

Fig. II.10

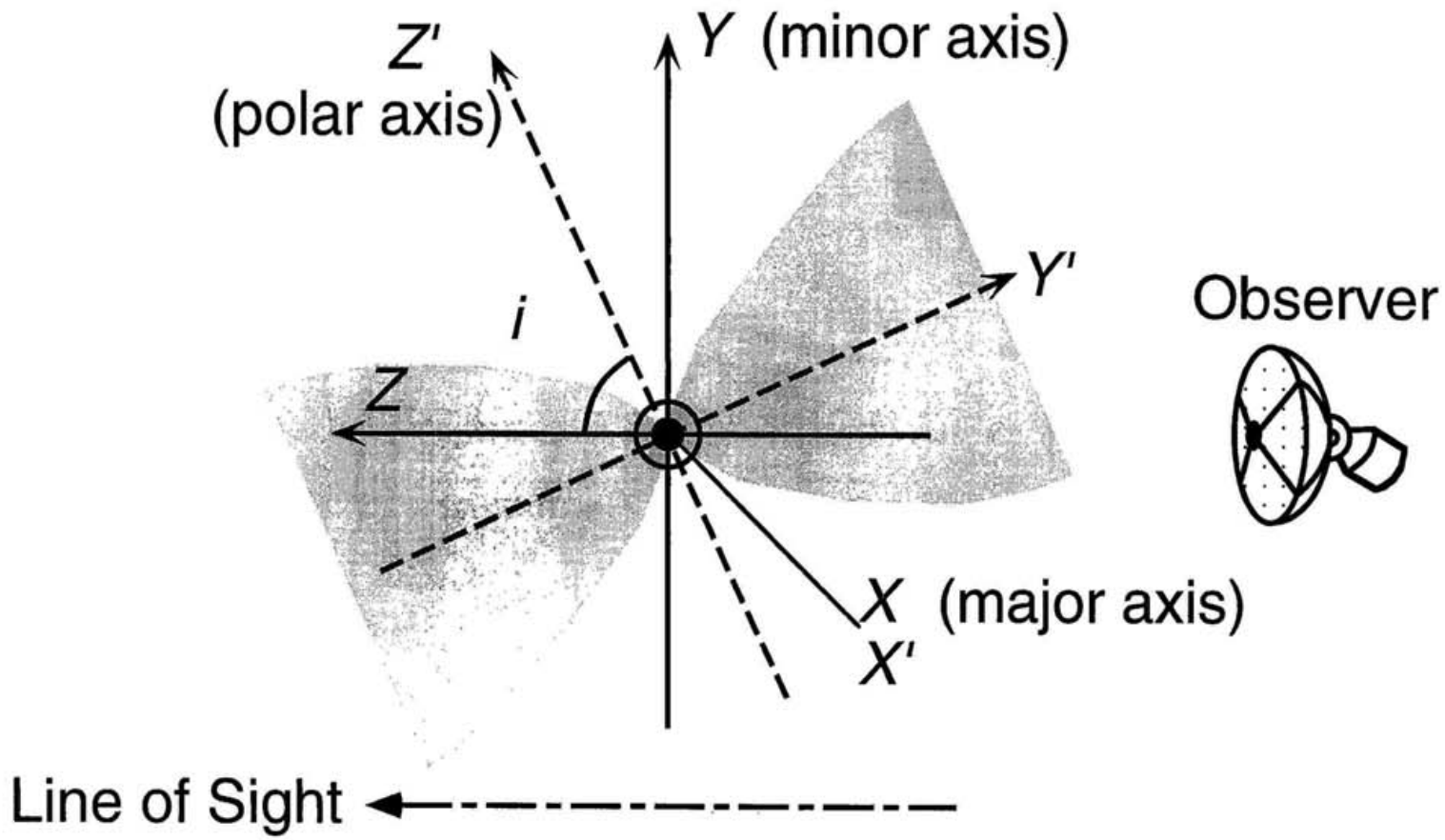
Z'
(polar axis)
Y (minor axis)
Y'
Observer
i
Z
X (major axis)
X'
Line of Sight

Fig. II. 11

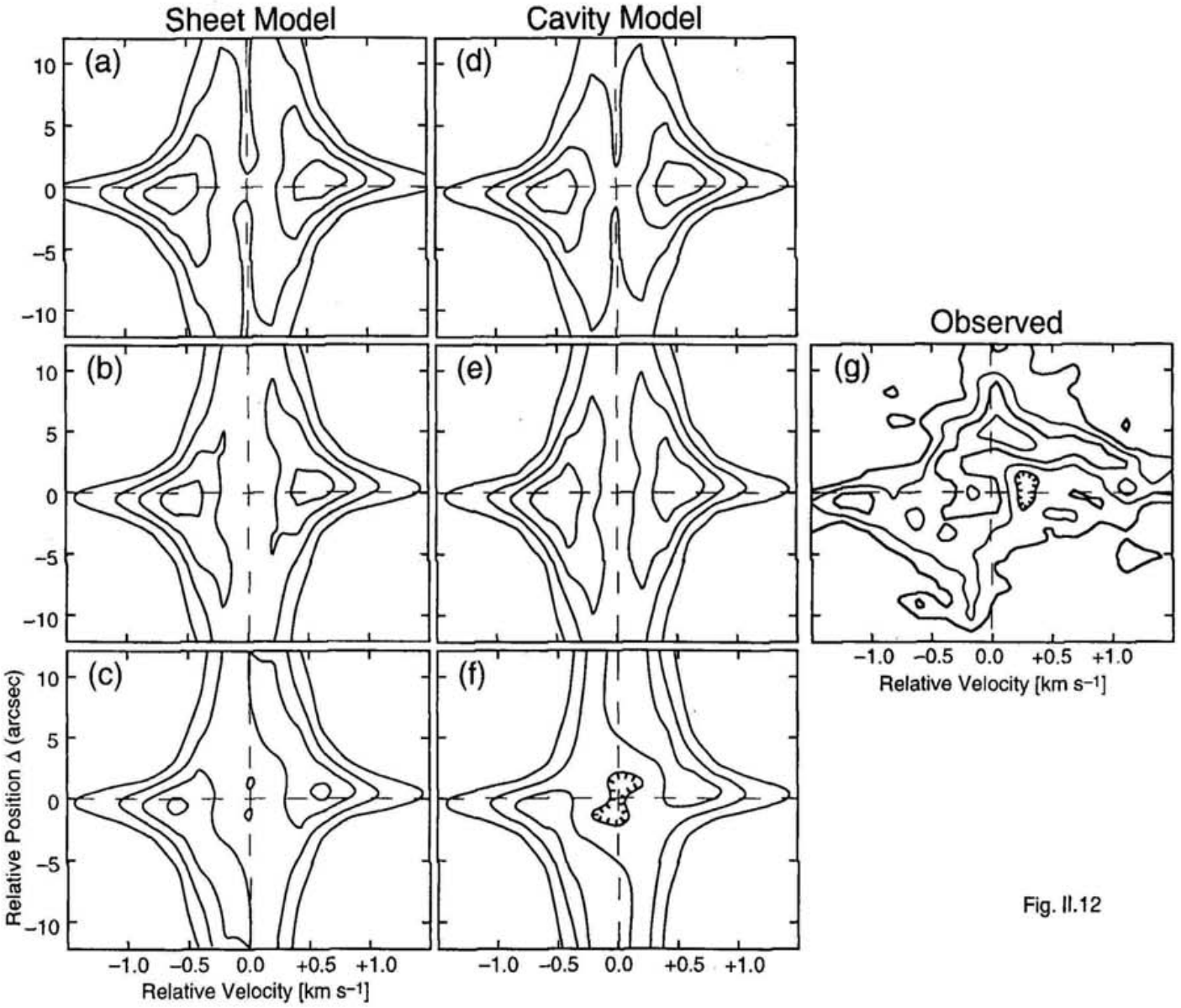
Sheet Model
Cavity Model
Observed
(a)
(b)
(c)
(d)
(e)
(f)
(g)
10
5
0
−5
−10
−1.0 −0.5 0.0 +0.5 +1.0
Relative Position Δ (arcsec)
Relative Velocity [km s−1]

Fig. II.12

Chapter III

Aperture Synthesis $C^{18}O$ ($J = 1 - 0$) Observations of L 1551 NE: Detection of a Flattened Circumstellar Envelope

ABSTRACT

We report the results of aperture synthesis $C^{18}O$ ($J = 1 - 0$) observations of the protostar candidate L 1551 NE with the Nobeyama Millimeter Array. We have detected an emission component centrally condensed around L 1551 NE, as well as a weak emission component extending in the north-south direction from the centrally condensed component. The centrally condensed component, 1580 AU × 810 AU in size, is elongated in the direction perpendicular to the outflow axis, indicating the existence of a flattened circumstellar envelope around L 1551 NE. The mass of the gas detected with the present observations is estimated to be $(3.6 - 6.3) \times 10^{-2} M_{\odot}$. The velocity structure in the centrally condensed component can be explained in terms of rotation motion in the flattened envelope, whereas no clear evidence for infall motion in the envelope has been obtained, though there is a marginal indication of infall motion in the centrally condensed component. This is probably because the infall velocity around L 1551 NE is too small to detect, which may be due to the extreme youth of L 1551 NE.

Subject headings: circumstellar matter — ISM: molecules — ISM: structure — stars: formation — stars: individual (L 1551 NE) — stars: pre-main sequence

III.1. Introduction

Low mass stars are formed through dynamical infall in the central parts of molecular cloud cores. Recent high-resolution observations of nearby young stellar objects with molecular emission lines have revealed in detail the structure and kinematics of circumstellar gas, and have provided direct evidences for dynamical infall around these sources (e.g., Hayashi, Ohashi, & Miyama 1993; Ohashi et al. 1996a; Saito et al. 1996; Ohashi et al. 1997a; Momose et al. 1997 [Chapter II of this thesis]). It is important to make high-resolution observations of gas associated with protostar candidates systematically, because the structure of protostar envelopes and mass accretion rate in the envelopes are obtained straightforwardly from these observational results.

L 1551 NE, which was discovered by Emerson et al. (1984), is the second brightest ($\sim 6 L_{\odot}$) protostar candidate in the Taurus molecular cloud. Mapping observations with continuum emissions at far-infrared and submillimeter wavelengths revealed that L 1551 NE is surrounded by the envelope with a density distibution shallower than $r^{-3/2}$ (Barsony

& Chandler 1993; Butner et al. 1995). A sensitive mapping observations with the ^{12}CO ($J = 3 - 2$) line show that the central star of L 1551 NE drives the energetic molecular outflows along the east(red)-west(blue) direction. More recently, Saito (1997) made aperture synthesis observations with the $H^{13}CO^+$ ($J = 1 - 0$) line using the Nobeyama Millimeter Array, and revealed the existence of dense gas extending along the direction perpendicular to the outflow axis. All these observational results suggest that the L 1551 NE is a mass-accreting protostar embedded within a dense circumstellar envelope.

In this chapter we report the results of aperture synthesis observations of L 1551 NE with the $C^{18}O$ ($J = 1 - 0$) line by using the Nobeyama Millimeter Array (NMA). Since the ambient cloud component around a protostar candidate in Taurus is generally optically thin for the $C^{18}O$ ($J = 1 - 0$) line, this is a proper line to reveal the density and kinematical structures of the infalling envelopes, as shown in some previous works (Momose et al. 1997; Ohashi et al. 1997a; Ohashi et al. 1997b). We describe the details of the observations in § 2, present the observational results in § 3, and discuss the gas mass and kinematics around L 1551 NE in § 4.

III.2. Observations

Aperture synthesis $C^{18}O$ ($J = 1 - 0$) observations were made during a period from 1995 December to 1996 March with the NMA, which is composed of six 10 m dishes. We used the tunerless SIS receivers (Sunada et al. 1993) whose system noise temperatures were typically 300 K (double sideband [DSB]) at the zenith. We employed the digital FFT spectral correlator FX, which gave a frequency resolution of 78 kHz, corresponding to the velocity resolution of 0.215 km s^{-1} at the frequency of the $C^{18}O$ ($J = 1 - 0$) line. Two array configurations, giving 30 baselines, were used for the observations. The minimum projected baseline length was 9 m so that our observations are insensitive to structures with sizes greater than 62″, corresponding to 8700 AU at the Taurus Molecular Cloud. The phase and gain of the array system were calibrated by every 30 minutes observations of 0528+134. We used the same observations of 0528+134 to obtain the complex pass band of the FX. The flux density of 0528+134 at 110 GHz was 7.2 Jy in 1995 December, 6.4 Jy in the beginning of February 1996, and 7.7 Jy from the end of February 1996 to March 1996. The continuum level, which was estimated from line-free channels with an effective bandwidth of 65 MHz, was subtracted from the visibility data.

III.3. Results

III.3.1. 110 GHz Continuum Emission

We made the map of the continuum emission with the CLEAN algorithm in the NRAO AIPS package (Figure III.1). Natural weighting was applied to the visibility data. The resultant synthesized beam size (HPBW) is $4''.5 \times 3''.9$ with the position angle of 7°, and the rms noise level in the map is 4.24 mJy beam^{-1}.

The map of the contiuum emission shows point-like structure with a feature extending southeastward to the peak position. This continuum emission is expected to originate mainly from the circumstellar disk around the central star, but the existence of the extended feature suggests that dust contained in the inner part of the envelope also contributes to the continuum emission. The total flux density of the continuum emission is 131 ± 17 mJy. We hereafter regard the poistion of the continuum emission peak, $(\alpha_{1950}, \delta_{1950})$=($04^h28^m50^s.566, +18°02'09''.32$), as the stellar position, which is consistent with the postion of the IRAS source (Draper, Warren-Smith, & Scarrott, 1985).

III.3.2. $C^{18}O$ ($J = 1 - 0$) Emission

We made maps of the $C^{18}O$ ($J = 1 - 0$) emission by applying natural weighting to the visibility data with a gaussian tapering function whose 30 % levels in the u- and v-directions are at 66 kλ and at 120 kλ, respectively. The resultant synthesized beam size (HPBW) is $5''.7 \times 5''.3$ (P.A. = 164°) and the rms noise level in the channel maps is 120 mJy beam^{-1}.

Figure III.2 shows the integrated intensity map of the $C^{18}O$ ($J = 1 - 0$) emission. The emission in Fig. III.2 can be decomposed into two components; one is a centrally condensed component with its peak at the stellar position, and the other is a component extending north and south of the centrally condesed component with lower contour levels. Assuming that the centrally condensed component is gaussian, we derive its beam denconvolved size to be $10''.7 \times 5''.8$ (P.A. = 166°), corresponding to 1500 AU × 810 AU at the distance 140 pc to the Taurus molecular cloud. The position angle of the centrally condensed component is almost perpendicular to the outflow axis, which is estimated from the symmetry axis of the fan-shaped reflection nebula associated with the blueshifted outflow lobe (Hodapp 1994; Moriarty-Schieven et al. 1995a). This indicates that L 1551 NE is surrounded by a flattened circumstellar envelope, as is L 1551 IRS 5 (Momose et al. 1997) or L 1527 (Ohashi et al.

1997a).

Saito (1997) made apreture synthesis observations of L 1551 NE with the $H^{13}CO^+$ ($J = 1 - 0$) line, and detected the spatially extended emission. Comparing our results with the map of the $H^{13}CO^+$ emission, the peak of the $C^{18}O$ ($J = 1 - 0$) emission is located at the stellar position determined from the dust continuum emission while that of the $H^{13}CO^+$ ($J = 1 - 0$) emission is located at $\sim 6''$ northeast to the central star, though both emissions are elongated in the direction perpendicular to the outflow axis. Some observational studies of outflows have suggested that the abundance of the HCO^+ molecule is greatly enhanced in the regions where the high-velocity stellar wind interacts with the ambient cloud (e.g., Lizano et al. 1988). Taking into account that L 1551 NE is located inside the red-lobe of the outflows ejected from L 1551 IRS 5, the positional shift of the $H^{13}CO^+$ ($J = 1 - 0$) emission peak may be due to the local abundance anomaly of the HCO^+ molecule induced by the interaction between the ambient cloud and the outflows from IRS 5.

We show in Figure III.3 the channel maps of the $C^{18}O$ ($J = 1 - 0$) emission. We take the systemic velocity of L 1551 NE ($v_{\rm sys}$) to be $V_{\rm LSR} = 6.67$ km s^{-1} (Fig. III.3*h*) based on the fact that the CS ($J = 5 - 4$) profile toward L 1551 NE obtained with the JCMT (HPBW = $20''$) has the peak velocity of $V_{\rm LSR} \sim 6.6$ km s^{-1} (Moriarty-Schieven et al. 1995b). The $C^{18}O$ ($J = 1 - 0$) emissions in the channel maps can be separated into the following three features: (i) a spatially compact feature $\lesssim 3''$ north to the central star at the velocities blueshifted by more than 0.64 km s^{-1} from $v_{\rm sys}$ (i.e., Figs. III.3*a* – 3*e*), (ii) another compact feature $\lesssim 2''$ south to the central star at the velocities redshifted by more than 0.63 km s^{-1} from $v_{\rm sys}$ (i.e., Figs. III.3*k* – 3*n*), and (iii) a spatially extended feature in the velocity range $|V_{\rm LSR} - v_{\rm sys}| < 0.43$ km s^{-1} (i.e., Figs. III.3*f* – 3*j*). Comparing the spatial distribution of the emission in Fig. III.2 with those of the emission features in Fig. III.3, we find that the two emission components in the integrated intensity map (Fig. III.2) originate from different velocity ranges from each other; The centrally condensed component in the integrated intensity map mainly originates from the compact emission features at higher velocities (Figs. III.3*a* – 3*e* and III.3*k* – 3*n*), though some emissions near the systemic velocity also contribute to this component (e.g., a bright emission near the star in Fig. III.3*g*). On the other hand, the spatially extended component in Fig. III.2 mainly originates from the emission feature near the systemic velocity (Figs. III.3*f* – 3*j*).

In order to clarify the velocity structure in the centrally condesed component, we have made the position-velocity (P-V) diagrams along the major and minor axes of the centrally

condensed component (Figures III.4*a* and III.4*b*). The P-V diagram along the major axis (Fig. III.4*a*) shows a velocity gradient in the north(blue)-south(red) direction that can also be identified in the channel maps. A similar velocity gradient was also seen in the $H^{13}CO^+$ ($J = 1 - 0$) maps around L 1551 NE (Saito et al. 1997). This velocity gradient can be interpreted as the rotation motion of gas in the flattened envelope around L 1551 NE. Such a kind of rotation motion has also been found in the cases of other protostar candidates (e.g., Hayashi et al. 1993 for HL Tauri; Momose et al. 1997 for L 1551 IRS 5; Ohashi et al. 1997a for L 1527). By connecting two peaks in Fig. III.4*a* (thick line), we derive the amount of the velocity shift due to rotation to be ~ 1.34 km s^{-1} at $r = 280$ AU or $2''$.

Unlike the P-V diagram along the major axis, there is no clear velocity gradient in the P-V diagram along the minor axis (Fig. III.4*b*), which is different from the cases of HL Tau (Hayashi et al. 1993) and L 1551 IRS 5 (Ohashi et al. 1996a; Saito et al. 1996; Momose et al. 1997). This may suggest that infall velocity in the envelope is too small to detect the infall motion in the envelope with the present observations. We will make further discussion on thie point in § 4.2.

III.4. Discussion

III.4.1. Mass

We can estimate the mass of the gas detected with the NMA by the following equation (Scoville et al. 1986):

$$M_{\rm gas} = 5.45 \times 10^{-4} T_{\rm ex} \exp\left(\frac{5.27}{T_{\rm ex}}\right) \frac{\tau_{\rm C^{18}O}}{1 - \exp\left(-\tau_{\rm C^{18}O}\right)} \left(\frac{d}{140\ {\rm pc}}\right)^2 \left[\frac{10^{-7}}{X({\rm C^{18}O})}\right] \int S_\nu dv \, M_\odot, \quad \text{(III.1)}$$

where $T_{\rm ex}$ is the excitation temperature of $C^{18}O$ at $J = 1$ level, d is the distance to L 1551 NE, $X(C^{18}O)$ is the fractional abundance of $C^{18}O$ relative to H_2, $\tau_{\rm C^{18}O}$ is the mean optical depth of the gas for the $C^{18}O$ ($J = 1 - 0$) line, and $\int S_\nu dv$ is the integrated flux in units of Jy km s^{-1}. On the assumption of the optically thin $C^{18}O$ ($J = 1 - 0$) emission ($\tau_{\rm C^{18}O} \ll 1$), the integrated flux of 8.14 Jy km s^{-1} with the present observations gives the total gas mass of $(3.0 - 6.3) \times 10^{-2} M_\odot$ with $X(C^{18}O) = 2.5 \times 10^{-7}$ (Chernicharo & Guélin 1987) and $T_{\rm ex} = (10 - 30)$ K. The assumption that the $C^{18}O$ ($J = 1 - 0$) emission is optically thin probably holds well since the maximum brightness temperature in the channel maps, 3.64 K in Fig. III.3*g*, is much smaller than the expected excitation temperature of $C^{18}O$.

The total gas mass estimated above is comparable to the mass derived from the continuum emission at 800μm with size $\sim 18''$ ($\sim 0.05 M_{\odot}$, Barsony & Chandler 1993), indicating that our observations revealed spatially compact structure around L 1551 NE farily well. It should be noted, however, that spatially extended components near the systemic velocity may be resolved out with our aperture synthesis observations. Therefore the above estimate of gas mass should be regarded as a lower limit to the gas mass within the field-of-view of the NMA (FWHM $\sim 65''$).

III.4.2. Gas Kinematics

As described in § 3, we have found a velocity gradient along the major axis of the centrally condensed component of the $C^{18}O$ ($J = 1 - 0$) emission. This velocity gradient can be attributed to the rotation motion in the flattened envelope. If the rotation velocity, ~ 1.34 km s^{-1} at $r = 280$ AU, is Keplerian, the dynamical mass inside this radius is derived to be $(0.57 M_{\odot} / \sin^2 i)$, where i is the inclination angle of the flattened envelope around L 1551 NE. Note that this dynamical mass should be regarded as the lower limit to the central stellar mass, because the rotation velocity in the envelope is smaller than Keplerian if the gas in the envelope is infalling to the central star-disk system.[1]

With the present observations, we do not find any clear evidence for infall motion in the flattened envelope, i.e., we do not find any velocity gradient along the minor axis. However, the existence of the energetic outflow associated with L 1551 NE (Moriarty-Schieven et al. 1995a; Moriarty-Schieven et al. 1995b) and its very cold spectral energy distribution (Barsony & Chandler 1993) imply that the mass infall toward the central star-disk system is going on. In fact, we find a marginal indication of the infall motion in the envelope around L 1551 NE by inspecting carefully the spatial distribution of the high-velocity features near the star, as described in the following. Figure III.5 shows the maps of the

[1]This argument becomes no longer valid if the centrally condensed component would originate from *outflowing* gas. However, we consider that the origin of the centrally condensed component is not outflowing gas based on the following two facts; (1) The high velocity features around L 1551 NE are located along the direction perpendicular to the outflow axis. (2) High-velocity components of the outflows generally exist at positions far from the central stars (e.g., Tamura et al. 1996; Chandler et al. 1996), but the high-velocity features around L 1551 NE are confined in the vicinity of the central star. It is therefore natural to consider that the centrally condensed component originates from gas which is bound by the gravity of the central star.

$C^{18}O$ ($J = 1 - 0$) emissions integrated over the velocity ranges of $V_{LSR} = (5.28 - 6.13)$ km s^{-1} for (a) and $V_{LSR} = (7.19 - 8.04)$ km s^{-1} for (b), respectively. Although the peak of the blueshifted emission is located at 3″ north to the star and that of the redshifted emission is located at 2″ south to the star, both emissions in Fig. III.5 show structure extending across the central star along the major axis; the blueshifted emission extends south to the star while the redshifted emission extends north to the star. Similar emission features extending across the central star have also been found in the $C^{18}O$ ($J = 1 - 0$) channel maps of L 1527 obtained with the NMA (Ohashi et al. 1997a). If the flattened envelope is observed with nearly edge-on configuration, the kinematics of such emission features cannot be explained by pure rotation, but additional radial motion in the envelope, such as infall, is required. In the case of L 1527, which is observed with an almost perfectly edge-on configuration (Tamura et al. 1996), the kinematics of these emission features is clearly explained in terms of motion composed of infall and rotation (Ohashi et al. 1997a). It is likely that L 1551 NE is also observed with nearly edge-on configuration ($i \approx 65°$), because the shape of the reflection nebula associated with L 1551 NE is quite similar to that around L 1551 IRS 5 ($i \approx 65°$, see Momose et al. 1997). Then the emissions in Fig. III.5 extending across the central star may be explained by infall motion with rotation in the inner regions of the envelope.

The reason we do not obtain clear evidence for infall motion is probably that the infall velocity in the flattened envelope is so small that the velocity resolution is not enough to detect the infall motion. This point may be related to the evolutionary status of L 1551 NE. Barsony & Chandler (1993) argued that the circumstellar envelope around L 1551 NE has a shallower density gradient [$\rho(r) \propto r^{-1/2}$] based on their mapping observations of the continuum emission at 800μm. Butner et al. (1995) also derived a similar conclusion from their observations of the dust emission at far-infrared wavelengths. Such a shallower density gradient is one of the common characteristics of "pre-protostellar" cores (Ward-Thompson et al. 1994; André, Ward-Thompson, & Motte 1996), suggesting that L 1551 NE is one of the youngest protostars with the envelope which holds fairly well the density distribution in the stage before the initial collapse. The extreme youth of the dynamical timescale of the molecular outflows associated with L 1551 NE ($\sim$ 2000 yr, Moriarty-Schieven et al. 1995a) is also consistent with the above argument. If L 1551 NE is extremely young, it is natural that the infall velocity in the envelope around L 1551 NE is much smaller than those around other protostars, such as L 1551 IRS 5 or L 1527.

— Figure Captions —

Fig. III.1.— The continuum emission at 110 GHz from L 1551 NE. The contour interval is 2σ, starting at 2σ ($1\sigma = 4.24$ mJy beam^{-1}). The dashed lines indicate the -2σ level.

Fig. III.2.— Integrated intensity map of the $C^{18}O$ ($J = 1-0$) emission from L 1551 NE. The contour spacing is 2σ, starting at 2σ ($1\sigma = 34.6$ mJy beam^{-1}). The dashed lines indicate negative contours, starting at -2σ level. The cross indicates the stellar position determined from the continuum emission at 110 GHz.

Fig. III.3.— The channel maps of the $C^{18}O$ ($J = 1 - 0$) emission around L 1551 NE. The contour spacing is 2σ, starting at 2σ ($1\sigma = 120$ mJy beam^{-1}). The dashed lines indicate negative contours, starting at -2σ. The line-of-sight velocity in LSR velocity is shown in the upper-right corner of each panel. The cross in each panel indicates the stellar position.

Fig. III.4.— Two position-velocity (P-V) diagrams in the centrally condensed component. Contours are drawn in the same manner as that in Figure III.3. The dot lines indicate the stellar position and the systemic velocity. (*a*) P-V diagram along the major axis of the centrally condensed component (P.A. = 166°). The thick line indicates the velocity gradient in the north(blue)-south(red) direction. (*b*) P-V diagram along the minor axis of the centrally condensed component (P.A. = 76 °).

Fig. III.5.— The $C^{18}O$ ($J = 1 - 0$) emissions integrated over the velocity ranges of (*a*) $V_{LSR} = (5.28 - 6.13)$ km s^{-1} and (*b*) $V_{LSR} = (7.19 - 8.04)$ km s^{-1}. The contour spacing is 2σ, starting at $\pm 2\sigma$ ($1\sigma = 60$ mJy beam^{-1}). The dashed lines indicate negative contours.

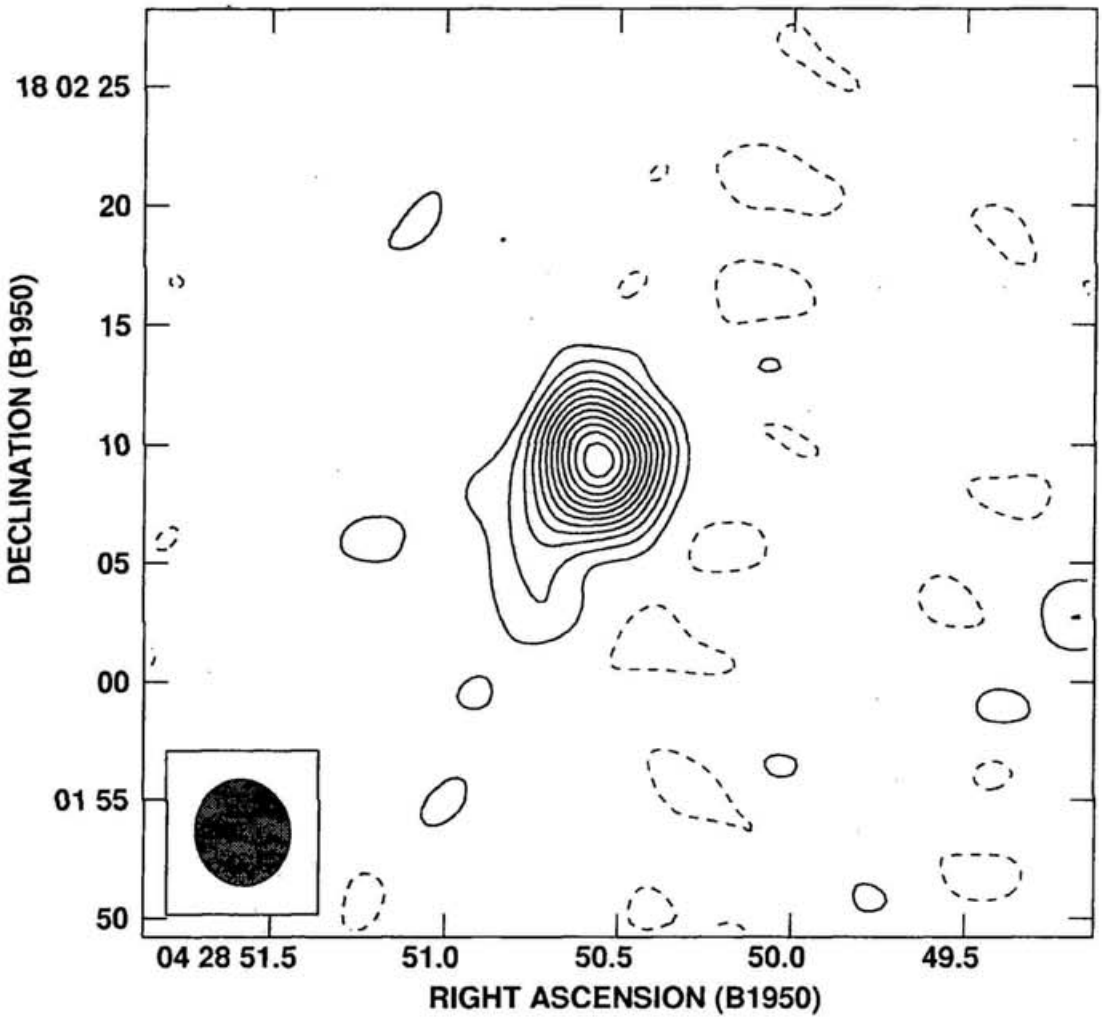
18 02 25
20
15
10
05
00
01 55
50
DECLINATION (B1950)
04 28 51.5
51.0
50.5
50.0
49.5
RIGHT ASCENSION (B1950)

Fig. III.1

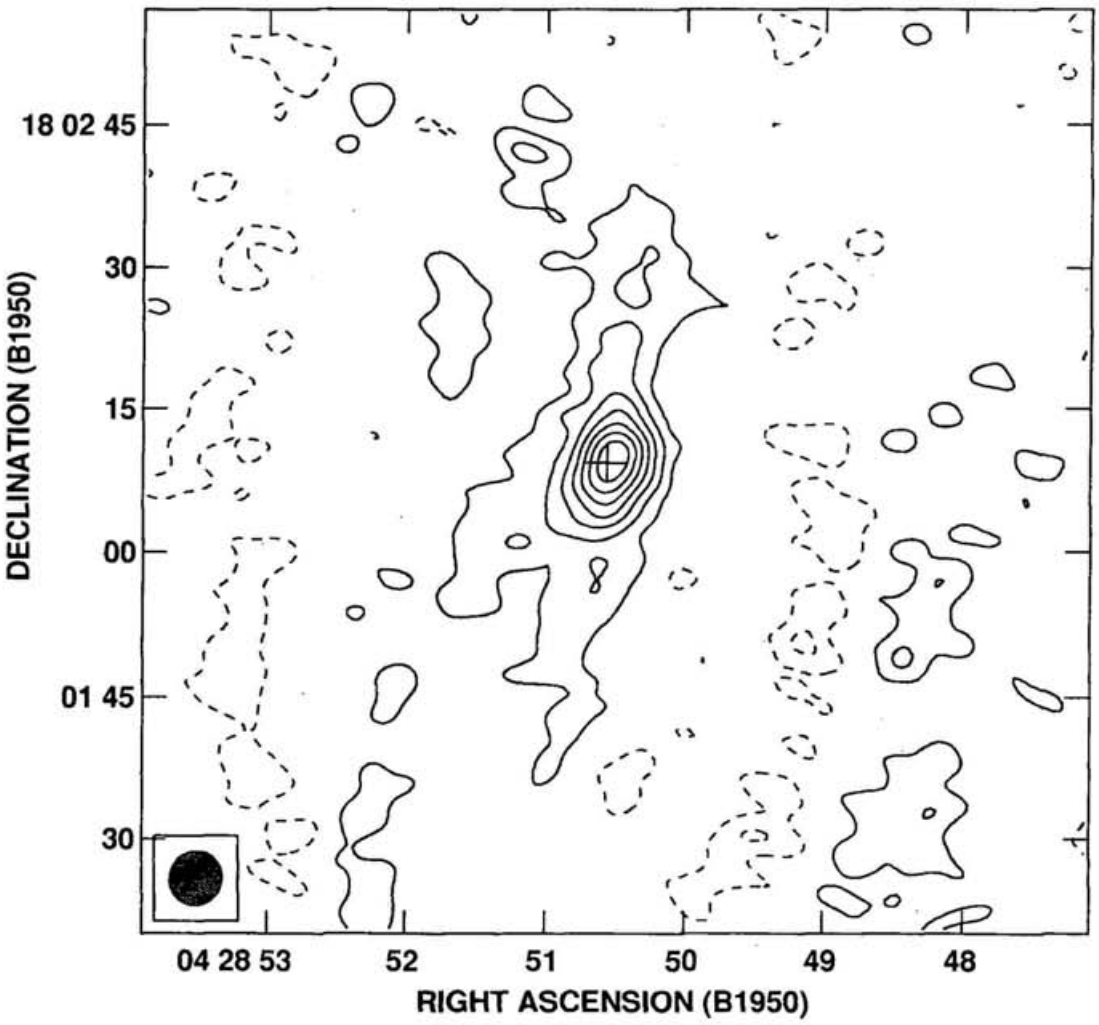
18 02 45
30
15
00
01 45
30
DECLINATION (B1950)
04 28 53
52
51
50
49
48
RIGHT ASCENSION (B1950)

Fig. III.2

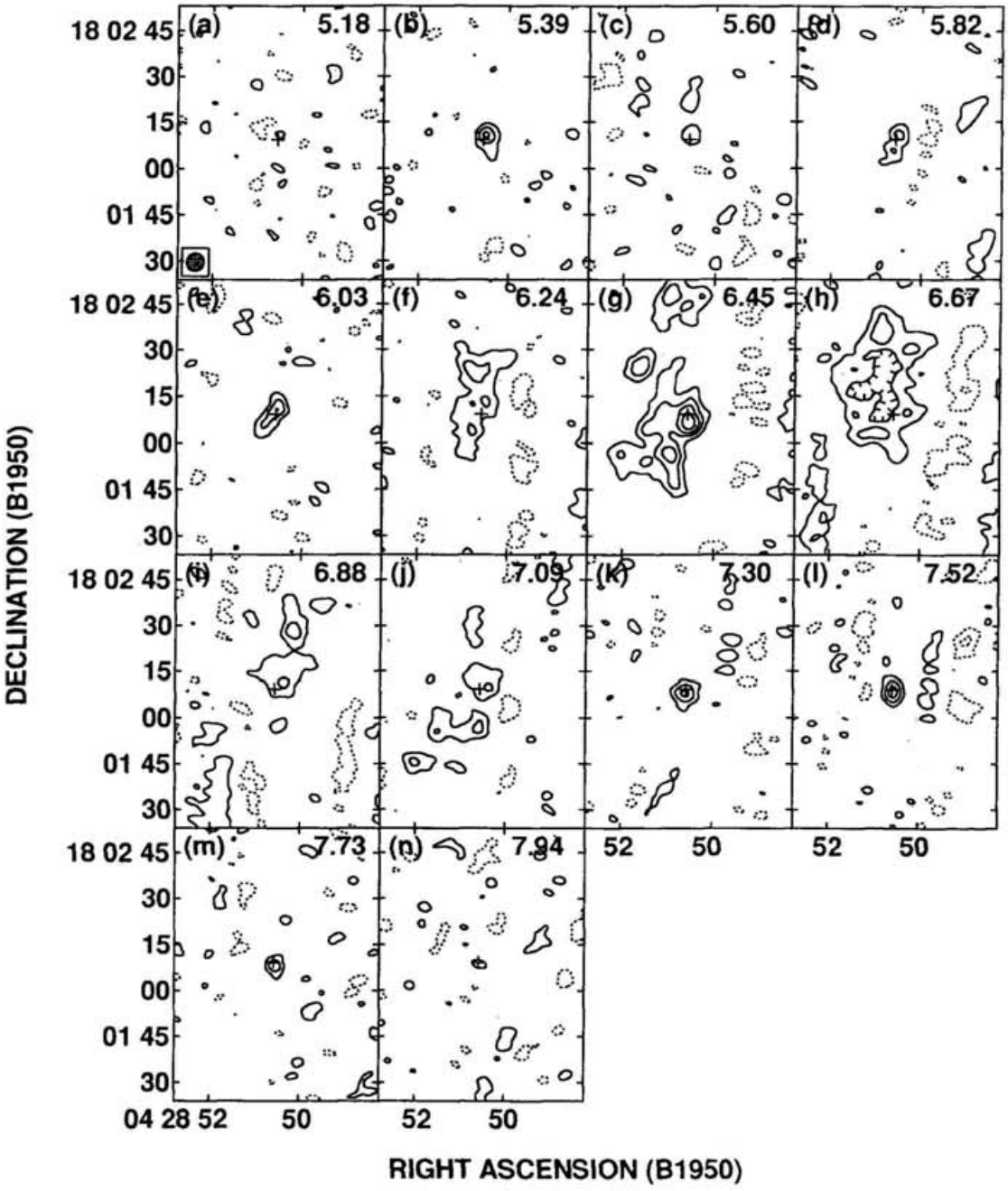
(a) 5.18
(b) 5.39
(c) 5.60
(d) 5.82
(e) 6.03
(f) 6.24
(g) 6.45
(h) 6.67
(i) 6.88
(j) 7.09
(k) 7.30
(l) 7.52
(m) 7.73
(n) 7.94
18 02 45
30
15
00
01 45
30
04 28 52
50
52
50
DECLINATION (B1950)
RIGHT ASCENSION (B1950)

Fig. III.3

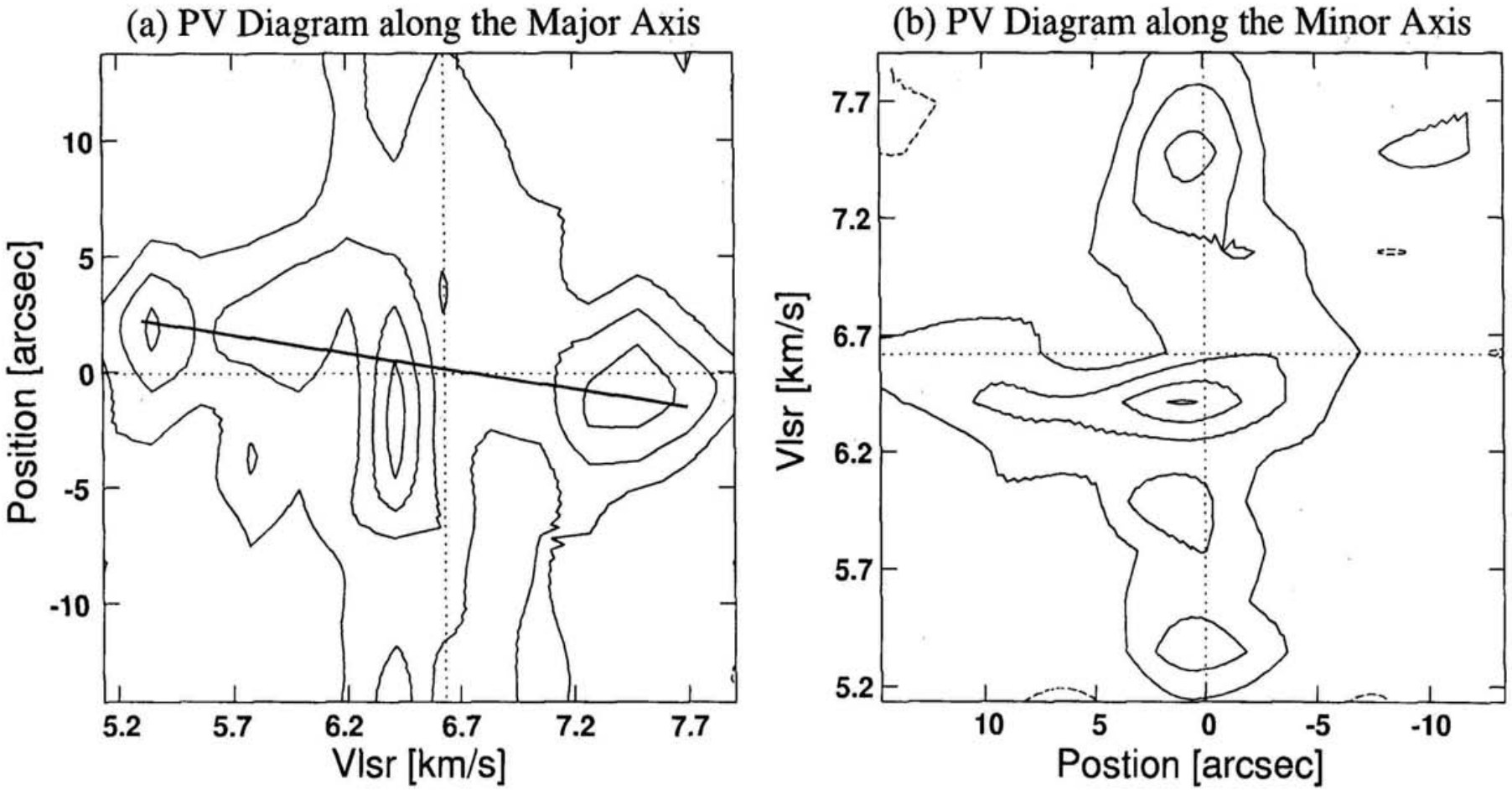
(a) PV Diagram along the Major Axis
Position [arcsec]
10
5
0
-5
-10
5.2
5.7
6.2
6.7
7.2
7.7
Vlsr [km/s]
(b) PV Diagram along the Minor Axis
Vlsr [km/s]
7.7
7.2
6.7
6.2
5.7
5.2
10
5
0
-5
-10
Postion [arcsec]

Fig. III.4

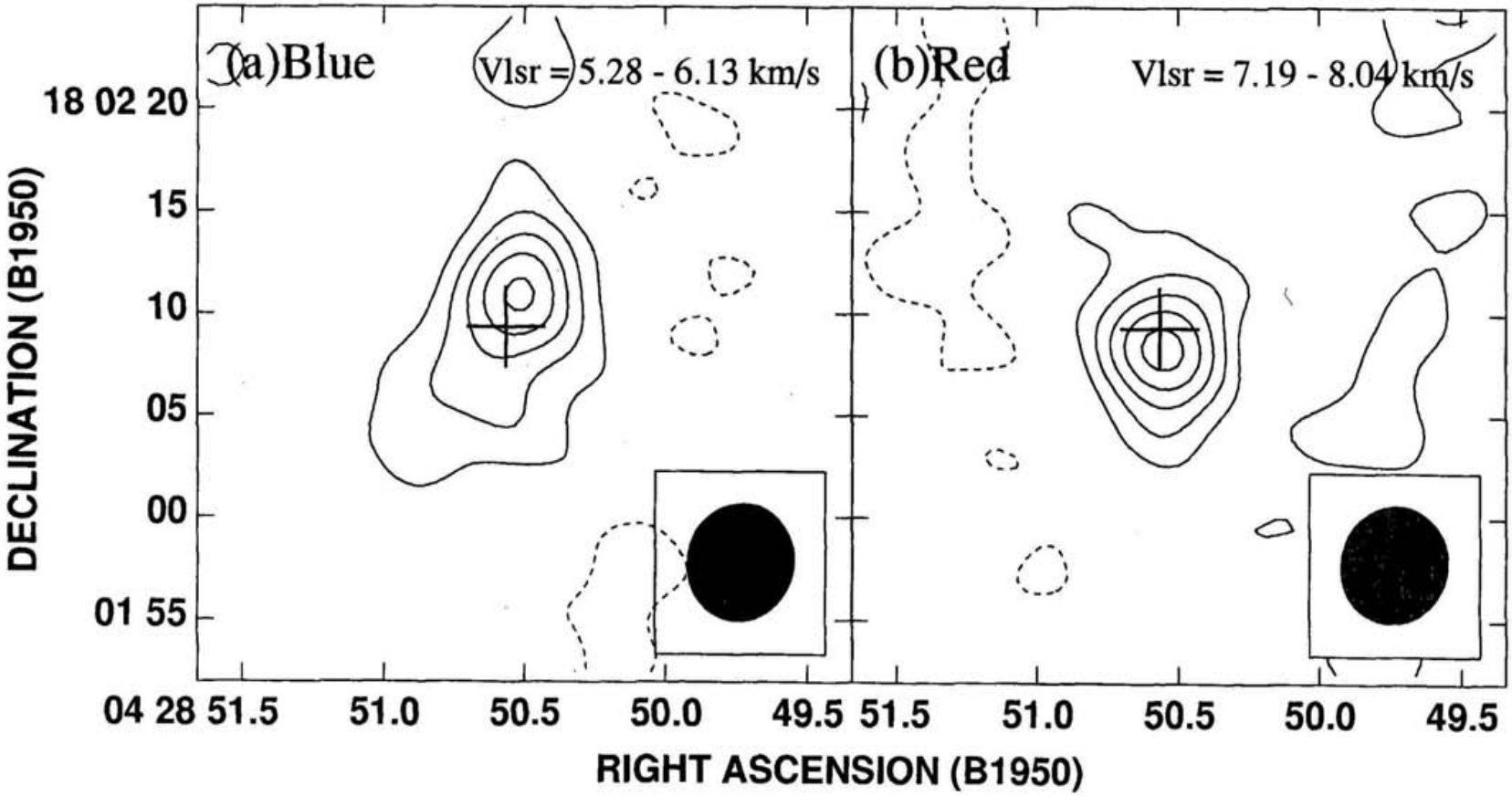
(a)Blue
Vlsr = 5.28 - 6.13 km/s
(b)Red
Vlsr = 7.19 - 8.04 km/s
18 02 20
15
10
05
00
01 55
DECLINATION (B1950)
04 28 51.5
51.0
50.5
50.0
49.5
51.5
51.0
50.5
50.0
49.5
RIGHT ASCENSION (B1950)

Fig. III.5

Chapter IV

The Dispersing Cloud Core around T Tauri

This chapter has been published in *The Astrophysical Journal* , **470**, 1001-1014 (1996) as
The Dispersing Cloud Core around T Tauri
by

Munetake MOMOSE[1], Nagayoshi OHASHI[2], Ryohei KAWABE[3], Masahiko HAYASHI[4], and Takenori NAKANO[3]

[1] Department of Astronomical Science, The Graduate University for Advanced Studies, Nobeyama Radio Observatory, Nobeyama, Minamimaki, Minamisaku, Nagano 384-13, Japan

[2] Harvard-Smithsonian Center for Astrophysics, MS78, 60 Garden Street, Cambridge, MA 02138.

[3] Nobeyama Radio Observatory, Nobeyama, Minamimaki, Minamisaku, Nagano 384-13, Japan

[4] SUBARU Project Office, National Astronomical Observatory, Mitaka, Tokyo 181, Japan

ABSTRACT

We have made ^{13}CO ($J = 1 - 0$) observations of T Tauri with the Nobeyama Millimeter Array (NMA) and with the Nobeyama 45 m telescope. The ^{13}CO ($J = 1 - 0$) emission detected with the NMA shows three different features: (1) a pair of ringlike features surrounding T Tauri with a radius of 30″ (corresponding to 4200 AU at the distance of 140 pc to T Tauri) at the velocities blueshifted and redshifted by less than 1 km s^{-1} from the systemic velocity, (2) a blueshifted compact feature 3″ east of T Tauri, and (3) another compact feature 7″ southwest of T Tauri at velocities redshifted by more than 1 km s^{-1}. On the other hand, the ^{13}CO maps obtained with the 45 m telescope show a smoothly extended feature near the systemic velocity, which is missed in the NMA observations, as well as the above-mentioned three features. The total masses of gas detected with the NMA and the 45 m telescope are estimated to be $(0.054 - 0.23)\ M_\odot$ and $(0.31 - 1.3)\ M_\odot$, respectively. The difference in the estimated mass between the two observations is mainly due to resolving out of the smoothly extended feature in the NMA observations.

The ^{13}CO rings are interpreted as biconical outflowing shells in a nearly pole-on configuration. The high-velocity stellar wind ejected from T Tauri is estimated to be energetic enough to drive these outflowing shells. We have analyzed the three-dimensional structure of the shells by correcting for the projection effect on the plane of the sky, and we have found that the spatial extent of the shells is nearly equal to or slightly smaller than the typical size of the molecular cloud cores in the Taurus Molecular Cloud. This fact indicates that the outflowing shells are part of the parent cloud core that still remains around T Tauri, which is now dispersing under the influence of the stellar wind. Such an environment around T Tauri is quite different from those around typical T Tauri stars, which are associated only with compact gaseous components. These results strongly suggest that T Tauri is one of the objects in the transitional phase from the protostar stage, in which a central star is deeply embedded in an infalling envelope, to the T Tauri stage, in which a central star is surrounded by a compact circumstellar disk instead of a spatially extended envelope.

Subject headings: circumstellar matter — ISM: jets and outflows — ISM: molecules stars: individual (T Tauri) — stars: pre-main-sequence

IV.1. Introduction

Understanding of the physical properties of young stellar objects has been greatly improved by the analysis of their spectral energy distributions (SEDs). Lada (1987) (see also Lada & Wilking 1984) proposed that young stellar objects can be divided into three classes by their spectral indices $\alpha_{\rm IR}$, which is the mean value of $d(\log \lambda F_\lambda)/d(\log \lambda)$ in the wavelength range between $\lambda = 1\mu$m and 10μm: class I with $\alpha_{\rm IR} > 0$, class II with $-2 < \alpha_{\rm IR} \leq 0$, and class III with $-3 < \alpha_{\rm IR} \leq -2$. Class I sources are often found at the centers of ammonia cores without optical counterparts in the Palomar Observatory Sky Survey prints (Myers et al. 1987; see also Beichman et al. 1986). Theoretical models have shown that SEDs of class I sources can be reproduced by the emission from mass-accreting protostars (Adams & Shu 1986; Kenyon, Calvet, & Hartmann 1993a). On the other hand, class II sources correspond to optically visible T Tauri stars. SEDs of many class II objects can be well explained with a system composed of a central star and a circumstellar disk (Kenyon & Hartmann 1987; Adams, Lada, & Shu 1987; Bertout, Basri, & Bouvier 1988; Miyake & Nakagawa 1995). On the basis of these studies, it is widely accepted that the SED classes introduced by Lada (1987) correspond to different evolutionary stages of young stellar objects (e.g., Adams et al. 1987).

In the course of evolution from class I (optically invisible) to class II (optically visible) sources, dissipation of the parent cloud cores should occur, probably due to mass accretion onto the central star-disk systems and/or due to dispersal produced by the outflow (e.g., Hayashi et al. 1994; Ohashi et al. 1991, 1996b). To gain a better understanding of the evolution processes from protostars to typical T Tauri stars, we have to investigate in detail the objects that are in a "transitional phase" between these two evolutionary stages. Some T Tauri stars with so-called flat spectrum are good candidates for such objects. They exhibit very flat SEDs in the whole range of infrared wavelengths ($\lambda = 1 - 100\mu$m) and luminosities with huge infrared excesses, which are significantly larger than the "stellar" luminosities. It is difficult to explain their SEDs with a central star plus disk model unless these T Tauri stars have active disks with an unorthodox radial temperature distribution, $T(r) \propto r^{-0.5}$ (Adams, Lada, & Shu 1988). Recently, Calvet et al. (1994, hereafter CHKW) have proposed an attractive explanation for the flat SEDs; the SEDs of two flat-spectrum T Tauri stars, HL Tauri and T Tauri, can be reproduced by introducing tenuous axisymmetric infalling envelopes which surround the central star-disk systems (see also Kenyon et al. 1993a). Recent observational results also show that HL Tauri is accompanied by a spatially extended envelope, suggesting that it is younger than typical T Tauri stars. Aperture

synthesis ^{13}CO ($J = 1 - 0$) observations of HL Tauri with the Nobeyama Millimeter Array (NMA) have shown that the kinematics of the disklike structure around HL Tauri with a radius of 1400 AU is dominated by infalling motion (Hayashi, Ohashi, & Miyama 1993). This suggests that HL Tauri is significantly younger than typical T Tauri stars in the sense that dynamical mass accretion onto the central star-disk system is still going on. Observations of HL Tauri with the *Hubble Space Telescope* (Stapelfeldt et al. 1995) have shown that there is no stellar component in the HL Tauri region at optical wavelengths, indicating that the central star is still deeply embedded in circumstellar material. It will be important to investigate physical properties of the other T Tauri stars with flat SEDs as well in order to clarify whether they are in the "transitional phase" from protostars to typical T Tauri stars.

T Tauri shows a typical flat SED (Adams et al. 1988; CHKW). It is well known that T Tauri is a rare example of visible T Tauri stars with a bipolar molecular outflow (Edwards & Snell 1982). T Tauri is a binary system, consisting of the main star T Tau(N) and an IR companion T Tau(S) with a linear separation of $0''.6$ (Dyck, Simon, & Zuckerman 1982). Near-infrared polarization images around T Tauri indicated that T Tauri is surrounded by a nonspherical dusty envelope with a spatial extent exceeding 10^3 AU (Weintraub et al. 1992; Whitney & Hartmann 1993). High-resolution interferometric observations with ^{12}CO ($J = 1 - 0$) have revealed the presence of a gaseous structure extending $\sim 10''$ around T Tauri (Weintraub, Masson, & Zuckerman 1989, hereafter WMZ). WMZ argued that the velocity field of the ^{12}CO ($J = 1 - 0$) emission could be explained by a disk in Keplerian rotation around T Tauri.

In this paper, we report the results of aperture synthesis ^{13}CO ($J = 1 - 0$) observations of T Tauri by using the Nobeyama Millimeter Array (NMA) and the results of ^{13}CO ($J = 1 - 0$) mapping observations around T Tauri with the Nobeyama 45 m telescope. In § IV.2 we describe the observational parameters. We present the results of these observations in § IV.3. In § IV.4.1 we discuss the origin of the ^{13}CO emission. In § IV.4.2 we investigate the driving mechanism and three dimensional structure of the shells, and in § IV.4.3, we discuss the physical nature of the shells and the evolutionary status of T Tauri.

IV.2. Observations

IV.2.1. ^{13}CO ($J = 1 - 0$) Observations with the Nobeyama Millimeter Array

Aperture synthesis ^{13}CO ($J = 1 - 0$) observations were made during a period from 1993 November to 1994 March with the NMA, which was composed of five 10 m dishes. We used the SIS receivers (Sunada et al. 1993) whose system noise temperatures were typically 400 K (double sideband [DSB]) at the zenith. We employed the digital FFT spectral correlator FX, which gave a frequency resolution of 156 kHz, corresponding to the velocity resolution of 0.425 km s^{-1}. The 110 GHz continuum emission from T Tauri was observed simultaneously with a bandwidth of 160 MHz. The phase and gain of the array system were calibrated by observing 0420−014 or 0528+134 every 30 minutes. The flux density of 0420−014 at 110 GHz was 2.3 Jy in 1993 November, and that of 0528+134 was 4.83 Jy at 110 GHz from February to March in 1994.

We made the observations for two fields of view; the first field is centered on the position of T Tauri [R.A.(1950) = $4^h19^m04^s.21$, decl.(1950) = +19°25′05″.4: Herbig & Bell 1988], and the second is on the position 37″.4 southwest (P.A. = 232°) of T Tauri. Two compact array configurations (giving 20 baselines) were used for the observations of both fields. Before making ^{13}CO images of each field, the continuum level was subtracted from the visibility data. After the conventional deconvolution process (CLEAN) and the correction for the primary beam (FWHM = 65″) attenuation in each field, the ^{13}CO images of the two fields were mosaicked in such a way as to minimize noise in each combined channel map. The size of the synthesized beam is 7″.2 × 5″.5 (FWHM) with P.A. of 140°. This corresponds to 1000 AU × 770 AU at the distance 140 pc of the Taurus Molecular Cloud. The minimum baseline in the observations was 5 kλ, so that our observations are insensitive to structures with sizes greater than 41″, corresponding to $\sim$ 5800 AU. The rms noise level in the combined channel map is 115 mJy beam^{-1} at the center of the field of view and 354 mJy beam^{-1} at the edge of the field of view.

IV.2.2. Observations with the Nobeyama 45 m Telescope

We made mapping observations of ^{13}CO ($J = 1 - 0$) on 1995 March 13 and 15 with the Nobeyama 45 m telescope. We used the SIS 2 × 2 focal plane array receiver (Sunada et al. 1995), which consists of four beams with almost identical half-power beamwidths of 17″

at 110 GHz. We employed acousto-optical spectrometers with a spectral resolution of 37 kHz, corresponding to the velocity resolution of 0.1 km s^{-1} at 110 GHz. The system noise temperature was typically 300 K (single sideband [SSB]) during our observations. Pointing of the telescope was checked once an hour by observing SiO ($J = 1 - 0$) maser of NML Tau at 43 GHz. The pointing accuracy was better than 4″. We observed Orion KL with ^{13}CO ($J = 1 - 0$) once a day in order to calibrate the difference in gain among the four beams. We mapped a 119″ × 119″ area around T Tauri with two different grid spacings; 12″ spacings for the inner 102″ × 102″ area, and 17″ spacings for the outer region. In § IV.3.2. we derive gas mass on the basis of T_R^*, which was introduced by Kutner & Ulich (1981). In converting the antenna temperature (T_A^*) to T_R^*, we assumed the forward scattering and spillover efficiency of the 45 m telescope to be 0.85.

IV.3. Results

Before showing our present results, we comment on the systemic velocity of T Tauri because it is an important parameter for understanding the results. Hartmann et al. (1986) have estimated the line-of-sight velocity of T Tauri to be $V_{HEL} = +19.1 \pm 1.2$ km s^{-1} (corresponding to $V_{LSR} = +8.2 \pm 1.2$ km s^{-1}) from spectroscopic observations of T Tauri at optical wavelengths. Recent CO observations toward T Tauri have shown that the peak velocities of the $J = 3 - 2$ and $J = 6 - 5$ lines are $V_{LSR} \approx +8$ km s^{-1} (Schuster et al. 1993). It is natural to regard the peak velocities of these higher CO transitions as the plausible systemic velocity of T Tauri because these lines originate in the warm and dense circumstellar material in the vicinity of T Tauri (Schuster et al. 1993). This systemic velocity estimated from the CO lines is consistent with that obtained by Hartmann et al. (1986). Based on these observational results, we assume the systemic velocity of T Tauri, V_{LSR}, to be +8.2 km s^{-1} unless otherwise specified.

IV.3.1. ^{13}CO ($J = 1 - 0$) Emission around T Tauri Obtained by the NMA Observations

IV.3.1.1. Morphology and Velocity Field

Figure IV.1 shows the mosaicked velocity channel maps of the ^{13}CO emission around T Tauri obtained with the NMA. ^{13}CO emission above the 3σ level was detected in the

velocity range between $V_{\rm LSR} = 5.85$ km s^{-1} and 9.67 km s^{-1}. The detected ^{13}CO emission can be characterized by the following three features: (1) spatially extended features that are found in the range between $V_{\rm LSR} = 7.12$ km s^{-1} and 8.82 km s^{-1}, (2) a compact feature 3″ east of T Tauri in the range from 5.85 km s^{-1} to 7.97 km s^{-1}, and (3) a faint, compact feature 7″ southwest of T Tauri seen in the maps at $V_{\rm LSR} = 9.25$ km s^{-1} and 9.67 km s^{-1}. In the following, we will describe morphology and velocity field of each feature in detail.

IV.3.1.1.1. The Spatially Extended Features

We have found some difference in the distribution of the extended features between blueshifted and redshifted velocities. To make the overall structures of the blueshifted and redshifted extended features clearer, we made two maps integrated over the velocity ranges of $V_{\rm LSR} = 7.12 - 7.55$ km s^{-1} and $V_{\rm LSR} = 8.40 - 8.82$ km s^{-1} as shown in Figure IV.2*a* and IV.2*b*, respectively. The extended feature at blueshifted velocities (Fig. IV.2*a*) consists of two regions of the emission. One is a blob covering the northeast area from T Tauri with a size of 35″ × 25″. The blob contains several emission peaks. The other emitting region appears at ∼ 35″ west of T Tauri and continues to the southwest of T Tauri with a width of ∼ 20″. Although this region also contains several peaks, the one at 45″ southwest of T Tauri is most prominent. Similarly to the blueshifted feature, the extended feature at redshifted velocities (Fig. IV.2*b*) also consists of two emitting regions. One is located at ∼ 30″ east of T Tauri with a size of 30″ × 15″. The other extends from ∼ 25″ west to ∼ 20″ south of T Tauri with several emission peaks that are connected mutually by diffuse emission.

We have identified two arcs in each extended feature by connecting the emission peaks as indicated by thick gray lines in Figures IV.2*a* or IV.2*b*. Hereafter we call the extended features "a pair of rings", though some parts of the rings seem to be missing (i.e., the southern part of the blueshifted ring and the northern part of the redshifted one). Both rings have a radius of ∼ 30″, which corresponds to ∼ 4200 AU at the distance to T Tauri. The central positions of the rings are different from each other; the center of the blue ring (Fig. IV.2*a*) is located at ∼ 15″ southwest of T Tauri, but the red one (Fig. IV.2*b*) is almost centered at the stellar position. Figure IV.3, showing a position-velocity diagram along a line connecting the centers of the two rings (P.A. = 77°) together with the integrated ^{13}CO ($J = 1 - 0$) intensity map, demonstrates clearly the positional difference between the centers of the red ring (denoted A, B and C) and the blue ring (denoted D, E and F).

Comparing our ^{13}CO observations with other observational results, we have found some important characteristics, which can be clues to understanding the origin of these rings. Figures IV.4*a* and IV.4*b* show our contour maps of the blueshifted ^{13}CO ring superposed on a K'-band image of the reflection nebula NGC 1555 (Hodapp 1994) and on an I-band coronagraphic image of T Tauri (Nakajima & Golimowski 1995), respectively. NGC 1555 clearly delineates the inner edge of the western arc of the blue ring (Fig. IV.4*a*). The reflection nebula in the vicinity of T Tauri is found to have similar curvature as the north-southeast arc of the blue ring (Fig. IV.4*b*). These results imply that the inner part of the blue ring is illuminated by the light from T Tauri. Figure IV.5 compares the ^{12}CO ($J = 3-2$) emission from the molecular outflow with moderately high velocities (blueshifted or redshifted by $2 - 13$ km s^{-1} from the systemic velocity) (Schuster 1994; Schuster et al. 1996) with the ^{13}CO rings, showing that the strongest parts of the blueshifted and redshifted outflows are located inside the blue and red rings, respectively. This fact implies that the dense gas traced by the ^{13}CO ($J = 1-0$) emission with low velocities surrounds the moderately high velocity outflow. These characteristics of the ^{13}CO rings are understood naturally by assuming that the origin of the rings is a pair of shells outflowing with small velocities. We will discuss this point further in § IV.4.1.

IV.3.1.1.2. The Spatially Compact Features

We have found a spatially compact feature $\sim 3''$ east of T Tauri in channel maps at all the blueshifted velocities $V_{\rm LSR} = 5.85 - 7.97$ km s^{-1}. This feature appears at $V_{\rm LSR} = 5.85$ km s^{-1} (Fig. IV.1*b*), has a bright peak with faint and diffuse emission around it at $V_{\rm LSR} = 6.27$ and 6.70 km s^{-1} (Figs. IV.1*c* – 1*d*), and becomes most prominent in the velocity range of $V_{\rm LSR} = 7.12 - 7.97$ km s^{-1} (Figs. IV.1*e* – 1*g*). The size of this feature is $5'' \times 5''$ at $V_{\rm LSR} = 7.12$ km s^{-1}. WMZ also detected this compact feature in the velocity range of $V_{\rm LSR} = 7.4 - 7.9$ km s^{-1} with their ^{13}CO ($J = 1 - 0$) observations. The other compact feature at $\sim 7''$ southwest of T Tauri is found in the maps at $V_{\rm LSR} = 9.25$ and 9.67 km s^{-1} (Figs. IV.1*j* – 1*k*), with a size of $4'' \times 10''$.

IV.3.1.2. Total Mass of the Observed Gas around T Tauri

We can estimate the total mass of the molecular gas detected with the NMA by the following equation (Scoville et al. 1986):

$$M_{\rm gas} = 5.37 \times 10^{-5} T_{\rm ex} \exp\left(\frac{5.29}{T_{\rm ex}}\right) \frac{\tau_{^{13}\rm CO}}{1 - \exp\left(-\tau_{^{13}\rm CO}\right)} \left(\frac{d}{140\ \rm pc}\right)^2 \left[\frac{10^{-6}}{X(^{13}\rm CO)}\right] \int S_\nu dv\ M_\odot, \quad \text{(IV.1)}$$

where $T_{\rm ex}$ is the excitation temperature of ^{13}CO at the $J = 1$ level, d is the distance to T Tauri, $X(^{13}\rm CO)$ is the fractional abundance of ^{13}CO relative to H_2, $\tau_{^{13}\rm CO}$ is the optical depth of the gas for the ^{13}CO ($J = 1 - 0$) line, and $\int S_\nu dv$ is the integrated flux in units of Jy km s^{-1}. On the assumption of optically thin ^{13}CO emission ($\tau_{^{13}\rm CO} \ll 1$), the integrated flux of 118 Jy km s^{-1} gives us the total gas mass of $(0.054 - 0.23)\ M_\odot$ with $T_{\rm ex} = 10 - 30$ K and $X(^{13}\rm CO) = (1 - 2) \times 10^{-6}$. If $\tau_{^{13}\rm CO}$ were considerably greater than 1, the above estimate of the gas mass would be a lower limit. However, WMZ estimated $\tau_{^{13}\rm CO}$ to be at most 1.14 at $V_{\rm LSR} = 7.6$ km s^{-1} from the peak intensities of the ^{12}CO ($J = 1 - 0$) and ^{13}CO ($J = 1 - 0$) lines obtained with their interferometric observations. Therefore, it is unlikely that we have underestimated significantly the total mass of the observed gas by assuming that the ^{13}CO ($J = 1 - 0$) emission is optically thin. Note that spacially extended components were resolved out in the NMA observations, so that the total gas mass within the field of view of the NMA observations may be underestimated, as will be described in the next section.

IV.3.2. ^{13}CO ($J = 1 - 0$) Emission around T Tauri Obtained by the Nobeyama 45 m Telescope and Comparison with the Results of the NMA Observations

Figure IV.6 shows channel maps of the ^{13}CO emission obtained by the 45 m telescope with a velocity resolution of 0.2 km s^{-1}. The resultant rms noise level is $T_{\rm R}^* = 0.104$ K. The overall distributions of the ^{13}CO emission in Figure IV.6 are similar to those obtained with the NMA (Fig. IV.1). In the channel maps (Figs. IV.6*d* – 6*g*) for $V_{\rm LSR} = 7.1 - 7.7$ km s^{-1}, we can find two prominent emission features: a peak located $\sim 20''$ northeast of T Tauri, and a ridgelike feature starting at $\sim 50''$ northwest of T Tauri and extending along the western edge of the channel maps. These two emission features are almost coincident with the blueshifted ring detected by the NMA observations (Fig. IV.2*a*). In the channel maps

(Figs. IV.6j – 6l) for $V_{\rm LSR}$ = 8.3 – 8.7 km s^{-1}, the ^{13}CO emission has a strong peak to the southwest of T Tauri, with an arclike extended feature opened toward T Tauri at lower contour levels. This feature seems to correspond to the southwestern arc of the redshifted ring seen in the NMA map (see Fig. IV.2b). At higher blueshifted ($\leq$ 6.9 km s^{-1}; Figs. IV.6a – 6c) and redshifted ($\geq$ 8.9 km s^{-1}; Figs. IV.6n – 6o) velocities, spatially compact features can be seen at $\sim$ 5″ east and at $\sim$ 5″ southwest, respectively, of T Tauri, as was also seen in the NMA channel maps (see Figs. IV.1b – 1d and IV.1j – 1k). On the other hand, the ^{13}CO emission in the channel maps near the systemic velocity, Figures IV.6h and IV.6i for $V_{\rm LSR}$ = 7.9 – 8.1 km s^{-1}, is distributed smoothly compared with the other channel maps in Figure IV.6, and each emission peak coincides well with the corresponding peak in the NMA channel maps.

In order to calculate the total mass of the molecular gas from the 45 m observations, the flux density in the field of view of the NMA observations was estimated from the flux density in the dashed rectangular area (see Fig. IV.6a) by correcting the difference in the solid angles. A total flux of 679 Jy km s^{-1} has been obtained for the velocity range $V_{\rm LSR}$ = 5.8 – 9.6 km s^{-1}. With this flux, equation (IV.1) gives the total gas mass of (0.31 - 1.3) $M_{\odot}$ under the same assumptions as for the NMA case. This is 5.8 times larger than the mass derived from the total flux obtained with the NMA.

The difference in the total flux and the estimated mass between the NMA and 45 m observations is mainly due to resolving out of the smoothly extended feature in the NMA observations. Figure IV.7 compares the total flux densities obtained with the NMA and with the 45 m telescope; the missing flux density at velocities blueshifted or redshifted by $>$ 0.5 km s^{-1} in the NMA observations is less than 75 % of the 45 m flux density, while in the velocity range of $V_{\rm LSR}$ = 7.7 – 8.7 km s^{-1} , more than 80 % of the 45 m flux density is missing in the NMA observations. It indicates that the smoothly extending feature is dominated near the systemic velocity, and this feature is not detected by the NMA observations.

IV.3.3. Continuum Emission Obtained by the NMA Observations

We detected unresolved continuum emission toward T Tauri at 110 GHz with the NMA. The position of the continuum emission is coincident with that of T Tauri (Herbig & Bell 1988), and with our angular resolution we could not separate the contribution of

the main star T Tau(N) from that of the IR companion T Tau(S), which locates 0.″6 south of the main star (Dyck et al. 1982). The total flux density of the continuum emission is 48 ± 7 mJy in the present observations. This is smaller than the previously obtained flux densities toward T Tauri, 75 mJy at 110 GHz (WMZ) and 56 ± 10 mJy at 98 GHz (Ohashi et al. 1996b), even if we take into account a possible systematic error in the flux calibration (≤ 10 %).

A possible cause for the smaller flux density obtained by our observations is the time variability of non-dust radiation which may contribute partly to the continuum emission at millimeter wavelengths. Recently, Skinner & Brown (1994) have analyzed high angular resolution images of T Tauri at centimeter wavelengths, and have interpreted the centimeter emission from T Tau(N) as free-free emission and that from T Tau(S) as nonthermal gyrosynchrotron emission. The contribution of the gyrosynchrotron emission to the continuum at 110 GHz may be negligible because of its negative spectral index between 2 and 3.6 cm obtained by simultaneous total flux measurements (Skinner & Brown 1994). On the other hand, the free-free emission may contribute significantly to the continuum emission at 110 GHz and may show time variability. For example, according to the spherical constant-velocity wind model by Panagia & Felli (1975), the spectral index of the predicted free-free emission is positive ($\alpha = +0.6$ where $S_\nu \propto \nu^\alpha$), and the emission shows time variability due to the variation of mass-loss rate and/or that of ionization degree (see also Panagia 1991). In order to confirm this for T Tauri, we need further photometric studies of the continuum emission at millimeter-centimeter wavelengths.

IV.4. Discussion

IV.4.1. Origin of the ^{13}CO Emission

To explain the ^{13}CO emission maps of T Tauri in a consistent manner, we propose a model of biconical outflowing shells in a nearly pole-on configuration as illustrated in Figure IV.8. In this model, we suppose that the axis of the outflowing shells is at an angle of about 10° with the line of sight and has a P.A.$\approx 257°$ (southwestward) on the sky on its near side. Herbst et al. (1986) estimated the angle between the line of sight and the rotation axis of T Tau(N) to be $8° - 13°$ from its rotation period and projected rotation velocity. Moreover, the near-IR polarization image of T Tauri can be reproduced well by the scattered light from dust contained in an axisymmetric envelope with a pole-on configuration (Weintraub

et al. 1992; Whitney & Hartmann 1993). The configuration and the shape of the biconical outflowing shell in our model are consistent with these estimates. The position angle on the sky of the shell axis in our model agrees roughly with that (270°) of the blueshifted jet ejected from T Tauri (Bührke, Brugel, & Mundt 1986; Böhm & Solf 1994). It is reasonable that the shell axis is nearly parallel to that of the outflow. In addition to the outflowing shells, a significant amount of the ambient gas component missed in the NMA observations is expected to exist around T Tauri, as shown in the maps obtained with the 45 m telescope.

The proposed model of the biconical outflowing shells can explain quite well the observational results described in the previous section, if the ^{13}CO rings originate from the shells. First, the assumed orientation of the shells relative to the line of sight explains easily why the blueshifted ring is located southwestward (P.A.$\approx$ 257°) compared with the redshifted one on the plane of the sky. Second, the reflection nebula NGC 1555 is observed along the inner edge of the blueshifted ring (see Fig. IV.4*a*) because the inner surface of the blueshifted shell, which is at the near side, reflects the light of T Tauri. Finally, the fact that the blueshifted and redshifted CO outflows are located inside the blue and red ^{13}CO rings, respectively (see Fig. IV.5) is understood naturally if we interpret the ^{13}CO rings as the projection on the sky of the swept-up shells outflowing with lower velocities and surrounding the higher velocity components of the outflow, though Schuster et al. (1997) explain their ^{12}CO ($J = 3 - 2$) outflow maps in a different way. The situation that the higher velocity components of the outflow are surrounded by dense gas with lower velocities has been found commonly in other molecular outflows, for example, in the cases of L1551-IRS 5 (Uchida et al. 1987; Moriarty-Shieven & Snell 1988) and Mon R2 (Xie, Goldsmith, & Patel 1993). We will discuss in detail the driving mechanism and the three-dimensional structure of the outflowing shells in later subsections.

The existence of an infalling envelope with a spatial extent exceeding 1000 AU around T Tauri was suggested in some previous studies (e.g., CHKW; Weintraub et al. 1992; van Langevelde, van Dishoeck, & Blake 1994a). The positional difference between the two ^{13}CO rings could be explained in terms of the infalling shell whose axis inclines northeastwards on its near side. It should be noted, however, that such an infalling model is incompatible with the relation between the ^{13}CO rings and the reflection nebula NGC 1555, and with the relation between the ^{13}CO rings and the moderately high velocity outflow; if the axis of the shell would incline northeastward on its near side, the reflection nebula should correspond to the inner edge of the red ring, and the red and blue lobes of the CO outflow should be surrounded by the blue and red rings, respectively, contrary to the observed structure. Our

outflowing shell model is consistent with the observed structure.

Some parts of the ^{13}CO rings seem to be missing in the maps with the NMA observations, i.e., the northern part of the red ring and the southern part of the blue ring (see Figs. IV.2*a* – 2*b*). These cases of missing emission may be attributed to the north(red)-south(blue) poorly-collimated outflow system associated with T Tauri, which was found by Solf, Böhm, & Raga (1988) (see also Böhm & Solf 1994). The physical nature of this outflow system is not so clear, because there are no similar outflow systems in the cases of other T Tauri stars (Böhm & Solf 1994). Nevertheless, an image of the H_2 emission line at $\lambda = 2\mu$m shows a structure elongated in the north-south direction (van Langevelde et al. 1994b), suggesting that the north-south outflow system is so energetic as to excite H_2 molecules by collisional heating. Such a poorly-collimated energetic outflow may break the shells if the axis of this outflow system deviates from that of the shells; i.e., the northern red lobe of the north-south outflow may have blown away the northern part of the redshifted outflowing shells, while the southern blue lobe may have blown off the southern part of the blueshifted outflowing shells.

On the other hand, the origin of the spatially compact features at 3″ east of T Tauri at all the blueshifted velocities and 7″ southwest of T Tauri at the velocities redshifted by more than 1 km s^{-1} is less certain. The velocity gradient in the east(blue)-west(red) direction cannot be explained by either Keplerian rotation or infall in a disklike structure if the axis of the disk is identical with that of the outflowing shells. Moreover, the line-of-sight velocities of the compact features are inconsistent with the velocities expected from either rotation or infall in the disklike structure, as shown below. The maximum line-of-sight velocity of the gas expected for Keplerian rotation is

$$0.62 \left(\frac{M_*}{2M_\odot}\right)^{1/2} \left(\frac{\sin i}{\sin 10^\circ}\right) \left(\frac{s}{1''}\right)^{-1/2} \text{km s}^{-1}, \tag{IV.2}$$

and that expected for disklike infall is

$$0.87 \left(\frac{M_*}{2M_\odot}\right)^{1/2} \left(\frac{\sin i \cos^{1/2} i}{\sin 10^\circ \cos^{1/2} 10^\circ}\right) \left(\frac{s}{1''}\right)^{-1/2} \text{km s}^{-1}, \tag{IV.3}$$

where s is the angular separation from T Tauri and i is the angle between the disk axis and the line of sight. The observed line-of-sight velocities for the compact features (blueshifted by 0.13 – 2.35 km s^{-1} at 3″ east and redshifted by 1.05 – 1.47 km s^{-1} at 7″ southwest of T Tauri) exceed the values obtained from equations (IV.2) and (IV.3). If the emission originates from an axisymmetric infalling envelope with bipolar cavities, the line-of-sight

velocity can be larger than equation (IV.3) and comparable to the observed velocities. In this case, however, it is difficult to explain the observed velocity gradient along the east-west direction because each of the blueshifted and redshifted components must be observed both east and west of T Tauri.

It is most plausible that these compact features originate from an outflowing gas that is on the surface of the geometrically thick disk around T Tauri as shown in Figure IV.8. In the eastern half of the disk, the outflowing gas on the nearer surface is observed as the blueshifted compact feature, while the outflowing gas on the farther surface is hardly observed with the NMA because the components whose line-of-sight velocities are close to the systemic velocity and are easily resolved out. Similarly, in the western half of the disk, we can observe only the gas on the farther surface of the disk as the redshifted compact feature. The reflection nebula in the vicinity of T Tauri discovered by Nakajima & Golimowski (1995) is well understood in terms of the scattered light from the surface of this geometrically thick disk. A similar outflowing gas with a disklike structure has also been found around DG Tauri by Kitamura, Kawabe, & Saito (1996).

IV.4.2. Physical Nature of the Outflowing Shells

IV.4.2.1. The Dynamical Time Scale of the Shells

We can identify six emission peaks designated A through F in the position-velocity (P-V) diagram along a line passing through T Tauri at P.A.= 77° (Fig. IV.3). As shown in the Appendix with a simplified model, we can obtained some restriction on the dynamical timescale of each emission peak from its projected distance from the star and line-of-sight velocity. From these restrictions we find that the dynamical time scale of the shell, $\tau_{\rm dyn}$, should satisfy

$$2.5 \times 10^4 \text{ yr} < \tau_{\rm dyn} < 7.3 \times 10^4 \text{ yr}. \qquad \text{(IV.4)}$$

IV.4.2.2. The Driving Source of the Outflowing Shells

It is accepted in general that the molecular outflows associated with low-mass young stellar objects are driven by the neutral components of winds or jets with extremely high velocities ($\geq$ 100 km s^{-1}) (e.g., Lizano et al. 1988; Koo 1989). These extremely high velocity

winds or jets (EHVs) are probably ejected from just the vicinity of stellar surfaces (see, e.g., Shu et al. 1994). Around T Tauri, the HI emission from EHVs has been marginally detected (Ruiz, Alonso, & Mirabel 1992). Ruiz et al. (1992) have estimated the physical quantities of the EHVs and have concluded that the EHVs can drive the molecular outflow associated with T Tauri. It would be natural to imagine that the outflowing shells are also driven by the EHVs. In order to examine this idea, we shall compare the momentum supply rate of EHVs with the momentum supply rates to the outflowing shells.

The momenta along the line of sight of the blueshifted and redshifted outflowing shells, $P_{\rm blue}$ and $P_{\rm red}$, are expressed as

$$P_{\rm blue} = \sum_{v_r<v_{\rm sys}} M(v_r)|v_r - v_{\rm sys}|, \tag{IV.5a}$$

$$P_{\rm red} = \sum_{v_r>v_{\rm sys}} M(v_r)|v_r - v_{\rm sys}|, \tag{IV.5b}$$

where $v_{\rm sys}$ is the systemic velocity and $M(v_r)$ is the gas mass in each radial velocity range. Assuming the optically thin ^{13}CO emission, $T_{\rm ex} = 10 - 30$ K, and $X(^{13}{\rm CO}) = (1-2)\times 10^{-6}$ in calculating $M(v_r)$ according to equation (IV.1), we obtain

$$P_{\rm blue} = (0.033 - 0.14)\ M_\odot\ {\rm km\ s^{-1}}, \tag{IV.6a}$$

$$P_{\rm red} = (0.006 - 0.026)\ M_\odot\ {\rm km\ s^{-1}}. \tag{IV.6b}$$

By taking the dynamical timescale of the shells $\tau_{\rm dyn} = 5\times 10^4$ yr (see eq. [IV.4]), the momentum supply rates to the blueshifted and redshifted shells are estimated, respectively, to be

$$\dot{P}({\rm shell})_{\rm blue} = P_{\rm blue}/\tau_{\rm dyn} = (6.6 - 28)\times 10^{-7}\ M_\odot\ {\rm km\ s^{-1}\ yr^{-1}}, \tag{IV.7a}$$

$$\dot{P}({\rm shell})_{\rm red} = P_{\rm red}/\tau_{\rm dyn} = (1.2 - 5.2)\times 10^{-7}\ M_\odot\ {\rm km\ s^{-1}\ yr^{-1}}. \tag{IV.7b}$$

In Table IV.1, we summarize $\dot{P}$(shell) given by equations (IV.7a) and (IV.7b), the momentum supply rates to the extended molecular outflow, $\dot{P}$(outflow), derived from Levreault's (1988) observations, and the momentum supply rate by the EHVs, $\dot{P}$(EHV), obtained by Ruiz et al. (1992). In principle, we can judge whether the EHVs can drive the shells or not by comparing $\dot{P}$(EHV) with $\dot{P}$(shell). However, $\dot{P}$(EHV) estimated by Ruiz et

al.(1992) is less certain, because the spatial extent of the EHVs was not directly obtained from their observations. On the other hand, $\dot{P}$(outflow) would give a lower limit to $\dot{P}$(EHV) because the molecular outflow around T Tauri must be driven by the EHVs ejected from T Tauri as in the cases of the other outflow sources (e.g., Lizano et al. 1988; Koo 1989). Hence, the comparison of $\dot{P}$(shell) with $\dot{P}$(outflow) would give some information on whether the EHVs can be the driving source of the shells.

Table IV.1 shows that $\dot{P}(\mathrm{outflow})_{\mathrm{blue/red}}$ are larger than $\dot{P}(\mathrm{shell})_{\mathrm{blue/red}}$ by an order of magnitude. Because of the uncertainty in τ_{dyn} as seen in equation (IV.4), $\dot{P}$(shell) in Table IV.1 has an uncertainty of a factor of ~ 2. Even if we take into account the fact that emission components of lower spatial frequencies are missing in the aperture synthesis observations, $\dot{P}$(shell) can hardly be underestimated by more than a factor of 10. This is because the NMA observations resolved out the emission mainly in the velocity range of $|v_r - v_{\mathrm{sys}}| < 0.5$ km s^{-1}, in which the ambient cloud emission predominates rather than that of the outflowing shells, as described in § IV.3.2 (see Fig. IV.7). Therefore, we can conclude that the EHVs are energetic enough to drive the outflowing shells around T Tauri.

IV.4.2.3. Three-dimensional Structure of the Shells: Dispersal of the Parent Cloud Core

In the Appendix we estimate the distance D_p of the emission peak p (p for A through F in Fig. IV.3) from the central star and its angular position ϕ_p measured from the axis of the shells (by definition $0° < \phi_p < 90°$). Because of the uncertainty in τ_{dyn} as shown in equation (IV.4), we can determine only the maximum and minimum values of ϕ_p and D_p. The results are shown in columns (2) through (5) of Table IV.2. In addition we list ϕ_p and D_p for the case of $\tau_{\mathrm{dyn}} = 5 \times 10^4$ yr in columns (6) and (7). As seen from Table IV.2, the estimated values of ϕ_p and D_p agree fairly well among the redshifted peaks (A through C) and among the blueshifted peaks (D through F) individually.

In Table IV.3, we list the distances and angular positions averaged among the blueshifted emission peaks in Figure IV.3 ($\overline{D}_{\mathrm{blue}}$, $\overline{\phi}_{\mathrm{blue}}$; first row), the redshifted peaks ($\overline{D}_{\mathrm{red}}$, $\overline{\phi}_{\mathrm{red}}$; second row), and all the peaks ($\overline{D}_{\mathrm{all}}$, $\overline{\phi}_{\mathrm{all}}$; third row) for the three cases of τ_{dyn} (2.5×10^4, 5×10^4, and 7.3×10^4 yr; see eq. [IV.4]). There are differences of a factor of ~ 2 between $\overline{D}_{\mathrm{blue}}$ and $\overline{D}_{\mathrm{red}}$ and between $\overline{\phi}_{\mathrm{blue}}$ and $\overline{\phi}_{\mathrm{red}}$. Such differences are well demonstrated in Figure IV.9, which shows the positions of all the emission peaks in Figure IV.3 for the case of $\tau_{\mathrm{dyn}} = 5 \times 10^4$ yr (see cols. [6] and [7] of Table IV.2). These differences may be

artifacts caused by the estimation error in the systemic velocity ($v_{\rm sys}$). For example, if $v_{\rm sys}$ is in fact +8.0 km s^{-1} instead of +8.2 km s^{-1}, these differences almost disappear, as shown in columns (8) and (9) of Table IV.3. It is easily understood that ($\overline{D}_{\rm blue}$, $\overline{\phi}_{\rm blue}$) and ($\overline{D}_{\rm red}$, $\overline{\phi}_{\rm red}$) are sensitive to a slight change in the systemic velocity. On the contrary, the values averaged for both blueshifted and redshifted peaks ($\overline{D}_{\rm all}$ and $\overline{\phi}_{\rm all}$) are rather insensitive to the adopted $v_{\rm sys}$ as seen in Table IV.3 (compare cols. [4] and [5] with cols. [8] and [9], respectively). Thus, we shall use only ($\overline{D}_{\rm all}$, $\overline{\phi}_{\rm all}$) in the following discussion.

It is noteworthy that the possible range of $\overline{D}_{\rm all}$, 4.7×10^3 AU to 9.3×10^3 AU (Table IV.3), is nearly equal to or slightly smaller than 10^4 AU, which is the typical radius of molecular cloud cores in the Taurus Molecular Cloud (Myers & Benson 1983). This fact implies that the pair of the outflowing shells is a part of the remaining cloud core around T Tauri. Moreover, the shells have the outflowing motion probably driven by the high-velocity stellar wind as discussed in § IV.4.2.2. Therefore, it can be concluded that a part of the molecular cloud core around T Tauri is now dispersing under the influence of the high-velocity wind ejected from T Tauri. Such a dispersing process will stop the growth of the central star and fix the mass of the forming star as investigated by Nakano, Hasegawa, & Norman (1995).

The averaged opening angle of all the emission peaks, $\overline{\phi}_{\rm all}$, lies between 28° and 54° (see Table IV.3); most of the parent cloud core at $\phi < \overline{\phi}_{\rm all}$ must have been blown off by the EHVs. Whitney & Hartmann (1993) calculated the images of scattered near-IR radiation employing model envelopes around young stellar objects. Comparing their model calculations with the near-IR observations of T Tauri (Weintraub et al. 1992), they found that the most plausible model is an envelope having parabolic holes with an opening angle of $\sim$ 30° at large radii. According to CHKW, the envelope model that can reproduce the SED of T Tauri also requires a bipolar cavity with an opening angle of 20°, which is somewhat smaller than our estimation. In summary, the values of $\overline{\phi}_{\rm all}$ we have obtained are in good agreement with those obtained in the previous studies.

IV.4.3. Evolutionary Stage of T Tauri and Unresolved Problems

Myers et al. (1987) (see also Beichman et al. 1986) have shown that class I sources tend to exist at the centers of ammonia cores, suggesting that these sources are deeply embedded within dense cloud cores with spatial extent of $\sim 10^4$ AU and that they are good

candidates for mass accreting protostars. On the other hand, recent observations with high spatial resolutions at mm wavelengths have revealed that typical class II sources (i.e., T Tauri stars) are accompanied by compact gaseous disks with radius smaller than 10^3 AU, which often show Keplerian rotation, instead of spatially extended gaseous structures. The latter category includes GG Tauri (Kawabe et al. 1993; Dutrey, Guilloteau, & Simon 1994), GM Aurigae (Koerner, Sargent, & Beckwith 1993), DM Tauri (Saito et al. 1995), and four other T Tauri stars (Koerner & Sargent 1995). It is now widely accepted that class I (or optically invisible) sources evolve into class II (or optically visible) sources as a result of dissipation of their envelopes (Beichman et al. 1986; Adams et al. 1987; Myers et al. 1987; Hayashi et al. 1994).

With this scenario of the evolution, one can naturally expect that there is a transitional phase between class I and class II sources in which a central source is associated with a spatially extended and dispersing envelope. The present observations suggest that T Tauri is a source in this transitional phase. It must be noted that the environment around T Tauri is quite different from those around both class I and class II sources. Class I sources are usually at or near the emission peaks of spatially extended cloud cores even if they are observed with a high angular resolution (e.g., Ohashi et al. 1996b), while T Tauri is not located at a peak of the well-defined cloud core. On the other hand, T Tauri is associated with a more extended gaseous structure compared with the typical class II sources like GG Tauri or DM Tauri. Such differences in environment may be due to an evolutional effect, i.e., T Tauri is older than class I sources but much younger than typical class II sources. This is consistent with our suggestion that T Tauri is in the transitional phase from a protostar to a typical T Tauri star.

In the Taurus Molecular Cloud, there are two other T Tauri stars that exhibit the characteristics expected for the transitional phase. One is HL Tauri, around which dynamical mass accretion onto the central star-disk system is still going on (Hayashi et al. 1993; Lin et al. 1994; see also Cabrit et al. 1996). The other is DG Tauri, which is accompanied by a "dispersing gaseous disk" with a radius of 2000 AU (Kitamura et al. 1996), suggesting that the remnant of the parent core is being blown off by the stellar wind as in the case of T Tauri. It is remarkable that all three T Tauri stars (T Tauri, HL Tauri, and DG Tauri) show flat SEDs with significant luminosity excesses at IR wavelengths. These observational facts may imply that the flat spectrum T Tauri stars are accompanied by spatially extended gaseous structures and are in the transitional phase from protostars to typical T Tauri stars.

One of the unresolved problems is whether infalling gas exists around T Tauri or not. Although the existence of the infalling envelope around T Tauri was suggested by some previous studies (Weintraub et al. 1992; Whitney & Hartmann 1993; CHKW; van Langevelde et al. 1994a), no direct evidence has been obtained in the present observations. Recent theoretical studies have shown that infalling envelopes around young stellar objects are expected to have disklike structures like that around HL Tauri (e.g., Galli & Shu 1993a, 1993b; Hartmann et al. 1994; Nakamura, Hanawa, & Nakano 1995). An infalling gaseous disk around T Tauri, even if it exists, would hardly be detected because of its nearly pole-on configuration (e.g., Herbst et al. 1986); the infalling gas in a disklike structure in a pole-on configuration is expected to have so small line-of-sight velocities that it is severely contaminated by the ambient molecular cloud. Further observations with higher velocity resolutions are required for settling this problem.

Another unresolved problem is the slight discrepancy in the opening angle of the shells between our estimation (37° if $\tau_{\rm dyn} = 5 \times 10^4$ yr) and that from the model constructed by CHKW (20°). CHKW discussed that if the opening angle of the shells is larger, the flux densities at mid- to far-infrared wavelengths become smaller than the observed ones because of the lack of dust with high temperatures (see Fig. 6 in CHKW). If the larger opening angle estimated from our observations is real, CHKW's discussion may suggest the existence of an additional source for mid- to far-infrared emission, e.g., a circumstellar disk with shallower radial gradient of the temperature (Adams et al. 1988) or the IR companion T Tau(S), whose contribution to the emission at wavelengths longer than 20μm has not been evaluated (see Ghez et al. 1991; Maihara & Kataza 1991).

IV.5. Conclusions

We have made aperture synthesis observations of T Tauri with the Nobeyama Millimeter Array (NMA) and mapping observations around T Tauri with the Nobeyama 45 m telescope with the ^{13}CO ($J = 1 - 0$) line. Our main results are summarized as follows:

1. We have found from the NMA observations a pair of ringlike ^{13}CO ($J = 1 - 0$) emissions with a radius of $\sim 30''$, corresponding to ~ 4200 AU at the distance 140 pc to T Tauri, detected at velocities blueshifted or redshifted by ~ 1 km s^{-1} from the systemic velocity. In addition to these ringlike features, two compact features have been detected in the vicinity of T Tauri. The total mass of the molecular gas detected with the NMA is

estimated to be $0.054 - 0.23\ M_{\odot}$ with the assumption of the optically thin ^{13}CO emission.

2. The maps obtained by the 45 m telescope show a smoothly extended feature near the systemic velocity, as well as the ringlike and compact features detected with the NMA. The total mass of the gas detected by the 45 m telescope is estimated to be $0.31 - 1.3\ M_{\odot}$ under the same assumption used for the NMA results. The difference in the estimated mass between the NMA and 45 m observations is mainly due to resolving out of the smoothly extended feature in the NMA observations.

3. The reflection nebula NGC 1555 associated with T Tauri well delineates the inner edge of the blueshifted ^{13}CO ring. Moreover, the ^{13}CO rings surround the moderately high velocity outflow. Such characteristics of the ^{13}CO rings as well as their morphology and velocity field can be well explained with a model of biconical outflowing shells in a nearly pole-on configuration.

4. The momentum supply rate of the stellar wind ejected from T Tauri is estimated to be much higher than the momentum supply rate to the outflowing shells. This suggests that the outflowing shells are driven by the high-velocity stellar wind.

5. We estimated the three-dimensional structure of the outflowing shells by correcting for the projection effect on the plane of the sky, and we found that the spatial extent of the shells is nearly equal to or slightly smaller than the typical size of the molecular cloud cores ($\sim 10^4$ AU in radius) in the Taurus Molecular Cloud. This indicates that the biconical outflowing shells are part of the parent cloud core around T Tauri, which is dispersing under the influence of the stellar wind.

6. The environment around T Tauri shown in the present observations is quite different from those around typical T Tauri stars in which central sources are associated with compact gaseous components. According to the widely accepted scenario in which embedded protostars evolve into optically visible T Tauri stars as a result of dissipation of their envelopes, the above difference in the environment is understood naturally as the difference in the evolutional phase, i.e., T Tauri is much younger than the other typical T Tauri stars and is in the transitional phase from a protostar to a typical T Tauri star.

7. We did not find any infalling gas around T Tauri in the present observations, although the existence of the infalling envelope around T Tauri has been predicted by some previous studies. It might be possible that the infalling gas is contaminated severely by the ambient molecular cloud if the infalling gas is confined to a disklike structure in a pole-on

configuration to us.

APPENDIX

IV.A. The Dynamical Timescale and the Three-Dimensional Structure of the Shells

We estimate the dynamical timescale and three-dimensional structure of the outflowing shells by using positions and velocities of the six emission peaks A through F in the shell features seen in the position-velocity (P-V) diagram at P.A. = 77° (Fig. IV.10*a*).

For simplicity, we adopt a model presented in Figure IV.10*b*. In this model, we suppose that the angle i between the axis of the shells and the line of sight is 10°, and that the gas in the shells is moving radially from the star. We assume also that the emission peaks are outside the cones with an opening angle of 10° and are more than 10° above or below the equatorial plane, which is perpendicular to the axis of the shells (the shaded area in Fig. IV.10*b*). It is found that the latter angle is a reasonable lower limit to the actual angle between the outflowing gas and the equatorial plane from the following estimation. A Keplerian disk in equilibrium has an effective half-thickness H given by $H/R \approx 2^{1/2} C_s / V_K$, where R is the distance from the central star, C_s is the isothermal sound velocity, and V_K is the Keplerian orbital velocity. For the mass of the central star $M_* = 2M_\odot$, $R = 10^3$ AU, and even a temperature as low as 10 K, we have $H/R \approx 0.20$, which corresponds to an angle of 11° to the star. We have even higher H/R for larger R. Thus the restriction we have placed on the positions of the emission peaks is not too strict. The positions of the emission peaks are specified by their radial distances from the star (e.g., D_A for peak A) and their angular positions measured from the axis of the shells (e.g., ϕ_A for A) (see Fig. IV.9*b*). For this model, ϕ_p (p: A through F) must be between 10° and 80°.

We estimate the dynamical timescale of the outflowing shells, τ_{dyn}, in the following way. First, we define the dynamical timescale τ_p for each emission peak as

$$\tau_p = \frac{D_p}{V_p}, \tag{IV.A1}$$

where V_p is the outflowing velocity of peak p. D_p and V_p are related to the two observed quantities, the projected distance from the star, d_p, and the line-of-sight velocity v_p, as follows (see Fig. IV.10*b*):

$$D_p = \frac{d_p}{\sin(\phi_p \pm i)}, \tag{IV.A2}$$

$$V_p = \frac{v_p}{\cos(\phi_p \pm i)}, \tag{IV.A3}$$

where the plus sign is for p = A, E, and F, and the minus sign for p = B, C, and D. Equations (IV.A1)–(IV.A3) give

$$\tau_p = \frac{d_p}{v_p \tan(\phi_p \pm i)}. \tag{IV.A4}$$

From the assumptions that $i = 10°$ and $10° < \phi_p < 80°$, we obtain upper or lower limits to τ_p:

$$\tau_p < \frac{d_p}{v_p \tan 20°} \quad \text{for } p = \text{A, E, and F,} \tag{IV.A5}$$

$$\tau_p > \frac{d_p}{v_p \tan 70°} \quad \text{for } p = \text{B, C, and D.} \tag{IV.A6}$$

Table IV.4 shows the restrictions on τ_p derived from equation (IV.A5) or (IV.A6) together with d_p and v_p. Assuming that all the emission peaks have the same dynamical timescale, $\tau_{\rm dyn}$, we can estimate the possible range of $\tau_{\rm dyn}$ in such a way that $\tau_{\rm dyn}$ should satisfy all the restrictions on τ_p, as

$$2.5 \times 10^4 \text{ yr} < \tau_{\rm dyn} < 7.3 \times 10^4 \text{ yr}. \tag{IV.A7}$$

For the allowable range of $\tau_{\rm dyn}$ given by equation (IV.A7), we can derive from equation (IV.A4) the range of ϕ_p for the emission peak p (p: A through F) as

$$\arctan\left[\frac{d_p}{v_p \max(\tau_{\rm dyn})}\right] \pm i < \phi_p < \arctan\left[\frac{d_p}{v_p \min(\tau_{\rm dyn})}\right] \pm i \tag{IV.A8}$$

where $i = 10°$, $\max(\tau_{\rm dyn}) = 7.3 \times 10^4$ yr, $\min(\tau_{\rm dyn}) = 2.5 \times 10^4$ yr, the minus sign is for p = A, E, and F, and the plus sign for p = B, C, and D.

We can also derive from equation (IV.A2) the range of D_p as

$$\frac{d_p}{\sin[\max(\phi_p) \pm i]} < D_p < \frac{d_p}{\sin[\min(\phi_p) \pm i]}, \tag{IV.A9}$$

where $\min(\phi_p)$ and $\max(\phi_p)$ are, respectively, the minimum and the maximum values of ϕ_p obtained from equation (IV.A8), the plus sign is for p = A, E, and F, and the minus sign for p = B, C, and D.

Columns (2) through (5) of Table IV.2 show the minimum and maximum values of ϕ_p and D_p derived from equations (IV.A8) and (IV.A9) for all the emission peaks. In addition, ϕ_p and D_p for the case of $\tau_{\rm dyn} = 5 \times 10^4$ yr are listed in columns (6) and (7). As seen from Table IV.2, the estimated values of ϕ_p and D_p agree fairly well among the redshifted peaks (A through C) and among the blueshifted peaks (D through F) individually. This agreement suggests that our simple three-dimensional model is physically reasonable.

Table IV.1. Momentum Supply Rates to the Outflowing Shells and to the Molecular Outflow, and the Momentum Supply Rate from the EHVs

Component	$\dot{P}$(Shell)[a] ($M_\odot$ km s^{-1} yr^{-1})	$\dot{P}$(Outflow)[b] ($M_\odot$ km s^{-1} yr^{-1})	$\dot{P}$(EHV)[c] ($M_\odot$ km s^{-1} yr^{-1})
Blue	$(6.6 - 28) \times 10^{-7}$	4×10^{-5}	6.6×10^{-5}
Red	$(1.2 - 5.2) \times 10^{-7}$	7×10^{-6}	...[d]

[a]The dynamical timescale of the shells, $\tau_{\rm dyn} = 5 \times 10^4$ yr, has been aopted.

[b]From Levreault 1988

[c]From Ruiz et al. 1992

[d]Cannot be established because of strong contamination by a cloud complex (see Ruiz et al. 1992).

Table IV.2. Ranges of the Distances and the Angular Positions of the Emission Peaks

p (1)	ϕ_p (Min.) [a] (deg) (2)	ϕ_p (Max.) [a] (deg) (3)	D_p (Min.) [a] (10^3 AU) (4)	D_p (Max.) [a] (10^3 AU) (5)	ϕ_p [b] (deg) (6)	D_p [b] (10^3 AU) (7)
A	34	61	3.0	4.1	45	3.5
B	53	80	2.9	4.0	64	3.4
C	35	64	5.1	10	44	7.4
D	20	38	3.6	9.7	25	6.7
E	16	45	5.6	11	25	8.0
F	10	37	7.8	17	18	12

[a]The dynamical timescale of the shells $\tau_{\rm dyn}$ is assumed to be between 2.5×10^4 yr and 7.3×10^4 yr (see eq. [IV.4]).

[b]$\tau_{\rm dyn} = 5 \times 10^4$ yr.

Table IV.3. The Mean Distance $\overline{D}$ and the Mean Angular Position $\overline{\phi}$ of the Emission Peaks for Some Values of $\tau_{\rm dyn}$

PEAKS	$\overline{D}$ [a] (10^3 AU)	$\overline{\phi}$ [a] (deg)	$\overline{D}$ [b] (10^3 AU)	$\overline{\phi}$ [b] (deg)	$\overline{D}$ [c] (10^3 AU)	$\overline{\phi}$ [c] (deg)	$\overline{D}$ [d] (10^3 AU)	$\overline{\phi}$ [d] (deg)
(1)	(2)	(3)	(4)	(5)	(6)	(7)	(8)	(9)
Blue	5.7	40	8.9	23	13	15	7.5	29
Red	3.7	71	4.8	51	6.0	41	6.5	34
All	4.7	54	6.8	37	9.3	28	7.1	32

[a] $\tau_{\rm dyn} = 2.5 \times 10^4$ yr and the systemic velocity of T Tauri, $V_{\rm LSR} = +8.2$ km s^{-1}, has been adopted.

[b] $\tau_{\rm dyn} = 5.0 \times 10^4$ yr and the systemic velocity of T Tauri, $V_{\rm LSR} = +8.2$ km s^{-1}, has been adopted.

[c] $\tau_{\rm dyn} = 7.3 \times 10^4$ yr and the systemic velocity of T Tauri, $V_{\rm LSR} = +8.2$ km s^{-1}, has been adopted.

[d] $\tau_{\rm dyn} = 5.0 \times 10^4$ yr and the systemic velocity of T Tauri, $V_{\rm LSR} = +8.0$ km s^{-1}, has been adopted.

Table IV.4. Restrictions on the Dynamical Timescale τ_p for Each Emission Peak

p	d_p[a] (10^3 AU)	v_p[b] (km s^{-1})	τ_p (10^4 yr)
A	2.8	+0.20	< 19
B	2.7	+0.20	> 2.5
C	4.1	+0.62	> 1.2
D	1.7	−0.65	> 0.47
E	4.6	−0.65	< 9.7
F	5.8	−1.08	< 7.3

[a]A distance to T Tauri of 140 pc has been adopted.

[b]A systemic velocity of T Tauri, $V_{LSR} = +8.2$ km s^{-1}, has been adopted.

— Figure Captions —

Fig. IV.1.— The pseudo-color velocity channel maps of the T Tauri region with the ^{13}CO ($J = 1 - 0$) line obtained by the NMA. The corresponding LSR velocity in km s^{-1} is noted in the upper right corner of each panel. The white dashed line indicates the field of view of our observations. The cross marks the position of T Tau(N) (Herbig & Bell 1988). It should be noted that the separation between T Tau(N) and the IR companion, T Tau(S), is so small ($\sim$ 0.″6, Dyck et al. 1982) that the positions of these two stars overlap each other in these channel maps.

Fig. IV.2.— Spatially extended features of the ^{13}CO ($J = 1 - 0$) emission with the NMA observations: the maps integrated over the velocity range (*a*) $V_{\rm LSR} = 7.12 - 7.55$ km s^{-1}, and (*b*) $V_{\rm LSR} = 8.40 - 8.82$ km s^{-1}. The systemic velocity is $V_{\rm LSR} = 8.2$ km s^{-1}. The gray lines connecting several peaks of the emission show a pair of "^{13}CO rings". The cross in each panel indicates the position of T Tau(N). The contour spacing is 2σ, starting at 3σ ($1\sigma = 124$ mJy beam^{-1}). Dashed lines are -3σ contours.

Fig. IV.3.— (*Top*) Integrated intensity map of the ^{13}CO ($J = 1 - 0$) emission. The contour spacing is 1.5σ, starting at 3σ ($1\sigma = 48.3$ mJy beam^{-1}). Dashed lines are -3σ contours. (*Bottom*) The position-velocity diagram cutting along the thick line (P.A. = 77°) in the upper panel. We adopt $V_{\rm LSR} = +8.2$ km s^{-1} as the systemic velocity of T Tauri. The letters A, B & C indicate the emission peaks contained in the redshifted rings and the letters D, E & F indicate those in the blueshifted rings, respectively. The contour spacing is 1.5σ, starting at 3σ ($1\sigma = 177$ mJy beam^{-1}). Dashed lines are -3σ contours.

Fig. IV.4.— (*a*) Contour map of the blueshifted ^{13}CO ($J = 1 - 0$) ring superposed on a K'-band image of the reflection nebula NGC 1555 (Hodapp 1994). (*b*) Contour map of the blueshifted ^{13}CO ($J = 1 - 0$) superposed on an I-band coronagraphic image of T Tauri (Nakajima & Golimowski 1995).

Fig. IV.5.— Maps of the ^{13}CO rings shown in Fig. IV.2 are superposed on the ^{12}CO ($J = 3 - 2$) maps drawn in dashed lines (Schuster 1994): *left*: The blueshifted ^{12}CO ($J = 3 - 2$) map integrated over $V_{\rm LSR} = -5$ to $+6$ km s^{-1}; *right*: the redshifted ^{12}CO ($J = 3 - 2$) map integrated over $V_{\rm LSR} = +9$ to $+21$ km s^{-1}.

Fig. IV.6.— Velocity channel maps of the T Tauri region in the ^{13}CO ($J = 1 - 0$) line, obtained by the Nobeyama 45 m telescope. The corresponding LSR velocity in km s^{-1} is

noted in the upper right corner of each panel. The cross indicates the position of T Tau(N). The contour spacing is 3σ, starting at 3σ (1σ = 0.104 K in T_R^*). The contours above T_R^* = 5.90 K are shown in white lines.

Fig. IV.7.— Comparision of the total flux densities obtained by the NMA (*solid line*) with those obtained by the 45 m telescope (*dashed line*). The total flux densities with the 45 m telescope were measured in the rectangular area indicated by the thick broken line in Fig. IV.6*a*, and were corrected for the difference in the solid angles between the two observations.

Fig. IV.8.— Schematic illustration of the biconical outflowing shell model. The shells, indicated by dots, are expected to be observed as the ^{13}CO rings. The reflection nebula NGC 1555 is interpreted as the inner surface of the nearer shell which scatters the stellar light. The origin of the spatially compact features near the star may be interpreted as the outflowing gas on the surface of the geometrically thick disk around T Tauri, indicated by the gray thick lines. A significant amount of the ambient gas is expected to exist around T Tauri, as indicated by the hatching.

Fig. IV.9.— Positions of the emission peaks for the case of $\tau_{\rm dyn} = 5 \times 10^4$ yr. All the peaks are plotted according to the absolute values of their coordinates.

Fig. IV.10.— (*a*) Position-velocity diagram at P.A. = 77°, the same as in Fig. IV.3. Six peaks of the emission contained in the shell features are marked by the letters A–F. (*b*) A model for estimating the dynamical timescale and the three-dimensional structure of the shells. We assume that each emission peak in (*a*) is in one of the shaded areas and is moving radially from the star. Each letter identifies the area to which the emission peak belongs.

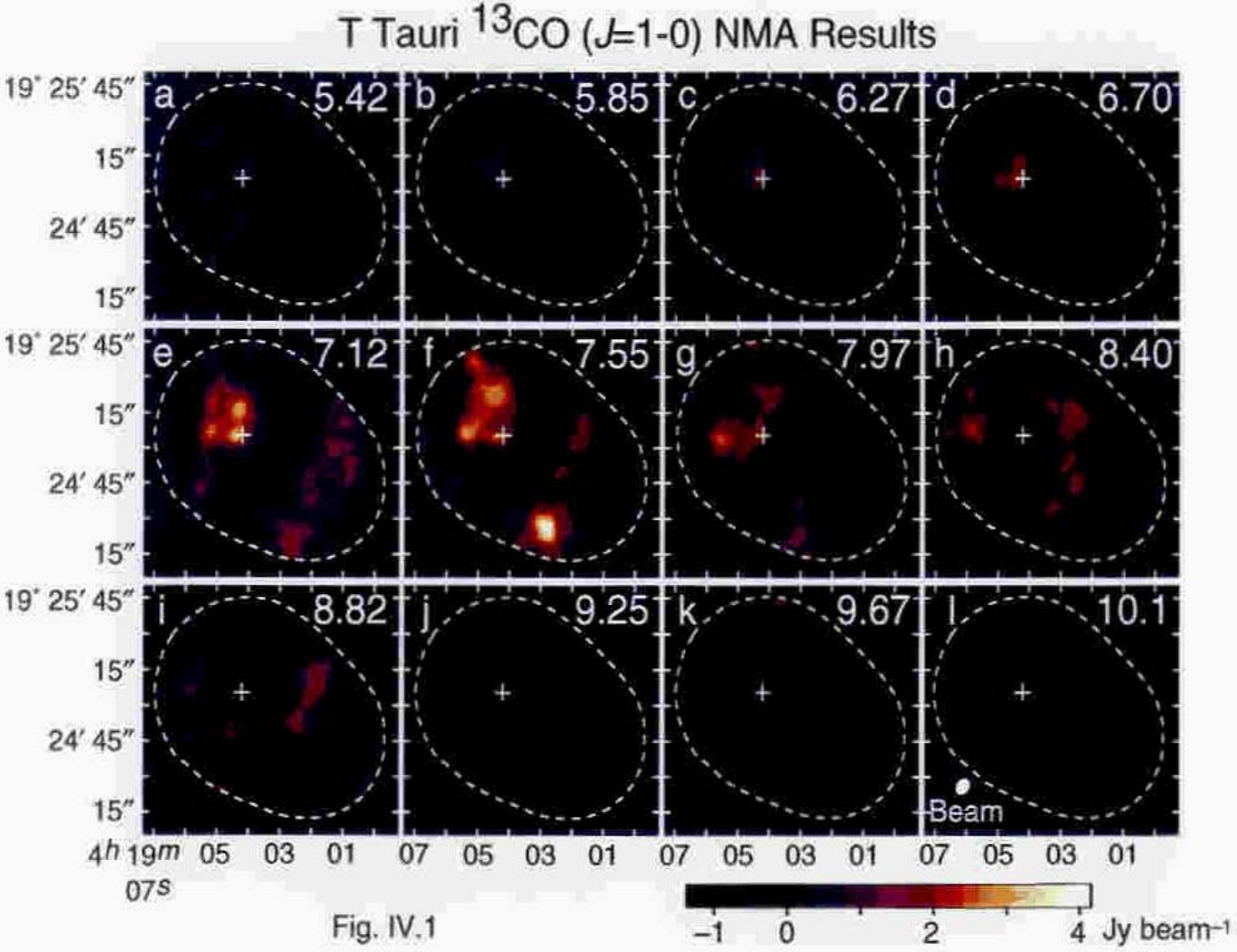
T Tauri ^{13}CO (J=1-0) NMA Results
a 5.42
b 5.85
c 6.27
d 6.70
e 7.12
f 7.55
g 7.97
h 8.40
i 8.82
j 9.25
k 9.67
l 10.1
Beam
19° 25′ 45″
15″
24′ 45″
15″
4^h 19^m 07^s
05 03 01 07 05 03 01 07 05 03 01 07 05 03 01
−1 0 2 4 Jy beam^{-1}

Fig. IV.1

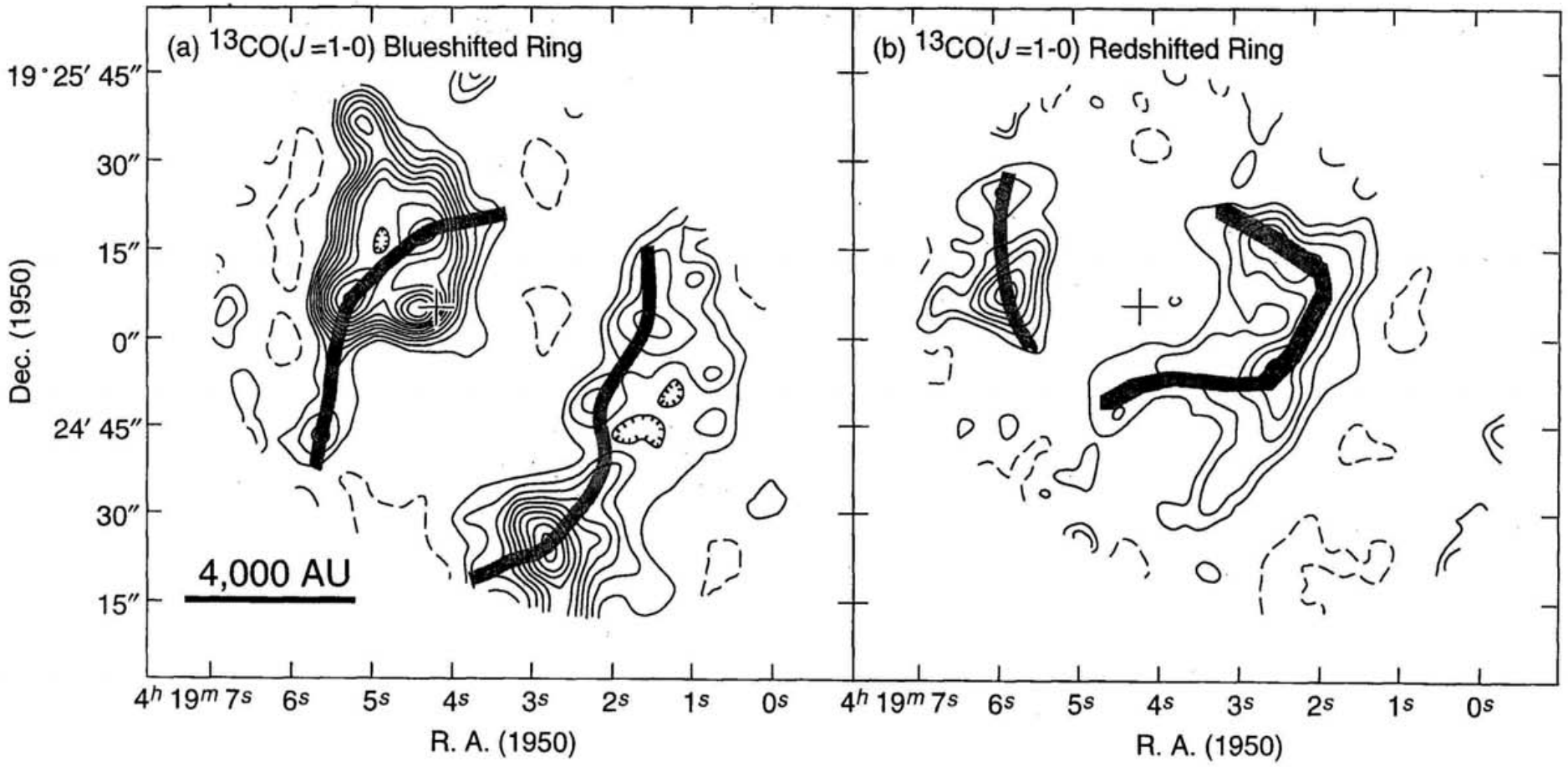
(a) ^{13}CO(J=1-0) Blueshifted Ring
(b) ^{13}CO(J=1-0) Redshifted Ring
19° 25′ 45″
30″
15″
0″
24′ 45″
30″
15″
Dec. (1950)
4,000 AU
4h 19m 7s
6s
5s
4s
3s
2s
1s
0s
R. A. (1950)

Figure IV.2

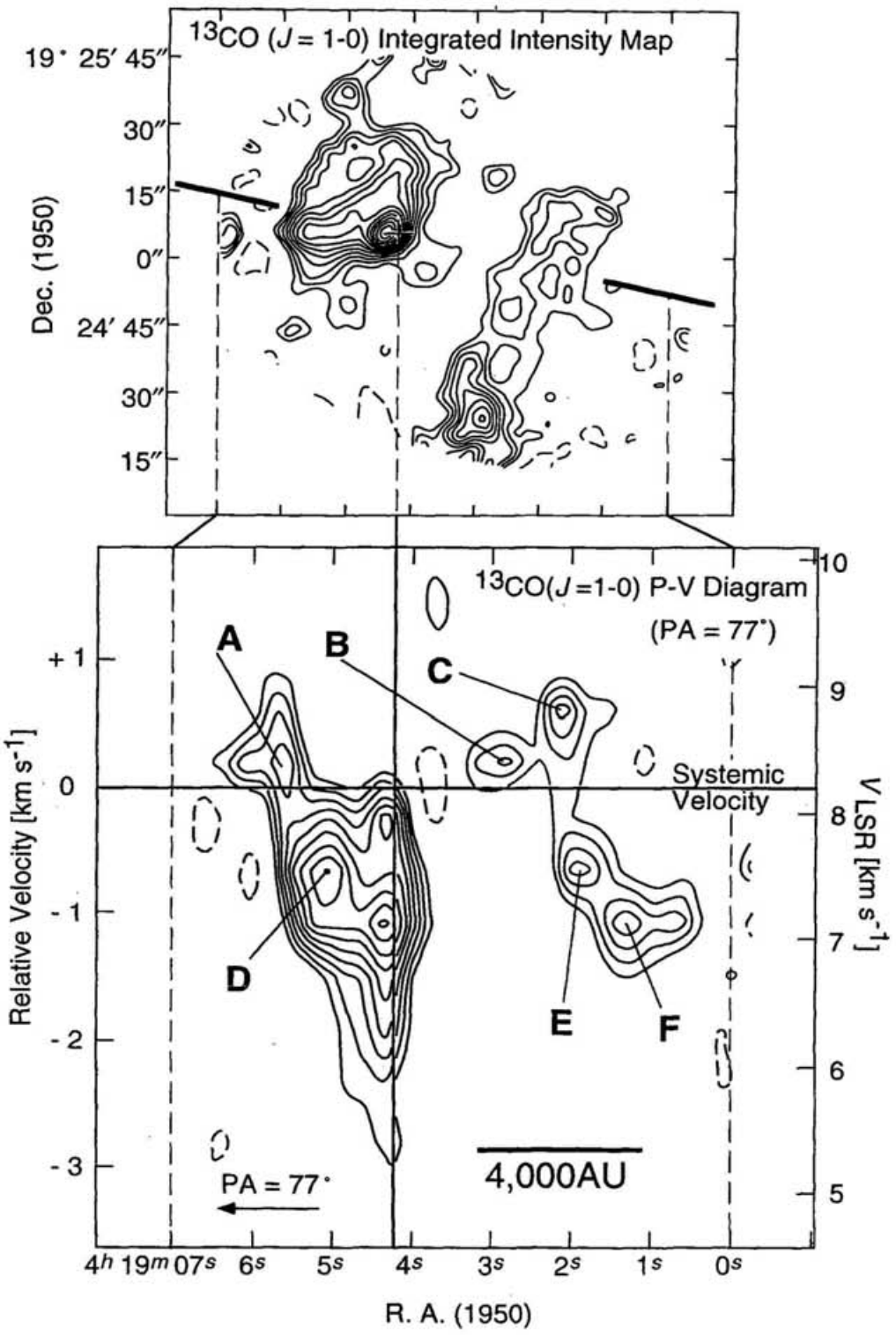
^{13}CO (J = 1-0) Integrated Intensity Map
19° 25′ 45″
30″
15″
0″
24′ 45″
30″
15″
Dec. (1950)
^{13}CO(J=1-0) P-V Diagram
(PA = 77°)
A
B
C
D
E
F
Systemic Velocity
+1
0
-1
-2
-3
Relative Velocity [km s^{-1}]
10
9
8
7
6
5
V_{LSR} [km s^{-1}]
PA = 77°
4,000AU
4^h 19^m 07^s
6^s
5^s
4^s
3^s
2^s
1^s
0^s
R. A. (1950)

Figure IV.3

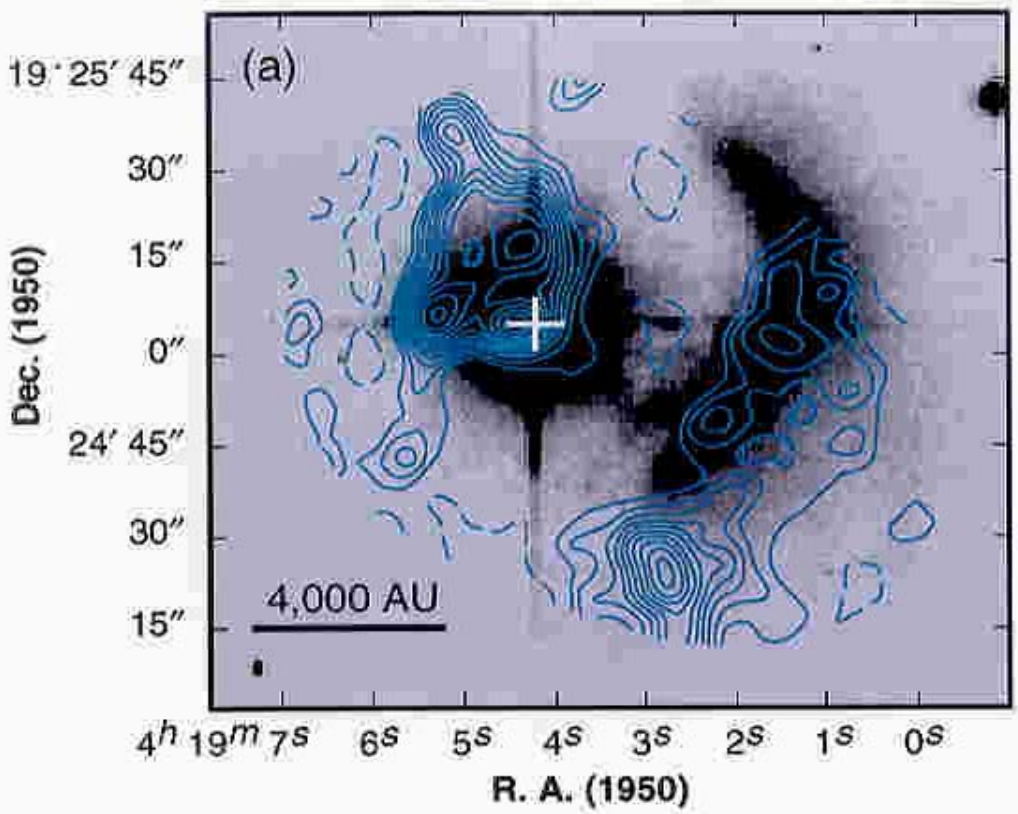
(a)
19° 25′ 45″
30″
15″
0″
24′ 45″
30″
15″
Dec. (1950)
4,000 AU
4h 19m 7s
6s
5s
4s
3s
2s
1s
0s
R. A. (1950)

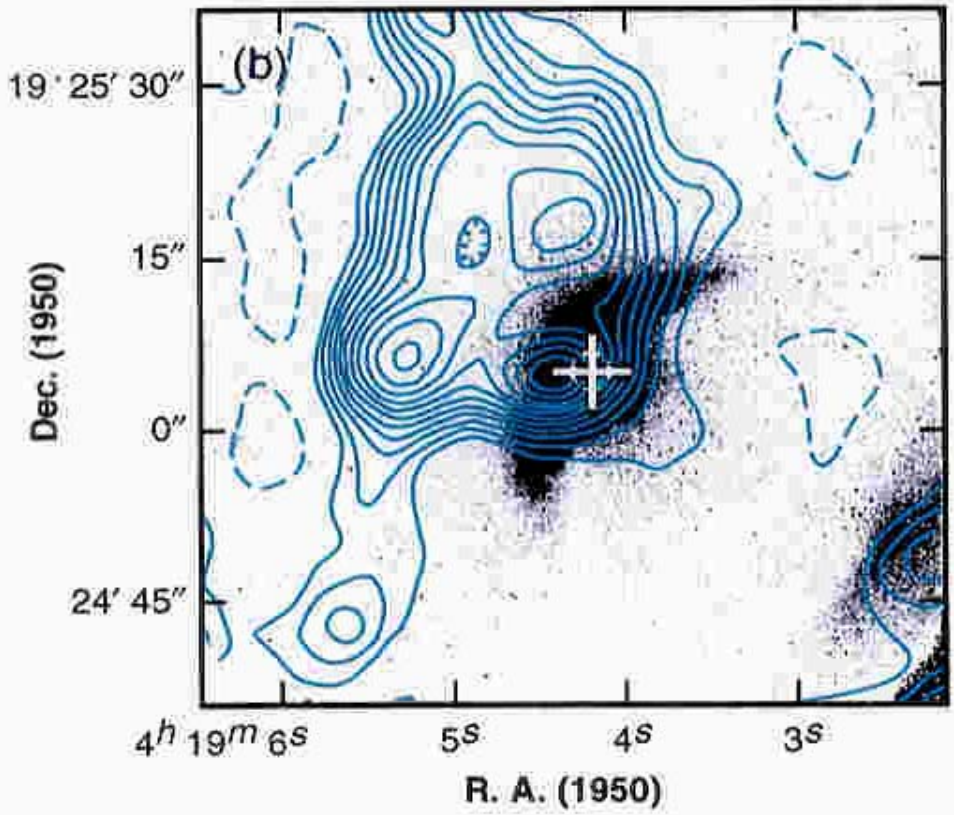
(b)
19° 25′ 30″
15″
0″
24′ 45″
Dec. (1950)
4h 19m 6s
5s
4s
3s
R. A. (1950)

Figure IV.4

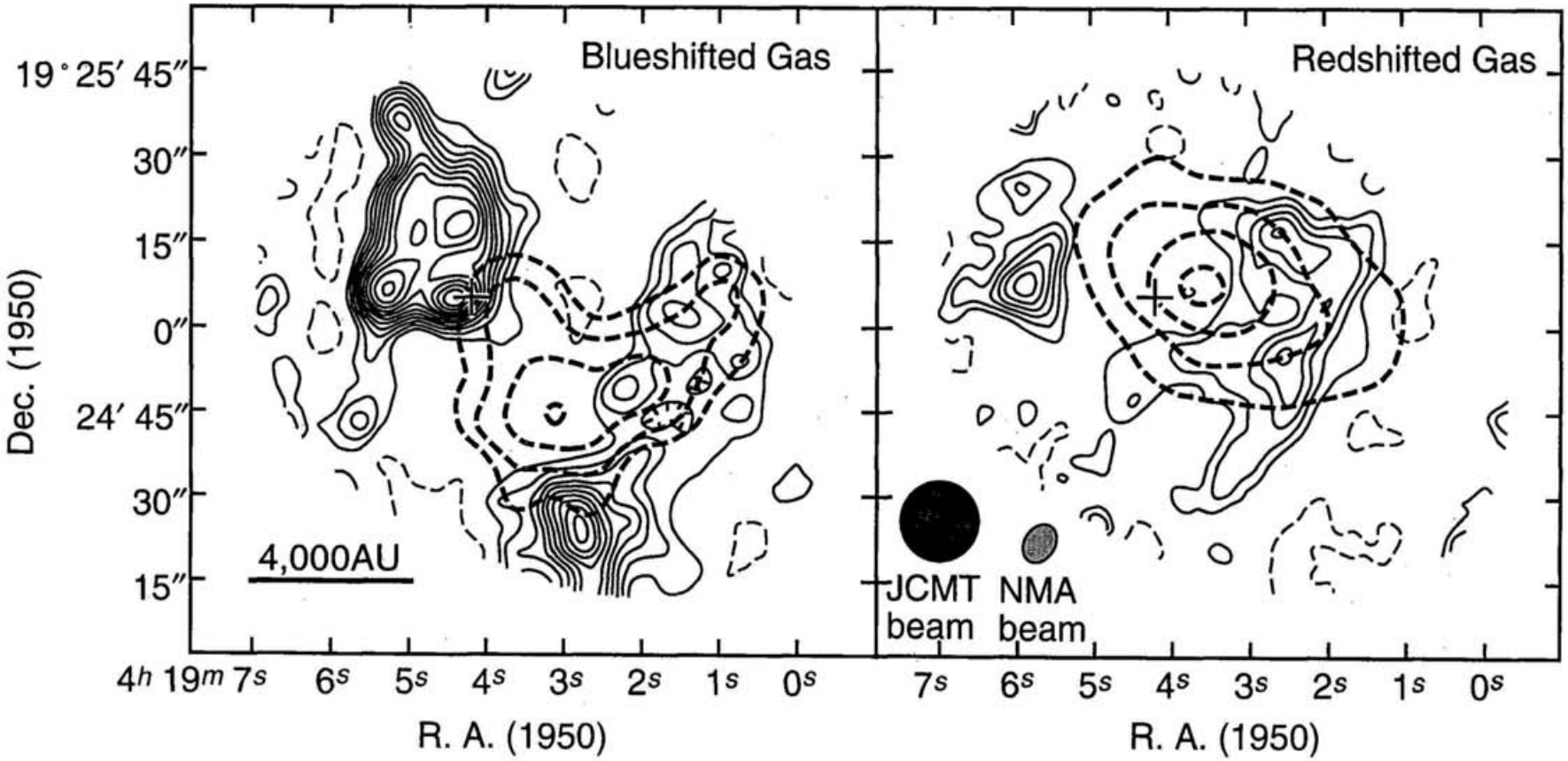
Blueshifted Gas
Redshifted Gas
19° 25′ 45″
30″
15″
0″
24′ 45″
30″
15″
Dec. (1950)
4,000AU
JCMT beam
NMA beam
4h 19m 7s
6s
5s
4s
3s
2s
1s
0s
R. A. (1950)
7s
6s
5s
4s
3s
2s
1s
0s
R. A. (1950)

Figure IV.5

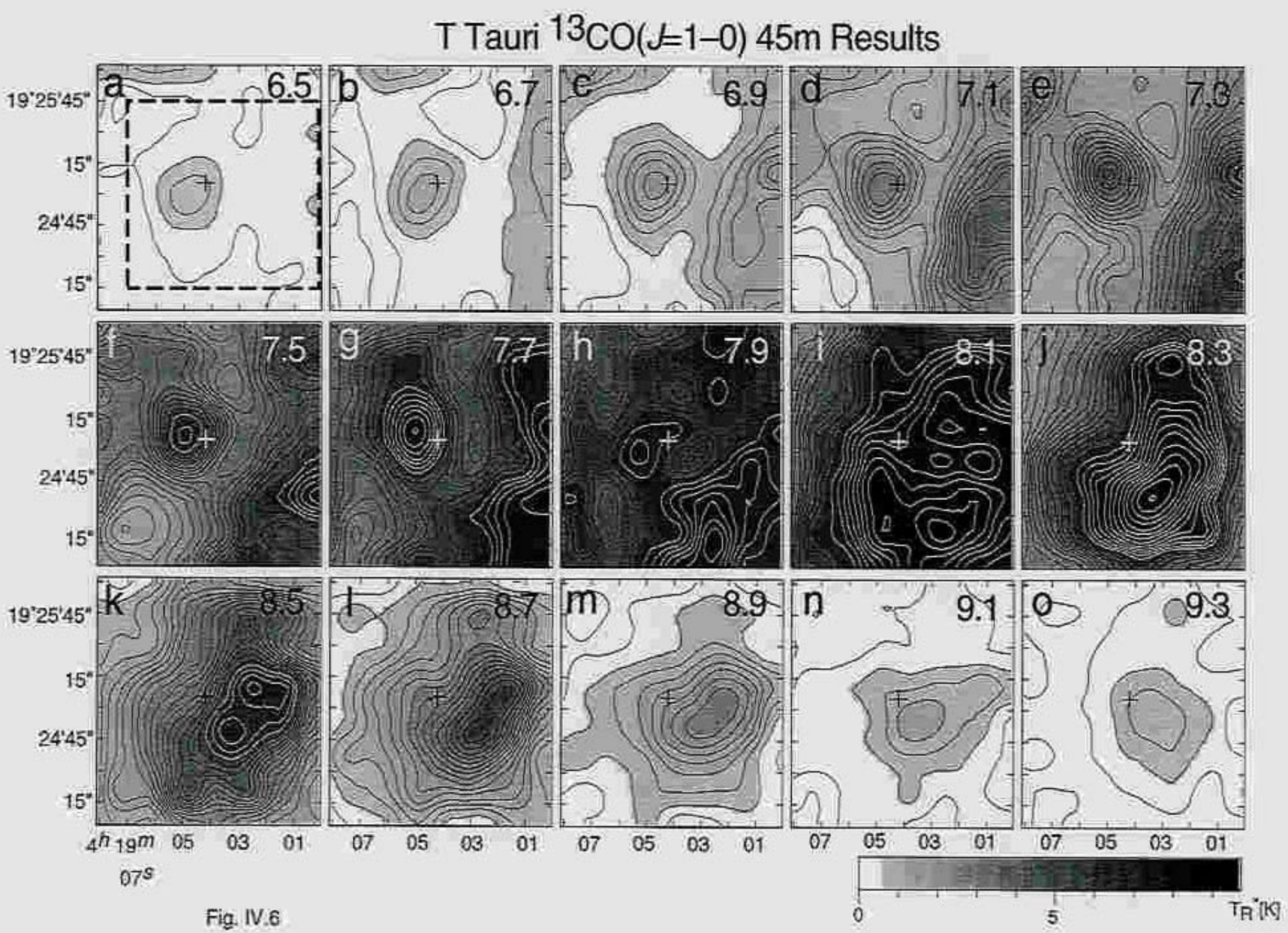
T Tauri ^{13}CO(J=1–0) 45m Results
a 6.5
b 6.7
c 6.9
d 7.1
e 7.3
f 7.5
g 7.7
h 7.9
i 8.1
j 8.3
k 8.5
l 8.7
m 8.9
n 9.1
o 9.3
19°25'45"
15"
24'45"
15"
$4^h19^m07^s$
05 03 01
07 05 03 01
0
5
T_R^* [K]

Fig. IV.6

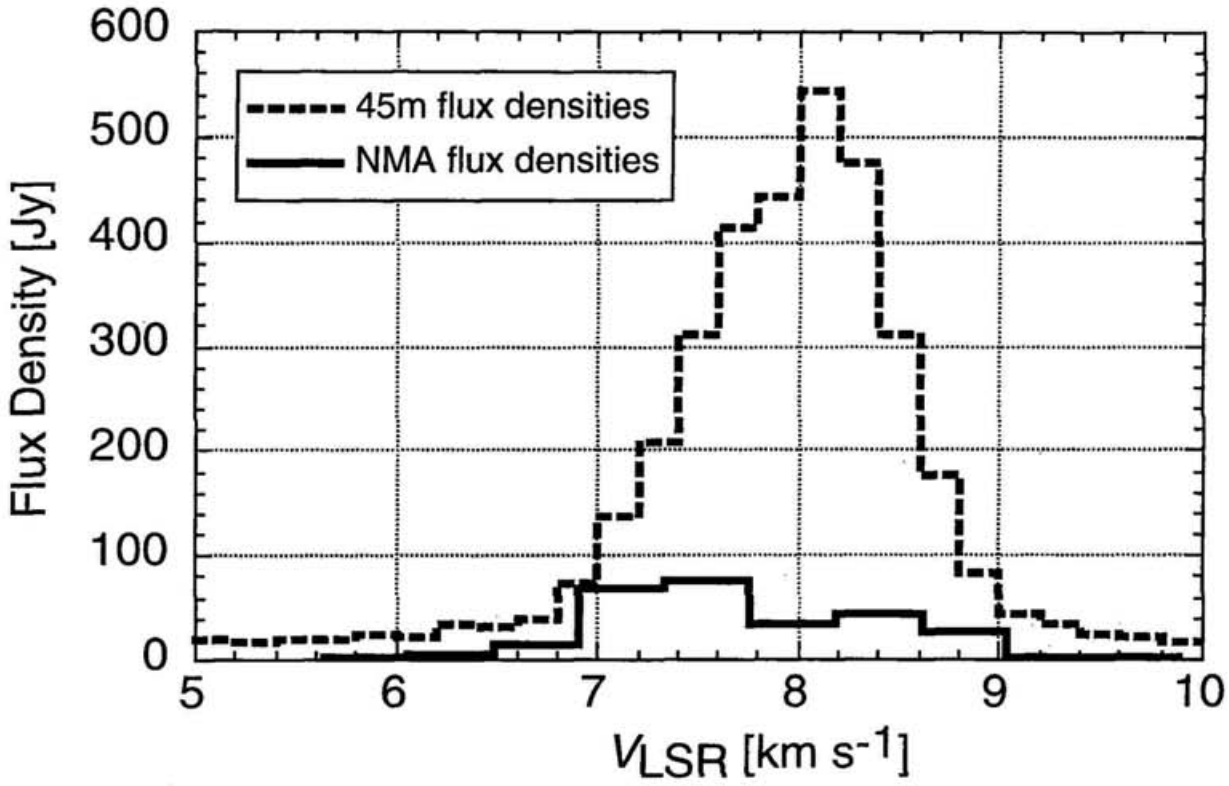
45m flux densities
NMA flux densities
Flux Density [Jy]
600
500
400
300
200
100
0
5
6
7
8
9
10
V_{LSR} [km s^{-1}]

Figure IV.7

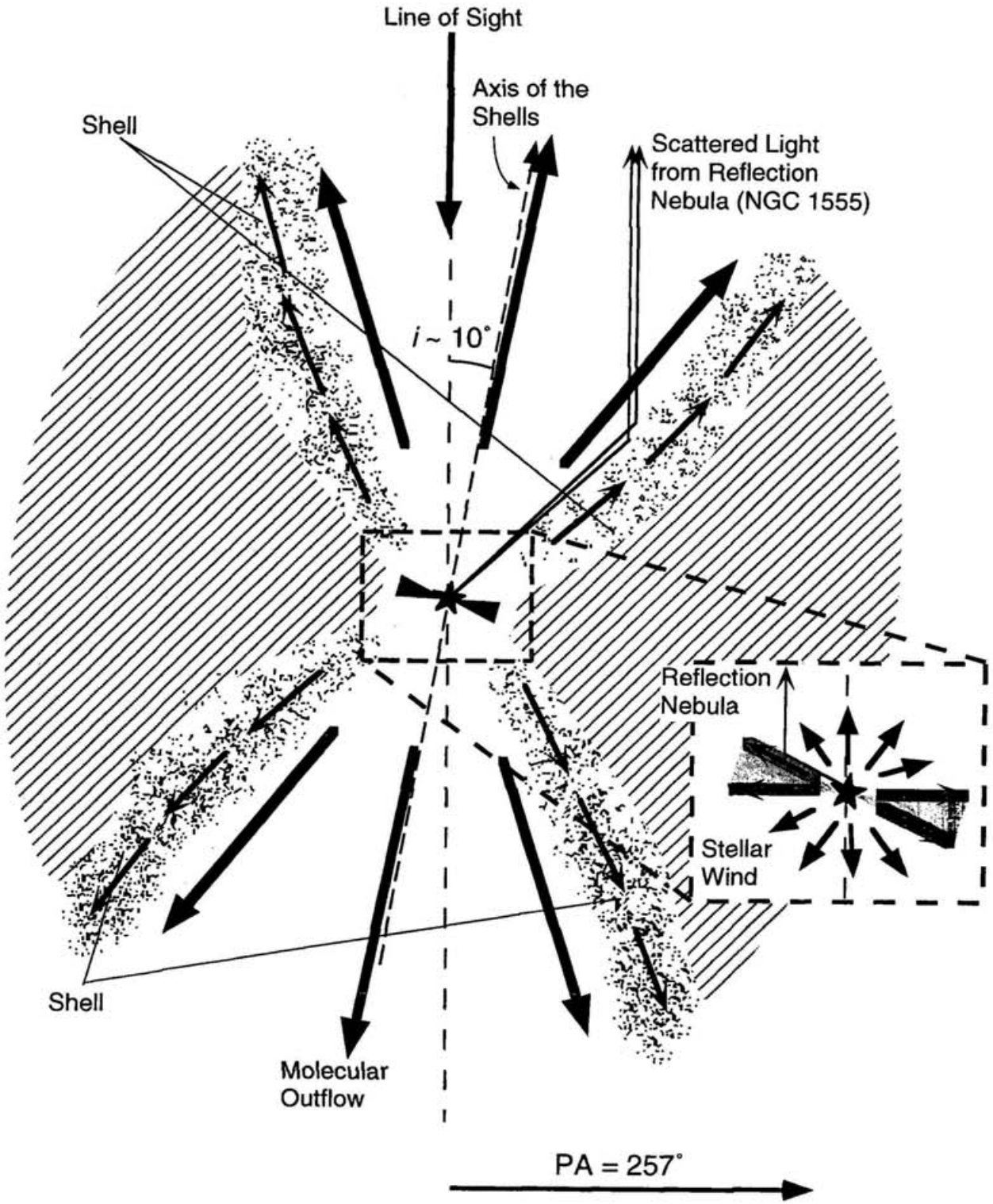
Line of Sight
Axis of the Shells
Shell
Scattered Light from Reflection Nebula (NGC 1555)
i ~ 10°
Reflection Nebula
Stellar Wind
Shell
Molecular Outflow
PA = 257°

Figure IV.8

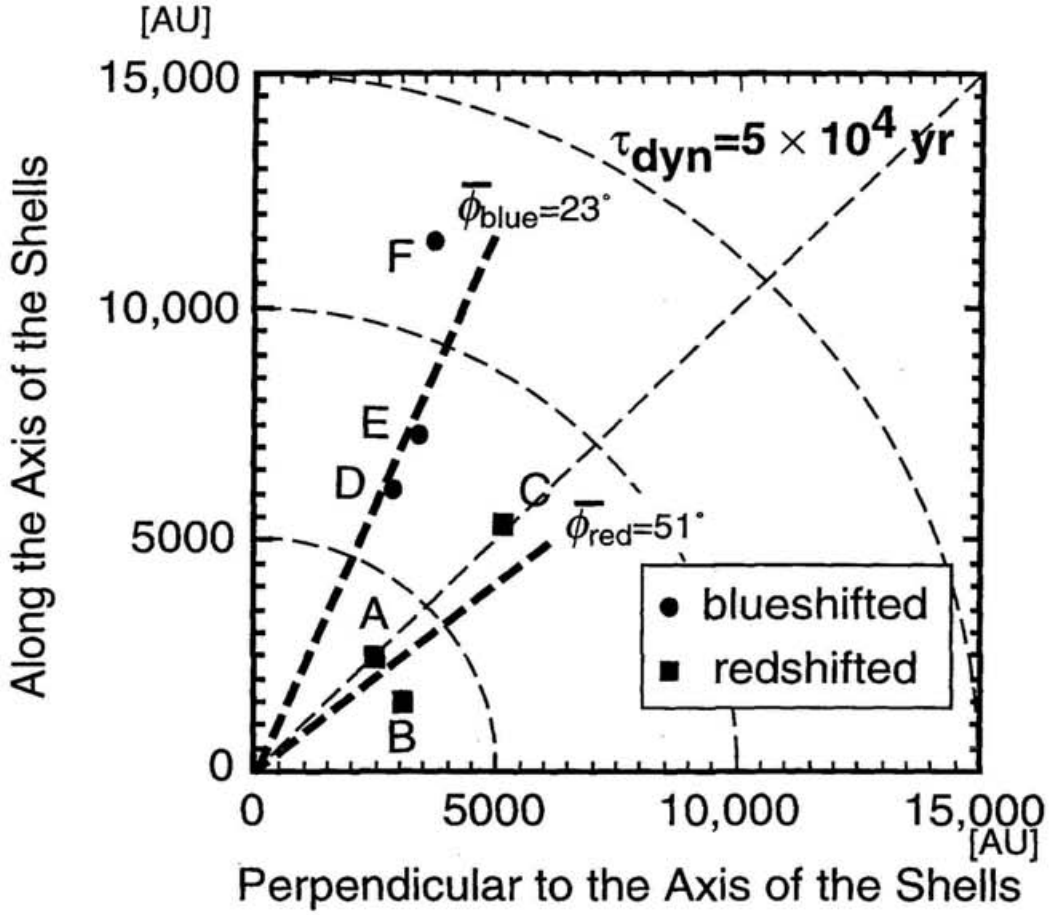
[AU]
15,000
10,000
5000
0
Along the Axis of the Shells
$\tau_{dyn}=5\times10^4$ yr
$\bar{\phi}_{blue}=23^\circ$
$\bar{\phi}_{red}=51^\circ$
F
E
D
C
A
B
blueshifted
redshifted
0
5000
10,000
15,000
[AU]
Perpendicular to the Axis of the Shells

Figure IV.9

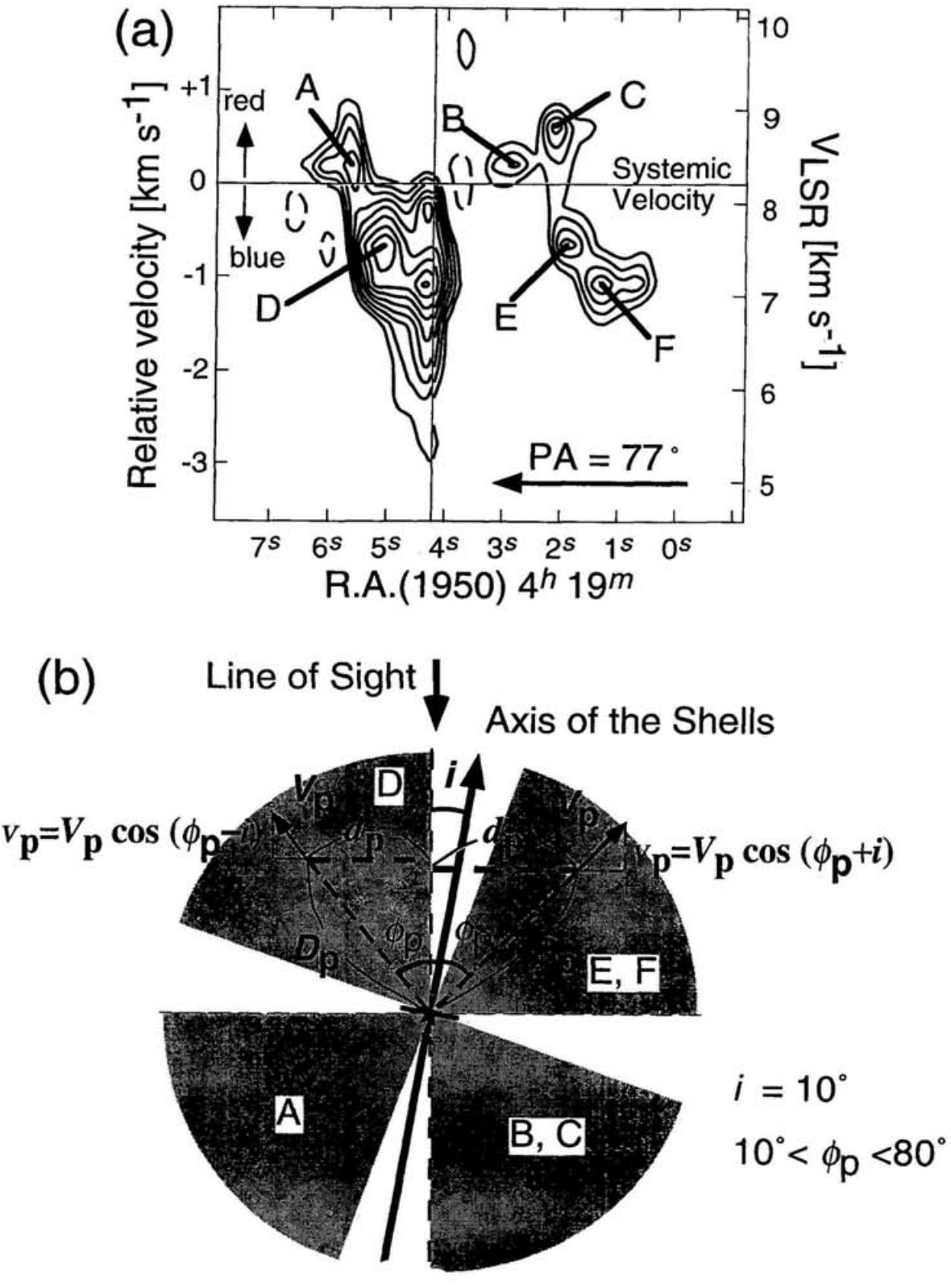
(a)
Relative velocity [km s-1]
+1
0
-1
-2
-3
red
blue
A
B
C
D
E
F
Systemic Velocity
PA = 77°
10
9
8
7
6
5
VLSR [km s-1]
7s 6s 5s 4s 3s 2s 1s 0s
R.A.(1950) 4h 19m
(b)
Line of Sight
Axis of the Shells
i
D
E, F
A
B, C
vp=Vp cos (φp−i)
vp=Vp cos (φp+i)
dp
Dp
φp
i = 10°
10°< φp <80°

Figure IV.10

Chapter V

Aperture Synthesis ^{13}CO ($J = 1 - 0$) Observations of Three T Tauri Stars with Flat Spectra at Infrared Wavelengths

ABSTRACT

We report the results of aperture synthesis ^{13}CO ($J = 1 - 0$) observations of three T Tauri stars with flat spectra at infared wavelengths (GV Tauri, Haro 6-13, DO Tauri) using the Nobeyama Millimeter Array (NMA). Spatially extended emissions around GV Tauri and Haro 6-13 are detected with the observations. The spatial extent of these emissions, much greater than 10^3 AU in size, is comparable to the typical size of the molecular cloud cores in the Taurus Molecular Cloud, suggesting that these two sources are still surrounded by the remanant parts of the parent cloud cores, and are in the transitional phase between the protostar stage and the T Tauri stage. However, the comparisons between the ^{13}CO ($J = 1 - 0$) profiles with the NMA and those of the $C^{18}O$ ($J = 1 - 0$) emissions with the Nobeyama 45 m telescope indicate that the present observations do not completely reveal the structures of the circumstellar gas, probably due to the absorption of the foreground gas.

Subject headings: circumstellar matter — ISM: molecules — stars: individual (GV Tauri, Haro 6-13, DO Tauri) — stars: pre-main-sequence

V.1. Introduction

T Tauri stars whose spectral energy distributions are flat in the entire range of the infrared wavelengths ($\lambda = 1 - 100\mu$m) are usually called "flat-spectrum T Tauri stars". Although the emitting mechanism for these flat spectra has still been in controversial (e.g., Adams, Lada, & Shu 1988; Calvet et al. 1994; Kitamura, Kawabe, & Saito 1996b), recent aperture synthesis ^{13}CO ($J = 1 - 0$) observations of flat-spectrum T Tauri stars have revealed that these sources seem to be commonly accompanied by circumstellar gas with the spatial extent greater than 10^3 AU (Hayashi, Ohashi, & Miyama 1993 for HL Tauri; Kitamura, Kawabe, & Saito 1996a for DG Tauri; Momose et al. 1996 [Chapter IV of this thesis] for T Tauri), which can be interpreted as the remnant parts of the parent cloud cores or the infalling envelopes. These observational results suggest that the flat-spectrum T Tauri stars are the sources that are in the transitional phase from the protostar stage, in which a central star is deeply embedded within an infalling envelope, to the T Tauri stage, in which a central star is surrounded by a compact circumstellar disk instead of a

spatially extended envelope. In order to confirm this point, we need further observations of circumstellar gas around other flat-spectrum T Tauri stars.

In this chapter, we report the results of aperture synthesis ^{13}CO ($J = 1 - 0$) observations of three flat-spectrum T Tauri stars in the Taurus Molecular Cloud by using the Nobeyama Millimeter Array (NMA). In § V.2, we describe how we select the sample of the present observations. We describe the details of the observations in § V.3, and present and discuss the observational results in § V.4.

V.2. Sample Selection

In order to select flat-spectrum T Tauri stars, we made a color-color diagram for 47 classical T Tauri stars (Hα emission-line strengths $W(\mathrm{H}\alpha) > 10$ Å) in the Taurus Molecular Cloud (Figure V.1). The photometric data of these T Tauri stars are taken from Strom et al. (1988) and Strom et al. (1989). The abscissa of Fig. V.1 is the value of $d(\log \lambda F_\lambda)/d(\log \lambda)$ between $\lambda = 1.65\mu$m and 12μm, which represents color in the region from near- to mid-infrared wavelengths, while the ordinate of Fig. V.1 is the value of $d(\log \lambda F_\lambda)/d(\log \lambda)$ between $\lambda = 25\mu$m and 60μm, which represents color in the region of far-infared wavelengths.

We define the sources with both color indexes greater than -0.5 as the flat-spectrum T Tauri stars. There are eight sources satisfying this criterion, and we select three of them (GV Tauri, Haro 6-13, DO Tauri) as the sample of the present obsersevations. Although GV Tauri (Haro 6-10) is a binary system (Leinert & Haas 1989), its angular separation is so small (1$''$.2 correponding to 170 AU) that the kinematical effect of the binary system on the outer regions of the remnant cloud core is probably negligible. Among the other five sources satisfying the above criterion, four of them have already been observed in the ^{13}CO ($J = 1 - 0$) line with the NMA (HL Tauri and XZ Tauri: Hayashi et al. 1993; DG Tauri: Kitamura et al. 1996a; T Tauri: Momose et al. 1996). The other one source, HP Tauri, is a wide-binary system (angular separation = 10$''$.0, corresponding to 1400 AU, Leinert et al. 1993), and is not appropriate for the sample of the present observations because the kinematical effect of the binary system on the remnant cloud core cannot be negligible. Therefore the ^{13}CO ($J = 1 - 0$) observations with the NMA have been completed for almost all the flat-spectrum T Tauri stars in Taurus with the present study.

V.3. Observations

The aperture synthesis ^{13}CO ($J = 1 - 0$) observations of the three flat-spectrum T Tauri stars were made during a period from 1994 November to 1995 March with the NMA, which is composed of six 10 m dishes. We used the tunerless SIS receivers (Sunada et al. 1993) whose system noise temperatures were typically 300 K (double sideband [DSB]) at the zenith. We employed the digital FFT spectral correlator FX, which gave a frequency resolution of 78 kHz, corresponding to the velocity resolution of 0.213 km s^{-1} at the frequency of the ^{13}CO ($J = 1 - 0$) line. Two array configurations, giving 30 baselines, were used for the observations. The minimum projected baseline length was 9 m so that our observations are insensitive to structures with size greater than 62″, corresponding to 8700 AU at the Taurus Molecular Cloud. The phase and gain of the array system were calibrated by every 30 minutes observations of 0528+134. During the period from 1994 November to 1995 March, we measured the flux density of 0528+134 at 110 GHz regularly (about $3 - 4$ times in a month) by observing Uranus or Mars. The complex pass band was obtained by the observations of 3C454.3 or 3C273.

We subtracted the continuum level from the visibility data, so it does not contaminate the ^{13}CO ($J = 1 - 0$) maps. We made ^{13}CO ($J = 1 - 0$) channel maps with the CLEAN algorithm in the NRAO AIPS package. In making the ^{13}CO ($J = 1 - 0$) maps, we applied the natural weighting to the visibility data. We show in Table V.1 the resultant synthesized beam size and the rms noise levels in the ^{13}CO ($J = 1 - 0$) channel maps as well as the positions of the field centers of the observations.

V.4. Results and Discussion

In the following, we present and discuss the observational results for each source separately. When we convert the observed integrated flux into the gas mass, we have assumed that the ^{13}CO emission is optically thin ($\tau_{^{13}\mathrm{CO}} \ll 1$), the excitation temperature of ^{13}CO at the $J = 1$ level is 20 K, and the fractional abundance of ^{13}CO relative to H_2 is 1×10^{-6} (see § IV.3.1.2 for the detail of the mass derivation). As discussed below, the assumption of the optically thin ^{13}CO ($J = 1 - 0$) emission may be bad, so the derived gas mass should be regarded as the lower limit for the mass of circumstellar gas.

V.4.1. GV Tauri

We show in Figure V.2 and Figure V.3 the integrated intensity map and the channel maps of the ^{13}CO $(J = 1 - 0)$ emissions around GV Tauri, respectively. The emissions above the 3σ level are detected in the velocity range of $V_{\rm LSR} = 6.67 - 7.95$ km s^{-1} (Fig. V.3*b* – 3*h*). Similar to the ^{13}CO $(J = 1 - 0)$ emissions around other flat-spectrum T Tauri stars (Hayashi et al. 1993; Kitamura et al. 1996a; Momose et al. 1996), the integrated ^{13}CO $(J = 1 - 0)$ emission around GV Tauri shows spatially extended distribution with size of $\sim 45''$, corresponding to ~ 6300 AU. The spatial extent of the detected ^{13}CO $(J = 1 - 0)$ emission is comparable to the typical size of the molecular cloud cores in the Taurus Molecular Cloud (e.g., Myers & Benson 1983; Mizuno et al. 1994), suggesting the existence of the remnant part of the parent cloud core around GV Tauri. The integrated flux of the detected ^{13}CO $(J = 1 - 0)$ emission is 14.6 Jy km s^{-1}, which corresponds to the gas mass of 2.0×10^{-2} $M_{\odot}$.

However, it is doubtful that the present ^{13}CO $(J = 1 - 0)$ observations *completely* reveal the structure of the circumstellar gas around GV Tauri. Figure V.4 shows comparisons between the ^{13}CO $(J = 1 - 0)$ profile with the present observations and the profiles of the ^{13}CO $(J = 1 - 0)$ and C^{18}O $(J = 1 - 0)$ lines with the Nobeyama 45 m telescope (HPBW $= 17''$ at 110 GHz) toward GV Tauri (Momose, unpublished data). The systemic velocity of GV Tauri is derived to be 6.47 km s^{-1} from the gaussian fitting of the C^{18}O $(J = 1 - 0)$ profile, which is expected to be optically thin and trace well the column density of the gas toward GV Tauri. As shown in Fig, V.4, we have detected the ^{13}CO $(J = 1 - 0)$ emissions with the NMA only in the velocity range redshifted from the systemic velocity. Such a situation can be explained if the optical thickness of the foreground gas for the ^{13}CO $(J = 1 - 0)$ line is so large at blueshifted velocities that it absorbs the emission from the circumstellar gas around GV Tauri. In order to completely reveal the structure of the circumstellar gas around GV Tauri, it is required to observe with a line whose optical thickness is much smaller than the ^{13}CO $(J = 1 - 0)$ line (see Chapter VI).

V.4.2. Haro 6-13

We show in Figure V.5 and Figure V.6 the integrated intensity map and the channel maps of the ^{13}CO $(J = 1 - 0)$ emissions around Haro 6-13, respectively. The emissions above the 3σ level are detected in the velocity ranges of $V_{\rm LSR} = 4.49 - 5.34$ km s^{-1} (Fig.

V.6b – 6f) and $V_{\rm LSR} = 6.84 - 7.05$ km s^{-1} (Fig. V.6b – 6f). Most of the ^{13}CO ($J = 1 - 0$) emissions in the first velocity range (Fig. V.6b – 6f) has their peaks $10'' - 20''$ south to the stellar position, and show structure elongated in the north-south direction. On the other hand, the prominent emission feature in the second velocity range (see Fig. V.6n) also shows structure elongated in the north-south direction, but its peak is located at $\sim 25''$ north to the central star. As a result, the integrated intensity map (Fig. V.5) shows structure elongated along the north-south direction across the central star, although the northern part of the emission is weaker than the southern part. The integrated flux of the detected ^{13}CO ($J = 1 - 0$) emission is 6.40 Jy km s^{-1}, which corresponds to the gas mass of 9.0×10^{-3} $M_{\odot}$.

Although the existence of the circumstellar gas with size greater than 1000 AU has been suggested, the present ^{13}CO ($J = 1 - 0$) observations do not completely reveal the structure of the circumstellar gas around Haro 6-13, as the case of GV Tauri. Figure V.7 shows the comparisons between the ^{13}CO ($J = 1 - 0$) profile with the present observations and the profiles of the ^{13}CO ($J = 1 - 0$) and C^{18}O ($J = 1 - 0$) lines with the Nobeyama 45 m telescope toward Haro 6-13 (Momose, unpublished data). As clearly seen in Fig. V.7, our observations with the NMA does not detect any ^{13}CO ($J = 1 - 0$) emission near the systemic velocity expected from the C^{18}O ($J = 1 - 0$) profile with the 45 m telescope ($V_{\rm LSR} \approx 6$ km s^{-1}). This is probably because the optical thickness of the foreground gas for the ^{13}CO ($J = 1 - 0$) line is so large near the systemic velocity that it absorbs the emission from the circumstellar gas around Haro 6-13. In order to interprete the present observational results unambiguously, we need to know the gaseous structure near the systemic velocity with further observations.

V.4.3. DO Tauri

With the present observations, we did not detect any significant emission around DO Tauri. Since the noise level in the channel maps of DO Tauri is similar to those in the channel maps of the other two sources (see row (6) in Table V.1), our observational results suggest that the amount of circumstellar gas around DO Tauri is much smaller than those around GV Tauri and Haro 6-13. Koerner & Sargent (1995) made aperture synthesis observations of DO Tauri with the CO ($J = 2 - 1$) line, and found a circumstellar gas disk 350 AU in radius and $1.5 \times 10^{-4} M_{\odot}$ in mass around DO Tauri. The present observations cannot detect such a compact gaseous component with mass smaller than $1 \times 10^{-3} M_{\odot}$.

Around DO Tauri, the spatially extended component of the parent cloud core may have already been dispersed perfectly.

V.5. Summary

We made aperture synthesis ^{13}CO ($J = 1 - 0$) observations of the three flat-spectrum T Tauri stars (GV Tauri, Haro 6-13, DO Tauri) in the Taurus Molecular Cloud using the Nobeyama Millimeter Array, and found spatially extended ^{13}CO ($J = 1 - 0$) emissions around GV Tauri and Haro 6-13. The spatial extent of these emissions, much greater than 10^3 AU in size, is comparable to the typical size of the molecular cloud cores in the Taurus Molecular Cloud, suggesting that these two sources are still surrounded by the remanant parts of the parent cloud cores, and are in the transitional phase between the protostar stage and the T Tauri stage. However, the comparisons between the ^{13}CO ($J = 1 - 0$) profiles with the NMA and the $C^{18}O$ ($J = 1 - 0$) profiles with the Nobeyama 45 m telescope indicate that the present observations do not completely reveal the structures of the circumstellar gas, probably due to the absorption of the foreground gas. In order to completely reveal the structures of the circumstellar gas around these sources, it is required to observe with a line whose optical thickness is much smaller than the ^{13}CO ($J = 1 - 0$) line, e.g., the $C^{18}O$ ($J = 1 - 0$) line (see Chapter VI).

Table V.1. Observational Parameters

			GV Tauri	Haro 6-13	DO Tauri
(1)	Field Center[a]	R.A.(B1950)	$04^h26^m21^s.89$	$04^h29^m13^s.6$	$04^h35^m24^s.18$
(2)		decl.(B1950)	24°26′30″.0	24°22′41″	26°04′55″.2
(3)	Synthesized Beam	(Size)	8″.4 × 5″.2	10″.0 × 5″.9	9″.7 × 5″.7
(4)		(P.A.)	168°	164°	161°
(5)	rms noise level[b]	(Jy beam^{-1})	168.1	159.1	190.2
(6)		(K)	0.38	0.27	0.34

[a]Identical with the stellar position listed in Herbig & Bell (1988).

[b]The noise level in a ^{13}CO ($J = 1 - 0$) channel map.

— Figure Captions —

Fig. V.1.— Color-color diagram for 47 classical T Tauri stars in the Taurus Molecular Cloud. The abscissa is the value of $d(\log \lambda F_\lambda)/d(\log \lambda)$ between $\lambda = 1.65\mu$m and 12μm while the ordinate is the value of $d(\log \lambda F_\lambda)/d(\log \lambda)$ between $\lambda = 25\mu$m and 60μm. The photometric data are taken from Strom et al. (1988) and Strom et al. (1989). We define eight sources with both color indexes greater than -0.5 as the flat-spectrum T Tauri stars. An arrow indicates a lower limit. An open circle denotes a source which cannot be obtained any lower limit for the 60μm flux, because of the contamination from a nearby bright source.

Fig. V.2.— The ^{13}CO ($J = 1 - 0$) integrated intensity map of GV Tauri. The contour spacing is 2σ, starting at $\pm 2\sigma$ ($1\sigma = 63.5$ mJy beam^{-1}). The cross indicates the stellar position. Negative contours are drawn by dashed lines.

Fig. V.3.— Velocity channel maps of the ^{13}CO ($J = 1 - 0$) line around GV Tauri. The corresponding LSR velocity in km s^{-1} is shown at the upper right corner of each panel. The cross indicates the stellar position. The contour spacing is 2σ, starting at $\pm 2\sigma$ ($1\sigma = 168.1$ mJy beam^{-1}).

Fig. V.4.— Compariosons of the ^{13}CO ($J = 1 - 0$) line profile obtained by the NMA observations with the profiles of the ^{13}CO ($J = 1 - 0$) and C^{18}O ($J = 1 - 0$) lines toward GV Tauri obtained with the Nobeyama 45 m telescope (Momose, unpublished).

Fig. V.5.— The ^{13}CO ($J = 1 - 0$) integrated intensity map of Haro 6-13. The contour spacing is 2σ, starting at $\pm 2\sigma$ ($1\sigma = 60.1$ mJy beam^{-1}). The cross indicates the stellar position. Negative contours are drawn by dashed lines.

Fig. V.6.— Velocity channel maps of the ^{13}CO ($J = 1 - 0$) line around Haro 6-13. The corresponding LSR velocity in km s^{-1} is shown at the upper right corner of each panel. The cross indicates the stellar position. The contour spacing is 2σ, starting at $\pm 2\sigma$ ($1\sigma = 159.1$ mJy beam^{-1}).

Fig. V.7.— Compariosons of the ^{13}CO ($J = 1 - 0$) line profile obtained by the NMA observations with the profiles of the ^{13}CO ($J = 1 - 0$) and C^{18}O ($J = 1 - 0$) lines toward Haro 6-13 obtained with the Nobeyama 45 m telescope (Momose, unpublished).

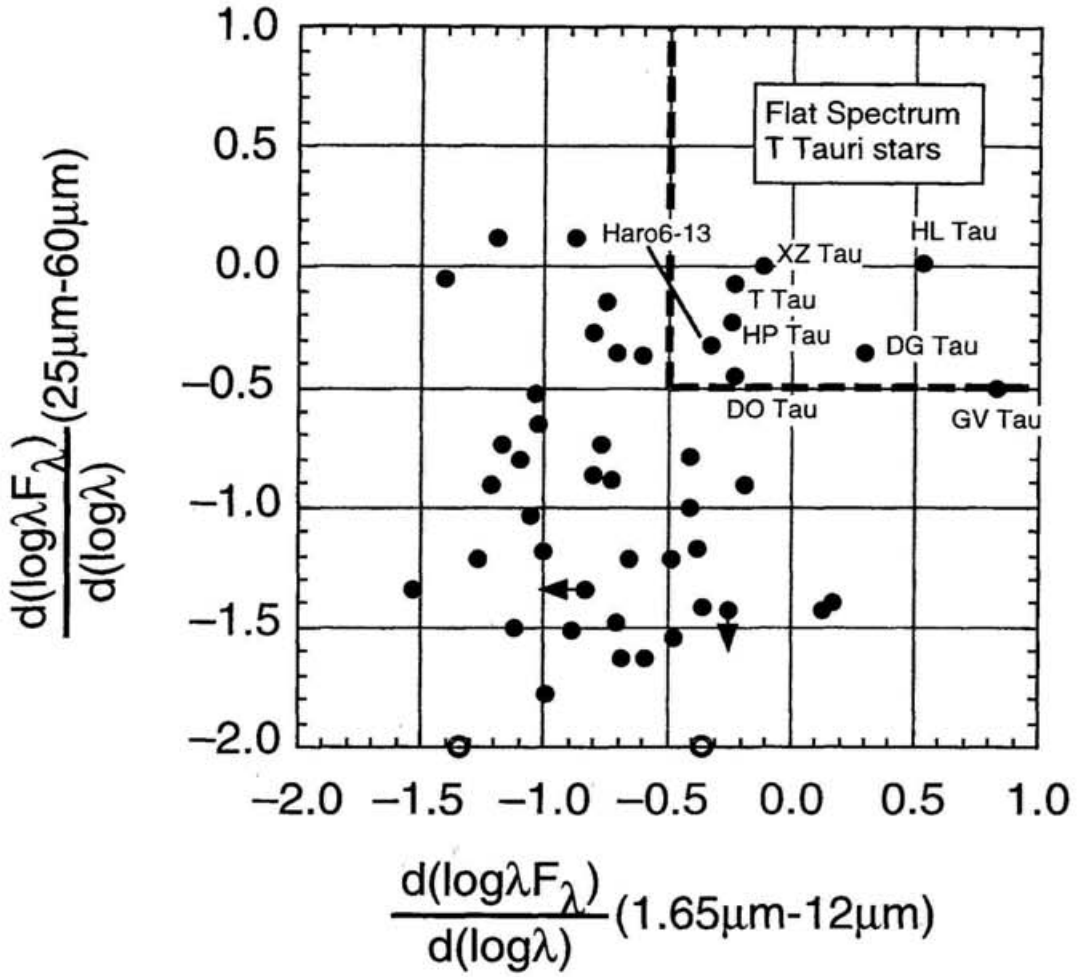
Flat Spectrum
T Tauri stars
Haro6-13
XZ Tau
HL Tau
T Tau
HP Tau
DG Tau
DO Tau
GV Tau
1.0
0.5
0.0
−0.5
−1.0
−1.5
−2.0
−2.0 −1.5 −1.0 −0.5 0.0 0.5 1.0
d(logλF_λ)/d(logλ) (25μm-60μm)
d(logλF_λ)/d(logλ) (1.65μm-12μm)

Fig. V.1

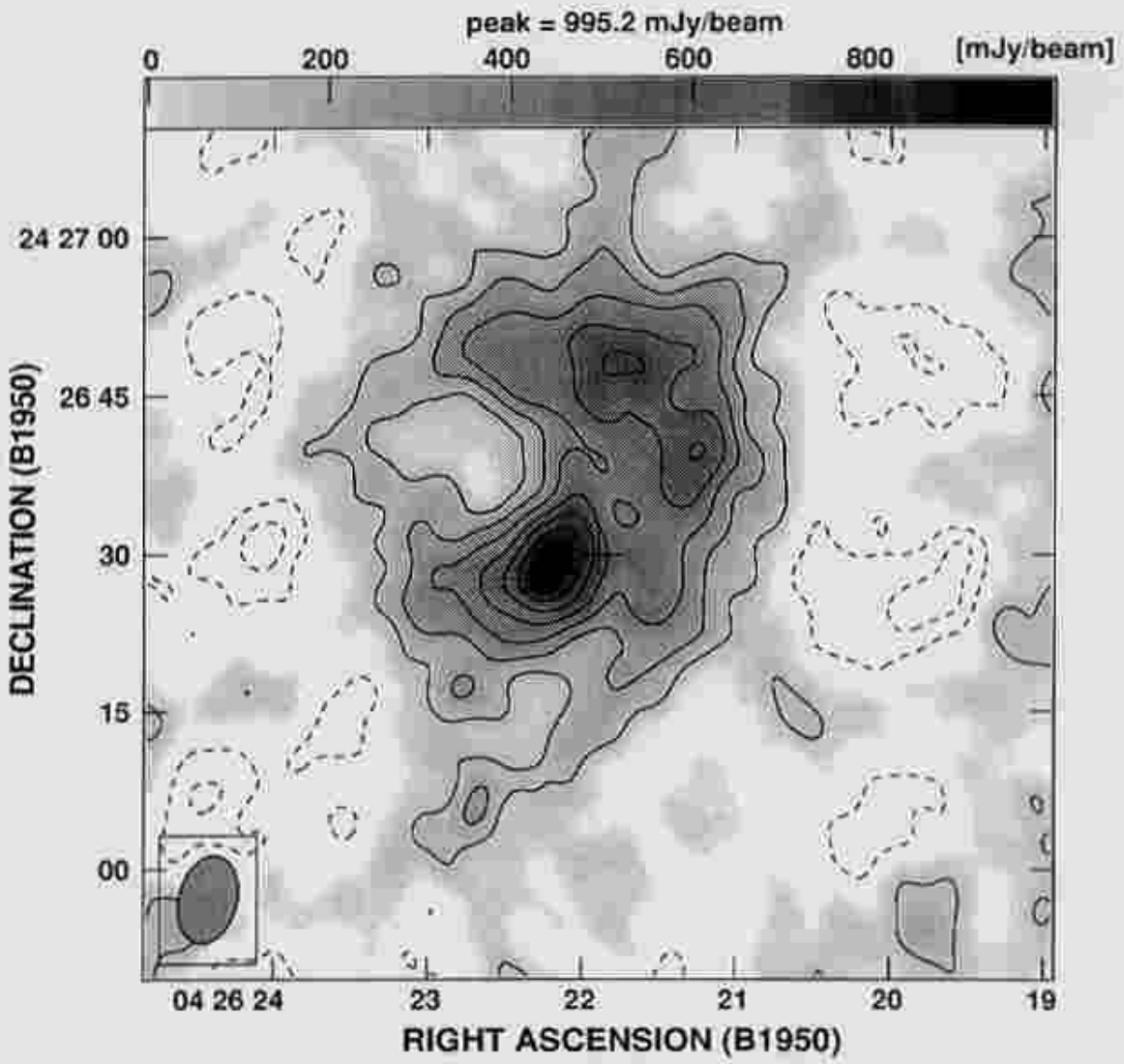
peak = 995.2 mJy/beam
0
200
400
600
800
[mJy/beam]
24 27 00
26 45
30
15
00
DECLINATION (B1950)
04 26 24
23
22
21
20
19
RIGHT ASCENSION (B1950)

Fig. V.2

Fig. V.3

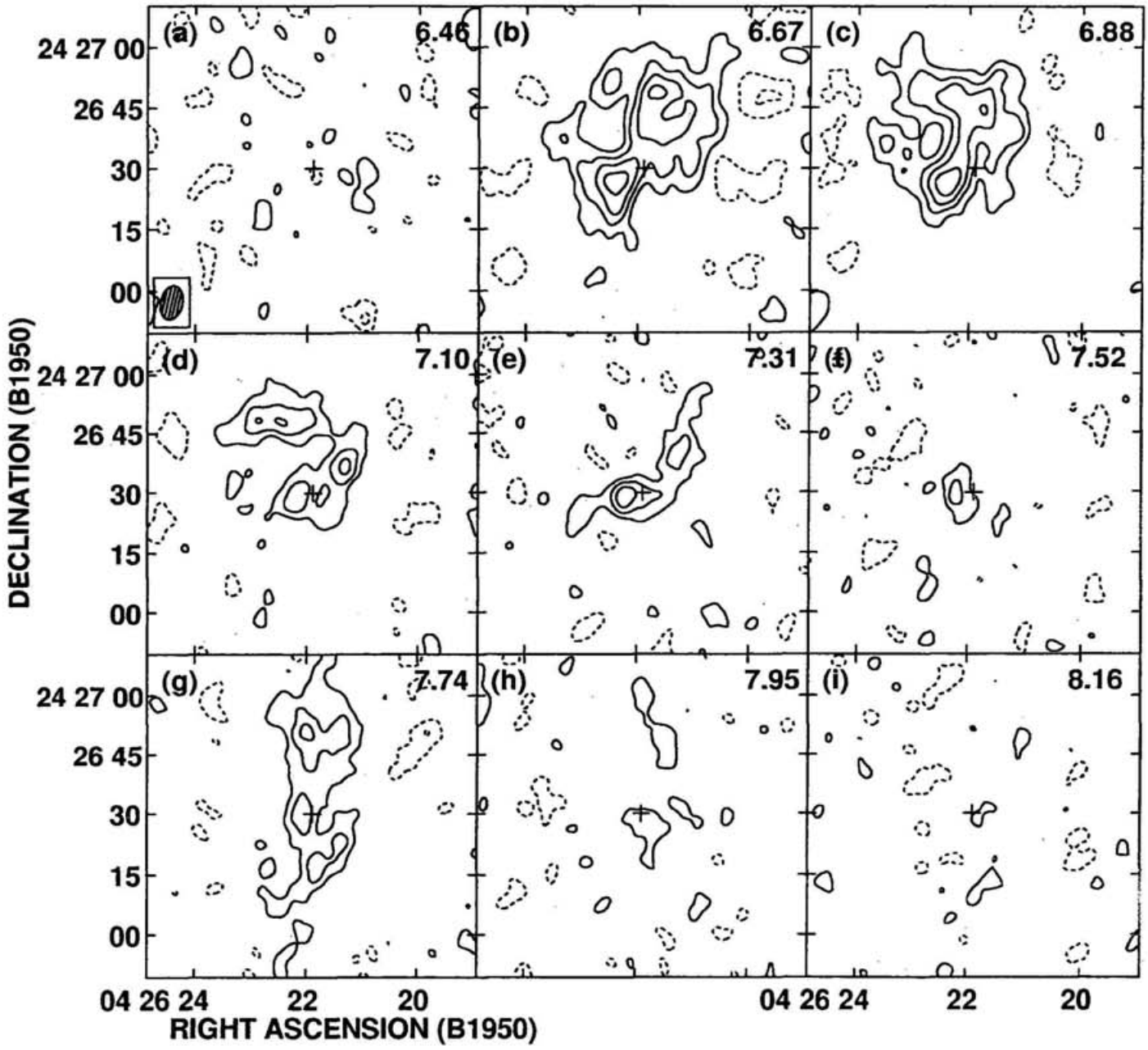
(a) 6.46
(b) 6.67
(c) 6.88
(d) 7.10
(e) 7.31
(f) 7.52
(g) 7.74
(h) 7.95
(i) 8.16
24 27 00
26 45
30
15
00
DECLINATION (B1950)
04 26 24
22
20
RIGHT ASCENSION (B1950)

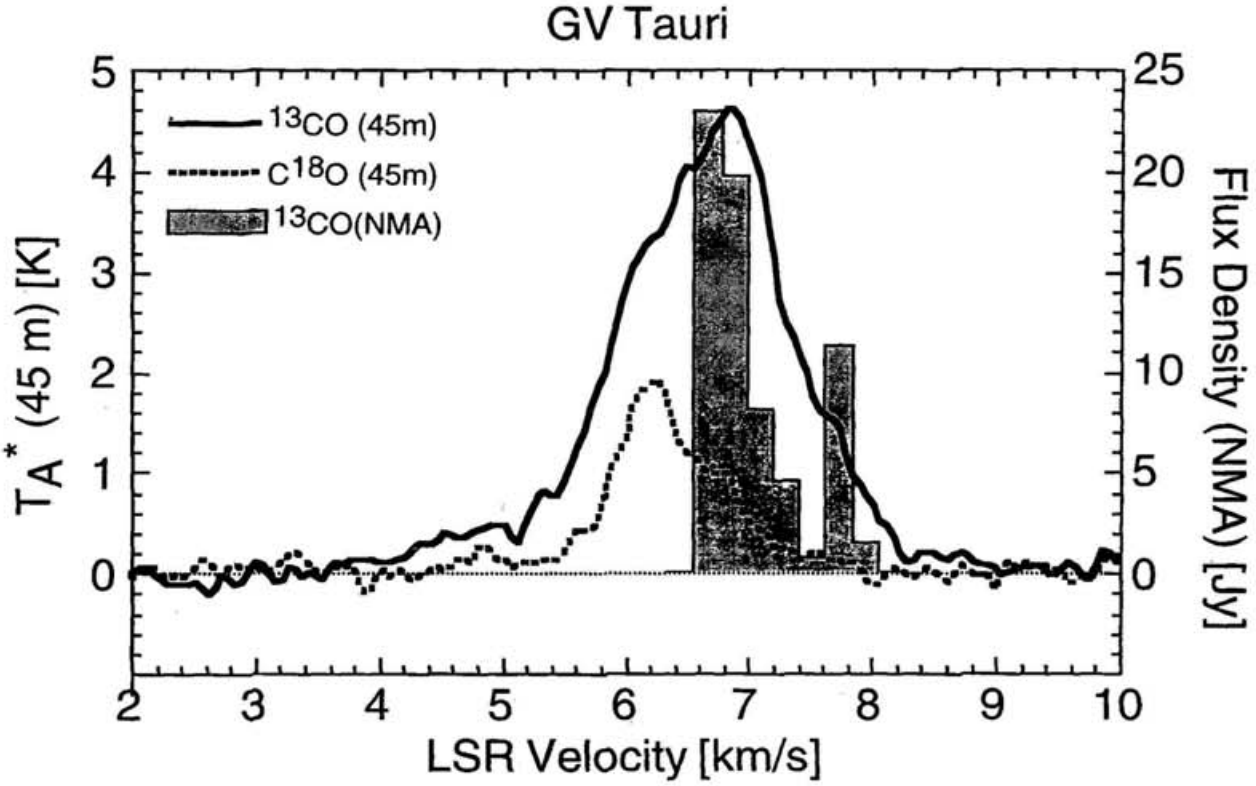
GV Tauri
^{13}CO (45m)
C^{18}O (45m)
^{13}CO(NMA)
T_A^* (45 m) [K]
Flux Density (NMA) [Jy]
LSR Velocity [km/s]
0
1
2
3
4
5
0
5
10
15
20
25
2
3
4
5
6
7
8
9
10

Fig. V.4

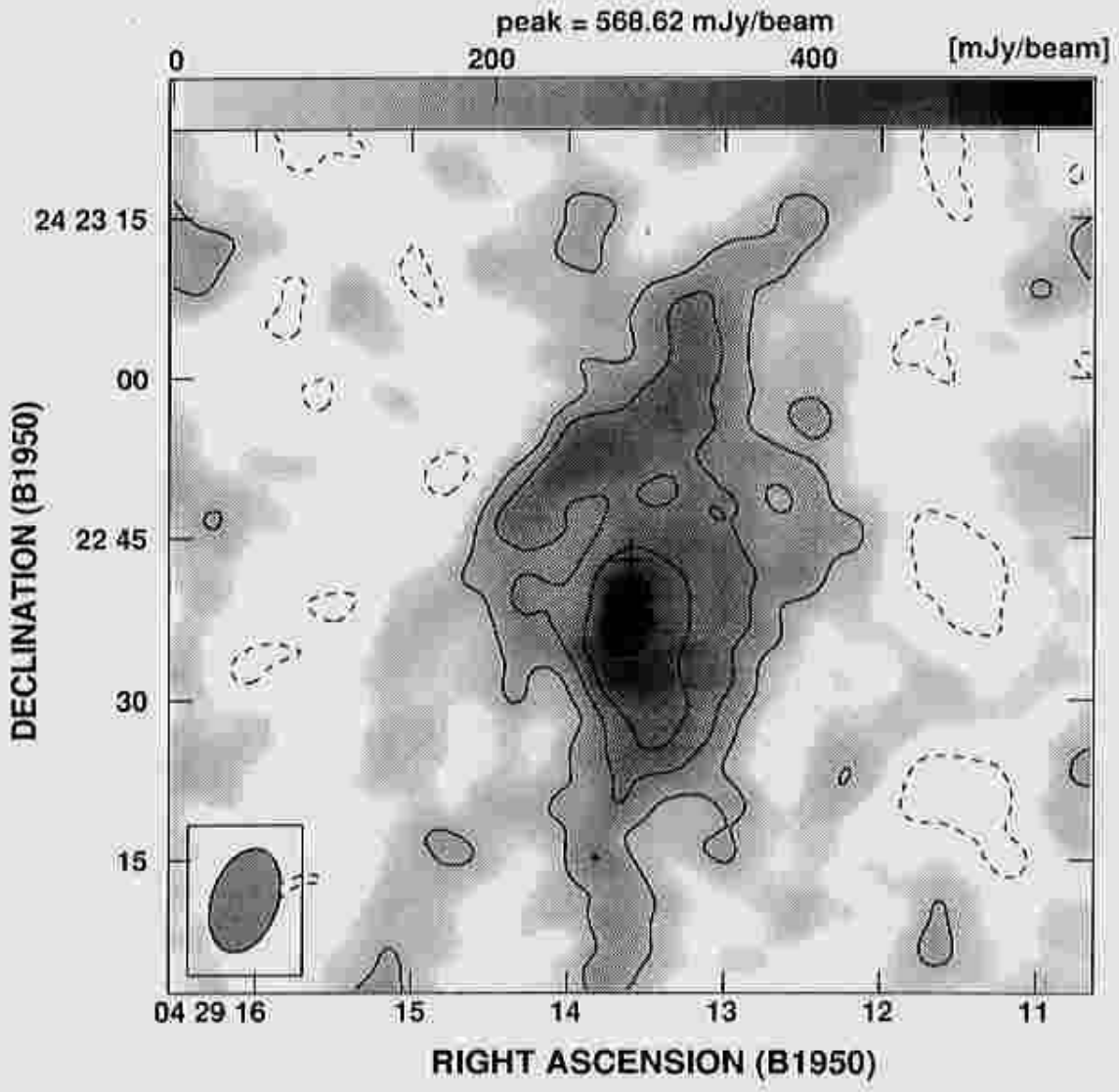
peak = 568.62 mJy/beam
0
200
400
[mJy/beam]
24 23 15
00
22 45
30
15
DECLINATION (B1950)
04 29 16
15
14
13
12
11
RIGHT ASCENSION (B1950)

Fig. V.5

Fig. V.6

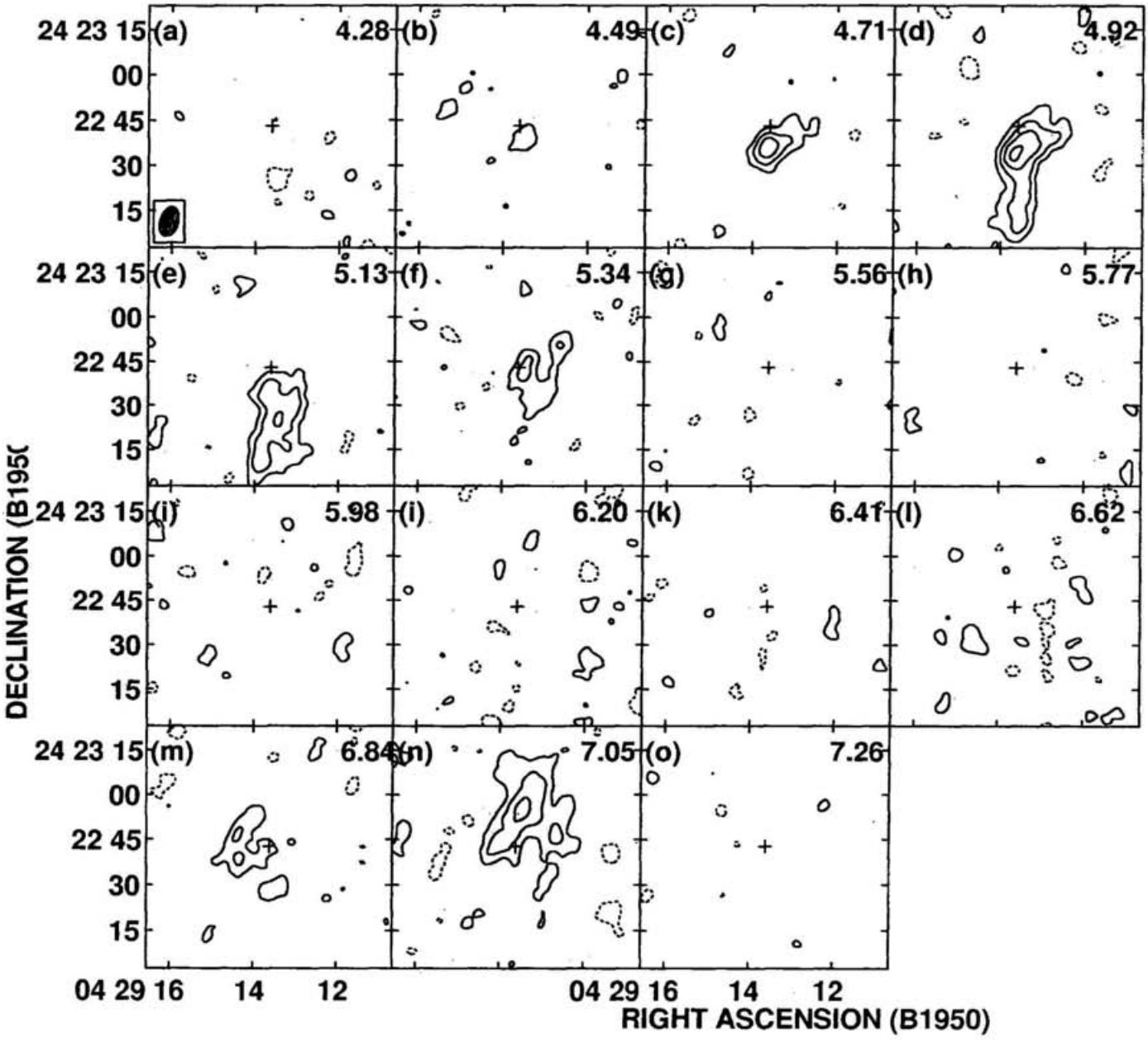
(a) 4.28
(b) 4.49
(c) 4.71
(d) 4.92
(e) 5.13
(f) 5.34
(g) 5.56
(h) 5.77
(i) 5.98
(j) 6.20
(k) 6.41
(l) 6.62
(m) 6.84
(n) 7.05
(o) 7.26
24 23 15
00
22 45
30
15
04 29 16
14
12
DECLINATION (B195(
RIGHT ASCENSION (B1950)

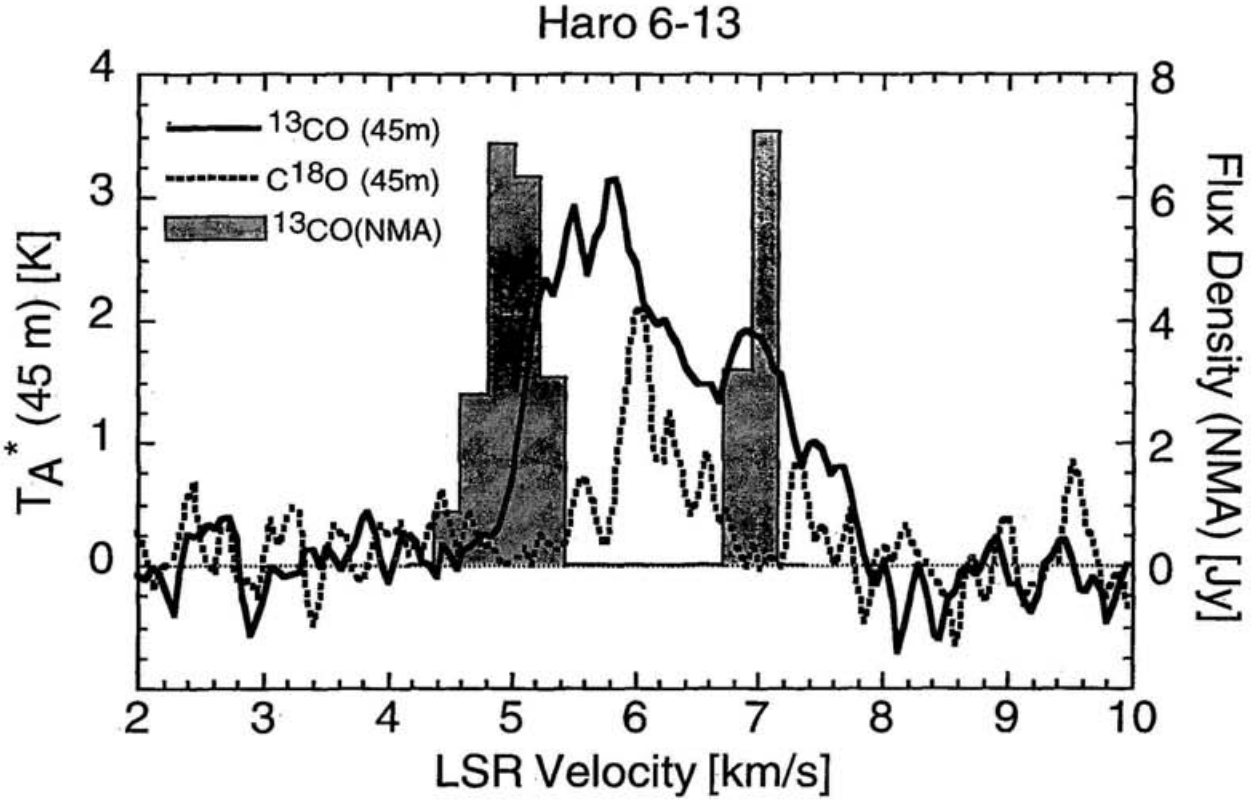
Haro 6-13
13CO (45m)
C18O (45m)
13CO(NMA)
TA* (45 m) [K]
Flux Density (NMA) [Jy]
LSR Velocity [km/s]
0
1
2
3
4
0
2
4
6
8
2
3
4
5
6
7
8
9
10

Fig. V.7

Chapter VI

Aperture Synthesis $C^{18}O$ ($J = 1 - 0$) Observations of Flat-Spectrum T Tauri Stars: The Evolution of Protostar Envelopes

ABSTRACT

We report aperture synthesis $C^{18}O$ ($J = 1 - 0$) observations of four T Tauri stars with flat spectra at infrared wavelengths in the Taurus Molecular Cloud by using the Nobeyama Millimeter Array. Spatially extended $C^{18}O$ ($J = 1 - 0$) emissions with size exceeding 10^3 AU were detected around three sources (T Tauri, HL Tauri, GV Tauri), indicating the existence of the remaining parts of the parent cloud cores around these T Tauri stars. Although the spatial extents of the gaseous structures around these T Tauri stars are comparable to those around protostar candidates, the distributions of the $C^{18}O$ ($J = 1 - 0$) emissions are quite different; unlike the cases of protostar candidates, the observed $C^{18}O$ ($J = 1 - 0$) emissions show no prominent peak at the stellar positions but have several bright peaks located far from the central stars. Such a difference in the spatial distribution of the $C^{18}O$ ($J = 1 - 0$) emission suggests that the degree of density concentration in the protostellar envelopes becomes weaker in the course of evolution from the protostar stage to the T Tauri stage. The typical sizescale for the protostellar collapse is also discussed.

Subject headings: circumstellar matter — ISM: jets and outflows — stars: molecules — ISM: structure — stars: formation — stars: individual (T Tauri, HL Tauri, GV Tauri) — stars: pre-main sequence

VI.1. Introduction

Low mass stars are formed through dynamical collapse of the circumstellar envelope in the central parts of molecular cloud cores. It is therefore important to investigate the structure and evolution of the circumstellar envelopes in order to understand the star formation process. Understanding of the envelope structure in the protostar stage, where a central star grows by mass accretion from an infalling envelope, has been improved by both theoretical and observational studies. A lot of theoretical studies have dealt with dynamical collapse in the protostar stage, particularly by means of numerical simulations (e.g., Narita, Nakano, & Hayashi, 1970; Stahler, Shu, & Taam 1980; Tomisaka 1996) and similarity analyses (e.g., Shu 1977; Nakamura, Hanawa, & Nakano 1995; Saigo & Hanawa 1998). These studies predict fundamental characteristics of the protostar envelopes, e.g., density and kinematical structures of the envelopes or mass accretion rate in the envelopes.

On the other hand, recent aperture synthesis observations of several protostar candidates have revealed their circumstellar environments in detail. The infalling motions around some protostar candidates have directly been detected (Ohashi et al. 1996a; Saito et al. 1996; Ohashi et al. 1997a). More recently, Momose et al. (1997) [Chapter II of this thesis] made high-resolution $C^{18}O$ ($J = 1 - 0$) observations of L 1551 IRS 5 using the Nobeyama Millimeter Array (NMA), and revealed the internal structure of the density distribution and kinematics in the protostellar envelope around L 1551 IRS 5 in detail. Such observations straightforwardly provide the physical nature of the protostellar envelopes, which can be compare with the results of theoretical studies.

Following the protostar stage, the dissipation of parent cloud cores should occur, probably due to mass accretion onto the central star-disk systems and/or due to dispersal induced by the energetic outflows ejected from the central stars (e.g., Hayashi et al. 1994; Ohashi et al. 1996b). The central stars are then revealed and observed as T Tauri stars even at the optical wavelengths. However, the detailed evolution process of circumstellar envelopes in the post-protostellar stage is still unclear. It is important to understand the evolution of protostar envelopes in the course from the protostar stage to the T Tauri stage, because it must be related to the termination mechanism of the infall, which is one of the least understood issues in the star formation process. In order to get some information on the evolution of protostar envelopes, we have to observe not only the protostars but also the young stellar objects that are in a "transitional phase" between the two evolutionary stages.

Some T Tauri stars with so-called flat-spectrum can be regarded as the objects that are in the transitional phase between the protostar stage and the T Tauri stage. Aperture synthesis ^{13}CO ($J = 1 - 0$) observations of flat-spectrum T Tauri stars have revealed that these sources are commonly accompanied by spatially extended ($> 10^3$ AU in radius) gaseous structures that can be interpreted as the remnant parts of the parent cloud cores or the protostellar envelopes (Hayashi, Ohashi, & Miyama 1993; Kitamura, Kawabe, & Saito 1996a; Momose et al. 1996 [Chapter IV of this thesis]; Chapter V). Although these ^{13}CO ($J = 1 - 0$) observations reveal the gas distribution and kinematics around these sources fairly well, ^{13}CO ($J = 1 - 0$) emissions originated from circumstellar gas near the systemic velocity seem to be absorbed by the forground gas in the cases GV Tauri, Haro 6-13 (Chapter V), and DG Tauri (Kitamura et al. 1996a). In order to completely reveal the structure of circumstellar gas around these sources, we need observations with a molecular line for which the optical thickness of the forground gas is negligible.

In this chapter, we report the results of aperture synthesis observations of four flat-spectrum T Tauri stars (T Tauri, HL Tauri, GV Tauri, and Haro 6-13) with the $C^{18}O$ ($J = 1 - 0$) line using the NMA[1]. Since the ambient clouds around these sources are expected to be optically thin for the $C^{18}O$ ($J = 1 - 0$) line, this is an appropriate line to reveal the density and kinematical structures of the circumstellar gas. We describe the details of the observations in § VI.2, and present observational results in § VI.3. In § VI.4, we compare the spatial ditributions of $C^{18}O$ ($J = 1 - 0$) emissions around the flat-spectrum T Tauri stars with those around protostar candidates, and discuss the evolution of protostar envelopes in the course from the protostar stage to the T Tauri stage.

VI.2. Observations

Aperture synthesis $C^{18}O$ ($J = 1 - 0$) observations of four flat-spectrum T Tauri stars were made during a period from 1995 November to 1996 March with the NMA, which is composed of six 10 m dishes. We used the tunerless SIS receivers (Sunada et al. 1993) whose system noise temperatures were typically 300 K (double sideband [DSB]) at the zenith. We employed the digital FFT spectral correlator FX, which gave a frequency resolution of 78 kHz, corresponding to the velocity resolution of 0.213 km s^{-1} at the frequency of the $C^{18}O$ ($J = 1 - 0$) line. Two array configurations, giving 30 baselines, were used for the observations. The minimum projected baseline length was 9 m so that our observations are insensitive to structures with size greater than 62″, corresponding to 8700 AU at the Taurus Molecular Cloud. The phase and gain of the array system were calibrated by every 30 minutes observations of 0528+134. During the period from 1995 November to 1996 March, we measured the flux density of 0528+134 at 110 GHz regularly (about once a week) by observing Uranus or Mars. The complex pass band was also obtained by the observations of 0528+134.

We subtracted the continuum level from the visibility data, and then made $C^{18}O$ ($J = 1 - 0$) channel maps with the CLEAN algorithm in the NRAO AIPS package. In making the $C^{18}O$ ($J = 1 - 0$) maps, we applied the natural weighting to the visibility data. We show in Table VI.1 the resultant synthesized beam size and the rms noise levels in the $C^{18}O$ ($J = 1 - 0$) channel maps as well as the positions of the field centers and the dates.

[1]We have not yet observed DG Tauri, simply beacuse of the shortage of observing time.

of the observations. All the $C^{18}O$ ($J = 1 - 0$) maps in this chapter have already been corrected for the primary beam (FWHM = 65″) attenuation. For T Tauri, we observed two fields of view and mosaicked in such a way as to minimize noise in the resultant images, as in the case of the previous ^{13}CO ($J = 1 - 0$) observations (see Momose et al. 1996). In this chapter we discuss the $C^{18}O$ ($J = 1 - 0$) emission components in the area where the primary beam response is greater than 50%. We also made maps of the continuum emissions at 110 GHz, and found that each of the continuum emissions is unresolved and is located at the stellar position. These continuum emissions originate from the compact circumstellar disks as discussed by some previous studies (e.g., Beckwith et al. 1990). The flux density of the continuum emission for each object is also listed in Table VI.1.

VI.3. Results

With the present observations, we detected siginificant $C^{18}O$ ($J = 1 - 0$) emissions around three objects (T Tauri, HL Tauri, GV Tauri) while did not detect any significant emission around Haro 6-13. These facts indicate that the amount of the circumstellar gas around Haro 6-13 is smaller than the other three sources, because the noise level in each set of the channel maps is not so different from the others (see row (10) in Table VI.1). In the following, we concentrate on the three objects around which the siginificant $C^{18}O$ ($J = 1 - 0$) emissions have been detected. We assume their systemic velocities (v_{sys}) to be the values listed in Table VI.2, which are taken from the peak velocities of the $C^{18}O$ ($J = 1 - 0$) profiles toward these sources with the Nobeyama 45 m telescope (HPBW = 17″ at 110 GHz: Momose, unpublished data).

VI.3.1. Gas Distribution and Kinematics

VI.3.1.1. T Tauri

Figure VI.1 shows the integrated intensity map of the $C^{18}O$ ($J = 1 - 0$) emission around T Tauri. In Fig. VI.1, we can identify two prominent emission features; One of them covers the northeastern and southeastern areas from T Tauri with its peaks located at $\sim 25''$ northeast, $\sim 25''$ east, and $\sim 25''$ southeast of T Tauri. The other extends from 50″ west to 45″ southwest of T Tauri with the several peaks of the emission. The spatial distribution of the $C^{18}O$ ($J = 1 - 0$) emission in Fig. VI.1 is quite similar to that of the

integrated ^{13}CO ($J = 1 - 0$) intensity map (see Fig. IV.3*a*).

Figure VI.2 is the velocity channel maps of the C^{18}O ($J = 1 - 0$) emission. The siginificant emission features are detected in the velocity range of $V_{\rm LSR} = 7.46 - 9.16$ km s^{-1} (Figs. VI.2*d* – 2*l*), and the marginal emission features are also detected in the two maps for $V_{\rm LSR} = 7.03$ and 7.24 km s^{-1} (Figs. VI.2*b* and VI.2*c*). The spatial distibution of the emissions in Fig. VI.2 is quite similar to those in the channel maps of the ^{13}CO ($J = 1 - 0$) line (Fig. IV.1) as described in the following. The emissions in the maps for the velocities blueshifted by 0.08 – 0.72 km s^{-1} from $v_{\rm sys}$ (Figs. VI.2*d* – 2*g*) can be divided into the following two features: (1) a feature covering the northeastern area from T Tauri. and (2) a feature that appears at $\sim 45''$ west of T Tauri and continues to the southwest of T Tauri. The emissions contained in the first feature are seen in Figs. VI.2*e* – 2*g* while those in the second feature are seen in Figs. VI.2*d* – 2*e*. These two features correspond to the "blueshifted ringlike emission" of the ^{13}CO ($J = 1 - 0$) line (see Fig. IV.2*a*). On the other hand, in the channel maps for the velocities redshifted by 0.56 – 0.98 km s^{-1} from $v_{\rm sys}$ (i.e., Figs. VI.2*j* – 2*l*), we can find bright emissions extending from $\sim 30''$ west to $\sim 30''$ southwest of T Tauri. In addition to these bright emissions, several weak emission features can also be seen, i.e., $\sim 35''$ southeast of T Tauri in Fig. VI.2*j*, $\sim 35''$ northeast of T Tauri in Fig. VI.2*k*, and $\sim 30''$ east and $\sim 10''$ south of T Tauri in Fig. VI.2*l*. All these emissions in Fig. VI.2*j* – 2*l* correspond well to the "redshifted ringlike emission" of the ^{13}CO ($J = 1 - 0$) line (see Fig. IV.2*b*).

We can also identify bright emission features located at $50'' - 1'$ west of T Tauri in three channel maps near the systemic velocity (i.e., Figs. VI.2*g* – 2*h*). We did not detect any ^{13}CO ($J = 1 - 0$) emission corresponding to these bright C^{18}O ($J = 1 - 0$) features. This may be because the optical thickness of the foreground gas is so large for the ^{13}CO ($J = 1 - 0$) line near the systemic velocity that it absorbs the ^{13}CO ($J = 1 - 0$) emissions corresponding to these bright C^{18}O ($J = 1 - 0$) features.

Basically, the spatial distributions of the C^{18}O ($J = 1 - 0$) emissions in the channel maps (Fig. VI.2) are quite similar to those of the ^{13}CO ($J = 1 - 0$) emissions whose velocity structures can well be explained by the dissipating motion under the influence of the high-velocity outflows (see Momose et al. 1996 for more detailed discussions). Most of the C^{18}O ($J = 1 - 0$) emissions therefore originate from the dispersing cloud core around T Tauri that was found with the ^{13}CO ($J = 1 - 0$) observations.

VI.3.1.2. HL Tauri

We show in Figure VI.3 the integrated intensity map of the $C^{18}O$ ($J = 1 - 0$) emission around HL Tauri. The emission is elongated in the direction roughly perpendicular to the optical jet ejected from HL Tauri (Mundt, Ray, & Bührke 1988). There is no prominent emission peak at the stellar position while there are several bright emission features in the area where the separation from the central star exceeds 20″.

Figure VI.4 is the velocity channel maps of the $C^{18}O$ ($J = 1 - 0$) emission. The emission features above the 3σ level are detected in the velocity range of $V_{LSR} = 5.96 - 7.24$ km s^{-1}. In the channel maps for the velocities blueshifted by $0.48 - 0.70$ km s^{-1} from v_{sys} (Figs. VI.4*b* – 4*c*), weak and extended emission features appear at around 20″ northwest of HL Tauri. At the velocity blueshifted by 0.27 km s^{-1} from v_{sys} (Fig. VI.4*d*), we can find an emission feature elongated in the direction perpendicular to the outflow axis. This feature shows similar spatial distribution to the ^{13}CO ($J = 1 - 0$) emission originating from the infalling disklike envelope around HL Tauri (Hayashi et al. 1993). In the channel map near the systemic velocity (Fig. VI.4*e*), two bright features located far from the star (i.e., $\sim 35''$ northwest and $\sim 25''$ south of HL Tauri) can be seen. In the two channel maps for the velocities redshifted by $0.15 - 0.37$ km s^{-1} from v_{sys} (Figs. VI.4*f* – 4*h*), the emission extends from 35″ northwest to 35″ south of HL Tauri. At the velocity redshifted by 0.58 km s^{-1} from v_{sys} (Fig. VI.4*h*), weak emission feature is located at $\sim 20''$ southwest of HL Tauri.

Cabrit et al. (1996) made mapping observations around HL Tauri with the ^{13}CO ($J = 1 - 0$) line using the IRAM 30 m telescope (HPBW = 20″), and obtained large-scale ($80'' \times 80''$) ^{13}CO ($J = 1 - 0$) intensity maps. Comparing our results with their ^{13}CO ($J = 1 - 0$) maps, we found that the above-mentioned characteristics of our $C^{18}O$ ($J = 1 - 0$) channel maps are quite consistent with those of the ^{13}CO ($J = 1 - 0$) maps with the IRAM 30 m telescope. This fact indicates that the forground gas toward HL Tauri is optically thin for both the ^{13}CO ($J = 1 - 0$) and $C^{18}O$ ($J = 1 - 0$) lines, and our observations successfully reveal the small-scale structure of the circumstellar gas associated with HL Tauri.

Since there is no high-resolution map of the molecular outflows around HL Tauri, the kinematics of the observed features is not so clear as the case of T Tauri. As shown in Appendix VI.A, we have found that the higher-velocity features in Figures VI.4*b*, VI.4*c*, VI.4*g*, and VI.4*h* originate from gas that is now dispersing, because the observed line-of-sight velocities are so large that these features should originate from gas which is not bound by the gravity of the central star. On the other hand, the emission features

near the systemic velocity (Figs. VI.4*d*, VI.4*e*, and VI.4*f*), we cannot judge only from our observational results whether the $C^{18}O$ ($J = 1 - 0$) emissions originate from infalling gas or dissipating gas (see Appendix VI.A). However, the emission features in Fig VI.4*d* probably originate from infalling gas, because their spatial distribution corresponds well to the infalling disklike envelope detected by the ^{13}CO ($J = 1 - 0$) observations (Hayashi et al. 1993). In summary, infalling gas and outflowing gas seem to coexist around HL Tauri within the region of ~ 5000 AU in radius.

VI.3.1.3. GV Tauri

Figure VI.5 is the integrated intensity map of the $C^{18}O$ ($J = 1 - 0$) emission around GV Tauri. Several emission peaks can be seen in this map, and most of them are located in the area where the separation from the central star exceeds 15″. On the other hand, there is no $C^{18}O$ ($J = 1 - 0$) emission in the northwestern and southwestern areas near the central star. As a result, the $C^{18}O$ ($J = 1 - 0$) emission in Fig. VI.5 shows ridgelike structure with an elliptical shape elongated in the northwest-southeast direction. Note that this direction is nearly perpendicular to the possible direction of the outflow (P.A. $\approx 65°$) suggested by the observations with some optical emission lines (Strom et al. 1986).

We show in Figure VI.6 the velocity channel maps of the $C^{18}O$ ($J = 1 - 0$) emission around GV Tauri. The emission above the 3σ level is detected in the velocity range of $V_{LSR} = 5.81 - 6.88$ km s^{-1}. Contrary to the results of the ^{13}CO ($J = 1 - 0$) observations (Chapter V), the $C^{18}O$ ($J = 1 - 0$) emissions are detected symmetrically with respect to the systemic velocity, suggesting that the present observations successfully revealed the structure of the circumstellar gas around GV Tauri. The spatial distribution of the emissions in each channel map is described as follows. In the channel maps for the blueshifted velocities (i.e., Figs. VI.6*b* – 6*d*), we can find an emission feature extending from $\sim 35''$ northwest to $\sim 35''$ south of GV Tauri. In particular, the emission in Fig. VI.6*c* is quite prominent. In the channel map for the systemic velocity (Fig. VI.6*e*), there are several emission peaks in the area where the separation from the central star exceeds 15″. At the velocity redshifted by 0.19 km s^{-1} from v_{sys} (Fig. VI.6*f*), there are two bright peaks of the emission: one is located at 20″ northwest of GV Tauri, and the other is located at 10″ southeast of GV Tauri. These two peaks are connected with weak emission, and the emission in Fig. VI.6*f* and that in Fig. VI.6*c* seem to have symmetric structures with respect to the central star. At the velocity redshifted by 0.40 km s^{-1} from v_{sys} (Fig. VI.6*g*),

only the emission peak 10″ southeast of GV Tauri remains bright.

As the case of HL Tauri, there is no high-resolution map of the molecular outflows around GV Tauri. For this reason, the kinematics of the observed features around GV Tauri is difficult to interpret. As described in Appendix VI.A, we cannot judge only from our observational results whether each of the emission features in Fig. VI.6 originates from infalling gas or dissipating gas. In order to understand the kinematics of the observed gas, we need a high-resolution map of the molecular outflows around GV Tauri.

VI.3.2. Gas Mass

We can estimate the mass of the gas detected with the NMA by the following equation (Scoville et al. 1986):

$$M_{\rm gas} = 5.45 \times 10^{-4} T_{\rm ex} \exp\left(\frac{5.27}{T_{\rm ex}}\right) \frac{\tau_{\rm C^{18}O}}{1 - \exp\left(-\tau_{\rm C^{18}O}\right)} \left(\frac{d}{140\ {\rm pc}}\right)^2 \left[\frac{10^{-7}}{X({\rm C^{18}O})}\right] \int S_\nu dv\ M_\odot, \quad \text{(VI.1)}$$

where $T_{\rm ex}$ is the excitation temperature of $C^{18}O$ at $J = 1$ level, d is the distance to the Taurus Molecular Cloud, $X(C^{18}O)$ is the fractional abundance of $C^{18}O$ relative to H_2, $\tau_{\rm C^{18}O}$ is the mean optical thickness of the gas for the $C^{18}O$ ($J = 1 - 0$) line, and $\int S_\nu dv$ is the integrated flux in units of Jy km s^{-1}. In Table VI.3, we summarized the observed integrated flux and the gas mass derived from equation (VI.1) for each object. In deriving the gas masses, we have assumed that $\tau_{\rm C^{18}O} \ll 1$, $T_{\rm ex} = 20$ K, $d = 140$ pc, and $X(C^{18}O) = 2.5 \times 10^{-7}$ (Chernicharo & Guélin 1987).

If $\tau_{\rm C^{18}O}$ were considerably larger than 1, the gas masses would be much larger than those in Table VI.3. However, the brightness temperture of each $C^{18}O$ ($J = 1 - 0$) feature in the channel maps (Figs. VI.2, VI.4, and VI.6) is at most 4.2 K (for the emission peak in Fig. VI.2*i*), which is much smaller than the expected excitation temperature of $C^{18}O$ molecule, suggesting that the detected $C^{18}O$ ($J = 1 - 0$) emissions are optically thin. Therefore we can conclude that the above estimations of gas mass with the assumption $\tau_{\rm C^{18}O} \ll 1$ are fairly good.

VI.4. Discussion

VI.4.1. Difference in the Distribution of Circumstellar Gas between Flat-Spectrum T Tauri Stars and Protostar Candidates

We have detected the $C^{18}O$ ($J = 1 - 0$) emissions with size greater than 1000 AU around three flat-spectrum T Tauri stars. Since the spatial extents of these gaseous emissions are comparable to the typical size of molecular cloud cores in the Taurus Molecular Cloud (e.g., Myers & Benson 1983; Mizuno et al. 1994), it is natural to consider that these gaseous structures are the parts of the remaining cloud cores around these stars. Such circumstellar environments around these flat-spectrum T Tauri stars are quite different from those around typical classical T Tauri stars that are only accompanied by compact gaseous disks with a radius smaller than 10^3 AU (e.g., Kawabe et al. 1993; Dutrey, Guilloteau, & Simon 1994; Saito et al. 1995; Koerner et al. 1995). These facts strongly suggest that the three flat-spectrum T Tauri stars, which are surrounded by the remnant cloud cores, are in the transitional phase between the protostellar stage, in which a central star is deeply embedded within the circumstellar envelope, to the T Tauri stage, in which a central star is surrounded by a compact circumstellar disk instead of a spatially extended envelope (Chapters IV and V; see also Ohashi et al. 1991; Hayashi et al. 1994; Ohashi et al. 1996b).

We have also made aperture synthesis $C^{18}O$ ($J = 1 - 0$) observations of three protostar candidates in Taurus (Chapters II and III; Ohashi et al. 1997a), and have deteced the $C^{18}O$ ($J = 1 - 0$) emissions with their sizescales greater than 10^3 AU. Although the spatial extents of the $C^{18}O$ ($J = 1 - 0$) emissions around the flat-spectrum T Tauri stars are comparable to those around protostar candidates, the distributions of the $C^{18}O$ ($J = 1 - 0$) emissions are quite different between the two categories. In order to compare the spatial distributions of the $C^{18}O$ ($J = 1 - 0$) emissions around the flat-spectrum T Tauri stars and those around the protostar candidates, we show in Figure VI.7 the $C^{18}O$ ($J = 1 - 0$) integrated intensity maps around three protostar candidates (L 1551 IRS 5, L 1551 NE, and L 1527) obtained with the NMA, and in Figure VI.8 the brightness distributions of the integrated $C^{18}O$ ($J = 1 - 0$) intensities around these sources. As shown in Fig. VI.7, the $C^{18}O$ ($J = 1 - 0$) emissions around the protostar candidates commonly show centrally condensed distributions with their peaks at the stellar positions. For all the cases in Fig. VI.8*a*, the mean brightness temperature gets higher as the separation from the central star gets smaller at least in the region where the separation is smaller than 20″. It should also be

noted that the $C^{18}O$ ($J = 1 - 0$) emissions around the protostar candidates have structures elongated in the directions perpendicular to the axes of the outflows (see Fig. VI.7), and that the velocity fields can be explained in terms of some motions induced by the gravity of the central stars, e.g., infall with slight rotation (see Chapter II and III; Ohashi et al. 1997a). On the other hand, the gaseous emissions around the flat-spectrum T Tauri stars have no prominent peak at the stellar positions. Instead, there are several bright emission peaks located far from the central stars (see Figs. VI.1, VI.3, and VI.5). As a result, the brightness distributions in Fig. VI.8*b* have some local maxima even in the outer regions, i.e., $\sim 23''$ far from the central star for the case of T Tauri, $\sim 15''$ far from the star for the case of HL Tauri, and $\sim 7''$ and $\sim 21''$ far from the star for the case of GV Tauri. Contrary to the cases of protostar candidates, the velocity fields in the gaseous structures around the flat-spectrum T Tauri stars are so complicated that they are not simply exlpained in terms of infall or rotation.

Since the $C^{18}O$ ($J = 1 - 0$) line is expected to trace well the column density of the circumstellar gas, the difference in the spatial distribution of the $C^{18}O$ ($J = 1 - 0$) emission is probably due to the difference in the density distribution of the circumstellar material; the degree of density concentration in the remaining cloud cores around the flat-spectrum T Tauri stars are much lower than that in the infalling envelopes around protostars. Thus the difference in the distributions of the $C^{18}O$ ($J = 1 - 0$) emissions described above suggests that the degree of density concentration in the protostar envelopes becomes weaker in the course of evolution from the protostar stage to the T Tauri stage.

VI.4.2. The Typical Sizescale for the Protostellar Collapse and the "Central Voids" in the Remaining Cloud Cores

The difference in the density structure of circumstellar gas between the protostars and the flat-spectrum T Tauri stars never developes unless there is a typical sizescale for the protostellar collapse. For example, if the protostellar collapse in a cloud core occurs only within the central region with a finite sizescale, the amount of circumstellar matter within the central region decreases monotonically with time, and as a result, the degree of density concentration will become weaker. Contrary to this, the degree of density concentration in a protostar envelope would never change with time if the infall region linearly expands with time and the mass infall rate is constant within the infall region, as the cases of "similarity solutions" for the protostellar collpase obtained by some theoretical studies (e.g., Shu 1977;

Nakamura et al. 1995; Saigo & Hanawa 1998). It is quite important to reveal the sizescale for the protostellar collapse because it must be related to the termination mechanism of mass accretion onto the central star-disk systems.

By inspecting carefully the $C^{18}O$ ($J = 1 - 0$) integrated intensity maps of the flat-spectrum T Tauri stars, we have found some characteristics that may be related to the sizescale for the protostellar collapse. When we connect the emission peaks in the integrated $C^{18}O$ ($J = 1 - 0$) emissions, all of them show ringlike structures roughly centered at the stellar positions, as shown in Figure VI.9. The inclination angle of T Tauri was derived to be $8° - 13°$ from its rotation period and rotational velocity (Herbst et al. 1986), and that of HL Tauri was estimated to be $\sim 65°$ from the ratio of the major to minor axis of the disklike infalling envelope (Hayashi et al. 1993). The inclination angle of GV Tauri is rather uncertain, but Kenyon, Calvet, & Hartmann (1993a) estimated to be $30° - 60°$ from the model fitting of the spectral energy distribution. Taking into accont these differences in the inclination angle, the existence of these ringlike emissions may indicate that flattened remnant cloud cores with "central voids" are commonly associated with these flat-spectrum T Tauri stars. This interpretation is consistent with the fact that the ringlike structures around HL Tauri and GV Tauri are elongated in the directions perpendicular to the outflow axes while the ringlike structure around T Tauri, which is observed with nearly pole-on configuration, is almost symmetric with respect to the central star. If this interpretation is true, it is natural to consider that the typical radius of the central voids in the remnant cloud cores around the flat-spectrum T Tauri stars, $\sim 30''$ or ~ 4200 AU in radius (see Fig. VI.9), must correspond to the sizescale of the infalling region in the protostellar stage, or the sizescale for the protostellar collapse. Interestingly, this sizescale is roughly coincident with the sizescale for the dynamical collapse estimated from the relationship between the rotation radius and local specific angular momentum of circumstellar gas, ~ 6000 AU in radius (Ohashi et al. 1997b; see also Goodman et al. 1993).

As discussed by Ohashi et al. (1997b), it remains unclear how the sizescale of the protostar collapse is determined. Two kinds of mechanisms that determine the sizescale of the protostellar collapse have so far been proposed. One is that the sizescale of the protostar collapse corresponds to the outer boundary of the infall region at the time when the outflows have dispersed the significant fraction of circumstellar material and the cloud core is no longer gravitationally bound (Nakano, Hasegawa, & Norman 1995). Another possibility is that the sizescale of the protostar collapse is related to the physical nature of the interstellar medium. For example, Ohashi et al. (1997b) pointed out that

their estimated sizescale for dynamical collapse corresponds to the sizescale where the non-thermal pressure due to the turbulent motion of gas becomes negligible compared with the thermal pressure (For the empirical relation between the Doppler width and spatial extent of a molecular emission line, see Larson (1981) and Fuller & Myers (1992)). This fact may imply that only the inner regions of cloud cores where the turbulent support is negligible can ungergo dynamical collapse while the outer regions cannot due to the support by turbulent pressure. As discussed in Momose et al. (1996) (see also § VI.3), the circumstellar gas around T Tauri is now dissipating under the influence of the high-velocity stellar wind, suggesting that the sizescale of protostellar collapse might determine mainly by the effect of the outflows. However, we cannot clearly identify the similar dissipating motion induced by the high-velocity outflows around the other two sources as described in § VI.3, and cannot detrermine which mechanism is more plausible only from our present observations. In order to clarify this point, further observations, especially the mapping observations of the molecular outflows at high-spatial resolutions, are required.

One might argue that the central postions of the ringlike structures are shifted from the stellar positions of HL Tauri and GV Tauri by $\sim 10''$. These positional shifts may be caused by the small relative motions of the stars to the remaining cloud cores. If we assume the timescale measured from the onset of the dynamical collapse to be $\sim 10^6$ yr for these flat-spectrum T Tauri stars, which is slightly longer than the timescale of the protostar stage, the positional shifts of $\sim 10''$ or ~ 1400 AU require the relative velocity between the stars and the cloud cores (on the plane of the sky) of only ~ 7 m s^{-1} ($= 1400\mathrm{AU}/10^6$ yr), which is much smaller than the sound velocity in the circumstellar gas or the speed of the stellar winds. Such a small relative motion is quite plausible, and thus the disagreement between the stellar positions and the central postions of the ringlike structures seen in Fig. VI.9 can easily be explined without change of our interpretation.

VI.4.3. Possible Mass Supply to the Inner Circumstellar Disks

As described in § VI.3, it is possible that part of the observed $C^{18}O$ ($J = 1 - 0$) emissions around HL Tauri and GV Tauri originates from gaseous components which are bound by the gravity of the central stars. This suggest that the gaseous components bound by the gravity of the central star may remain even in the early phase of the T Tauri stage. Although the mass of such a gaseous component (several $\times 10^{-2} M_\odot$) is negligible compared with the central stellar mass, they will play an important role in sustaining the mass of an

inner circumstellar disk for a longer period.

Beckwith et al. (1990) measured masses of circumstellar disks around 86 T Tauri stars with the observations of the 1.3 mm continuum emission, and found that the disk mass is typically $\sim 0.02 M_{\odot}$, and it does not change with stellar age of $10^5 - 10^7$ yr. On the other hand, Hartigan, Edwards, & Ghandour (1995) derived the mass accretion rates from circumstellar disks to the central T Tauri stars ($\dot{M}_*$) from their spectroscopic observations at optical and ultraviolet wavelengths, and revealed that $\dot{M}_*$ is $\gtrsim 10^{-7} M_{\odot}$ yr^{-1} until the stellar age becomes $\sim 10^6$ yr. These two observational results conflict with each other if there is no mass supply to the circumstellar disks in the T Tauri stage. Our observational results may suggest that these two observational results can actually be compatible; if the tenuous circumstellar material around the flat-spectrum T Tauri stars will settle on the circumstellar disks gradually, it will compensate the mass accretion to the central stars and keep the disk mass to be $\sim 0.02 M_{\odot}$ over the entire stage of T Tauri stars.

VI.5. Summary

We have made aperture synthesis observations of four flat-spectrum T Tauri stars with the $C^{18}O$ ($J = 1 - 0$) emissions by using the Nobeyama Millimeter Array (NMA). Our main results are summarized as follows:

1. Among the four stars observed with the present study, we have detected siginificant $C^{18}O$ ($J = 1 - 0$) emissions around three sources (T Tauri, HL Tauri, and GV Tauri). The spatial extents of these emissions exceed 10^3 AU, and comparable to the typical size of the molecular cloud cores in the Taurus Molecular Cloud. These facts indicate that the three flat-spectrum T Tauri stars are still accompanied by the parts of the remaining molecular cloud cores, and they are in the transitional phase between the protostar stage, in which a central star is deeply embedded within the circumstellar envelope, to the T Tauri stage, in which a central star is surrounded by a compact circumstellar disk instead of a spatially extended envelope. The gas masses detected with the present observations are $0.156 M_{\odot}$ for T Tauri, $0.0441 M_{\odot}$ for HL Tauri, and $0.0449 M_{\odot}$ for GV Tauri.

2. All the $C^{18}O$ ($J = 1 - 0$) emissions around the three flat-spectrum T Tauri stars have no prominent peak at the stellar position, but have several peaks which are located far from the central stars ($\gtrsim 20''$). Such spatial distributions of the $C^{18}O$ ($J = 1 - 0$) emissions around the flat-spectrum T Tauri stars are quite different from those of the $C^{18}O$

($J = 1 - 0$) emissions around protostar candidates, which show centrally condensed, disklike structure with their peaks at the stellar positions. The difference in the spatial distribution of the $C^{18}O$ ($J = 1 - 0$) emissions between the two categories can be interpreted as the difference in the density distributions of the circumstellar material, i.e., the degree of density concentration in the protostar envelopes gets weaker in the course of evolution from the protostar stage to the T Tauri stage.

3. All the $C^{18}O$ ($J = 1 - 0$) emissions around the three flat-spectrum T Tauri stars seem to show ringlike structures roughly centered at the stellar positions and elongated in the directions perpendicular to the outflow axes. The existence of these ringlike structures may indicate that the flattened remnant cloud cores with "central voids" are commonly associated with these sources. If this interpretation is true, the typical radius of these central voids, $\sim 30''$ or ~ 4200 AU in radius, must correspond to the typical sizescale for the dynamical collapse in the stage of protostars.

4. Since the observed $C^{18}O$ ($J = 1 - 0$) emission features around T Tauri show similar spatial distribution to that of the ^{13}CO ($J = 1 - 0$) emissions detected with the NMA, these features originate from gas now dissipating under the influence of the high-velocity wind from T Tauri, as the ^{13}CO ($J = 1 - 0$) emission features. On the other hand, most of the $C^{18}O$ ($J = 1 - 0$) emission features around HL Tauri and GV Tauri cannot be judged whether these features originate from infalling gas or from dissipating gas solely from our observational results. If part of the $C^{18}O$ ($J = 1 - 0$) emission features originate from gaseous components which are bound by the gravity of central stars, they will play an important role in sustaning the mass of an inner circumstellar disk in the T Tauri stage.

APPENDIX

VI.A. Simple Analysis of Gas Kinematics around HL Tauri and GV Tauri

Since there is no high resolution maps of the molecular outflows around HL Tauri and GV Tauri, we examine whether each of the $C^{18}O$ ($J = 1 - 0$) emission features around these two sources should originate from gas which is not bound by the gravity of the central star as follows. When we observed the emission originating from a gas element that is in the free-fall motion around the stellar mass of M, the observed line-of-sight velocity $V_{\rm los}$ is expressed by

$$V_{\rm los} = -\left(\frac{2GM}{L}\right)^{1/2} \cos\phi \sin^{1/2}\phi, \qquad \text{(VI.A1)}$$

where L is the projected distance between the star and the gas element on the plane of the sky, and ϕ is the angle between our line of sight and the line connecting the star and the gas element. For some fixed value of L, $|V_{\rm los}|$ takes the maximum value Max.($|V_{\rm los}|$) when $\sin\phi = 1/\sqrt{3}$, and Max.($|V_{\rm los}|$) is then expressed by

$$\begin{aligned} \text{Max.}(|V_{\rm los}|) &= 0.62\left(\frac{2GM}{L}\right)^{1/2} \\ &= 2.21\left(\frac{M}{1M_\odot}\right)^{1/2}\left(\frac{s}{1''}\right)^{-1/2} \text{ km s}^{-1}, \end{aligned} \qquad \text{(VI.A2)}$$

where s is the angular separation between the observed gas element and the star on the plane of the sky. Using equation (VI.A2), one can judge whether an observed emission feature should originate from gas which is not bound by the gravity of the central star; if an emission feature with the separation s has a relative line-of-sight velocity greater than Max.($|V_{\rm los}|$), this feature should originate from gas which is not bound by the gravity of the central star.

In order to examine the observational results more easily, we define Max.(s) given by

$$\text{Max.}(s) = \left(\frac{V_{\rm los}}{2.21 \text{ km s}^{-1}}\right)^{-2}\left(\frac{M}{1M_\odot}\right) \text{ arcsec.} \qquad \text{(VI.A3)}$$

The meaning of Max.(s) is that a emission feature at the relative line-of-sight velocity of $V_{\rm los}$ should be located inside the area where $s <$ Max.(s) if the emission feature originates from gas which is bound by the gravity of the central star.

Table VI.4 summarize Max.(s) for each channel map of HL Tauri or GV Tauri. In calculating Max.(s) listed in Table VI.4, we take M to be $0.55M_\odot$ for HL Tauri (Hayashi et

al. 1993) and $2.5M_{\odot}$ for GV Tauri (Leinert & Haas 1989). We have found that the emission features around HL Tauri seen in Figs. VI.4*b*, VI.4*c*, VI.4*g*, and VI.4*h* should originate from gas which is not bound by the gravity of the central star, because they are located in the areas where $s >$ Max.(s) listed in Table VI.4. Other emission features around HL Tauri and GV Tauri are located in the areas where $s <$ Max.(s), indicating that we cannot judge whether these emission features originate from gas bound by the gravity of the central star or from gas which is not bound by the gravity of the central star.

Table VI.1. Observational Parameters

			T Tauri	HL Tauri	GV Tauri	Haro 6-13
(1)	First Field Center[a]	R.A.(B1950)	$04^h19^m04^s.21$	$04^h28^m44^s.42$	$04^h26^m21^s.89$	$04^h29^m13^s.60$
(2)		decl.(B1950)	19°25′05″.4	18°07′36″.2	24°26′30″.0	24°22′42″.9
(3)	Second Field Center	R.A.(B1950)	$04^h19^m02^s.00$	—	—	—
(4)		decl.(B1950)	19°24′45″.0	—	—	—
(5)	Date[b]	D Config.	Nov. 27, 29, Dec. 18	Nov. 30, Dec. 1	Dec. 5, 21, 30	Nov. 06[e], 09[d], Jan. 1
(6)		C Config.	Feb. 10, 11	Mar. 10[d]	Mar. 5, 8	Mar. 16
(7)	Synthesized Beam	(Size)	9″.0 × 5″.9	9″.9 × 4″.7	9″.1 × 5″.3	11″.8 × 6″.4
(8)		(P.A.)	159°	163°	156°	171°
(9)	rms noise level[c]	(Jy beam^{-1})	145	117	99.1	130
(10)		(K)	0.27	0.25	0.20	0.17
(11)	110 GHz Continuum	(mJy)	56.7 ± 5.3	151.6 ± 4.6	22.4 ± 5.5	26.1 ± 4.7

[a]Identical with the stellar position listed in Herbig & Bell (1988).

[b]From 1995 November to 1996 March.

[c]The noise level in a $C^{18}O$ ($J = 1 - 0$) channel map.

[d]Only five elements were available.

[e]Only four elements were available.

Table VI.2. Systemic Velocity (in $V_{\rm LSR}$) of the Observed Stars

T Tauri	HL Tauri	GV Tauri
8.18 km s^{-1}	6.66 km s^{-1}	6.48 km s^{-1}

Table VI.3. Integrated Flux and the Gas Mass

	T Tauri	HL Tauri	GV Tauri
Integrated Intensity S_ν (Jy km s^{-1}).....	27.4	7.73	7.88
Gas Mass ($M_\odot$)[a].....	0.156	0.0441	0.0449

[a]Assuming that $\tau_{C^{18}O} \ll 1$, $T_{ex} = 20$ K, $d = 140$ pc, and $X(C^{18}O) = 2.5 \times 10^{-7}$.

Table VI.4. Integrated Flux and the Gas Mass

	HL Tauri			GV Tauri	
Figure VI.4	V_{los}[a] (km s^{-1})	Max.(s) ($''$)	Figure VI.6	V_{los}[a] (km s^{-1})	Max.(s) ($''$)
b	−0.70	5.5	*b*	−0.67	27.2
c	−0.48	11.6	*c*	−0.45	60
d	−0.27	36.8	*d*	−0.24	211
e	−0.06	746	*e*	−0.03	1.3×10^4
f	+0.15	119	*f*	+0.19	338
g	+0.37	19.6	*g*	+0.40	76
h	+0.58	7.9	—	—	—

[a]The line-of-sight velocity relative to the systemic velocity

— Figure Captions –

Fig. VI.1.— The $C^{18}O$ ($J = 1-0$) integrated intensity map of T Tauri. The contour spacing is 2σ, starting at $\pm 2\sigma$ (1σ = 43.6 mJy beam^{-1}). The cross indicates the stellar position. Negative contours are drawn by dashed lines.

Fig. VI.2.— Velocity channel maps of the $C^{18}O$ ($J = 1 - 0$) line around T Tauri. The corresponding LSR velocity in km s^{-1} is shown at the upper right corner of each panel. The cross indicates the stellar position. The contour spacing is 2σ, starting at $\pm 2\sigma$ (1σ = 145 mJy beam^{-1}).

Fig. VI.3.— The $C^{18}O$ ($J = 1 - 0$) integrated intensity map of HL Tauri. The contour spacing is 2σ, starting at $\pm 2\sigma$ (1σ = 44.2 mJy beam^{-1}). The cross indicates the stellar position. Negative contours are drawn by dashed lines.

Fig. VI.4.— Velocity channel maps of the $C^{18}O$ ($J = 1 - 0$) line around HL Tauri. The corresponding LSR velocity in km s^{-1} is shown at the upper right corner of each panel. The cross indicates the stellar position. The contour spacing is 2σ, starting at $\pm 2\sigma$ (1σ = 117 mJy beam^{-1}).

Fig. VI.5.— The $C^{18}O$ ($J = 1 - 0$) integrated intensity map of GV Tauri. The contour spacing is 2σ, starting at $\pm 2\sigma$ (1σ = 40.4 mJy beam^{-1}). The cross indicates the stellar position. Negative contours are drawn by dashed lines.

Fig. VI.6.— Velocity channel maps of the $C^{18}O$ ($J = 1 - 0$) line around GV Tauri. The corresponding LSR velocity in km s^{-1} is shown at the upper right corner of each panel. The cross indicates the stellar position. The contour spacing is 2σ, starting at $\pm 2\sigma$ (1σ = 99.1 mJy beam^{-1}).

Fig. VI.7.— The $C^{18}O$ ($J = 1 - 0$) integrated intensity maps of three protostar candidates obtained with the NMA; (*a*) the map of L 1551 IRS 5 (Momose et al. 1997), (*b*) the map of L 1551 NE (Chapter III), and (*c*) the map of L 1527 (Ohashi et al. 1997a). Primary beam attenuation in each map has already been corrected. The cross in each panel indicates the stellar position. The contour spacing in each map is 2σ, starting at $\pm 2\sigma$ (1σ = 46.9 mJy beam^{-1} for (*a*), 1σ = 34.6 mJy beam^{-1} for (*a*), and 1σ = 44 mJy beam^{-1} for (*c*)). Negative contours are drawn by dashed lines. The arrows indicate the directions of the outflows (*filled lines* : blueshifted, *dashed lines* : redshifted), that are determined from Uchida et al.

(1987) for (*a*), Hodapp (1994) for (*b*), and Tamura et al. (1995) for (*c*).

Fig. VI.8.— Brightness distributions in units of brightness temperature [K] of the $C^{18}O$ ($J = 1 - 0$) integrated intensities with the NMA for protostar candidates (*a*) and flat-spectrum T Tauri stars (*b*). Each data point is obtained by averaging the intensity of $C^{18}O$ ($J = 1 - 0$) emission in an annulus centered on the stellar position, whose width is $2''$.

Fig. VI.9.— Ringlike structures connecting the emission peaks (*thick dashed lines*) in the $C^{18}O$ ($J = 1 - 0$) integrated intensities of the three flat-spectrum T Tauri stars.

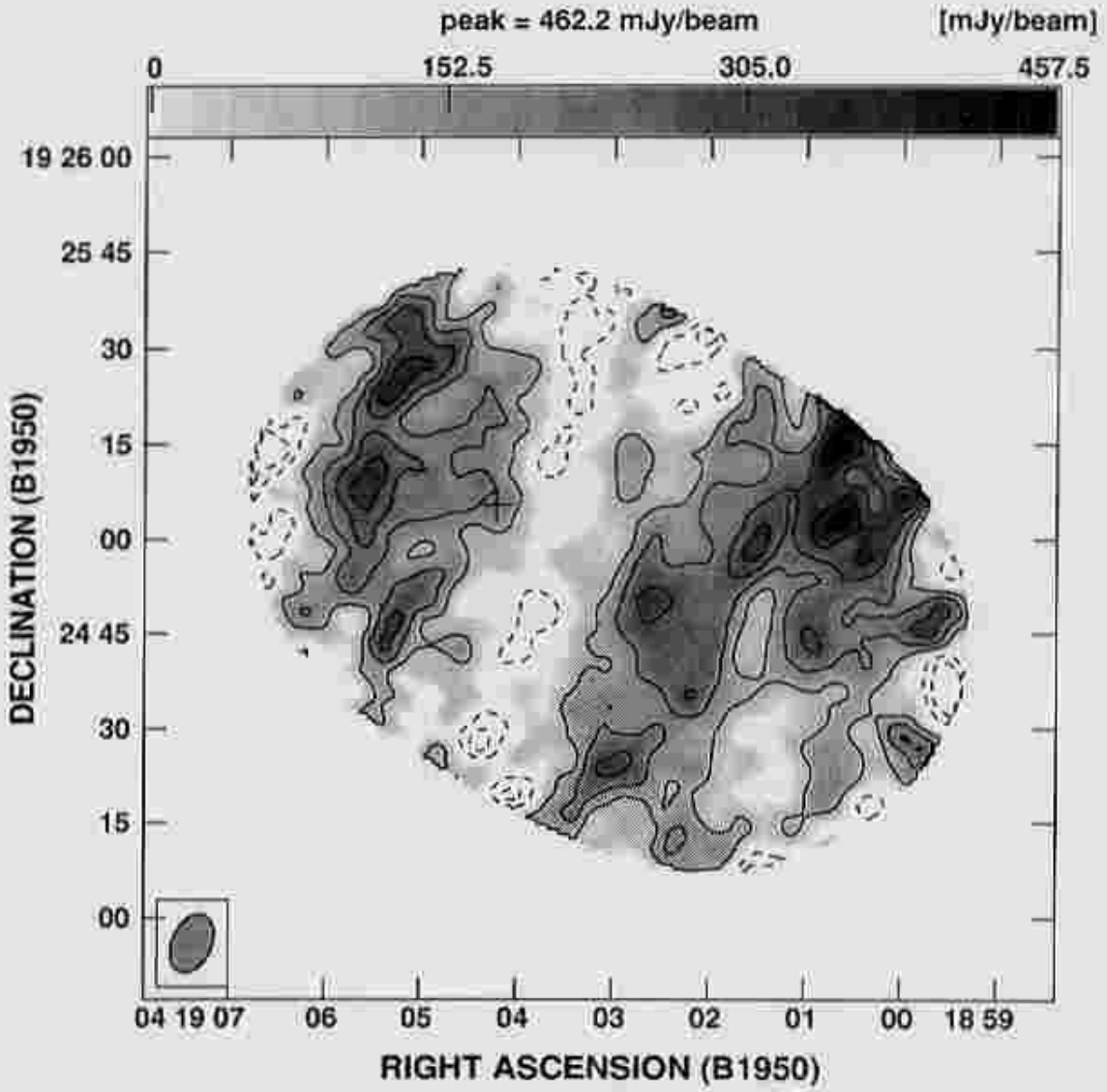
peak = 462.2 mJy/beam
[mJy/beam]
0
152.5
305.0
457.5
19 26 00
25 45
30
15
00
24 45
30
15
00
DECLINATION (B1950)
04 19 07
06
05
04
03
02
01
00
18 59
RIGHT ASCENSION (B1950)

Fig. VI.1

Fig. VI.2

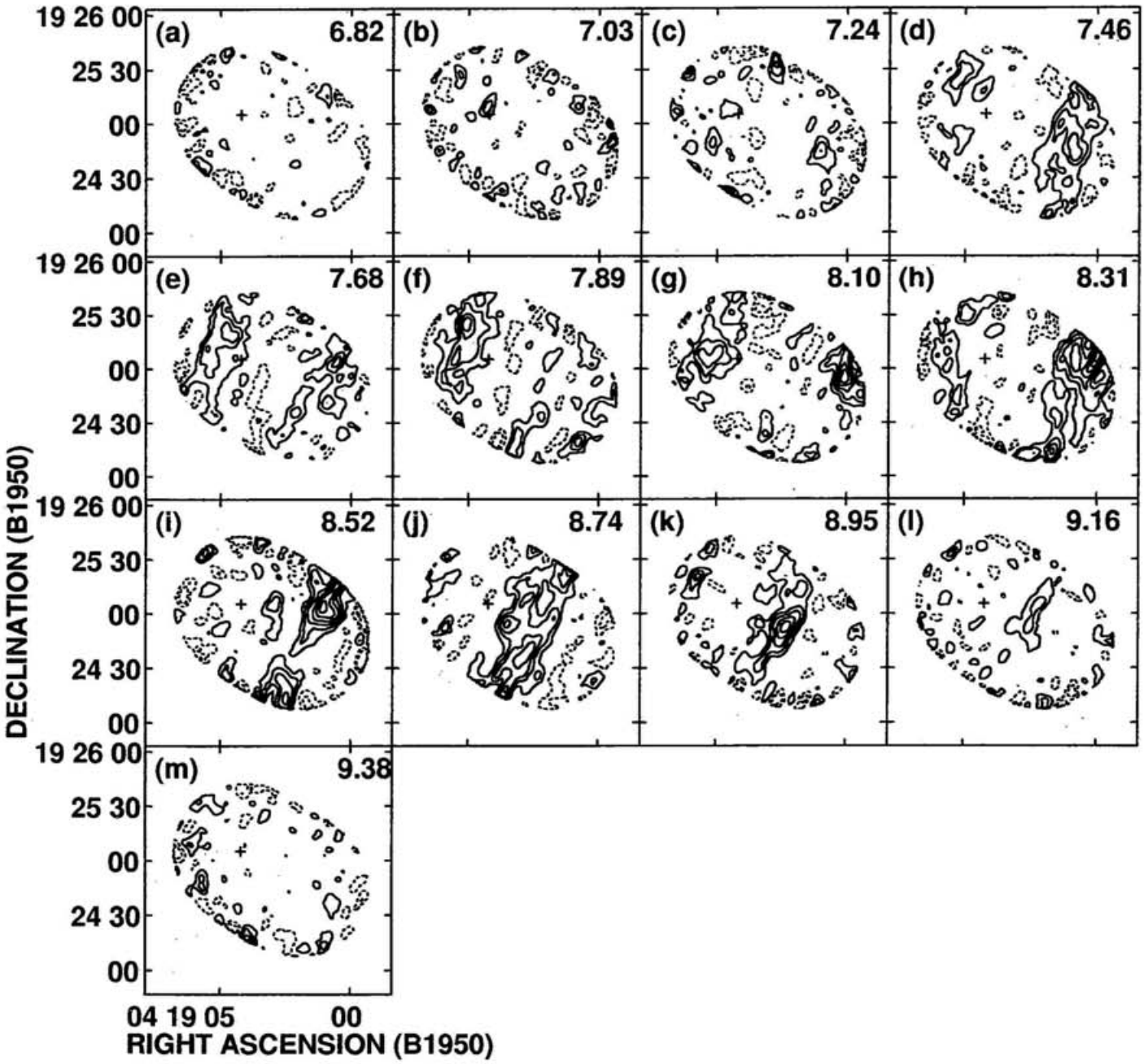
(a) 6.82
(b) 7.03
(c) 7.24
(d) 7.46
(e) 7.68
(f) 7.89
(g) 8.10
(h) 8.31
(i) 8.52
(j) 8.74
(k) 8.95
(l) 9.16
(m) 9.38
19 26 00
25 30
00
24 30
00
DECLINATION (B1950)
04 19 05
00
RIGHT ASCENSION (B1950)

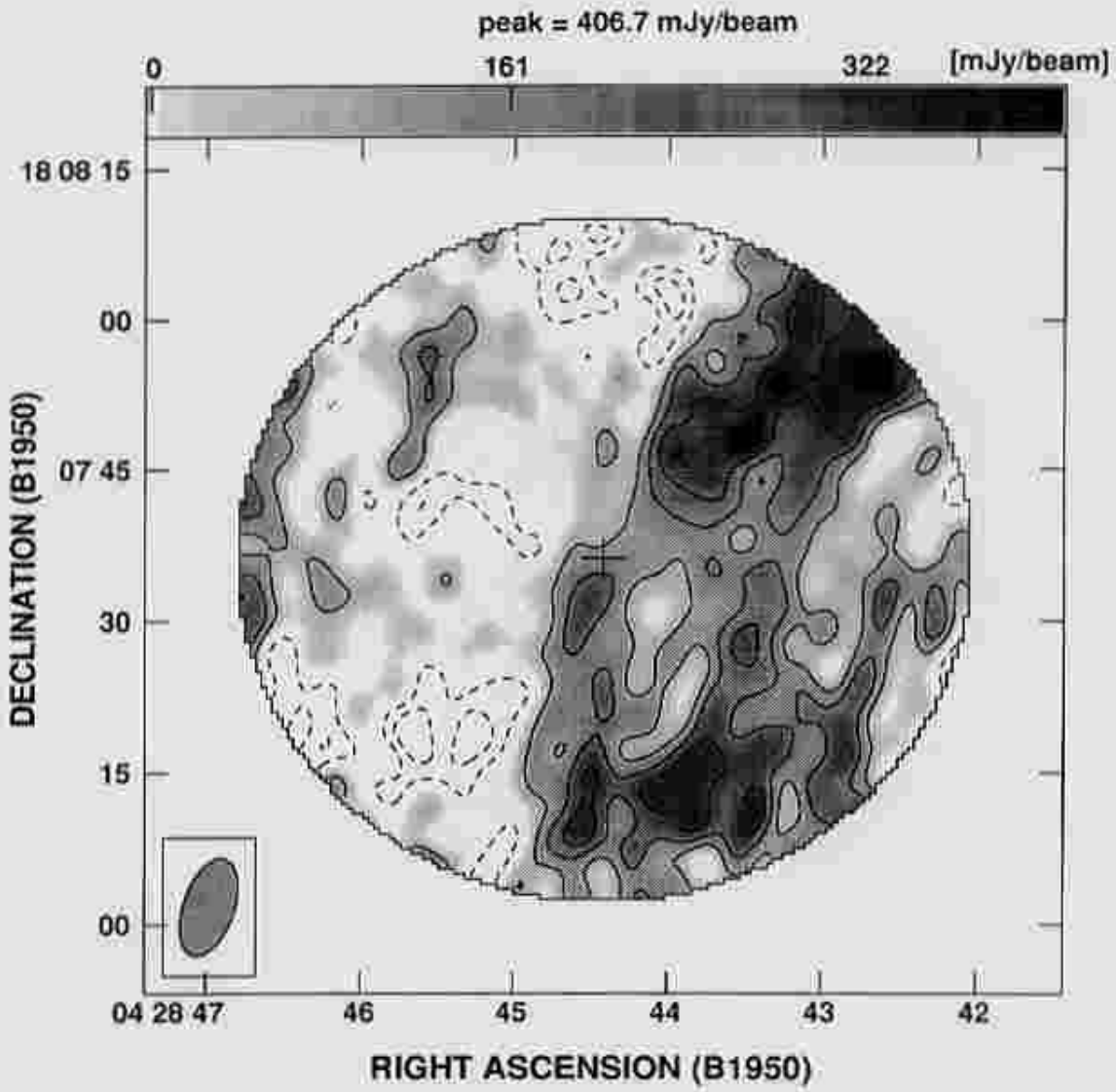
peak = 406.7 mJy/beam
0
161
322
[mJy/beam]
18 08 15
00
07 45
30
15
00
DECLINATION (B1950)
04 28 47
46
45
44
43
42
RIGHT ASCENSION (B1950)

Fig. VI.3

Fig. VI.4

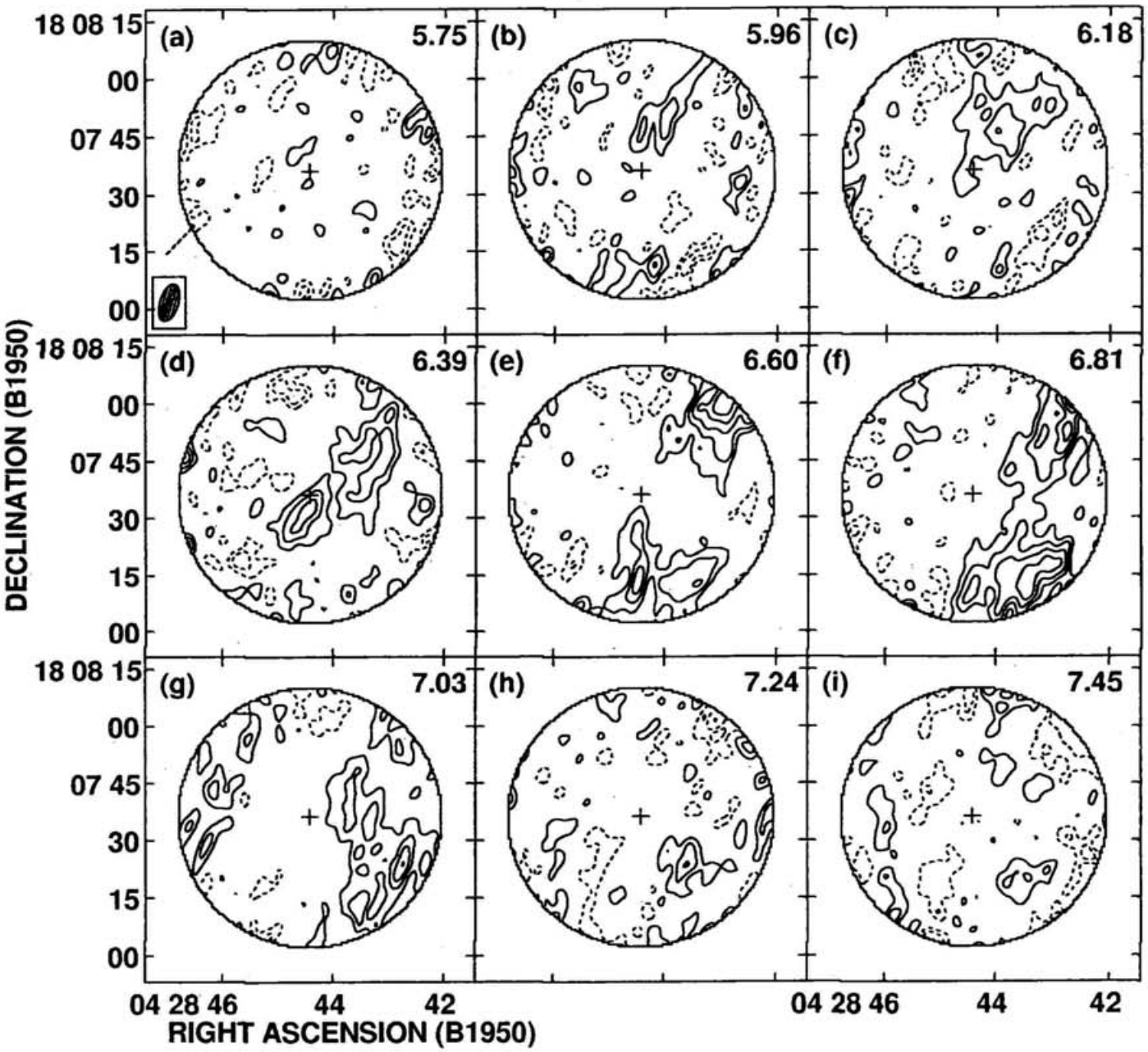
(a) 5.75
(b) 5.96
(c) 6.18
(d) 6.39
(e) 6.60
(f) 6.81
(g) 7.03
(h) 7.24
(i) 7.45
18 08 15
00
07 45
30
15
00
DECLINATION (B1950)
04 28 46
44
42
RIGHT ASCENSION (B1950)

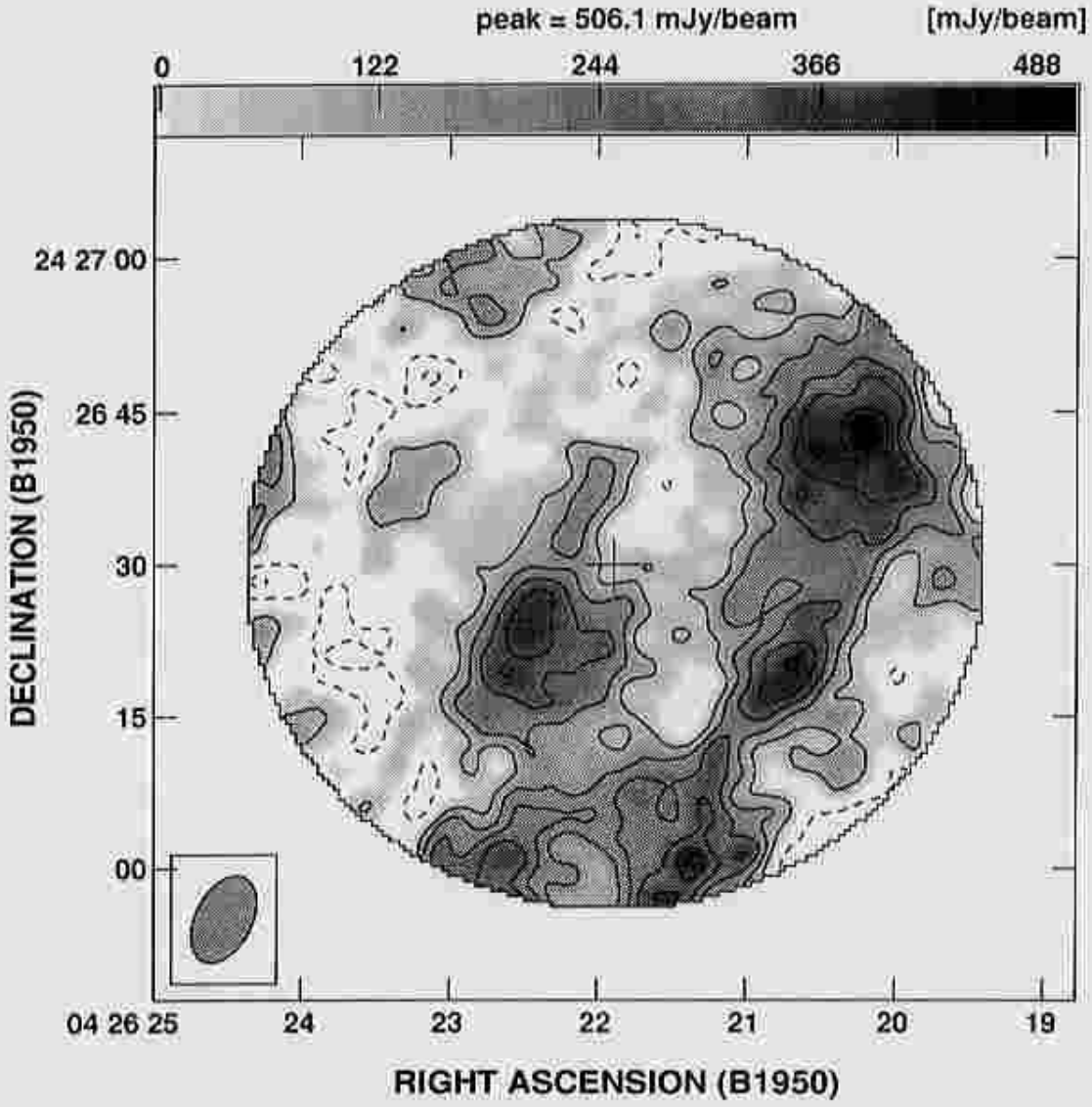
peak = 506.1 mJy/beam
[mJy/beam]
0
122
244
366
488
24 27 00
26 45
30
15
00
DECLINATION (B1950)
04 26 25
24
23
22
21
20
19
RIGHT ASCENSION (B1950)

Fig. VI.5

Fig. VI.6

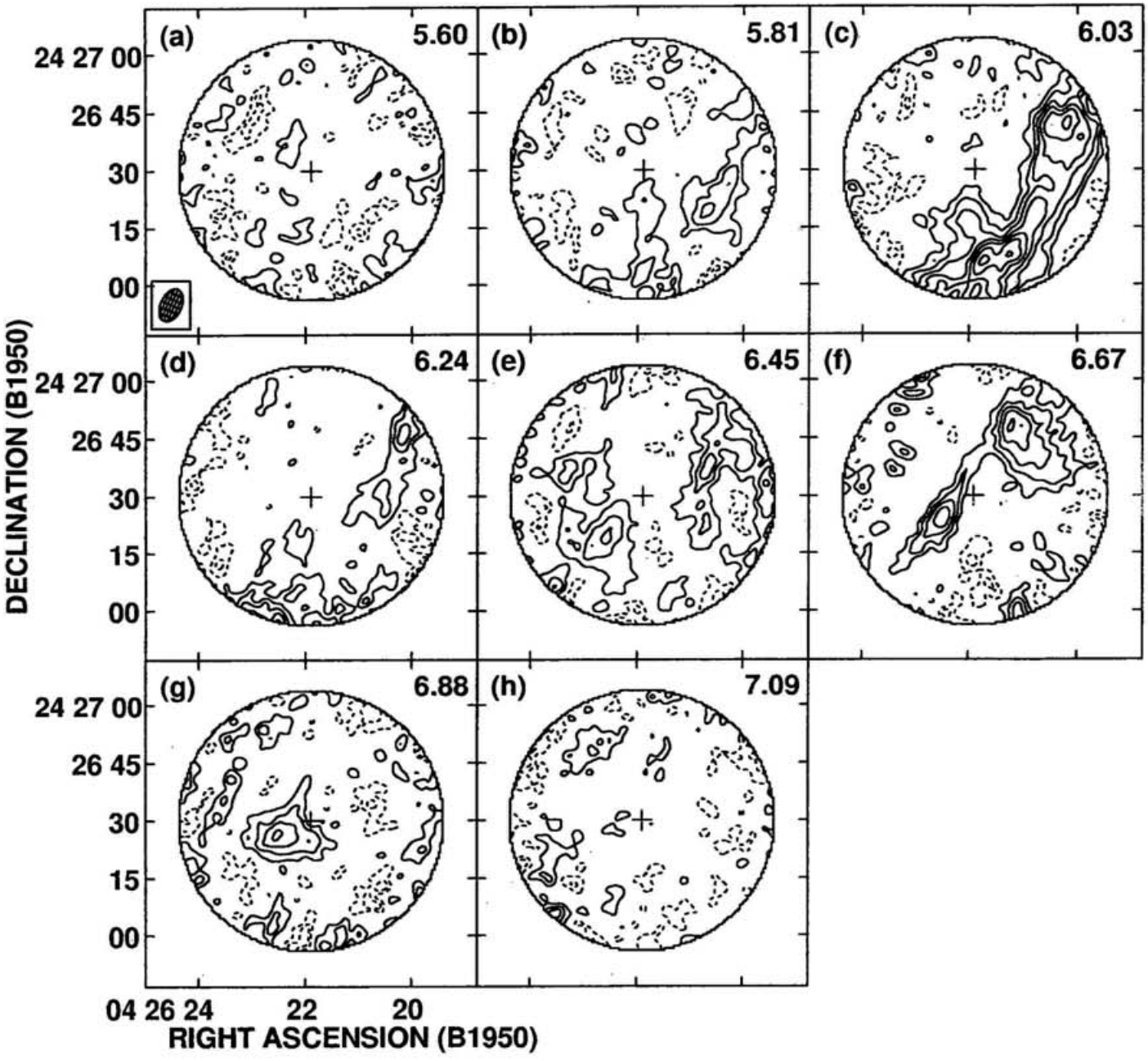
(a) 5.60
(b) 5.81
(c) 6.03
(d) 6.24
(e) 6.45
(f) 6.67
(g) 6.88
(h) 7.09
24 27 00
26 45
30
15
00
DECLINATION (B1950)
04 26 24
22
20
RIGHT ASCENSION (B1950)

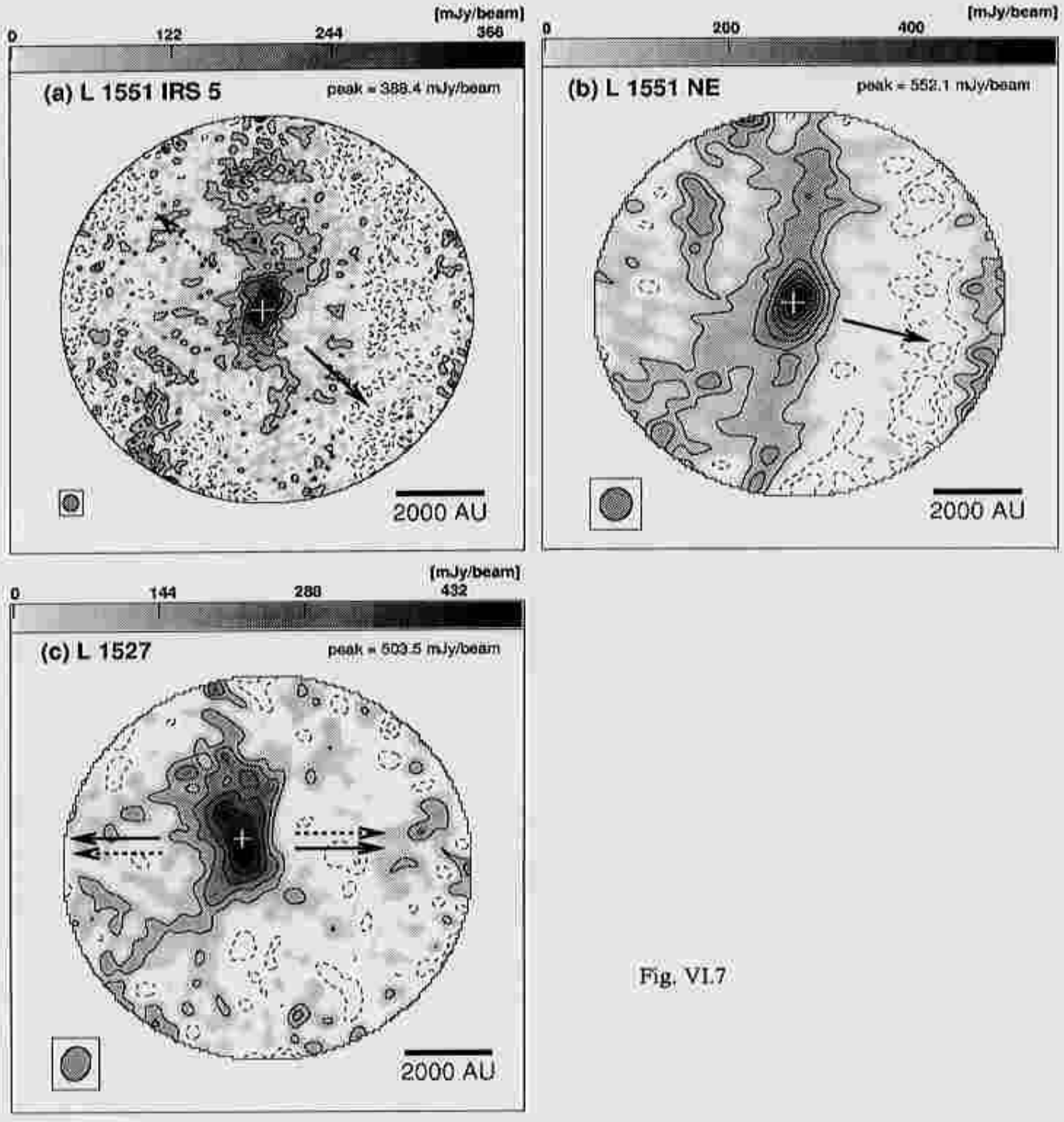
[mJy/beam]
0
122
244
366
(a) L 1551 IRS 5
peak = 388.4 mJy/beam
2000 AU
[mJy/beam]
0
200
400
(b) L 1551 NE
peak = 552.1 mJy/beam
2000 AU
[mJy/beam]
0
144
288
432
(c) L 1527
peak = 503.5 mJy/beam
2000 AU

Fig. VI.7

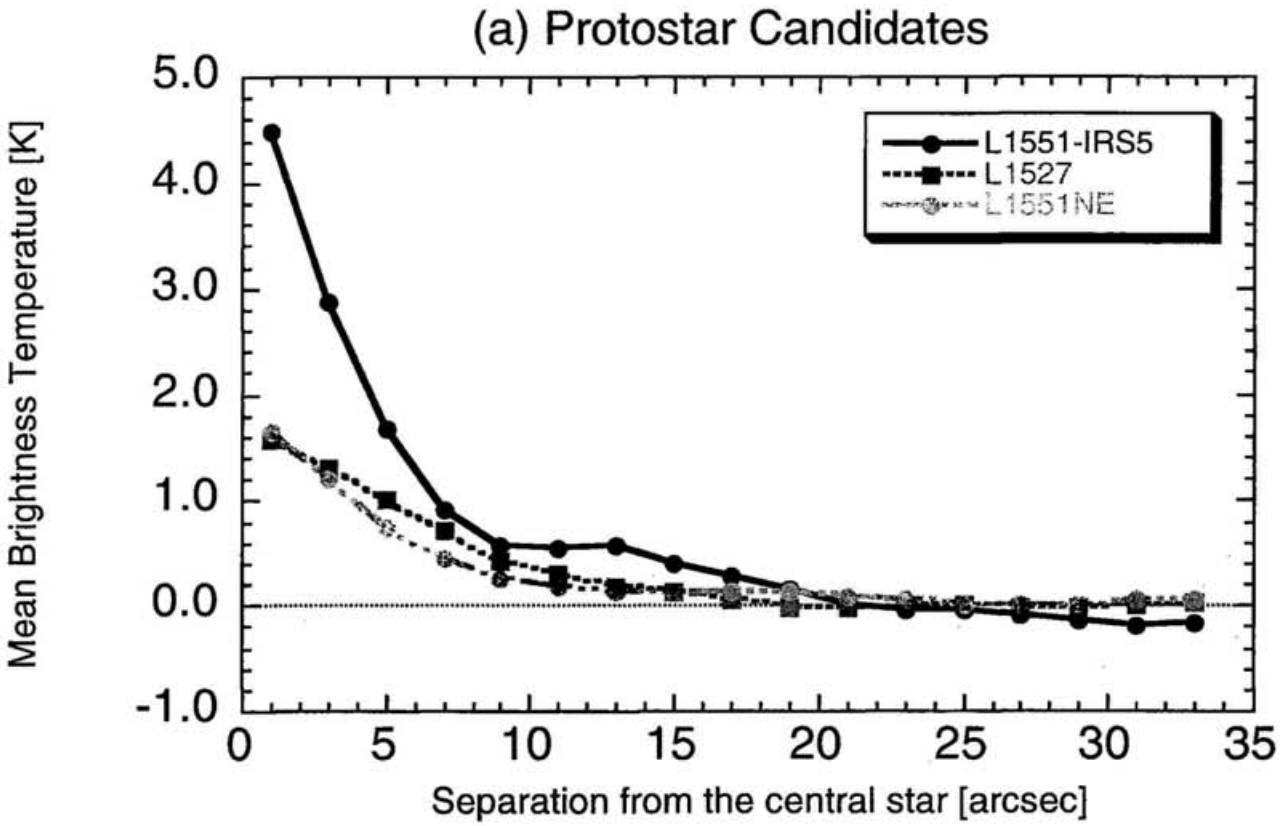
(a) Protostar Candidates
Mean Brightness Temperature [K]
5.0
4.0
3.0
2.0
1.0
0.0
-1.0
0
5
10
15
20
25
30
35
Separation from the central star [arcsec]
L1551-IRS5
L1527
L1551NE

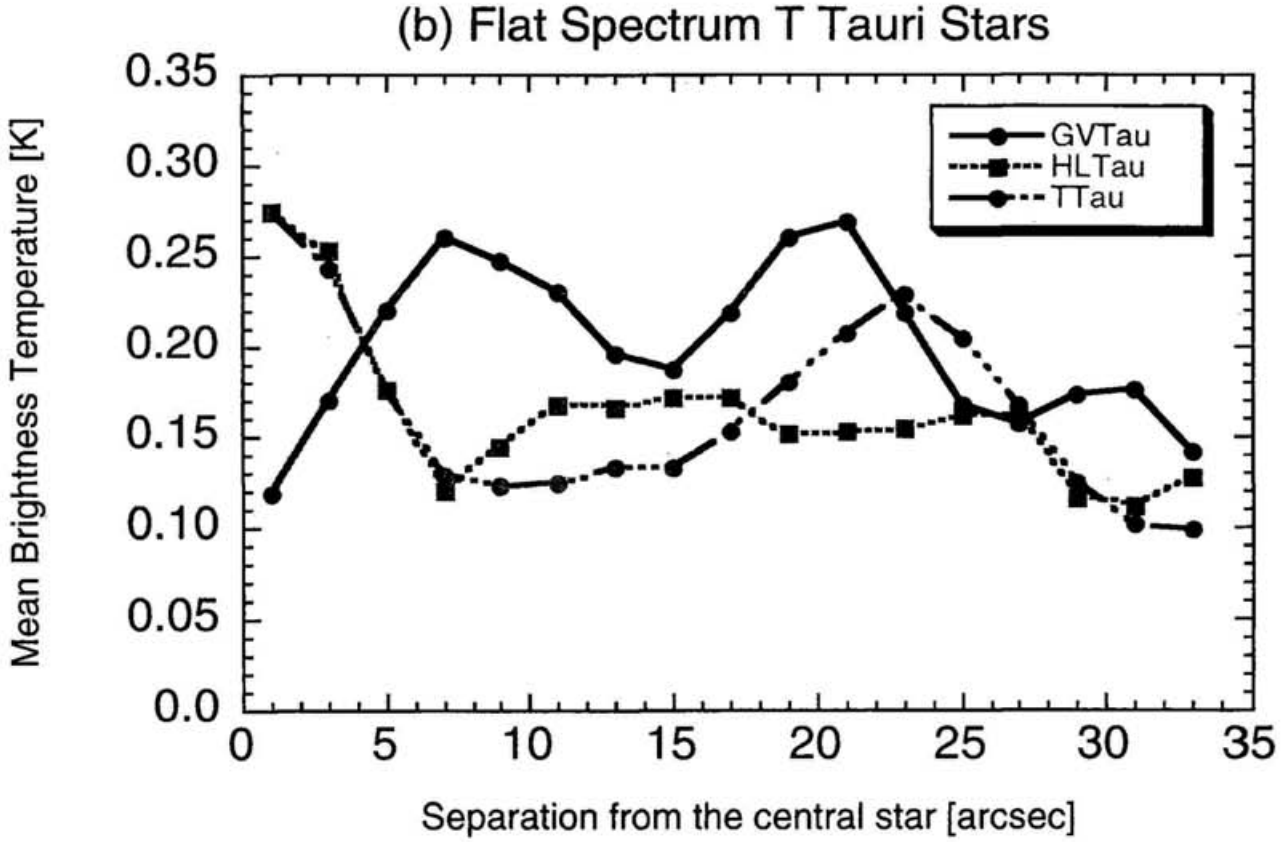
(b) Flat Spectrum T Tauri Stars
Mean Brightness Temperature [K]
0.35
0.30
0.25
0.20
0.15
0.10
0.05
0.0
0
5
10
15
20
25
30
35
Separation from the central star [arcsec]
GVTau
HLTau
TTau

Fig. VI.8

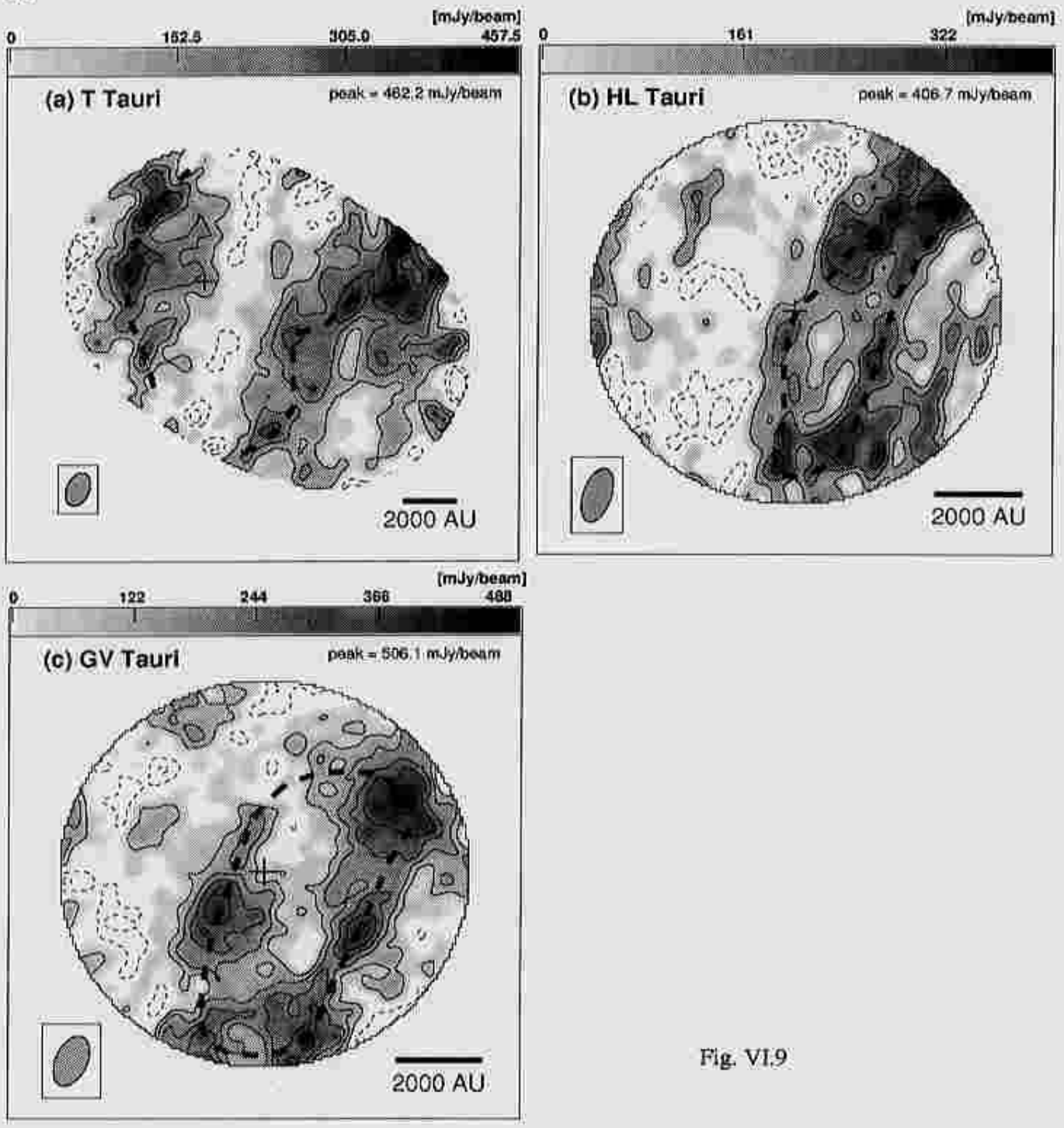
[mJy/beam]
0
152.5
305.0
457.5
(a) T Tauri
peak = 462.2 mJy/beam
2000 AU
[mJy/beam]
0
161
322
(b) HL Tauri
peak = 406.7 mJy/beam
2000 AU
[mJy/beam]
0
122
244
366
488
(c) GV Tauri
peak = 506.1 mJy/beam
2000 AU

Fig. VI.9

Chapter VII

Summary

The motivation of this study is to reveal the structure and evolution of circumstellar envelopes around low-mass young stellar objects. For this purpose, I have made observations of circumstellar gas with its sizescale of $\lesssim$ 5000 AU around young stellar objects in the Taurus Molecular Cloud, which is one of the nearest formation sites of low-mass stars, by using the Nobeyama Millimeter Array (NMA) and the Nobeyama 45 m telescope. The main results obtained with the present study are described in the following.

VII.1. The Structure of Circumstellar Envelopes around Protostar Candidates

In order to understand the circumstellar environment in the protostar stage, I made the aperture synthesis $C^{18}O$ ($J = 1 - 0$) observations of two protostar candidates L 1551 IRS 5 and L 1551 NE (Chapters II and III). The $C^{18}O$ ($J = 1 - 0$) emissions around L 1551 IRS 5 and L 1551 NE both show structures greater than 10″ in size and elongated in the directions perpendicular to the outflow axes. These $C^{18}O$ ($J = 1 - 0$) emissions indicate the existence of flattened envelopes with their sizes greater than 1400 AU around these sources.

The circumstellar envelope around L 1551 IRS 5, 2380 AU × 1050 AU in size and 0.062 $M_\odot$ in total mass, is perfectly resolved with the spatial resolution of 2.″8 × 2.″5 (corresponding to 390 AU × 350 AU), and its detailed structure are revealed as described in the following:

[Velocity Field] The velocity field in the envelope can be explained in terms of infall with rotation. The infall velocity in the outer part ($\gtrsim$ 300 AU) is equal to the free-fall velocity around a central mass of $\sim 0.1 M_\odot$, e.g., 0.5 km s^{-1} at r = 700 AU, while the rotation velocity, 0.24 km s^{-1} at the same radius, gets prominent at inner radii with a radial dependence of r^{-1}, indicating that the gas in the envelope is infalling dynamically conserving the angular momentum. According to these velocity distributions, the infall velocity is much larger than the rotation velocity in the outer regions of the envelope, whereas both velocities become comparable at the innermost part of the envelope ($r \approx$ 150 AU), which roughly coincides with the size of the dust continuum emission at 110 GHz. Around this radius, the infall motion probably shifts to the centrifugally supported motion, and a circumstellar disk (= protoplanetary disk) is being formed.

[Density Distribution] The comparisons of the observational results with the model calculations show that the envelope around L 1551 IRS 5 has (1) a moderately flattened density distribution, or (2) a spherical envelope with a bipolar cavity whose half-opening

angle is about 50°. Although it is impossible to judge which density distribution is more plausible, the results of the model calculations suggest that the infalling envelope around L 1551 IRS 5 has a geometrically thick, disklike density distribution.
[Mass Accretion Rate] The mass accretion rate is derived to be $\sim 6 \times 10^{-6} M_{\odot}$ yr^{-1} from the mass and outer radius of the envelope and the infall velocity in the envelope.

On the other hand, the velocity structure of the circumstellar envelope around L 1551 NE remains unclear. Although the observed velocity field near the star can be explained by rotation motion, no clear evidence for infall motion in the envelope has been obtained. This is probably because the infall velocity around L 1551 NE is too small to detect, which may be due to the extreme youth of L 1551 NE.

VII.2. Flat-Spectrum T Tauri Stars: The Objects in the "Transitional Phase" between the Protostar Stage and the T Tauri Stage

In order to investigate the evolution of circumstellar envelopes in the course from the protostar stage to the T Tauri stage, it is important to select the sources that are in the "transitional phase" between the two evolutionary stages, and compare their circumstellar environments with those around protostars. Both the observational and theoretical studies suggested that some T Tauri stars with so-called flat spectrum are good candidates for such objects (Hayashi, Ohashi, & Miyama 1993; Kitamura, Kawabe, & Saito 1996a; Calvet et al. 1994). I selected four flat-spectrum T Tauri stars that had not been observed in detail (T Tauri, GV Tauri, Haro 6-13, DO Tauri), and made aperture synthesis ^{13}CO ($J = 1 - 0$) observations of these sources (Chapters IV and V).

The ^{13}CO ($J = 1 - 0$) observations of T Tauri with the NMA and the Nobeyama 45 m telescope found a pair of "ringlike features" surrounding T Tauri with a radius of 30″ (corresponding to 4200 AU) at the velocities blueshifted and redshifted by less than 1 km s^{-1} from the systemic velocity. Comparisons between the spatial distributions of the ringlike features and those of the high-velocity outflows ejected from T Tauri suggest that these ^{13}CO ($J = 1 - 0$) rings can be interpreted as biconical outflowing shells in a nearly pole-on configuration. Since the spatial extent of the ^{13}CO ($J = 1 - 0$) rings is comparable to the typical size of the molecular cloud cores in the Taurus Molecular Cloud ($5000 - 10000$ AU in radius: Myers & Benson 1983; Mizuno et al. 1994), these outflowing shells are the part of the parent cloud core which is now dispersing under the influence of the stellar wind.

Such circumstellar environment around T Tauri is quite different from those around typical T Tauri stars that are accompanied by only compact ($< 10^3$ AU in radius) circumstellar disks. Therefore, it is strongly suggested that T Tauri is in the transitional phase between the protostar stage and the T Tauri stage.

Among the other three sources, the ^{13}CO ($J = 1 - 0$) emissions were detected around two objects (GV Tauri, Haro 6-13). Although the ^{13}CO ($J = 1 - 0$) observations did not completely reveal the circumstellar gas associated with these two sources, probably due to the absorption of the foreground gas, the detected ^{13}CO ($J = 1 - 0$) emissions have spatial extents much greater than the 10^3 AU, as is the case of T Tauri. These ^{13}CO ($J = 1 - 0$) emissions suggest the existence of the remnant parts of the molecular cloud cores, implying that GV Tauri and Haro 6-13 can also be regarded as the sources in the transitional phase between the protostar stage and the T Tauri stage.

VII.3. The Difference in the Circumstellar Environment between the Protostars and the Flat-Spectrum T Tauri Stars

I made aperture synthesis $C^{18}O$ ($J = 1 - 0$) observations of four flat-spectrum T Tauri stars around which spatially extended ^{13}CO ($J = 1 - 0$) emissions were detected, and compare the sptial distributions of the $C^{18}O$ ($J = 1 - 0$) emissions around these sources with those around protostars in order to investigate the evolution of the protostar envelopes (Chapter VI).

Spatially extended $C^{18}O$ ($J = 1 - 0$) emissions with size exceeding 10^3 AU were detected around three sources (T Tauri, HL Tauri, GV Tauri) with these observations. All these $C^{18}O$ ($J = 1 - 0$) emissions show no prominent peak at the stellar positions, but have several bright peaks located far from the central stars (Figure VII.1). Such spatial distributions are clearly different from those of the $C^{18}O$ ($J = 1 - 0$) emissions around protostars, which commonly show centrally condensed, disklike structure with their peaks at the stellar positions (Figure VII.2). The difference in the spatial distribution of the $C^{18}O$ ($J = 1 - 0$) emissions between the two categories can be interpreted as the difference in the density distributions of the circumstellar material, i.e., the degree of density concentration in the protostar envelopes gets weaker in the course of evolution from the protostar stage to the T Tauri stage.

The difference in the density structure of circumstellar gas between the protostars

and the flat-spectrum T Tauri stars implies the existence of the typical sizescale for the protostellar collapse, i.e., gravitational collapse in the protostar stage occurs only in the inner regions of molecular cloud cores with a finite sizescale. Interestingly, the $C^{18}O$ ($J = 1 - 0$) emissions around the flat-spectrum T Tauri stars seem to show "ringlike structures" $\sim$ 4000 AU in raidus, which are roughly centered at the stellar positions and are elongated in the directions perpendicular to the outflow axes. The existence of these ringlike structures may indicate that the flattened remnant cloud cores with "central voids" are commonly associated with these sources. If this is true, the typical radius of the central voids in the remnant cloud cores around the flat-spectrum T Tauri stars, $\sim 30''$ or $\sim$ 4200 AU in radius, must correspond to the sizescale of the infalling region in the protostellar stage, or the sizescale for the protostellar collapse.

VII.4. Overview of the Structure and Evolution of Protostar Envelopes

Figure VII.3 is the schematic illustration of the structure of a circumtellar envelope in each evolutionary stage that is based on the results of the present study. In the protostar stage, a central star-disk system grows by accretion of matter by dynamical collapse of the flattened envelope in the central part of a molecular cloud core. In the transitional phase from the protostar stage to the T Tauri stage, the degree of density concentration in the inner regions ($r \lesssim$ 4000 AU) of a cloud core becomes much smaller compare with the protostar stage, though there still remains remnant parts of the cloud core outside this region. Such a structure may formed by the gravitational collapse in the protostar stage occuring only in the inner regions of molecular cloud cores. The remnant parts of the cloud core will dissipate due to the accretion to the circumstellar disk and/or the dispersion induced by the energetic stellar wind, and finally, only the circumstellar disk with radius of $\sim$ 100 AU remains in the T Tauri stage.

— Figure Captions —

Fig. VII.1.— The $C^{18}O$ ($J = 1 - 0$) integrated intensity maps of three flat-spectrum T Tauri stars obtained with the NMA (Chpater IV); (*a*) the map of T Tauri, (*b*) the map of HL Tauri, and (*c*) the map of GV Tauri. The cross in each panel indicates the stellar position.

Fig. VII.2.— The $C^{18}O$ ($J = 1 - 0$) integrated intensity maps of three protostar candidates obtained with the NMA; (*a*) the map of L 1551 IRS 5 (Chapter II), (*b*) the map of L 1551 NE (Chapter III), and (*c*) the map of L 1527 (Ohashi et al. 1997a). The cross in each panel indicates the stellar position. The arrows indicate the directions of the outflows (*filled lines* : blueshifted, *dashed lines* : redshifted).

Fig. VII.3.— A schematic illustration of the evolution of circumstellar envelope around young stellar objects.

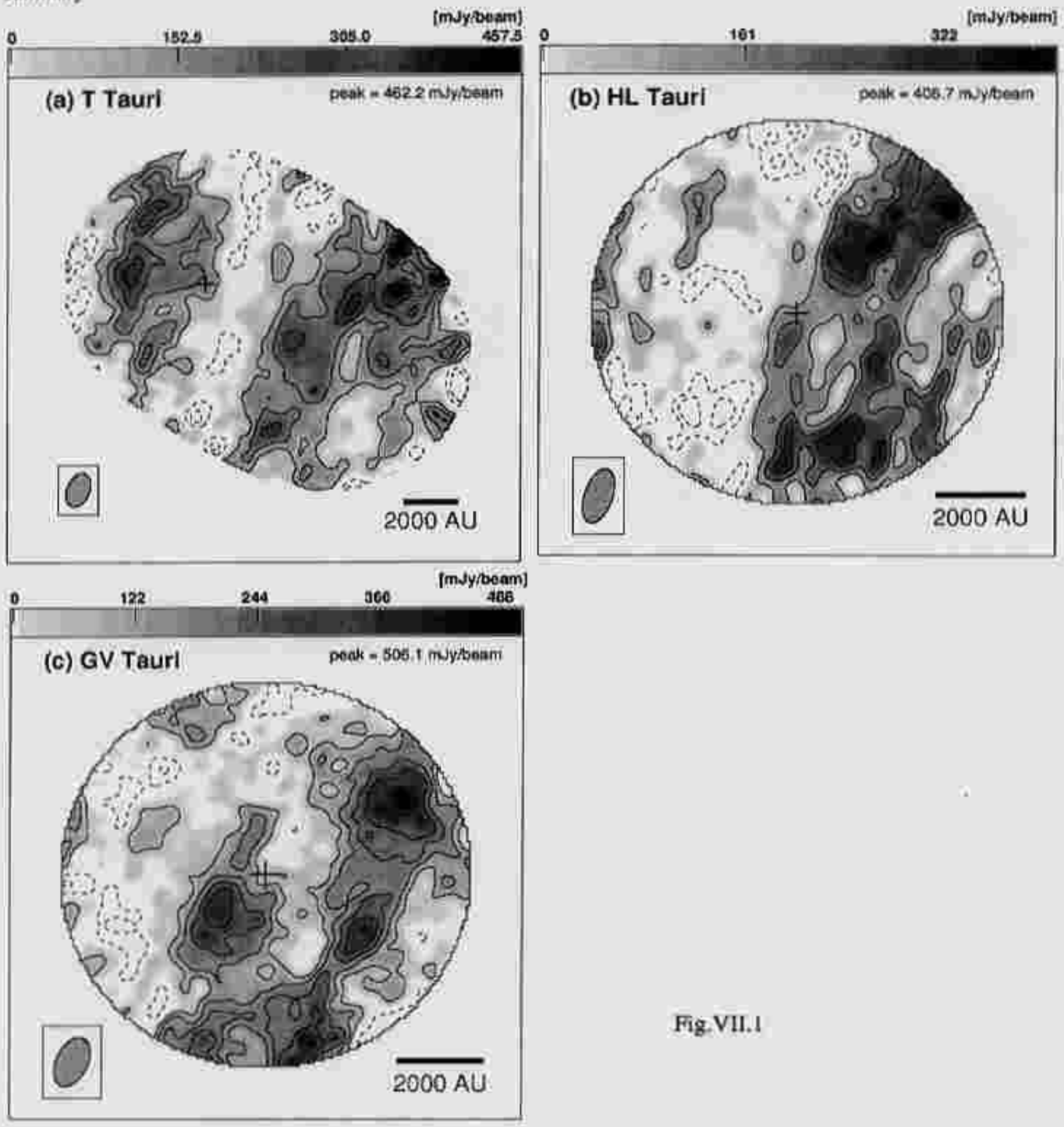
[mJy/beam]
0
152.5
305.0
457.5
(a) T Tauri
peak = 462.2 mJy/beam
2000 AU
[mJy/beam]
0
161
322
(b) HL Tauri
peak = 406.7 mJy/beam
2000 AU
[mJy/beam]
0
122
244
366
488
(c) GV Tauri
peak = 505.1 mJy/beam
2000 AU

Fig. VII.1

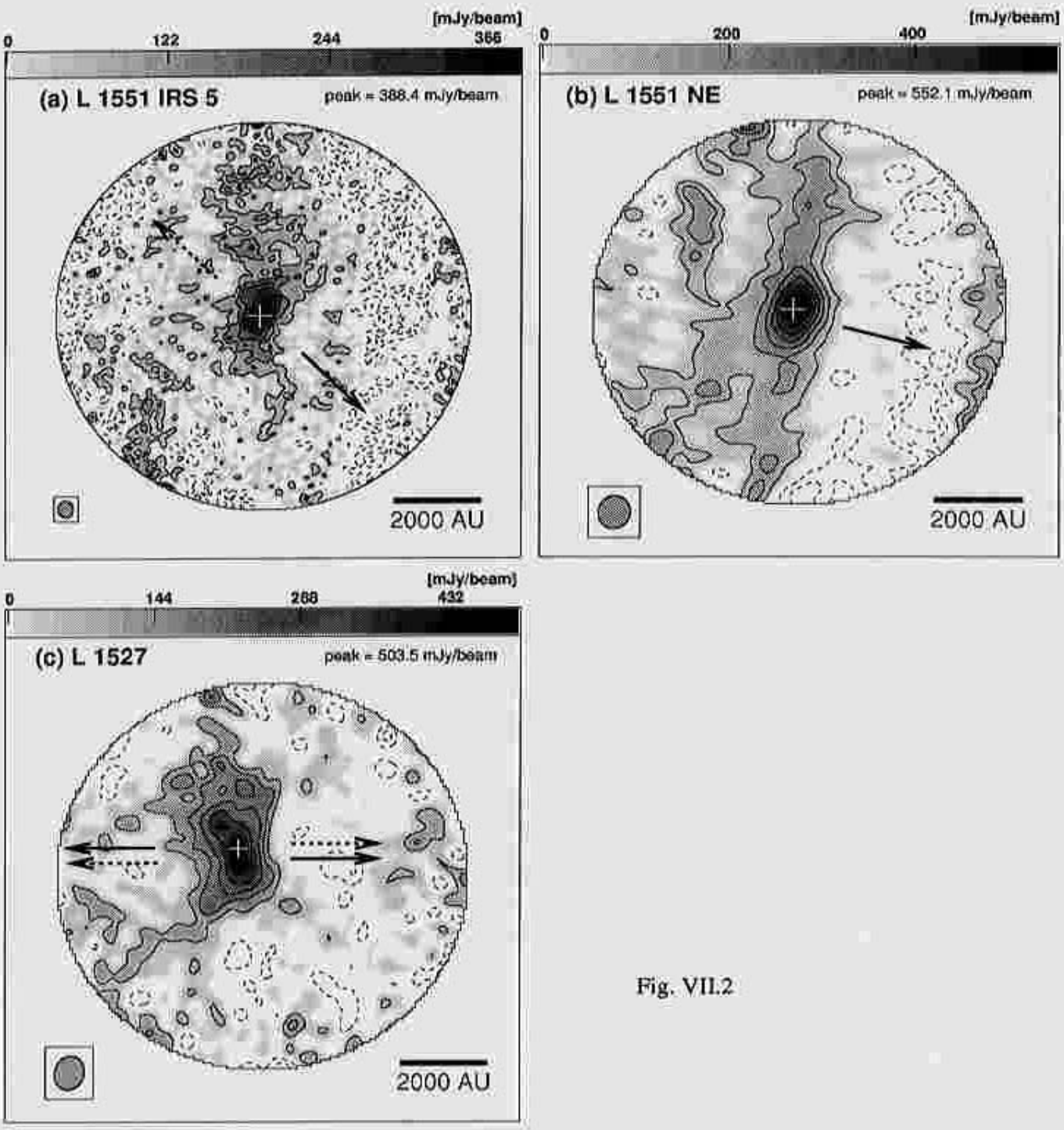
[mJy/beam]
0
122
244
365
(a) L 1551 IRS 5
peak = 388.4 mJy/beam
2000 AU
[mJy/beam]
0
200
400
(b) L 1551 NE
peak = 552.1 mJy/beam
2000 AU
[mJy/beam]
0
144
288
432
(c) L 1527
peak = 503.5 mJy/beam
2000 AU

Fig. VII.2

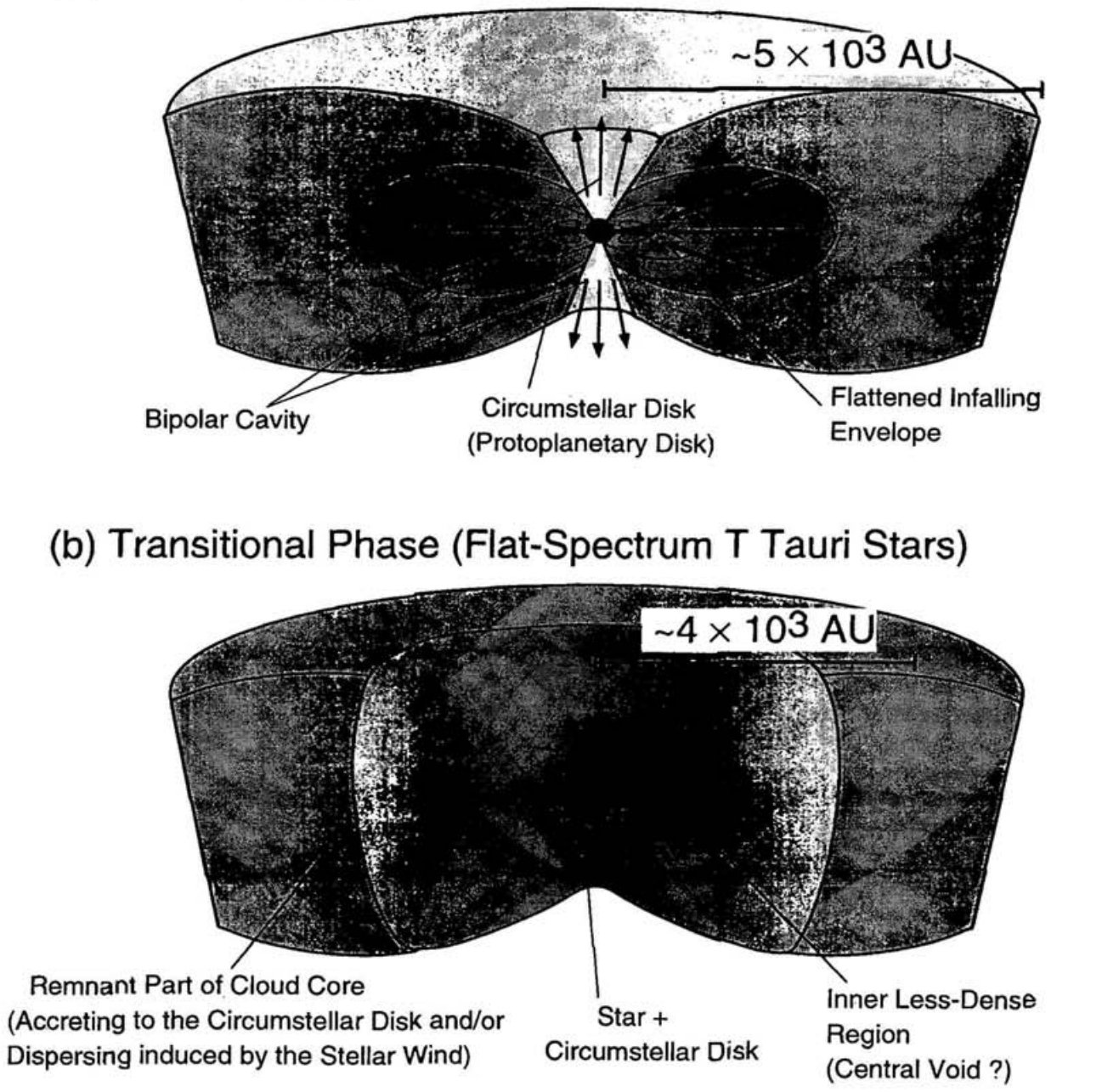
(a) Protostar Stage
~5 × 10³ AU
Bipolar Cavity
Circumstellar Disk
(Protoplanetary Disk)
Flattened Infalling
Envelope
(b) Transitional Phase (Flat-Spectrum T Tauri Stars)
~4 × 10³ AU
Remnant Part of Cloud Core
(Accreting to the Circumstellar Disk and/or
Dispersing induced by the Stellar Wind)
Star +
Circumstellar Disk
Inner Less-Dense
Region
(Central Void ?)
(c) T Tauri Stage
100 AU
Star + Circumstellar Disk

Figure VII.3

BIBLIOGRAPHY

Adams, F. C., Lada, C. J., & Shu, F. H. 1987, ApJ, 312, 788

Adams, F. C., Lada, C. J., & Shu, F. H. 1988, ApJ, 326, 865

Adams, F. C., & Shu, F. H. 1986, ApJ, 308, 836

André, P., Ward-Thompson, D., & Motte, F. 1996, A&A, 314, 625

Bachiller, R., Tafalla, M., & Chernicharo, J. 1994, ApJ, 425, L93

Barsony, M. & Chandler, C. J. 1993, ApJ, 406, L71

Beckwith, S. V. W., & Sargent, A. I. 1993, in Protostars and Planets III, ed. E. H. Levy & J. I. Lunine (Arizona), 521

Beckwith, S. V. W., Sargent, A. I., Chini, R. S., & Güsten, R. 1990, AJ, 99, 924

Beichman, C. A., Myers, P. C., Emerson, J. P., Harris, S., Benson, P. J., & Jennings, R. E. 1986, ApJ, 307, 337

Benson, P. J., & Myers, P. C. 1989, ApJS, 71, 89

Bertout, C., Basri, G., & Bouvier, J. 1988, ApJ, 330, 350

Bőhm, K. H., & Solf, J. 1994, ApJ, 430, 277

Bűhrke, T., Brugel, E. W., & Mundt, R. 1986, A&A, 163, 83

Butner, H. M., Moriarty-Schieven, G .H., Ressler, M. E., & Werner, M. W. 1995, in ASP Conf. Ser., 73, Airborne Astronomy Symposium on the Galactic Ecosystem, ed. M. R. Haas, J. A. Davidson, and E. F. Erickson (San Francisco: ASP), 235

Cabrit, S., Guilloteau, S., André, P., Bertout, C., Montmerle, T., & Schuster, K. 1996, A&A, 305, 527

Calvet, N., Hartmann, L., Kenyon, S. J., & Whitney, B. A. 1994, ApJ, 434, 330 (CHKW)

Cassen, P., & Moosman, A. 1981, Icarus, 48, 353

Chandler, C. J., Terebey, S., Barsony, M., Moore, T. C. T., & Gautier, T. N. 1996, ApJ, 471, 308

Chernicharo, J., & Guélin, M. 1987, A&A, 176, 299

Chikada, Y. et al. 1987, Proc. IEEE, 75, 1203

Cohen, M., Harvey, P. M., Schwartz, R. D., & Wilking, B. A. 1984, ApJ, 278, 671

Cohen, M., & Kuhi, L. V. 1979, ApJS, 21, 743

Draper, P. W., Warren-Smith, R. F., & Scarrott, S. M. 1985, MNRAS, 216, 7P

Dutrey, A., Guilloteau, S., & Simon, M. 1994, A&A, 286, 149

Dyck, H. M., Simon, T., & Zuckerman, B. 1982, ApJ, 255, L103

Edwards, S., & Snell, R. L. 1982, ApJ, 261, 151

Elias, J. H. 1978, ApJ, 224, 857

Emerson, J. P. et al. 1984, ApJ, 278, L49

Fuller, G. A., Ladd, E. F., Padman, R., Myers, P. C., & Adams, F. C. 1995, ApJ, 454, 862

Fuller, G. A., & Myers, P. C. 1992, ApJ, 384, 523

Galli, D., & Shu, F. H. 1993a, ApJ, 417, 220

Galli, D., & Shu, F. H. 1993b, ApJ, 417, 243

Ghez, A. M. et al. 1991, AJ, 102, 2066

Goodman, A. A., Benson, P. J., Fuller, G. A., & Myers, P. C. 1993, ApJ, 406, 528

Hartigan, P., Edwards, S., & Ghandour, L. 1995, ApJ, 452, 736

Hartmann, L., Boss, A. P., Calvet, N., & Whitney, B. A. 1994, ApJ, 430, L49

Hartmann, L., Calvet, N., & Boss, A. P. 1996, ApJ, 464, 387

Hartmann, L., Hewett, R., Stahler, S., & Mathieu, R. 1986, ApJ, 309, 275

Hartmann, L., Kenyon, S., & Hartigan, P. 1993, in Protostars and Planets III, ed. E. H. Levy & J. I. Lunine (Arizona), 497

Hayashi, C. 1966, ARA&A, 4, 171

Hayashi, C., Nakazawa, K., & Nakagawa, Y. 1985 in Protostars and Planets II, ed. D. C. Black & M. S. Matthews (Arizona), 1100

Hayashi, M. 1994 in ASP Conf. Ser., 59, Astronomy with Millimeter and Submillimeter Wave Interferometry, ed. M. Ishiguro & Wm. J. Welch (San Francisco: ASP), 212

Hayashi, M., Hasegawa, T., Ohashi, N., & Sunada, K. 1994, ApJ, 426, 234

Hayashi, M., Ohashi, N., & Miyama, S. M. 1993, ApJ, 418, L71

Herbig, G. H., & Bell, K. R. 1988, Lick Observatory Bull. No.1111

Herbst, W. et al. 1986, ApJ, 310, L71

Hodapp, K. -W. 1994, ApJS, 94, 615

Kaifu, N. et al. 1984, A&A, 134, 7

Kawabe, R., Ishiguro, M., Omodaka, T., Kitamura, Y., & Miyama, S.M. 1993, ApJ, 404, L63

Keene, J., & Masson, C. R. 1990, ApJ, 355, 635

Kenyon, S. J., Calvet, N., & Hartmann, L. 1993a, ApJ, 414, 676

Kenyon, S. J., & Hartmann, L. 1987, ApJ, 323, 714

Kenyon, S. J., Whitney, B. A., Gomez, M. & Hartmann, L. 1993b ApJ, 414, 773

Kitamura, Y., Kawabe, R., & Saito, M. 1996a, ApJ, 457, 277

Kitamura, Y., Kawabe, R., & Saito, M. 1996b, ApJ, 465, L137

Koerner, D. W., Sargent, A. I., & Beckwith, S. V. W. 1993, Icarus, 106, 2

Koerner, D. W., & Sargent, A. I. 1995, AJ, 109, 2138

Kőnigl, A., & Ruden, S. P. 1993, in Protostars and Planets III, ed. E. H. Levy & J. I. Lunine (Arizona), 641

Koo, B. -C. 1989, ApJ, 337, 318

Kutner, M. L., & Ulich, B. L. 1981, ApJ, 250, 341

Lada, C. J. 1987, in IAU Symp. 115, Star Forming Regions, ed. M. Peimbert & J. Jugaku (Dordrecht: Reidel), 1

Lada, C. J., & Wilking, B. A. 1984, ApJ, 287, 610

Lada, E. A., Strom, K. M., & Myers, P. C. 1993, in Protostars and Planets III, ed. E. H. Levy & J. I. Lunine (Arizona), 245

Larson, R. B. 1981, MNRAS, 194, 809

Lay, O. P., Carlstrom, J. E., Hills, R. E., & Phillips, T. G. 1994, ApJ, 434, L75

Leinert, Ch. et al. 1993, A&A, 278, 129

Leinert, Ch. & Haas, M. 1989, ApJ, 342, L39

Levreault, R. M. 1988, ApJS, 67, 283

Lin, D. N. C., Hayashi, M., Bell, K. R., & Ohashi, N. 1994, ApJ, 435, 821

Lizano, S. et al. 1988, ApJ, 328, 763

Looney, L. W., Mundy, L. G., & Welch, J., ApJ, 484, L157

Lucus, P. W., & Roche, P. F. 1996, MNRAS, 280, 1219

Maihara, T., & Kataza, H. 1991, A&A, 249, 392

Miyake, K., & Nakagawa, Y. 1995, ApJ, 441, 361

Mizuno, A., Onishi, T., Hayashi, M., Ohashi, N., Sunada, K., Hasegawa, T., & Fukui, Y. 1994, Nature, 368, 719

Momose, M., Ohashi, N., Kawabe, R., Hayashi, M., & Nakano, T. 1996, ApJ, 470, 1001 (Chapter IV of this thesis)

Momose, M., Ohashi, N., Kawabe, R., Hayashi, M., & Nakano, T. 1997 submitted to ApJ (Chapter II of this thesis)

Moriarty-Schieven, G. H., Butner, H. M., & Wannier, P. G. 1995a, ApJ, L55

Moriarty-Schieven, G. H., & Snell, R. L. 1988, ApJ, 332, 364

Moriarty-Schieven, G. H., Wannier, P. G, Butner, H. M., Mangum, J. G., Tamura, M. & Olmsted, V. K. 1995b, ApJ, 455, 190

Mundt, R., & Fried, J. W. 1983, ApJ, 274, L83

Mundt, R., Ray, T. P., & Bührke, T. 1988, ApJ, 333, L69

Mundt, R., Stocke, J., Strom, S. E., Strom, K. M., & Anderson, E. R. 1985, ApJ, 297, L41

Myers, P. C., & Benson, P. J. 1983, ApJ, 266, 309

Myers, P. C., Fuller, G. A., Mathieu, R. D., Beichman, C. A., Benson, P. J., & Schild, R. E. 1987, ApJ, 319, 340

Myers, P. C., Linke, R. A., & Benson, P. J. 1983, ApJ, 264, 517

Myers, P. C., Mardones, D., Tafalla, M., Williams, J. P., & Wilner, D. J. 1996, ApJ, 465, L133

Nakajima, T., & Golimowski, D. A. 1995, AJ, 109, 1181

Nakamura, F., Hanawa, T., & Nakano, T. 1995, ApJ, 444, 770

Nakano, T. 1998 ApJ in press

Nakano, T., Hasegawa, T., & Norman, C. 1995, ApJ, 450, 183

Narita, S., Nakano, T., & Hayashi, C. 1970, Prog. Theor. Phys., 43, 672

Ohashi, N., Hayashi, M., Ho, P. T. P., & Momose, M. 1997a, ApJ, 475, 211

Ohashi, N., Hayashi, M., Ho, P. T. P., Momose, M., & Hirano, N. 1996a, ApJ, 466, 957 (Paper I)

Ohashi, N., Hayashi, M., Ho, P. T. P., Momose, M., Tamura, M., Hirano, N., & Sargent, A. I. 1997b, ApJ, 488, 317

Ohashi, N., Hayashi, M., Kawabe, R., & Ishiguro, M. 1996b, ApJ, 466, 317

Ohashi, N., Kawabe, R., Hayashi, M., & Ishiguro, M. 1991, AJ, 102, 2054

Onishi, T., Mizuno, A., Kawamura, A., Ogawa, H., & Fukui, Y. 1996, ApJ, 465, 815

Palla, F. 1991, in IAU Symp. 147, Fragmentation of Molecular Clouds and Star Formation. ed. E. Falgarone, F. Boulanger & G. Duvert (Dordrecht: Reidel), 331

Panagia, N. 1991, in The Physics of Star Formation and Early Stellar Evolution, ed. C. J. Lada & N. D. Kylafis (Dordrecht: Kluwer), 565

Panagia, N., & Felli, M. 1975, A&A, 39, 1

Ruiz, A., Alonso, J. L., & Mirabel, I. F. 1992, ApJ, 394, L57

Saigo, K., & Hanawa, T. 1998, ApJ in press

Saito, M. 1997, Ph.D. Thesis, The University of Tokyo

Saito, M. et al. 1995, ApJ, 453, 384

Saito, M., Kitamura, M., Kawabe, R., & Sunada, K. 1996, ApJ, 473, 464 (Paper II)

Sargent, A. I., Beckwith, S., Keene, J., & Masson, C. R. 1988, ApJ, 333, 936

Schuster, K. F. 1994, Ph.D. Thesis, Max-Plnack-Institut fűr Extraterrestrische Physik

Schuster, K. F., Harris, A. I., Anderson, N., & Russell, A. 1993, ApJ, 412, L67

Schuster, K. F., Harris, A. I., & Russell, A. P. G. 1997, A&A, 321, 568

Scoville, N. Z., Sargent, A. I., Sanders, D. B., Claussen, M. J., Masson, C. R., Lo, K. Y., & Phillips, T. G. 1986, ApJ, 303, 416

Shu, F. H., 1977, ApJ, 214, 488

Shu, F. H., Najita, J., Ostriker, E., Wilkin, F., Ruden, S., & Lizano, S. 1994, ApJ, 429, 781

Skinner, S. L., & Brown, A. 1994, AJ, 107, 1461

Solf, J., Bőhm, K. H., & Raga, A. 1988, ApJ, 334, 229

Stahler, S. W., Shu, F. H., & Taam, R. 1980. ApJ, 241, 637

Stapelfeldt, K. R. et al. 1995, ApJ, 449, 883

Strom, K. M., Strom, S. E., Edwards, S., Cabrit, S., & Skrutskie, M. F. 1989, AJ, 97, 1989

Strom, K. M., Strom, S. E., Kenyon, S. J., & Hartmann, L., W. 1988, AJ, 95, 534

Strom, K. M., Strom, S. E., & Vrba, F. J. 1976, AJ, 81, 320

Strom, K. M., Strom, S. E., Wolff, S. C., Morgan, J. & Wenz, M. 1986, ApJS, 62, 39

Sunada, K., Kawabe, R., & Inatani, J. 1993, Int. J. Infrared Millimeter Waves, 14, 1251

Sunada, K., Noguchi, T., Tsuboi, M., & Inatani, J. 1995, in ASP Conf. Ser., 75, Multi-Feed Systems for Radio Telescopes, ed. D. T. Emerson & J. M. Payne (San Francisco: ASP), 230

Tamura, M., Ohashi, N., Hirano, N., Itoh, Y., & Moriarty-Schieven, G. H. 1996, AJ, 112, 2076

Tatematsu, K. et al. 1993, ApJ, 404, 603

Terebey, S., Shu, F. H., & Cassen, P. 1984, ApJ, 286, 529

Tomisaka, K. 1996, PASJ, 48, L97

Uchida, Y., Kaifu, N., Shibata, K., Hayashi, S. S., Hasegawa, T., & Hamatake, H. 1987, PASJ, 39, 907

Ulich, R. K. 1976, ApJ, 210, 377

van Langevelde, H. J., van Dishoeck, E. F., & Blake, G. A. 1994a, 425, L45

van Langevelde, H. J., van Dishoeck, E. F., van der Werf, P. P., & Blake, G. A. 1994b, A&A, 287, L25

Walker, C. K., Narayanan, G., & Boss, A. P. 1994, ApJ, 431, 767

Ward-Thompson, D., Scott, P. F., Hills, R. E., & André, P. 1994, MNRAS, 268, 276

Weintraub, D. A., Kastner, J. H., Zuckerman, B., & Gatley, I. 1992, ApJ, 391, 784

Weintraub, D. A., Masson, C., & Zuckerman, B. 1989, ApJ, 344, 915 (WMZ)

Whitney, B. A., & Hartmann, L. 1993, ApJ, 402, 605

Xie, T., Goldsmith, P. F., & Patel, N. 1993, ApJ, 419, L33

Zhou, S. 1992, ApJ, 394, 204

Zhou, S., Evans, N. J., II, Kőmpe, C., & Walmsley, C. M. 1993, ApJ, 404, 232

Zhou, S., Evans, N. J., II, Wang, Y., Peng, R., & Lo, K. Y. 1994, ApJ, 433, 131